UNIVERSITÀ DEGLI STUDI DI PADOVA
Dipartimento di Fisica e Astronomia “Galileo Galilei”

CORSO DI DOTTORATO DI RICERCA IN ASTRONOMIA
CICLO XXXV

Expanding the sample of electron capture supernova candidates

Direttore della scuola: Ch.mo Prof. Giovanni Carraro
Supervisore: Dr. Andrea Pastorello

Dottorando: Giorgio Valerin

Sommario

Le supernove a cattura elettronica (ECSN) sono una classe di esplosioni che avvengono al collasso di un nucleo di O-Ne-Mg, invece che al più comune collasso di un nucleo di Fe. Questi eventi dovrebbero essere la conclusione del percorso evolutivo di stelle isolate con masse comprese tra 8 e 10 $M_{\odot}$: le ECSN segnano il confine tra le stelle abbastanza massive da esplodere come supernove (SNe) e le stelle che evolveranno in nane bianche. Ad oggi, tuttavia, non c'è ancora stata un'identificazione univoca di una ECSN. Il motivo per cui le ECSN sono così sfuggenti è duplice. Prima di tutto, questi transienti dovrebbero essere 10 volte meno energetici di una SN standard: questo limita la ricerca delle ECSN all'universo locale. D'altra parte, le proprietà attese per le ECSN presentano una parziale sovrapposizione con altre esplosioni deboli, rendendo difficile un'identificazione certa.
In questo lavoro analizzerò sei transienti, studiando se le loro proprietà sono compatibili con una ECSN. I primi due oggetti appartengono alla sottoclasse delle SNe IIP a bassa luminosità. SN 2021aai è un oggetto di transizione che collega la famiglia delle SNe IIP deboli con le SNe IIP standard. Il suo progenitore, caratterizzato attraverso un modello idrodinamico, è probabilmente una supergigante rossa (RSG). L'origine di SN 2020cxd è meno chiara: questa SN, debole anche nella famiglia di SNe a bassa luminosità, è compatibile sia con il collasso di un nucleo di Fe che con una ECSN. Infine, presenterò le proprietà di quattro Transienti Rossi a Luminosità Intermedia (ILRTs), in particolare AT 2019abn, AT 2019ahd, AT 2019udc e NGC 300 OT. Se gli ILRTs siano davvero degli eventi terminali è stato oggetto di discussione, vista la loro bassa luminosità e la mancanza di materiale ad alta velocità nei loro spettri. Tuttavia, ho trovato delle righe larghe negli spettri in fasi avanzate di AT 2019ahd e NGC 300 OT che possono mostrare che gli ILRT sono davvero delle SNe, forse anche ECSN.

Abstract

Electron capture supernovae (ECSNe) are a class of explosions expected to arise from the collapse of a degenerate O-Ne-Mg core, rather than from the more classical Fe core collapse. Such events should be the endpoint of the evolution of single stars with masses between 8 and 10 $M_{\odot}$: ECSNe mark the threshold between the stars massive enough to explode as supernovae (SNe) and stars which evolve into white dwarfs. To this day, however, there has not been a clear and undisputed ECSN detection. The reason behind the elusiveness of ECSNe is twofold. Firstly, these transients are expected to release 10 times less energy than a standard SN: their faintness limits the search for ECSNe to the local universe. On the other hand, the expected properties of ECSNe present some overlap with other weak explosions, hindering a definite identification.
In this work I analyse six transients, investigating if their properties are compatible with an ECSN origin. The first two objects belong to the Low Luminosity SNe IIP subclass. SN 2021aai is a transitional object, linking the family of faint SNe IIP with the standard SNe IIP. Its progenitor star, characterised through hydrodynamical modelling, is most likely a red supergiant (RSG). The origin of SN 2020cxd is less clear: this SN, faint even among the low luminosity SNe subclass, is compatible both with a Fe core collapse from a low mass RSG and with an ECSN event. Finally, I study the properties of four Intermediate Luminosity Red Transients (ILRTs), namely AT 2019abn, AT 2019ahd, AT 2019udc and NGC 300 OT. Whether ILRTs are actually terminal explosions has been debated, given their low luminosity and lack of fast ejecta in their spectra. However, I find evidence of broad lines in the late time spectra of AT 2019ahd and NGC 300 OT which may prove that ILRTs are indeed SNe events, and possibly ECSNe.

List of Papers

Valerin et al. (2022); G. Valerin, M. L. Pumo, A. Pastorello, A. Reguitti, N. Elias-Rosa, C. P. Gútierrez, E. Kankare, M. Fraser, P. A. Mazzali, D. A. Howell, R. Kotak, L. Galbany, S. C. Williams, Y.-Z. Cai, I. Salmaso, V. Pinter, T. E. Müller-Bravo, J. Burke, E. Padilla Gonzalez, D. Hiramatsu, C. McCully, M. Newsome, C. Pellegrino. *Low luminosity Type II supernovae - IV. SN 2020cxd and SN 2021aai, at the edges of the sub-luminous supernovae class.* MNRAS, 513, 4983.

Valerin et al. (2023); G. Valerin, A. Pastorello, A. Reguitti, S. Benetti, Y.–Z. Cai, T.-W. Chen, N. Elias–Rosa, D. Eappachen, M. Fraser, A. Gangopadhyay, E. Y. Hsiao, D. A. Howell, J. Jencson, E. Kankare, R. Kotak, C. Inserra, L. Izzo, P. A. Mazzali, K. Misra, G. Pignata, S. J. Prentice, D. J. Sand, S. J. Smartt, M. D. Stritzinger, S. Valenti, J.∼P. Anderson, J. E. Andrews, R. C. Amaro, C. R. Benn, S. Brennan, F. Bufano, E. Callis, E. Cappellaro, C. McCully, M. Ergon, A. Fiore, M. D. Fulton, L. Galbany, M. Hamuy, T. Heikkilä, D. Hiramatsu, E. Karamehmetoglu, H. Kuncarayakti, G. Leloudas, M. Lundquist, J. Mauerhan, T. E. Müller-Bravo, M. Nicholl, P. Ochner, E. Padilla Gonzalez, E. Paraskeva, C. Pellegrino, D. E. Reichart, T. M. Reynolds, R. Roy, F. Salgado, I. Salmaso, M. Turatto, L. Tomasella, S. D. Van Dyk, S. Wyatt, D. R. Young. *Intermediate Luminosity Red Transients I - Photometric properties* (To be submitted to MNRAS)

Valerin et al. (2023); G. Valerin, A. Pastorello, A. Reguitti, S. Benetti, Y.–Z. Cai, T.-W. Chen, N. Elias–Rosa, D. Eappachen, M. Fraser, A. Gangopadhyay, E. Y. Hsiao, D. A. Howell, J. Jencson, E. Kankare, R. Kotak, C. Inserra, L. Izzo, P. A. Mazzali, K. Misra, G. Pignata, S. J. Prentice, D. J. Sand, S. J. Smartt, M. D. Stritzinger, S. Valenti, J.∼P. Anderson, J. E. Andrews, R. C. Amaro, C. R. Benn, S. Brennan, F. Bufano, E. Callis, E. Cappellaro, C. McCully, M. Ergon, A. Fiore, M. D. Fulton, L. Galbany, M. Hamuy, T. Heikkilä, D. Hiramatsu, E. Karamehmetoglu, H. Kuncarayakti, G. Leloudas, M. Lundquist, J. Mauerhan, T. E. Müller-Bravo, M. Nicholl, P. Ochner, E. Padilla Gonzalez, E. Paraskeva, C. Pellegrino, D. E. Reichart, T. M. Reynolds, R. Roy, F. Salgado, I. Salmaso, M. Turatto, L. Tomasella, S. D. Van Dyk, S. Wyatt, D. R. Young. *Intermediate Luminosity Red Transients II - Spectroscopic properties* (To be submitted to MNRAS)

Contents

List of Figures

Chapter 1

Introduction

Supernovae (SNe) consists in the violent explosion of a star, resulting in a massive release of energy in a short time. In SNe, matter is accelerated up to a velocity of few 10^4 km s^{-1}, corresponding to a kinetic energy of the order of $\sim 10^{51}$ erg. Such energy is roughly equal to the gravitational binding energy of the stellar core prior the explosion: any powering mechanism driving the SN event should match this binding energy in order to have a successful explosion of the star. In contrast, only a small fraction of the energy is released in the form of radiation, typically $\sim 10^{49}$ erg. SNe have an evolutionary timescale around $\sim$100 days, and their luminosity can rival with the luminosity of their host galaxy, allowing us to discover and study exploding stars even at great distances.

The first step taken to understand SNe was to accurately classify each object based on its spectroscopic properties near maximum luminosity. Originally, SNe were divided in two classes: the so called "Type I", which lack hydrogen, and "Type II", characterized by hydrogen rich spectra (Minkowski 1941). This simple dichotomy was progressively refined thanks to systematic surveys, which greatly increased the number of discovered SNe (e.g. Zwicky 1968). In Figure 1.1 is shown a taxonomic map displaying an updated SN classification (Turatto 2003). Type I, or hydrogen poor, SNe are divided in three subclasses, depending on the different chemical signatures characterizing their optical spectra. Objects showing strong Si II features are classified as SNe Ia. On the other hand, transients with spectra dominated by He I lines without evidence of Si II lines are labelled as SNe Ib. Finally SNe with very weak Si II features and no He I lines are classified as SNe Ic.

A first distinction within Type II, or hydrogen rich, SNe, is based on their light curve shape rather than their spectral features (Barbon et al. 1979). The light curves of SNe IIL display, immediately after maximum luminosity, a fast and linear decline in magnitudes (hence the "L"). Conversely, SNe IIP are characterized by a long period of roughly constant luminosity called "plateau" (hence the "P"), which may last up to $\sim$140 days (Valerin et al. 2022). There are indeed two other important SNe II subclasses. SNe IIb display Balmer lines in their early spectra, but later on their evolution resembles that of a Type Ib SN. Finally, SNe IIn are characterized by narrow spectral lines (hence the "n") with a full width at half maximum (FWHM) of few 100 km s^{-1}, one order of magnitude smaller than the typical FWHM of the emission lines in classical SNe.

Of course, such schematic classification cannot precisely describe the variety of phenomena that we observe today. In recent years, abundant efforts have been directed towards the discovery of a larger and larger number of optical transients. In particular, wide field surveys have been used to scan the

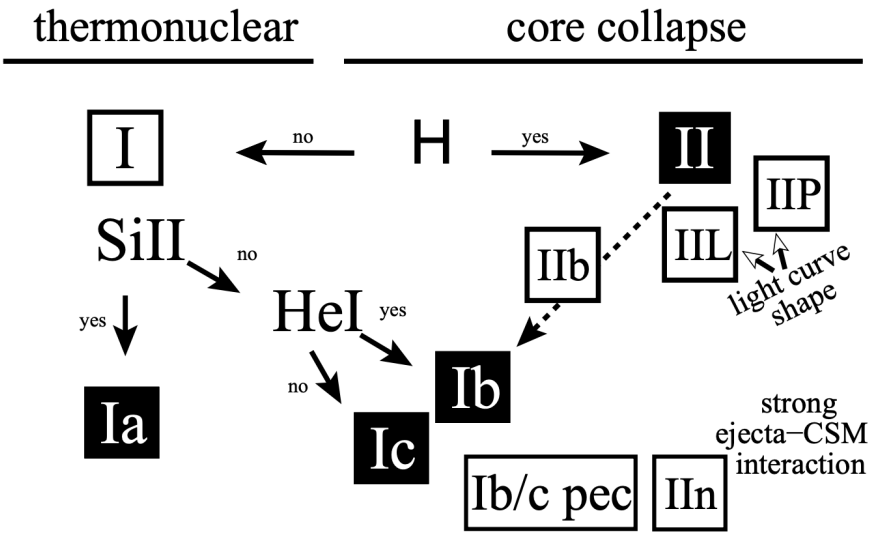

Figure 1.1: Schematic overview of SNe taxonomy. The four main SN types are displayed with black squares (Figure from Turatto 2003)

whole sky in order to detect new transients. Some notable examples of such projects are SkyMapper (Keller et al. 2007), the Palomar Transient Factory (Law et al. 2009), Pan-STARRS (Kaiser et al. 2010), and the ongoing All-Sky Automated Survey for Supernovae (Shappee et al. 2014), which has discovered more than 1000 SNe on its own. Once a transient is discovered, it is paramount to classify it through spectroscopic observations: in this context, the Public European Southern Observatory Spectroscopic Survey of Transient Objects (PESSTO) consortium has proven to be an effective tool to quickly obtain spectra of newly discovered objects (Smartt et al. 2015a). Finally, high cadence surveys like the Zwicky Transient Facility (ZTF, Graham et al. 2019) not only provide alerts regarding new transients, but they also produce well sampled light curves for previously discovered objects, in the case of ZTF with a limiting magnitude of ∼19 mag. A similar result is obtained serendipitously with all-sky surveys that were not specifically designed to discover SNe: an excellent example is given by the Asteroid Terrestrial-impact Last Alert System (ATLAS) survey (Tonry et al. 2018). As the name suggests, ATLAS was born to detect asteroids that could impact Earth, but by observing the whole sky searching for moving objects, this survey proved to be effective also in discovering and monitoring SNe.

With such abundance of SNe discovered by a variety of surveys, it is inevitable to find outliers and peculiar transients, which cannot fit in the simple scheme presented in Figure 1.1. Furthermore, the classification discussed so far focuses on the different observable features found in SNe, but we did discuss why such differences arise. The following sections will present the different mechanisms that lead to the explosion of a star and the consequences on the observed characteristics of the resulting SN.

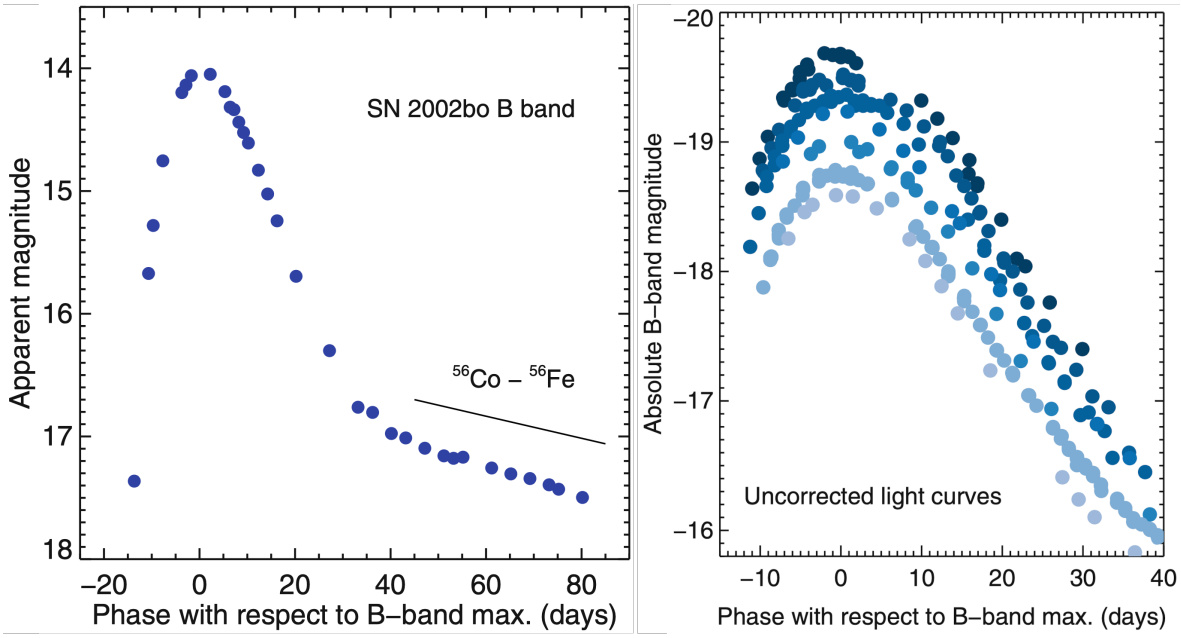

Figure 1.2: Left panel: example of a classical light curve of a SN Ia, dominated by radioactive decay of ^{56}Ni. Right panel: display of the homogeneity of SNe Ia. Different objects show quite similar behaviour (Figures from Maguire 2017)

1.1 Thermonuclear Supernovae: Type Ia

Type Ia SNe originate from a thermonuclear explosion of a white dwarf (WD), typically with a chemical composition dominated by carbon and oxygen. These stars are in hydrostatic equilibrium thanks to the electron degeneracy pressure, which balances the gravitational force that would otherwise cause the star to shrink. Such configuration, however, is only stable up to a threshold mass, called Chandrasekhar mass (M_{Ch}), which is approximately 1.4 $M_{\odot}$. There are two main progenitor channels that explain how a WD could reach the M_{Ch}, both of which envision some interaction with a companion star: the single degenerate and double degenerate scenarios (Maeda & Terada 2016).

In the single degenerate scenario, the WD is in a binary system with a non degenerate star (usually a red giant or a main sequences star), which is progressively stripped of the outer envelopes due to Roche Lobe overflow. The stripped material is accreted on the WD, which progressively increases in mass until M_{Ch} is reached. Such process is similar to what happens in Classical Novae, which we can directly observe in the Milky Way, but in order to have a SN Ia the accretion rate must be constrained in a specific range. On the other hand, in the double degenerate scenario, the binary system consists of two WDs. Their orbit progressively shrinks due to loss of angular momentum driven by gravitational waves emission, resulting in a violent impact and a subsequent explosion. To our current knowledge, both progenitor channels could contribute to produce the observed population of SNe Ia.

1.1.1 Explosion Mechanism

Regardless of the manner in which the M_{Ch} is reached, the subsequent physical processes are quite similar. While approaching the critical M_{Ch}, carbon burning is ignited in the core of the star. Since

matter is in a strongly degenerate state, the energy released by the nuclear burning does not cause an expansion of the gas, as would happen in an ideal gas. The additional energy leads instead to a temperature increase, boosting the rates of nuclear reactions which release even more energy: this feedback loop results in an explosive wave of nuclear reactions sweeping through the star, synthesising abundant ^{56}Ni and other Fe peak elements. Depending on the speed with which nuclear reactions travel within the star, there are two different modes of dynamical combustion: a subsonic nuclear burning front causes a deflagration, while a supersonic nuclear burning front leads to a detonation (Branch & Wheeler 2017a). In the case of a deflagration, pressure waves can rearrange the unburned material, causing an expansion, before the arrival of the nuclear burning front. On the other hand, since detonations are intrinsically supersonic, no expansion can occur in the unburned material before the burning front sweeps through the whole star. Therefore, deflagrations and detonations differ for the density at which matter undergoes explosive nuclear reactions, heavily influencing the results of the nucleosynthesis. The two modes are not mutually exclusive: there are models in which the explosion starts as a deflagration and evolves into a detonation (Khokhlov 1991). In any case, the energy released is sufficient to gravitationally unbind the entire star, therefore no remnant is left behind.

1.1.2 Observable Properties

Since M_{Ch} is similar for all the exploding stars, the observable properties of SNe Ia are remarkably homogeneous. First of all, the large amount of ^{56}Ni synthesized defines the main properties of the light curve shape in SNe Ia. In fact, the two decay processes ^{56}Ni $\rightarrow$ ^{56}Co (half life 6.1 days) and ^{56}Co $\rightarrow$ ^{56}Fe (half life 77.3 days) power the peak and the late tail of the light curve, respectively (Figure 1.2, left panel). The light curve shapes of SNe Ia tend to be similar, and their absolute magnitude peaks around M_B = -19.1 mag (Ashall et al. 2016), with a modest scatter (Figure 1.2, right panel). Ultimately, this homogeneity allowed us to use SNe Ia as standard candles and discover the accelerated expansion of the universe (Riess et al. 1998). As for the spectra, they are characterized by broad lines with expansion velocities between 10000 and 25000 km s^{-1} at early times, with an abundance of intermediate mass elements' features (Figure 1.3). In fact, during the explosion, the core of the WD undergoes complete nuclear burning, producing Fe peak elements, while outer layers of the star are only partially processed, resulting in the nucleosynthesis of intermediate-mass elements like Si, Ca and Mg (Maguire 2017).

SNe Ia are observed in all galaxy types, albeit with different rates (Hamuy et al. 1996). This reflects the fact that binary systems made up by two WD, or by a WD and a non-degenerate star, can be remarkably long lived: therefore, even galaxies without any star formation can host Type Ia SNe. In this context, it is useful remembering that WDs are the expected evolutionary outcome of stars with initial mass up to ~8 $M_\odot$.

1.2 Core Collapse Supernovae

While thermonuclear explosions of WDs account for the observed SNe Ia, a different explosion mechanism drives the other SNe classes, from Types Ib and Ic to Type II SNe. Despite their diversity in observables, in fact, all these phenomena are linked to the collapse of the stellar core. The physical details of the collapse is still debated, due to the broad range of topics involved and tightly coupled: hydrodynamics, turbulence, weak and strong particle interactions, and neutrino transport just to name a few. In the next paragraph will be presented the key features characterizing core collapse events.

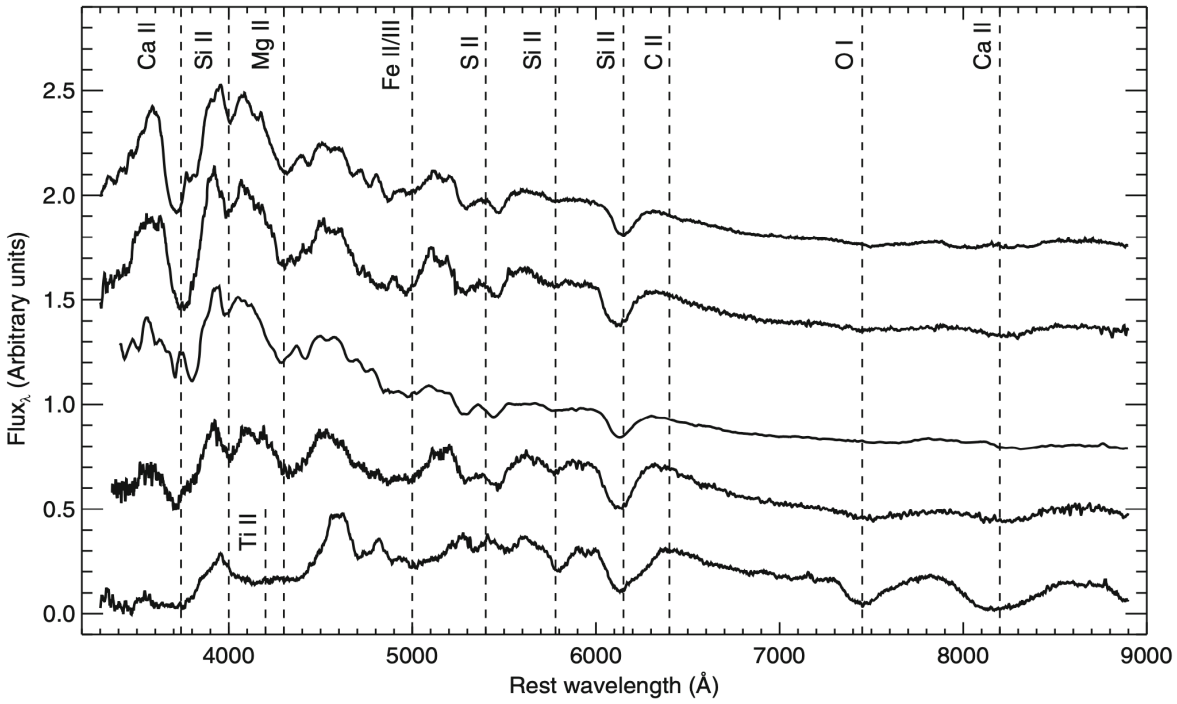

Figure 1.3: Optical spectra of SNe Ia around maximum light. The most prominent features are marked with dashed lines (Figure from Maguire 2017)

1.2.1 Classical Explosion Mechanism

The evolution of stars with masses greater than ~8 $M_\odot$ at zero age main sequence (ZAMS) is not halted by the electron degeneracy pressure, therefore forming a core of heavy elements which will eventually collapse. In particular, stars with masses larger than 12 $M_\odot$ develop cores that are dominated by iron-group elements, especially ^{56}Fe. ^{56}Fe has the largest binding energy among all elements, and all the possible nuclear reactions involving ^{56}Fe are endergonic: such a structure is doomed to collapse. The initial instability in such stars is caused by photodisintegration of ^{56}Fe, which becomes relevant at $\sim 10^{10}$ K. Breaking a nucleus with high binding energy into α particles requires ~2 MeV per nucleon (Branch & Wheeler 2017b): this energy is drained from the radiation field supporting the star, therefore leading to the collapse of the whole core.

During the collapse, the pressure is dominated at first by relativistically degenerate electrons, and subsequently by relativistically degenerate neutrinos, when densities larger than 10^{12} g cm^{-3} lead to neutrino trapping within the star. The collapse of the Fe core is close to homologous, meaning that the velocity of a given mass point is proportional to the radius at which that mass point is located at a given instant. Following this homologous contraction relation ($v \propto r$ at a given time) there will be a radius where the inflow velocity will be equal to the speed of sound. At larger radii, pressure waves cannot maintain an homologous collapse, hence matter will be in free fall ($v \propto r^{-1/2}$). This different behaviour divides the collapsing star in two regions: the core, which is contracting homologously, and the outer layers, which are in free fall (Mezzacappa 2005).

During the homologous collapse of the core, electron captures on atomic nuclei result in a progres-

sively more neutron-rich matter - a process called *neutronization*. Another consequence of electron captures is the acceleration of the collapse, since the electron degeneracy pressure is reduced when electrons are bound together with a proton through the inverse β-decay. As the core reaches nuclear densities ($\rho_{nuc} \sim 3 \times 10^{14}$ g cm^{-3}) the neutrons, which are now predominant in the core, become a uniform mass of degenerate nucleons. As a consequence, the equation of state "stiffens", the pressure rises steeply and the collapse is no longer homologous (Branch & Wheeler 2017b). The collapse of the core is finally halted when the central density is $\sim 2\rho_{nuc}$: a "proto-neutron star" is born. At this point, the free falling outer layers impact on the dense inner core, causing a compression and a subsequent "bounce" of this stiff matter. This bounce powers a shock that travels through the infalling material. The so called "prompt mechanism" is the scenario in which such bounce shock is sufficient to drive the explosion.

However, to our understanding the bounce shock is not sufficient to unbind and expel the outer layers of the star. In fact, part of the energy provided by the shock is spent to dissociate Fe into α particles, while the remaining part is quenched by the ram pressure of the infalling material (Bethe 1990). Therefore, in order to have an explosion, at least one additional powering mechanism is needed. A promising approach is the energy deposition by neutrinos. In fact, neutrinos carry 100 times more energy than the kinetic energy released during a SN explosion. Just retrieving 1% of the energy dissipated through neutrinos would be sufficient to power the whole explosion. Despite their extremely small cross section, at densities $\sim 10^{12}$ g cm^{-3} neutrinos get trapped in the stellar plasma, supporting the idea that such mechanism is indeed plausible. In any case, detailed three-dimensional hydrodynamical simulations are needed to explore the effects of such a complex event (Janka et al. 2007).

1.2.2 The physics behind the outliers

Obviously, the schematic core collapse process just described cannot account for all the observed events, which span several order of magnitudes in brightness. One first important consideration is that for standard SNe II, the peak luminosity appears to be correlated with the progenitor mass. In fact, from the lower end of the progenitor mass spectrum we expect to find relatively weak explosions originating from Fe core collapse. This is corroborated by the correlation between several parameters: lower peak luminosity is linked to lower expansion velocity and lower ^{56}Ni synthesised, all pointing towards a weaker explosion coming from a relatively low mass progenitor (Hamuy 2003; Pastorello et al. 2004; Spiro et al. 2014).

In section 1.2.1, the origin of the instability that leads to the core collapse in stars with $M_* > 12\ M_\odot$ is identified in the photodissociation of ^{56}Fe. There is, however, a second mechanism that contributes to triggering the collapse of the stellar core: the inverse β-decay process ($p + e \rightarrow n + \nu$), also known as electron capture. In stars with lower ZAMS masses ($M_* < 12\ M_\odot$), and consequently lower central temperature, photodissociation becomes less relevant and electron captures are the main drivers of instability and collapse. Such events are analyzed more in detail in Section 1.3.

Faint supernovae can also by linked to fallback of material on a black hole. In fact, the core collapse of massive stars ($M_* > 25\ M_\odot$), may give birth to a black hole, rather than a neutron star (Zhang et al. 2008). In these circumstances, a relevant fraction of the ejecta cannot escape the gravitational field of the central compact object, resulting in low velocity ejecta and low amounts of ^{56}Ni observed. This fallback process has been invoked to explain weak explosion, despite the large ZAMS mass of the exploding star (Zampieri et al. 1998a). However, in suitable conditions (mainly depending on the angular momentum of the material) the accretion on the black hole can release significant amount of

energy, supporting bright and long lasting events (Dexter & Kasen 2013).

Weak explosions and fallback on a black hole can therefore account for sub-luminous SNe. On the other hand, it is necessary to invoke different physical processes to explain extremely bright events. Although there has been no confirmed detection of such transients so far, explosions of extremely massive stars are expected to be driven by the instability generated by electron-positron pair production in the stellar core (Rakavy & Shaviv 1967). These events are called Pair Instability SNe (PISN), and occur when an oxygen core grows between 60 and 130 $M_{\odot}$. The contraction of the core ignites oxygen nuclear burning, leading to a violent release of energy and the complete unbinding of the star, with no remnant left behind. The expected synthesised ^{56}Ni is in the range of tens of $M_{\odot}$, making PISN the brightest thermonuclear explosions in the Universe (Heger & Woosley 2002).

While no confirmed PISN has been detected yet, there is a class of SNe which is surprisingly bright. Explosions with a peak luminosity around 10^{44} erg s^{-1} are labelled Superluminous SNe (SLSNe). Some of them display hydrogen lines in their spectra, falling in the SLSN II classification, while other events do not display any hydrogen feature, therefore belonging to the SLSN I class. In the case of SLSNe II, their brightness has been interpreted as the result of the conversion of kinetic energy of the expanding ejecta into radiation, through interaction with Circumstellar Material (CSM) (Smith & McCray 2007). This mechanism is also found in the more standard subclass of SNe IIn, which is described in Section 1.2.4. As for SLSNe I, the additional energy source could lie in a central engine, such as the spin down of a newly formed magnetar. In fact, neutron stars with large magnetic fields ($\sim 10^{15}$ G) and small rotation periods (<30 ms) can deposit their rotational energy in the ejecta, substantially modifying the light curve of the SN (Kasen & Bildsten 2010).

1.2.3 Standard hydrogen rich Supernovae: Types IIP and IIL

Despite sharing the same explosion mechanism, core collapse SNe do not present the homogeneity of their thermonuclear cousins. Type IIP and IIL SNe are often labelled as "normal Type II SNe", since they account for ~70% of all the core collapse events (Li et al. 2011), and are therefore a useful starting point for our discussion. Observational studies were carried out on archival images obtained before the SN explosion in order to directly detect the progenitor star. These efforts were crowned with success, and it was shown that the progenitor stars of SNe IIP were Red Super Giants (RSGs) with Zero Age Main Sequence (ZAMS) masses between 8 and 18 $M_{\odot}$, in line with the core collapse framework already presented (Smartt 2009a, 2015). While these findings improved our understanding of SNe IIP, progenitors of other core collapse SNe remain elusive, even for the "standard" class of SNe IIL.

However, direct detection of the progenitor is not the only arrow in our quiver: information about the progenitor star and the explosion mechanism can be recovered also observing the light curves of the SNe events. In the very first hours after collapse, the light curve is dominated by X-rays and UV radiation, a consequence of the bounce shock reaching the outer layers of the exploding star (Falk & Arnett 1977). This very short lived phase, called shock breakout, is followed by a longer phase where the ejecta emit radiation while cooling and recombining. The very fast rise in the light curves of SNe IIP is explained by the fact that soon after the shock breakout, most of the envelope is ionized, and the radiation originates from the outer part of the ejecta, travelling with no delay linked to diffusion time (Arcavi 2017).

As the envelope cools down, hydrogen starts to recombine. A recombination front is formed in the ejecta at a temperature of ~5500 K, separating the inner material, still ionized, and the outer material,

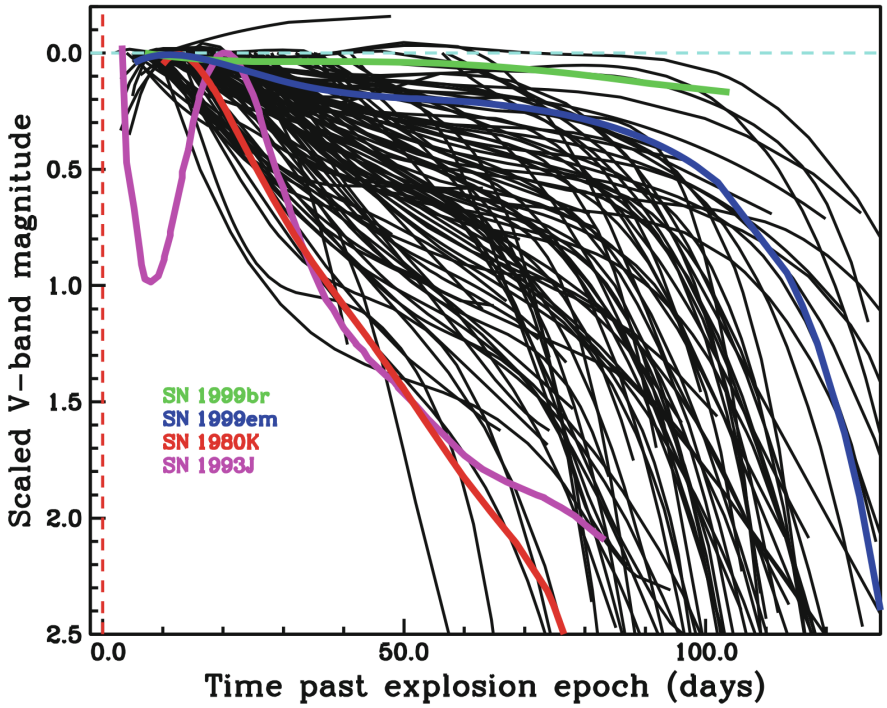

Figure 1.4: Scaled *V*-band light curves of SNe IIP and IIL showing a continuous distribution, rather than two distinct families (Figure from Anderson et al. 2014)

already recombined. Given the large difference in opacity between ionized and neutral hydrogen, the recombination front also coincides with the photosphere. As the hydrogen recombination front progressively recedes in mass, the envelope radius increases: as a result the photosphere remains roughly at the same position for several weeks. Combining this fact with the constant temperature at the recombination front, it is clear why SNe IIP present a period of constant luminosity (Branch & Wheeler 2017b). For the reasons highlighted above, the plateau consists in the progressive emission as radiation of the energy deposited by the bounce shock on the envelope, with the ionized material acting as an energy storage. The late tail of the light curve consists in a linear decline in magnitude (0.0098 mag d^{-1}) powered by the same mechanism for all SN types: ^{56}Co decay, similarly to thermonuclear SNe. The luminosity of the SN during this phase can be used to constrain the ^{56}Ni mass synthesised during the explosion, which for SNe IIP typically spans from few 10^{-4} to 10^{-2} $M_{\odot}$ (Hamuy 2003; Spiro et al. 2014).

While SNe IIP and IIL were hystorically identified as distinct classes, based on the different shape of their light curves, recent evidences suggest that they are instead a single population with a continuous distribution of decline rates (Anderson et al. 2014). Such behaviour is displayed in Figure 1.4, where it appears impossible to clearly separate two families of transients. An additional clue on the link between SNe IIP and SNe IIL is the presence of a clear drop separating the late linear decline and the previous evolution. This suggests that SNe IIL are characterized by an optically thick phase just like SNe IIP, without staying at a constant luminosity (Valenti et al. 2015). This drop in luminosity is observed in SNe IIL around the 100 days mark, the same phase when the plateau typically ends in SNe IIP. These observations suggest that SNe IIP and IIL originate from similar progenitors, RSGs, with the notable difference that SNe IIL progenitors must present hydrogen envelopes with smaller

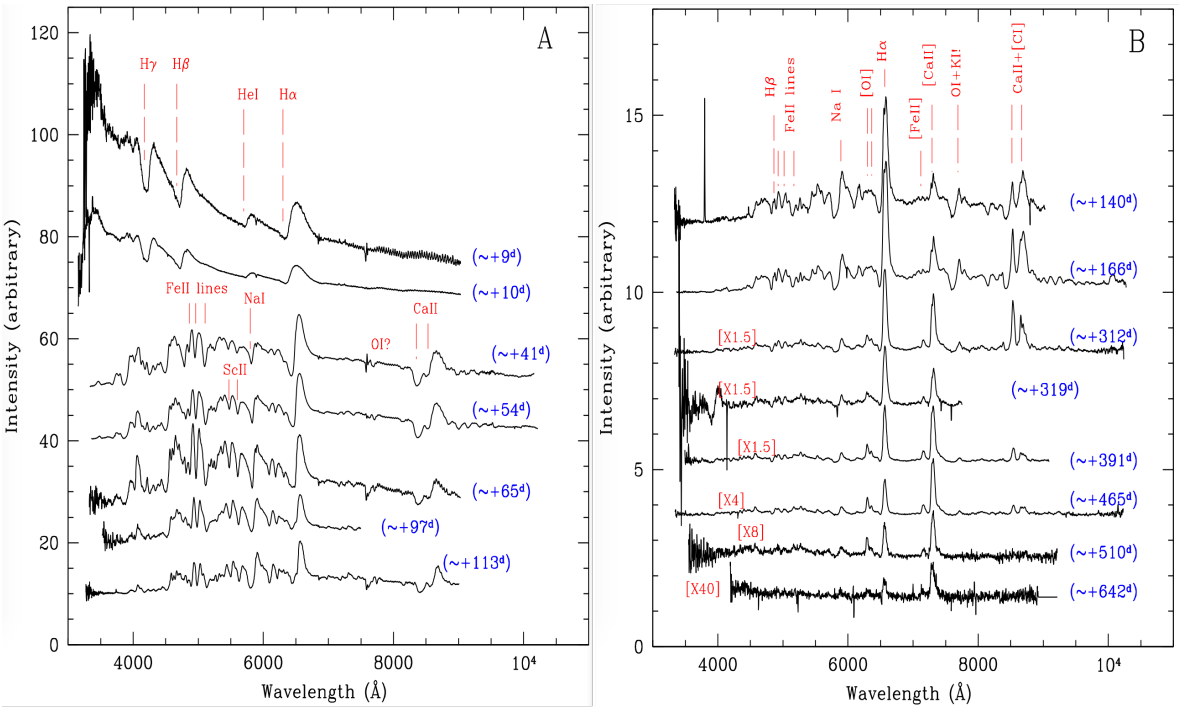

Figure 1.5: Spectral evolution from the early plateau (on the left) to the nebular phase (on the right) of SN 1999em, a standard Type IIP SN (Figure from Elmhamdi et al. 2003)

masses compared to SNe IIP progenitors, therefore unable to sustain a constant luminosity for ~100 days.

The characteristics associated with a cooling mass of ionized hydrogen can be appreciated in the spectra of SNe IIP. As clearly shown in the standard Type IIP SN 1999em, early spectra display a hot continuum (T > 10000 K) with broad H and He lines (Figure 1.5 A). From the characteristic P-Cygni profile it is possible to infer an expansion velocity at early phases up to 16000 km s^{-1} (Elmhamdi et al. 2003). As the envelope cools with time, the spectral continuum becomes redder and new lines appear in the spectra, in particular Ca II, Fe II, Sc II and Ba II. The recombination wave recedes in mass, therefore ejecta with lower velocities are found at the photosphere: as a consequence, the lines become narrower with time. As the SN fades from the plateau, the spectral continuum vanishes, leaving the spectra dominated by prominent emission lines such as Hα, [Ca II] $\lambda\lambda$ 7291,7323, the Ca II near-IR triplet, [O I] $\lambda\lambda$ 6300,6364 and the Na I D (Figure 1.5 B). When measurable, the strength of the [O I] $\lambda\lambda$ 6300,6364 forbidden lines in the nebular spectra is particularly interesting, since the luminosity of these lines can be used as a proxy of the Zero Age Main Sequence (ZAMS) mass of the progenitor star (Fransson & Chevalier 1989).

SNe IIL present spectral features similar to SNe IIP, but with some distinctive features. At early phases, H emission lines appear to be weak and narrow. Furthermore, when the Balmer lines become strong the blue absorption characteristic of the P-Cygni profile is weak or absent (e.g. Branch et al. 1981), and this has been interpreted as the line source function declining less sharply with radius in SN IIL compared to SN IIP (Branch & Wheeler 2017c). Both the narrow lines and the absence of a clear P-Cygni profile can be explained with a relevant amount of Circumstellar Material (CSM)

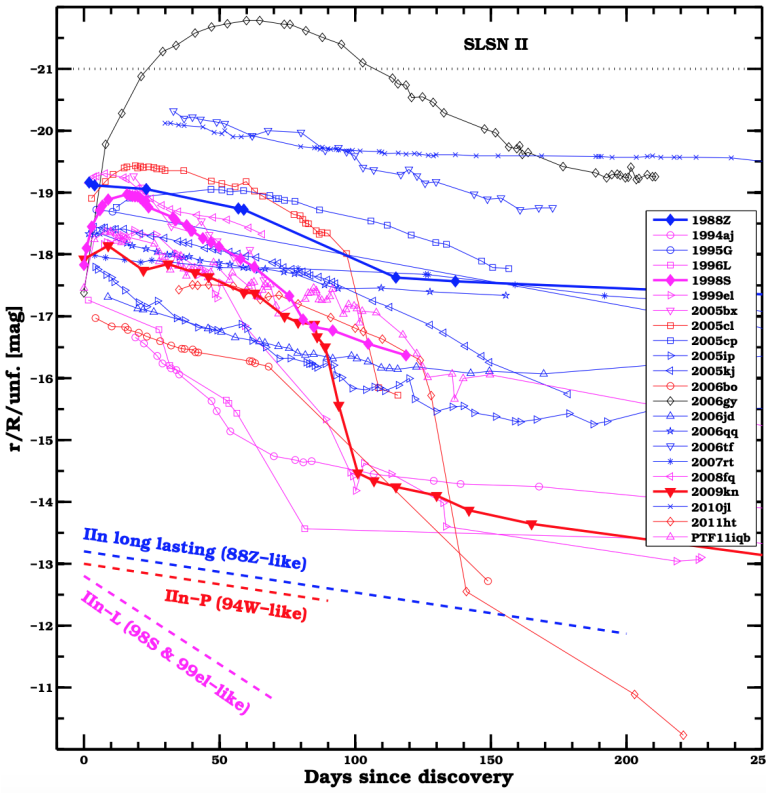

Figure 1.6: Absolute light curves of several interacting transients, spanning a wide range of peak magnitudes and light curve shapes (Figure from Taddia et al. 2015)

surrounding the progenitors of SNe IIL at the time of explosion. These properties of SNe IIL are indeed shared with SNe IIn, which are described in the following subsection.

1.2.4 Interacting Supernovae: Type IIn

Type IIn SNe are characterized by spectra with narrow emission lines (few 10 to few 1000 km s^{-1}). The reason for such low velocity measures is not a weaker explosion, but rather in the position of the photosphere. In SNe IIn the photosphere does not lie within the fast ejecta, but within dense, slow moving CSM which was built up before the explosion through mass loss episodes. In these conditions, the interaction between the fast ejecta and the slow CSM becomes a key feature in defining the characteristics of the transient. In SN explosions the kinetic energy is two orders of magnitude greater than the radiated energy. Therefore, even a small fraction of the kinetic energy converted in radiative energy through CSM interaction would be enough to power transients that are much brighter compared to non-interacting SNe. Indeed, CSM interaction may play an important role in some SLSNe, extreme events with absolute magnitudes M_V < -21 mag. Furthermore, CSM interaction may support the luminosity of a transient for years without faltering, although this is not an ubiquitous characteristic of SNe IIn.

The outcome of CSM interaction can be quite heterogeneous: the radiation released depends on many parameters like the velocity of the ejecta, their density profile, the density profile of the CSM, the speed of the shock and the fraction of kinetic energy deposited during the interaction (Chevalier &

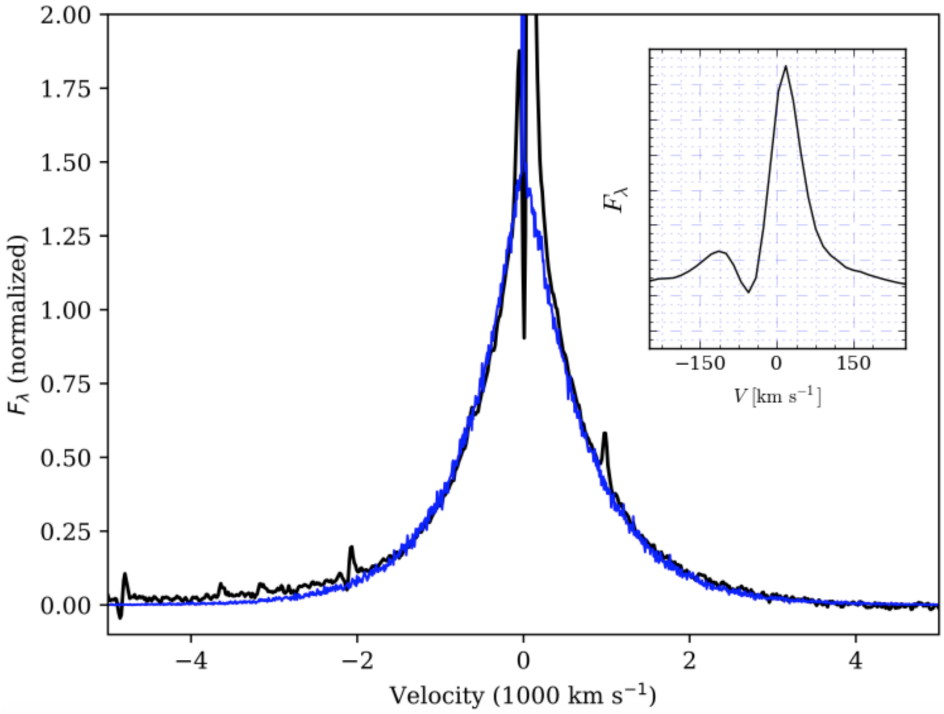

Figure 1.7: Hα profile of SN 2015da, a Type IIn SN with clear evidence of narrow P-Cygni (Figure from Tartaglia et al. 2020)

Fransson 2017 and references therein). This variability results in light curves with a wide range of peak absolute magnitudes, different decline rates and duration (Figure 1.6). This has lead to attempts to further group the transients in sub-types, based on their photometric properties (Taddia et al. 2015). An intuitive example is the photometric distinction between SNe IIn-P and IIn-L, reminiscent of the standard Type II sub-classes.

Spectra of SNe IIn are characterized by a blue continuum in the early phases, with narrow emission lines superimposed. The line profile can be broadened around the base (up to a few 1000 km s^{-1}), but this is an effect of electron scattering, rather than a Doppler broadening due to a velocity profile (Chevalier & Fransson 2017). Some events display a very narrow absorption blueward of the Hα line: this narrow P-Cygni profile can be used to estimate the expansion velocity of the slow moving CSM (Figure 1.7). At late times, SNe IIn spectra are characterized by strong Hα emission, rarely displaying the forbidden lines [Ca II] $\lambda\lambda$ 7291,7323 and [O I] $\lambda\lambda$ 6300,6364 which are observed in the nebular spectra of standard SNe II. A typical feature appearing in the late spectra of SNe IIn is the depression of the red wing of the emission lines, especially Hα (e.g. Fransson et al. 2002). This feature has been linked with dust formation, since the newly formed dust would preferentially block the radiation coming from the material receding with respect to the observer, therefore causing an effective blueshift in the emission lines. Occasionally, other oxygen forbidden lines are detected at late phases.

Given their large variability and the complex nature of the CSM interaction process, SNe IIn can be a puzzling class of transient. One of their most challenging aspect is the impossibility to probing the fast ejecta located underneath the thick CSM, preventing a comparison with better understood events.

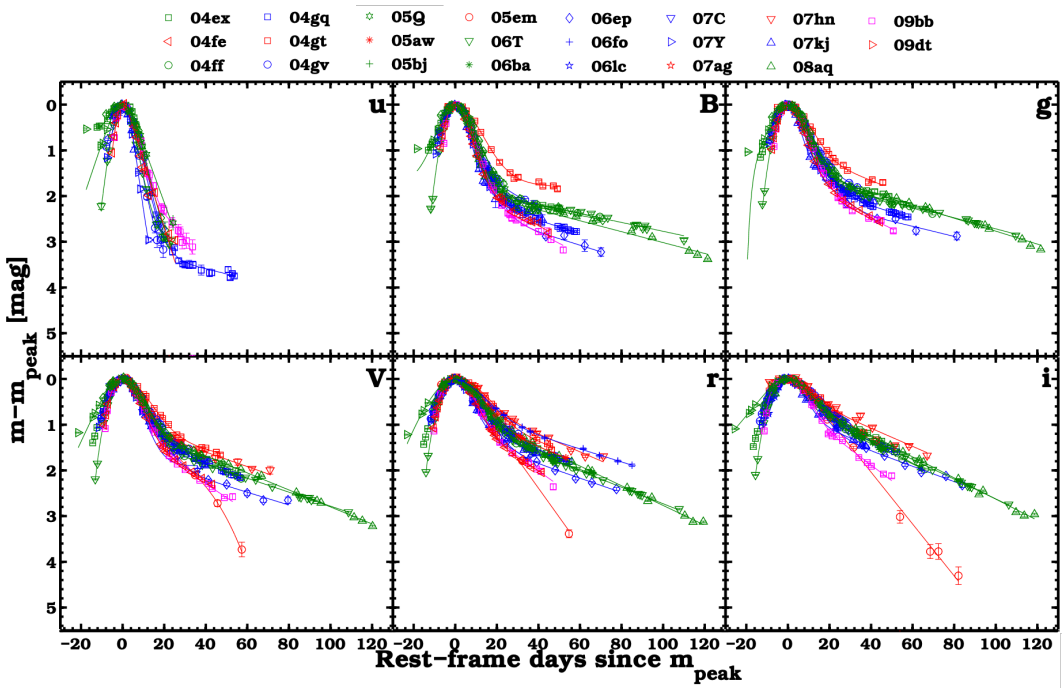

Figure 1.8: Multi band light curves from 26 SNe normalized at peak magnitude. SNe Ib are represented in blue, SNe Ic in red and magenta, SNe IIb in green (Figure from Taddia et al. 2018).

1.2.5 Stripped envelope Supernovae: Types Ib, Ic and IIb

Despite their apparent heterogeneity, SNe Ib, Ic and IIb can be grouped together under the label of "hydrogen poor" or "stripped envelope" SNe. In fact, all three classes likely originate from the core collapse of a massive star (15 - 50 $M_{\odot}$) that has shed a significant part of their envelope, either through stellar wind or binary interaction (Smith 2014). The degree of stripping determines the observed SN type: a star retaining part of its hydrogen envelope will explode as a SN IIb, a star that lost all its hydrogen envelope while still presenting its helium envelope will explode as a SN Ib, and finally a star stripped of both the hydrogen and helium layers will appear as a SN Ic after its core collapse.

The light curves of stripped envelope SNe are reminiscent of those of SNe Ia, suggesting that ^{56}Ni radioactive decay plays an important role in shaping their evolution. Their peak luminosity is spread over $\sim$ 3 mag (Pian & Mazzali 2017), compatible with different amount of ^{56}Ni synthesised (with an average value around 0.1-0.2 $M_{\odot}$). However, once the light curve peaks are normalized (Taddia et al. 2018), it is evident that SNe Ib, Ic and IIb share similar light curve properties (Figure 1.8).

Early spectra of stripped envelope SNe present a photospheric phase, similarly to all other SNe discussed so far, in which the optically thick ejecta emit a continuum that is well approximated by a black body. During the early phases, expansion velocities measured through the line broadness can reach 30000 km s^{-1}, and they decline as the photosphere recedes through the ejecta (Figure 1.9, left panel). The differences between the different sub-types of stripped envelope SNe are less marked in the nebular spectra (Figure 1.9, right panel). In particular, the forbidden doublet [O I] $\lambda\lambda$ 6300,6364 clearly separates the core collapse events from the thermonuclear Type Ia SNe (Patat et al. 2001).

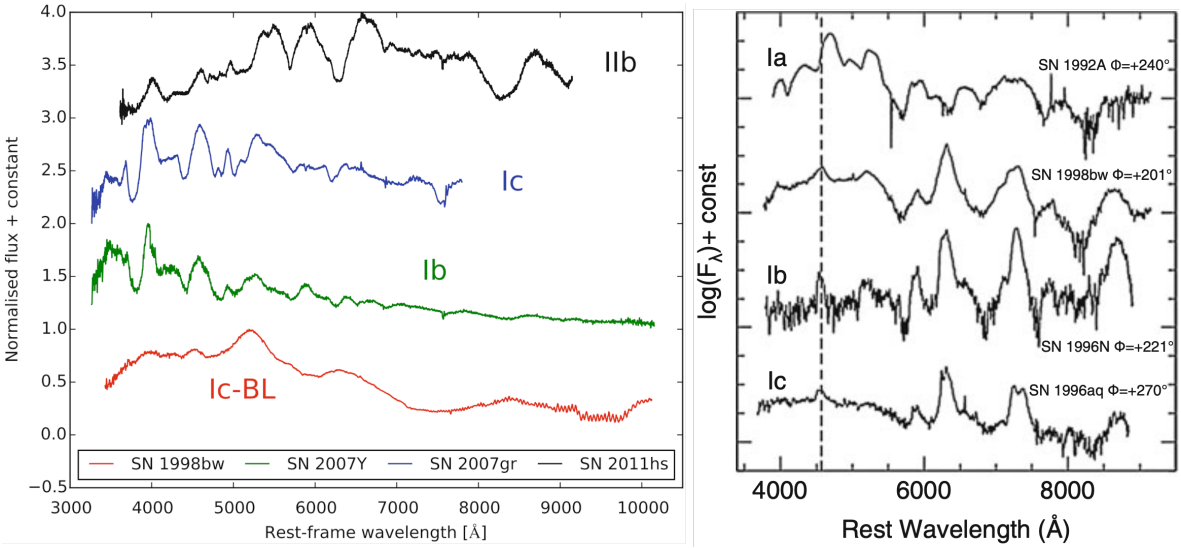

Figure 1.9: Spectra from different classes of stripped envelope SNe during the photospheric phase (left panel) and nebular phase (right panel; figures from Pian & Mazzali 2017; Patat et al. 2001).

1.3 Electron Capture Supernovae: Theory

The least massive single stars that undergo core collapse are expected to have a ZAMS mass between 8 and 10 $M_\odot$, and they are expected to develop a degenerate O-Ne-Mg core, rather than a Fe core. At the end of the evolution of the star, electron captures on ^{20}Ne and ^{24}Mg effectively reduce the Chandrasekhar mass of a degenerate O-Ne-Mg core, ultimately causing its collapse. Given the importance of the inverse β-decay in this event, SNe originating from such collapse are called "electron capture SNe" (ECSN). The explosion of an ECSN could be explained simply with the prompt mechanism described in section 1.2.1, due to the lower masses involved (Branch & Wheeler 2017d).

Single star channel: Super Asymptotic Giant Branch

The evolution of a star before its demise as an ECSN deserves some further discussion. Let M_{up} be the ZAMS mass over which carbon is ignited in the core. Stars with initial masses between 0.5 $M_\odot$ and M_{up} will develop a CO core and will become Asymptotic Giant Branch (AGB) stars. Pinpointing the exact value of M_{up} is no easy feat, but it should lie between 6 and 9 $M_\odot$ (Nomoto & Leung 2017). On the other hand, stars with ZAMS larger than $\sim$ 10 $M_\odot$ are expected to complete all the nuclear burning cycles, ending their evolution with a Fe core which will succumb to instabilities and collapse.

Stars with masses between M_{up} and 10 $M_\odot$, instead, successfully ignite carbon, leading to the formation of an O-Ne-Mg core. Electron degeneracy in this core is sufficient to support the star and halt the contraction, preventing subsequent nuclear burning in the core. The structure of the star is rearranged, and nuclear reactions are ignited in shells that undergo thermal pulses. These objects are named "Super-AGB" (SAGB) stars due to the similarity with AGB stars (e.g. Siess 2007). The fate of SAGB stars depends on the competing effects of core growth and mass loss. Core growth is mainly determined by the outward movement of the H burning shell, while mass loss is driven by thermal pulses, which are even more frequent than in AGB stars, coupled with dust driven winds (Doherty

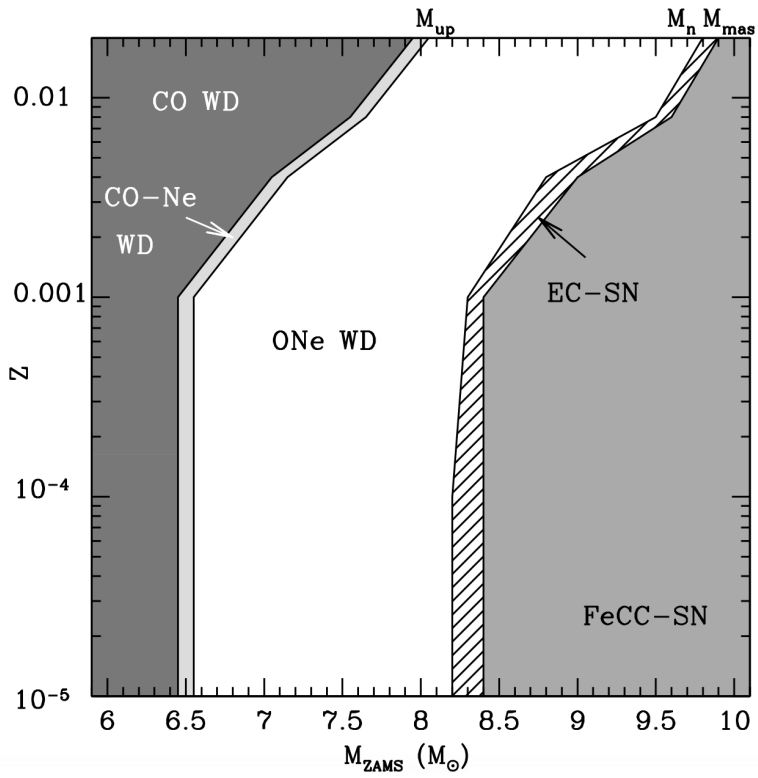

Figure 1.10: Evolutionary endpoint of intermediate mass single stars based on their ZAMS mass and metallicity. Notice the narrow range of masses accounting for the ECSN channel (figure from Doherty et al. 2017).

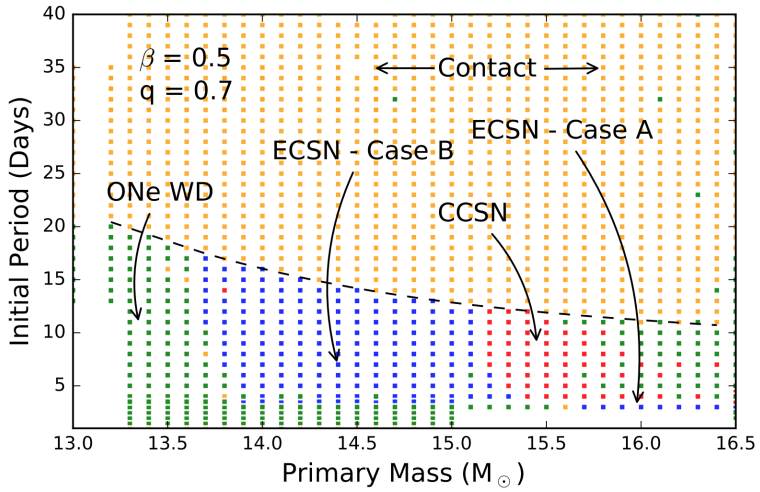

Figure 1.11: Expected final fate for the primary star of a binary system with a fixed mass ratio (q) and mass loss efficiency (β; figure from Poelarends et al. 2017).

et al. 2017). If enough mass is lost, nuclear burning processes are quenched and the star will end its life as a O-Ne-Mg white dwarf. On the other hand, if the core can grow up to ~ 1.4 $M_\odot$, the star can explode as an ECSN. The fate of intermediate mass stars depending on their mass is shown in Figure 1.10. These theoretical calculations depend on the metallicity of the star, but also on other effects that are challenging to model, such as convective overshooting, mixing and mass loss rates (Poelarends et al. 2008).

1.3.1 Binary System Channel

SAGB stars that result in ECSN are the watershed that divide the stars which end their lives as white dwarfs and the stars that explode after the collapse of their core. The range of ZAMS masses over which ECSN are expected to occur is rather small (Figure 1.10), but this only applies to single stars. In fact, binary interaction can significantly influence the evolutionary path of a star, potentially relaxing the mass constraints to obtain an ECSN. Mass transfer on a companion star during the hydrogen core burning phase could quench the nuclear burning process, resulting in a smaller helium core compared to a single star with the same ZAMS mass. In such scenario, even stars that would normally develop an Iron core could explode as ECSN instead.

On the other hand, mass transfer during the hydrogen shell burning phase can prevent the formation of a convective hydrogen envelope, therefore inhibiting the second dredge up. The second dredge up effectively reduces the mass of the stellar core by carrying H-exhausted matter from the core to the surface of the star. If the second dredge up is avoided, the core will be more massive compared to a single star with the same ZAMS mass: therefore even stars that would normally end their lives as O-Ne-Mg white dwarfs could undergo the core collapse. Accounting for these effects, a first estimate was given, stating that ECSNe could originate from stars with ZAMS masses in the range of 8 to 17 $M_\odot$, provided they are in a binary system (Podsiadlowski et al. 2004).

Of course, when considering binary interaction the parameter space becomes significantly larger compared to the single star scenario. The mass and metallicity of the primary star are still key variables, but it is necessary to add the mass ratio, the period of the system and the mass loss efficiency in order

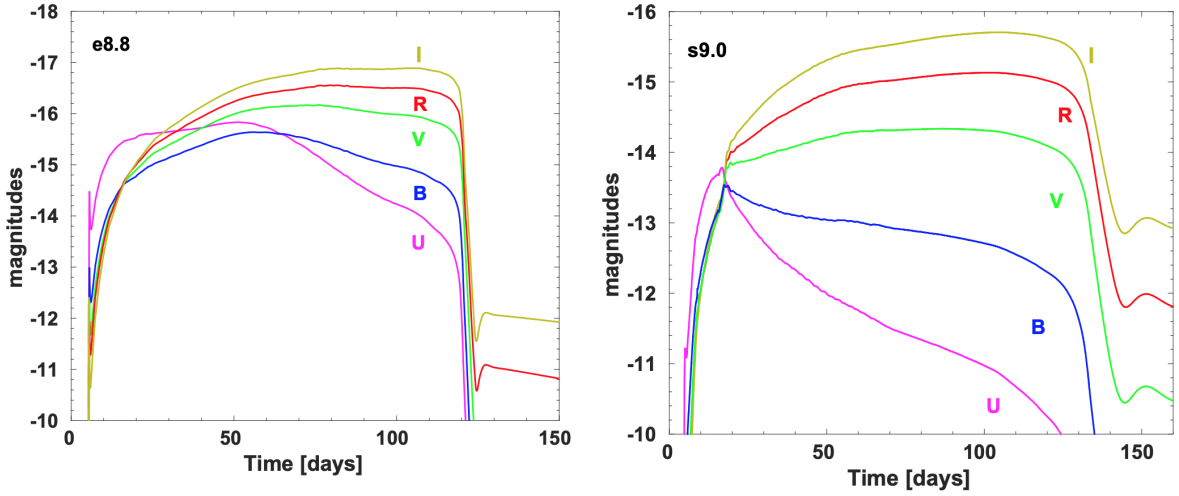

Figure 1.12: Synthethic broadband light curves for an ECSN on the left and a Fe core collapse SN on the right (figure from Kozyreva et al. 2021).

to have a reasonable model. A more recent study, aimed to explore this parameter space, yielded a ZAMS mass range between 13.5 and 18 $M_\odot$ for stars potentially exploding as ECSN after binary interaction (figure 1.11). (Poelarends et al. 2017)

1.3.2 Expected Electron Capture Supernovae Features

The lack of observational data on ECSN leaves few solid anchors for theoretical work to start from. However, there are some characteristic that we expect to observe in an ECSN. The first, obvious feature is that ECSNe from the single star channel should exhibit a SAGB progenitor with a low mass (8 - 10 $M_\odot$). Such stars reach bolometric luminosities of $\sim 10^5$ $L_\odot$ (Poelarends et al. 2008), but since dust formation is a relevant process in their outer layers, SAGB stars could be impossible to detect in the optical domain, due to dust extinction. In the case of the binary channel, instead, the progenitor star is expected to be stripped of its hydrogen layers due to mass transfer to the companion star (e.g. Tauris et al. 2013). Regardless of the progenitor scenario, hydrodynamical models of ECSN explosion envision a kinetic energy of just $\sim 10^{50}$ erg, a factor of 10 smaller compared to the average SN event, denoting a weak explosion and low speed of the ejected material (Kitaura et al. 2006). Finally, the explosion would yield only few 10^{-3} $M_\odot$ of ^{56}Ni, causing a fainter late linear decline compared to other SNe (Wanajo et al. 2009).

With these characteristics, it could be challenging to distinguish an ECSN from a faint Fe core collapse event, especially in the impossibility to study the progenitor star in detail. Indeed, Pumo et al. (2009) suggest that ECSN may display light curves similar to faint SNe IIP or IIL, depending on the amount of hydrogen they are able to retain during their evolution. Kozyreva et al. (2021) also caution about the degeneracy of observables between ECSN and low mass Fe core collapse SNe. Their study reveals that, despite the similarities between the two explosions, an ECSN event could be recognized by the shape of the *U* and *B* band light curves, which display a behaviour not observed in any of the currently known transients (Figure 1.12). Interestingly, the light curves of the ECSN reproduced on the left panel of Figure 1.12 are brighter than the light curves of a more traditional Fe core collapse

SN originating from a star with a similar mass (displayed in the right panel of the same figure). The reason lies in the radius of the progenitor star at the time of explosion: SAGB stars are expected to have extended envelopes (R > 1000 $R_\odot$, Doherty et al. 2017), larger than typical RSG stars. A larger radius with a similar mass leads to a lower diffusion time, ultimately resulting in a brighter transient that evolves more quickly towards the nebular phase. Indeed, in their models Kozyreva et al. (2021) adopt a radius of 1200 $R_\odot$ for the progenitor of the ECSN, and a radius three times smaller for the progenitor of the Fe core collapse SN. It is worth noticing, however, that this study does not account for the presence of dust or CSM, which are likely to be present around a SAGB star and could heavily influence the observed properties of ECSNe.

1.4 Electron Capture Supernovae: Candidates

While to this date there is no smoking gun evidence for an ECSN event, there is no lack of candidates. In this section will be reviewed the main events and classes of transients that have been associated with the collapse of an O-Ne-Mg core, their main features and the reasons why they were tentatively identified as ECSN events.

1.4.1 SN 1054: the Crab Supernova

Despite lacking a proper photometric and spectroscopic follow-up of the actual event, the Crab SN has been proposed to be an ECSN event. Through the study of the resulting Crab Nebula, in fact, it was possible to infer different properties of the explosion and the progenitor system. First of all, the mass of the progenitor star is estimated to be between 8 and 12 $M_\odot$, perfectly in line with the single SAGB star scenario for an ECSN (Davidson & Fesen 1985). The presence of a neutron star as a remnant corroborates the core collapse scenario, excluding a thermonuclear explosion. Furthermore, the chemical composition of the Nebula is rich in helium, but relatively poor in oxygen and Iron-peak elements compared to other core collapse events (e.g. MacAlpine & Satterfield 2008, Smith 2013). A low energetic core collapse of an O-Ne-Mg core well reproduces both the nucleosynthesis and the expansion velocity ($\sim$1500 km s^{-1}) observed today in the Crab Nebula (Kitaura et al. 2006). Finally, synthetic light curves characterized by a short plateau appear to be consistent with the (few) observations available for SN 1054 (Tominaga et al. 2013).

All these clues consistently point toward an ECSN origin for the Crab SN, but there is one consideration which disfavours the ECSN scenario. When a neutron star is born after a core collapse, it receives a "natal kick" due to the inevitable asymmetric mass ejection during the explosion. The magnitude of said kick depends on the explosion energy, as well as the degree of symmetry of the process. The typical neutron star receives a kick of few 100 km s^{-1} at birth, and the Crab pulsar does not strongly depart from this norm, with a measured velocity of $\sim$160 km s^{-1}. This measure, however, is in contrast with the predicted kick received by the neutron star born from an ECSN: the collapse of an O-Ne-Mg core is not only sub-energetic, but also highly symmetrical, resulting in a natal kick of just few km s^{-1} (Gessner & Janka 2018). Given the high velocity observed for the Crab pulsar, SN 1054 may not have been an ECSN.

1.4.2 Type IIn-P as ECSN: SN 2011ht

As detailed in the previous subsection, most observed properties of SN 1054 seem to be compatible with an ECSN scenario. However, the bright ($\sim$ -18 mag) peak magnitude recorded for this event

clashes with the expectation of a weak explosion of an O-Ne-Mg core. To explain this feature, CSM interaction can be invoked: an efficient conversion of kinetic energy into radiation can account for both the brightness and the low velocities observed in SN 1054. In particular, SN 1054 may belong to those interacting transients displaying a pleateau in their light curves, which are labelled SNe IIn-P (Smith 2013).

The prototype object for this class is SN 2011ht (Mauerhan et al. 2013). The spectra of SN 2011ht display narrow emission lines (few 10^2 km s^{-1}) on top of broad asymmetric wings that can be attributed to electron scattering. Narrow P-Cygni absorptions superimposed to the emissions line reveal the presence of a slow wind along the line of sight. These characteristics are typically found in SNe IIn, and reflect the interaction between the ejecta and the CSM. Interestingly, an outburst was detected one year prior the explosion of SN 2011ht, which was likely associated with a mass loss episode that contributed to form the dense wind observed after the explosion (Fraser et al. 2013).

However, the peak magnitude reached by SN 2011ht is only $M_V \sim$ -17 mag, which is rather subluminous for a type IIn SN. Mauerhan et al. (2013) identify a plateau lasting ~120 days in the bolometric light curve, followed by a sharp decline of several magnitudes. From the late time decline, it is possible to infer a ^{56}Ni mass around 6×10^{-3} $M_\odot$, which is significantly lower than the expectations of a classical SN explosion. The subtype IIn-P was born by grouping together SN 2011ht with SNe 1994W and 2009kn in light of their similar properties (Mauerhan et al. 2013). Given the low amount of ^{56}Ni ejected, and their possible low mass progenitors, Smith (2013) suggests that the subclass SNe IIn-P may be linked to ECSN events. In this case, the CSM interaction would explain the brightness of these transients despite the low kinetic energy of the explosion.

1.4.3 Faint SNe I: SN 2008ha-like

Another potential ECSN candidate was identified in SN 2008ha. This object is characterized by very low radiated energy (~10^{47} erg), small amount of ^{56}Ni synthesized (3×10^{-3} $M_\odot$) as well as slow ejecta (2000 km s^{-1} at maximum brightness) and consequently low kinetic energy (2×10^{48} erg) (Foley et al. 2009). Spectra of SN 2008ha are completely lacking hydrogen features, while presenting significant emission lines originating from Fe and intermediate mass elements (Ca in particular). SN 2008ha is a relevant member of the so-called "Type Iax" SN subtype (Foley et al. 2013). Given the low energy involved in these events, some SNe Iax have been tentatively associated to ECSN. Their lack of hydrogen can be explained through binary evolution, during which the outer layers of the progenitor star are stripped, leading to a faint, fast evolving and hydrogen poor transient (Moriya & Eldridge 2016).

At the same time, the physical origin of SNe Iax may be linked to the deflagration of a CO White Dwarf, similarly to SNe Ia. Their low luminosity can be the symptom of a small amount of ejected mass, and possibly even a non-terminal event, which does not cause the complete disruption of the star. A strong proof that associates SNe Iax with thermonuclear explosions is the presence of Co II lines in the *H* and *K* bands, albeit at lower velocities compared to standard SNe Ia (Jha 2017 and references therein). Remarkably, the scenario of a weak thermonuclear deflagration is also supported by the direct detection of the progenitor system for a SNe Iax event. Through the study of archival images, McCully et al. (2014) identified the progenitor system that would give birth to SN 2012Z: a white dwarf accreting material from a helium star. Furthermore, the late time luminosity of SN 2012Z suggests that the event was not terminal, and that a bound remnant was left after the deflagration, ruling out a faint CC SN event (McCully et al. 2022).

1.4.4 A rather faint SN IIn: SN 2018zd

The transient SN 2018zd sparked debate as an interesting ECSN candidate. The main features during most of its evolution, from the light curve shape to the spectral lines, are similar to SNe IIP, although the peak magnitude of $M_B \sim$ -18 mag is brighter than the average SN IIP event (Zhang et al. 2020). Remarkably, spectra taken within 10 days from the explosion display signs of flash ionisation (Gal-Yam et al. 2014). During this initial phase, spectra of SN 2018zd are dominated by lines originating from highly ionized elements such as He II, C IV and N V. These spectral features arise from the CSM surrounding the progenitor star, heated by the high energy photons generated by the explosion. By measuring the strength of the [O I] $\lambda\lambda$ 6300, 6364 doublet in the nebular phase, Zhang et al. (2020) constrain the mass of the progenitor of SN 2018zd between 12 and 15 $M_\odot$, with a preference for the lower value. According to this estimate, SN 2018zd may arise from the collapse of a low mass Fe core, or a high mass O-Ne-Mg core.

Hiramatsu et al. (2021) report additional properties of SN 2018zd that could discriminate between the ECSN scenario and the classical Fe core collapse. First of all, the flash ionisation features are compatible with a He, C and N rich CSM, with a low abundance of O: such composition is more in line with the atmosphere of a SAGB star, rather than a RGB. Weak C, O and Mg lines in the nebular spectra can also be indicative of an ECSN origin for SN 2018zd. Hiramatsu et al. (2021) also identify the progenitor star in archival images: despite having a single detection and several upper limits, the spectral energy distribution (SED) of the star appears to be more compatible with a SAGB rather than a RGB star. Furthermore, the ^{56}Ni mass inferred from the late time decline amounts to $8.6 \pm 0.5 \times 10^{-3}$ $M_\odot$, which would be close to the upper limit for an ECSN (Hiramatsu et al. 2021). This consistent picture, however, is quite sensitive to the distance adopted for the host galaxy, NGC 2146: Hiramatsu et al. (2021) adopt 9.6 ± 1.0 Mpc by using the standard candle method, but they caution that if the distance to NGC 2146 is larger than 12 Mpc, SN 2018zd cannot be an ECSN. In fact, a larger distance would change the estimated ^{56}Ni mass over 10^{-2} $M_\odot$, also increasing the luminosity of the progenitor star. Ultimately, this would strongly favour the Fe core collapse of a RGB star, rather than an ECSN event. Indeed, this is the interpretation suggested by Callis et al. (2021), which adopt a distance of $15^{+6.1}_{-3.0}$ Mpc for NGC 2146, and therefore classify SN 2018zd as a standard, Fe core collapse SN, surrounded by a dense wind.

1.4.5 Faint SNe IIP

On the subject of weak Fe core collapse event, we find the class of faint SNe IIP, also labelled Low Luminosity SNe IIP (LL SNe IIP). This subclass is introduced by Pastorello et al. (2004), that notice the exceptionally low expansion velocities and ^{56}Ni synthesised (2-8 $\times$ 10^{-3} $M_\odot$) of few SN events, namely SNe 1994N, 1999br, 1999eu and 2001dc. However, since their spectroscopic and photometric evolution is consistent with classical SNe IIP, they were identified as the least luminous IIP events, belonging to a continuous distribution rather than to a separated class. In the following years, the photometric and spectroscopic data gathered for SN 2005cs provided a reliable benchmark for LL SNe IIP (Pastorello et al. 2006, 2009). The progenitor star was inferred to be of relatively low mass before explosion (below 10 $M_\odot$, Maund et al. 2005). However, the lack of Near Infrared (NIR) detection of the progenitor excludes a SAGB star in favour of a RGB star: SN 2005cs was the result of a Fe core collapse, not an ECSN (Eldridge et al. 2007).

Observing a larger sample of LL SNe IIP, it becomes clear that there is a continuum of features among the SNe IIP class (Spiro et al. 2014). In figure 1.13 it is possible to appreciate that fainter events

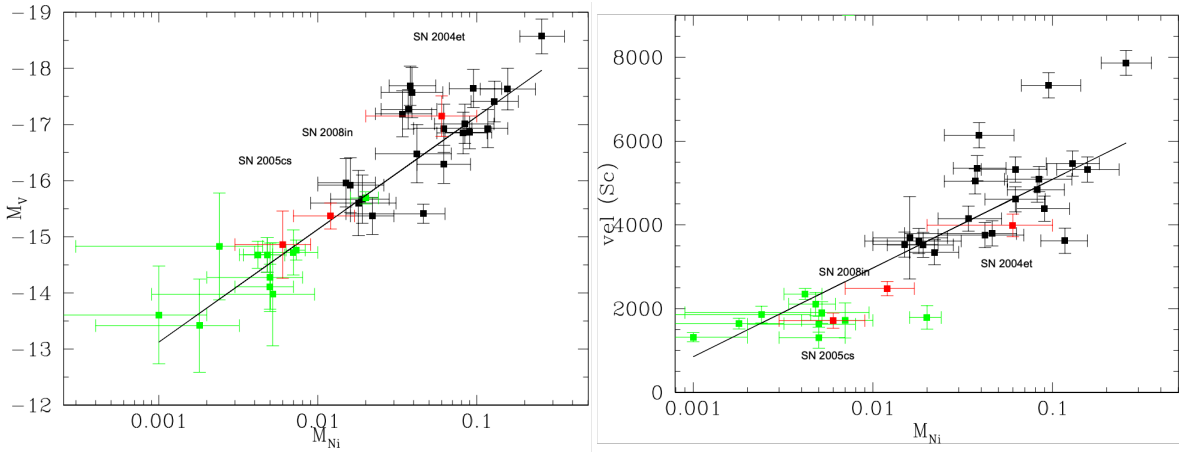

Figure 1.13: Correlation between the ^{56}Ni synthesised and the plateau magnitude (on the left) and expansion velocity (on the right) for a sample of LL SNe and standard SNe IIP (figures from Spiro et al. 2014).

are associated with less synthesised ^{56}Ni, and the same applies to events displaying low expansion velocities (indicative of a weak explosion). It becomes tempting to infer that all SNe IIP events, even LL SNe IIP, originate from Fe core collapse of RGB stars. In this context, stars with lower mass would lead to the weaker explosions, with low expansion velocity, low luminosity and low ^{56}Ni synthesised. However, we know that ECSN may display characteristics similar to SNe IIP, depending on the evolution of the progenitor SAGB star (Pumo et al. 2009). While we are relatively certain that the bulk of SNe IIP originate from the Fe core collapse of a RSG star, we may be observing ECSN at the lower end of the energy spectrum of SNe IIP.

1.4.6 Intermediate Luminosity Red Transients

Intermediate Luminosity Red Transients (ILRTs) are a class of faint transients that fulfill remarkably well the theoretical expectations for ECSNe. A first key point is that their light curves are similar to SNe IIP/L: a single peak followed by a steady decline, and finally a linear decline in magnitude compatible with the ^{56}Ni decay (e.g. Botticella et al. 2009; Bond et al. 2009). The striking difference between ILRTs and standard SNe is the peak magnitude, which for ILRTs is always below -15 mag. Consistently, the late time linear decline is also faint and the inferred ^{56}Ni mass is typically few 10^{-3} $M_\odot$, as displayed in the left panel of Figure 1.14 (Cai et al. 2021). Opposed to LL SNe IIP, the correlation between the observed properties of ILRTs is not straightforward (as clearly seen in the right panel of Figure 1.14). The reason is that CSM interaction plays an important role at all times during their evolution: the expansion velocities measured through the FWHM of the emission lines is not informative of the expansion velocities of the ejecta, which are hidden by the CSM. The presence of optically thick CSM, in fact, prevents us from directly observing what lies underneath, rendering the study of ILRTs more challenging.

The true nature of ILRTs has puzzled researchers for years. Given their low luminosity, they were sometimes associated with stellar outbursts or other non-terminal events (e.g. Kashi et al. 2010; Humphreys et al. 2011). However, thanks to the long term monitoring of SN 2008S and NGC 300 2008OT-1, Adams et al. (2016) found that the transients were significantly weaker than their progeni-

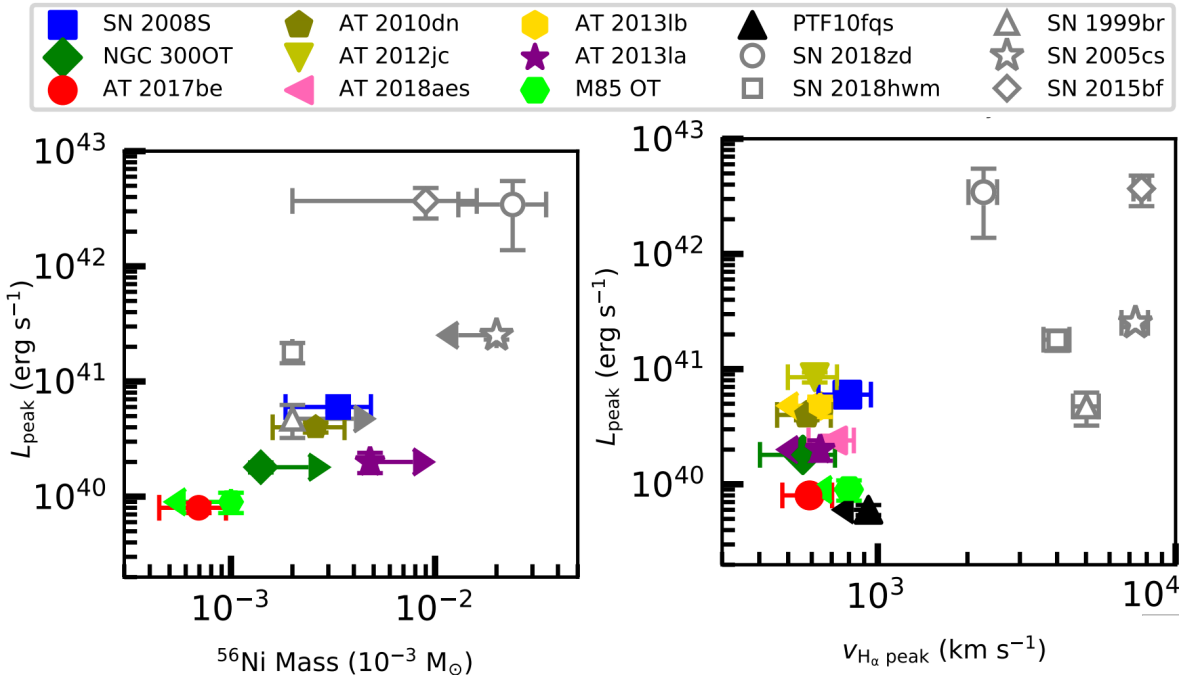

Figure 1.14: Correlation between the peak luminosity and the ^{56}Ni synthesised (on the left) and expansion velocity of Hα (on the right) for a sample of ILRTs (figures from Cai et al. 2021).

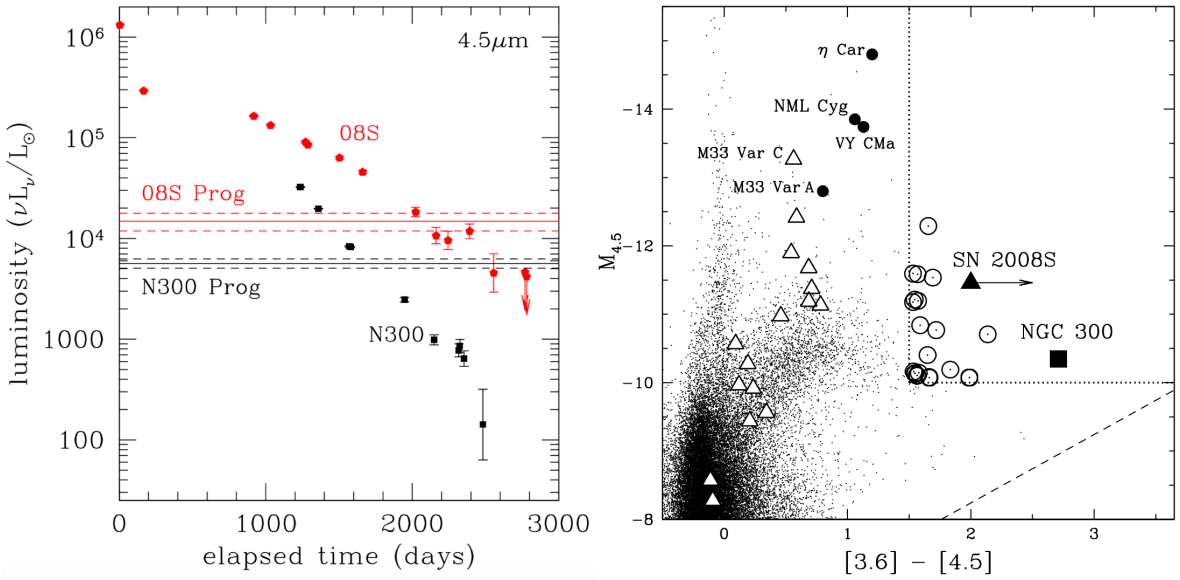

Figure 1.15: Left panel: photometric follow-up years after peak luminosity for SN 2008S and NGC 300 2008OT-1, compared to the luminosity of their progenitor. Right panel: progenitors of SN 2008S and NGC 300 2008OT-1 in the colour-magnitude diagram (figures from Adams et al. 2016; Thompson et al. 2009).

tors, years after peak luminosity (Figure 1.15, left panel). The amount of dust required to explain such dimming is exceedingly high, therefore the most logical explanation for this behaviour is that ILRTs are indeed terminal explosions, where the star is destroyed. In addition to the low luminosity and low ^{56}Ni mass inferred for ILRTs, the most notable connection to ECSN comes from the detection of their progenitors. In particular, thanks to their proximity, it was possible to detect the progenitors of SN 2008S and NGC 300 2008OT-1 in several bands in archival images. Both progenitor stars are not detected in the optical bands, but they are quite luminous in the infrared domain, suggesting that these stars are heavily dust obscured Thompson et al. (2009). On the colour-magnitude diagram, ILRTs progenitors are more red than AGB stars (Figure 1.15, right panel): such "Extreme AGB stars" are perfect candidates for being SAGB stars, suggesting an ECSN origin for ILRTs. Last but not least, the rate calculated for ILRTs is ∼8% of all core collapse events, in line with the expectations for ECSN (Cai et al. 2021).

After a brief overlook on the data reduction process, in the following chapters we will present the analysis of faint transients that can be associated to ECSN events. In particular, in Chapter 3 we discuss the properties of two faint SNe IIP: SNe 2020cxd and 2021aai. In Chapters 4 and 5 we present the photometric and spectroscopic data collected for a sample of four ILRTs, namely AT 2019abn, AT 2019ahd, AT 2019udc and NGC 300 OT. Finally, in Chapter 6 we discuss the role of dust, from progenitors to late time observations, for ILRTs in general and NGC 300 OT in particular.

Chapter 2

Methodology

The analysis presented in the following sections is based on photometric and spectroscopic observations of different transients over the course of several months - in some cases years. Our follow-up campaigns focus on the ultraviolet, optical and Near-Infrared (NIR) domains, with the goal of gathering data every few days. Oftentimes, to obtain such a high cadence monitoring of our targets, it was necessary to employ different telescopes with different instrumental configurations. In this section we will present the software and methods used to extract information from the raw images obtained at the telescopes. Both for photometry and spectroscopy, the data reduction procedure is based on the Image Reduction and Analysis Facility (`IRAF`, Tody 1986, 1993), a software specifically designed for image processing developed within the astronomical community.

2.1 Image preparation

Regardless of its origin, every image undergoes the same preliminary reduction steps. Firstly, each image contains an offset to ensure that the counts always result positive. To remove this term, each telescope collects several bias frames every day, which are images taken with null exposure time that only contain the artificial offset added by the electronics. `IRAF` contains a specific task (`ZEROCOMBINE`) to combine the different bias frames into a single image, typically called "Master Bias". In order to apply the bias correction to each subsequent image, it is sufficient to run the `CCDPROC` task.

After the bias correction, each image is trimmed in order to isolate the section of the frame that is scientifically relevant. Additionally, the flat-field correction is applied to account for the different response of the pixels within the CCD. Similarly to the bias frames, flat field frames are obtained daily at each telescope by illuminating the CCD with a uniform source of light. Each filter or grism used will have several associated flat field frames. These frames are combined together through the task `FLATCOMBINE` into a so-called "Master Flat". In the case of photometric data, the flat field correction is the last step of the pre-reduction procedure, applied once again with the `CCDPROC` task.

For the spectroscopic data, the Master Flat needs to undergo an additional correction. The `RESPONSE` task consists in a normalization procedure that aims at filtering out the wavelength dependence in the counts along the dispersion axis.

2.2 Long slit spectroscopy

The tools needed to process spectroscopic data are included in the `IRAF` package `CTIOSLIT`. First of all, a one dimensional spectrum of the target is extracted from the two dimensional image with the task `APALL`, which simultaneously performs a backgroud subtraction in order to avoid contamination from the sky emission lines and the host galaxy signal. The one dimensional spectrum is then calibrated in wavelength making use of standard spectral lamps, typically showing He, Ne, Ar, Hg and Kr lines: these features are identified with the task `IDENTIFY`. The conversion from pixel to Åis performed through the task `DISPCOR`. An additional control on the position of the sky emission lines (mainly [O I] lines) is performed, to ensure the accuracy of the calibration: a rigid wavelength shift is applied to the spectrum in case of mismatch between the expected and observed position of the sky emission lines after wavelength calibration. Measuring the average full width at half maximum (FWHM) of the sky emission lines provides the resolution of the spectrum, which of course depends on the instrument used but also on the slit width and weather conditions.

These procedures are repeated from the spectrum of a standard star (belonging to the list of ESO spectrophotometric standards[1]), which is routinely obtained during every observation run. Using the tasks `STANDARD` and `SENSFUNC` the observed flux of the standard star is compared to the tabulated flux values of the same object, effectively checking the sensitivity of the CCD over the wavelength range of incident radiation. This allows us to build a sensitivity curve: given that the weather conditions may vary from night to night, the response of the CCD will seldom be exactly the same. The sensitivity curve is used to recover the observed flux of the target in physical units (ergs s^{-1} cm^{-2} $Å^{-1}$): this flux calibration is performed with the task `CALIBRATE`.

The next step consists in removing the telluric absorption bands caused by the atmosphere of the Earth. To do so, the telluric bands are isolated in the spectrum of the standard star, and then used to correct the spectrum of the target through the task `TELLURIC`. Additionally, spectra undergo one further flux calibration based on the photometric magnitude of the transient. The task `CALCPHOT` returns the apparent magnitude of the target in a given photometric band by integrating the spectral flux of the target while accounting for the sensitivity of the chosen filter at different wavelengths. It is therefore possible to compare the apparent magnitude of the target measured on the spectrum with the apparent magnitude obtained through multi-band photometry, which has been corrected through a more robust zero point correction, as detailed in the following section. This additional flux calibration is effectively a scaling factor applied to the spectra through the Pogson relation:

$$\frac{I}{I_0} = 10^{-0.4(m_{phot}-m_{spec})} \tag{2.1}$$

where I represents the calibrated flux, I_0 is the original spectral flux and m the apparent magnitudes obtained from the photometry and spectroscopy. Once the spectra have been calibrated in wavelength and flux, they are also corrected for redshift and reddening. The redshift value considered is typically the redshift of the host galaxy reported in the NASA/IPAC Extragalactic Database (NED[2]), and the correction is applied through the `DOPCOR` task. On the other hand, there is no general method to recover the extinction for every transient, so the reddening estimation will be discussed separately in each case. Once the reddening is known, the correction is performed with the task `DEREDDEN`,

[1] https://www.eso.org/sci/observing/tools/standards/spectra/stanlis.html
[2] https://ned.ipac.caltech.edu

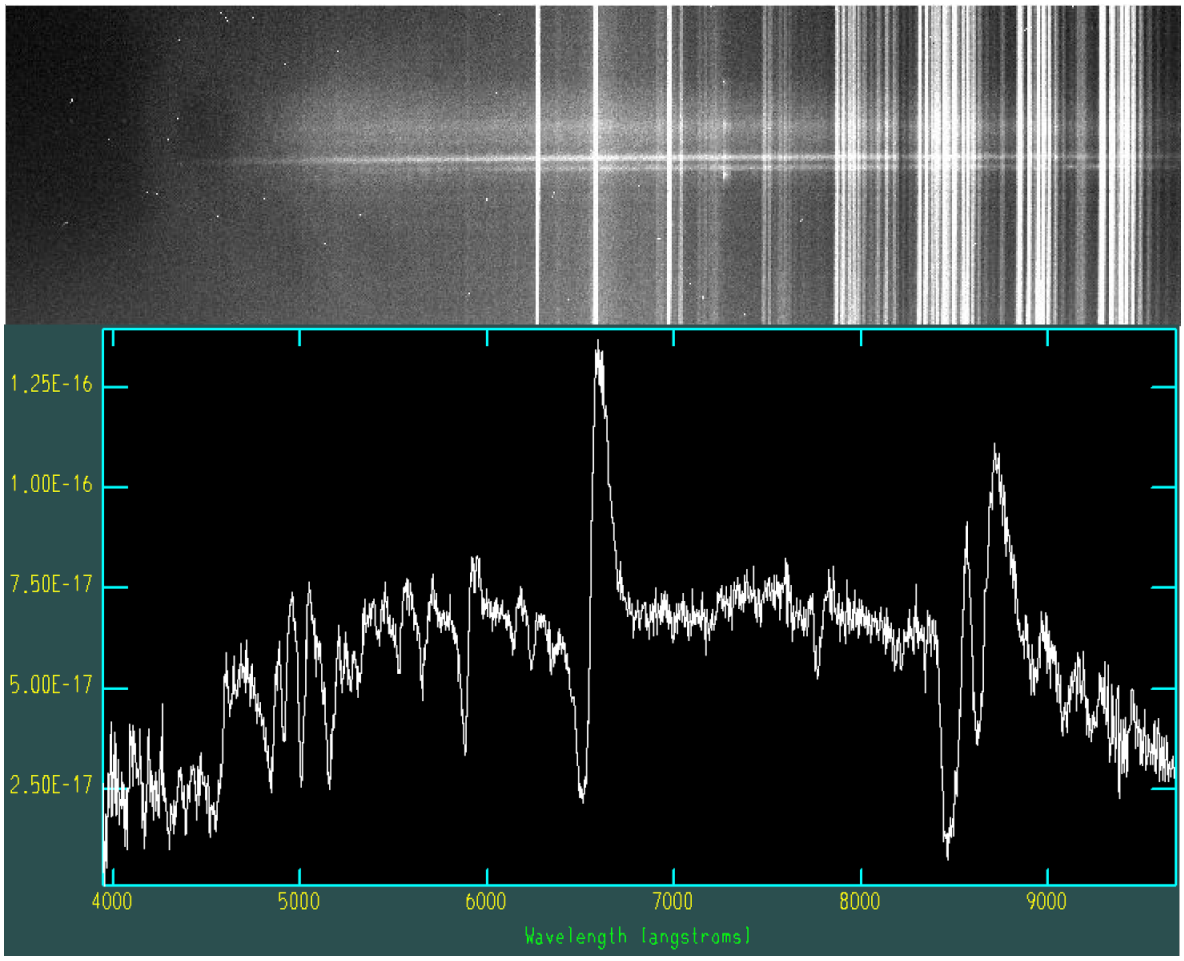

Figure 2.1: On the top panel, a two dimensional spectrum that was trimmed and corrected for bias and flat field. The two horizontal traces are respectively the spectrum of SN 2021aai and a nearby bright source. On the bottom panel is shown the one dimensional spectrum of SN 2021aai calibrated in wavelength and flux.

assuming a reddening law $R_V = 3.1$ (Cardelli et al. 1989). An example of the final product of this reduction procedure is shown in Figure 2.1.

2.3 Photometry

There are two main approaches to calculate the instrumental magnitude of a transient. Aperture photometry is the most straightforward technique, which consists in integrating the counts within a circular region centered on the target. An annular region around the integration region is used to estimate and subtract the contribution of the background. Typically, the median value of the counts in the annulus is taken to obtain a robust background noise estimate, less sensitive to outlier values due to cosmic rays or bad pixels. Aperture photometry can be performed by using the `IRAF` package `APPHOT`, which allows for manipulation of parameters such as the size and position of the integration area and

the annulus used to estimate the background noise. Aperture photometry has the advantage of being rather simple and not assuming any particular shape of the signal. However, this simplification may result in large inaccuracies when the background is not uniform. For this reason, aperture photometry is suitable for calculating the magnitude of isolated targets on a homogeneous background, features which are seldom found in optical and NIR bands for our targets.

A more elaborate method to recover the instrumental magnitude is the fitting of a *point spread function* (PSF) model on the target. In this context, the PSF model is built for each frame on selected stars in the field. The background around the object is fitted with a low order polynomial and then subtracted. Finally, the PSF is fitted to the target and the instrumental magnitude is retrieved. Following this procedure, it is possible to accurately calculate instrumental magnitudes even in crowded environments on uneven background. To perform this procedure quickly and efficiently, a dedicated pipeline was developed.

2.3.1 SNOoPY

The SuperNOva PhotometrY (SNOoPY) pipeline is a collection of `Python` based script calling `IRAF` tasks (Cappellaro 2014). SNOoPY is specifically designed to calculate magnitudes through PSF fitting on images collected with different instruments and telescopes. In particular, source extraction is managed with the `SEXTRACTOR` package and `DAOPHOT` is used to perform the PSF fitting. A detailed discussion of every single SNOoPY task can be found in the work by Tartaglia (2015): here we will present the data reduction process with this pipeline.

Firstly, relevant information about the various telescopes and CCDs such as geographic location, gain, *read out noise* (RON) and pixel-scale are stored in a configuration file, allowing for the simultaneous reduction of data from different instruments. Additional information (mainly Modified Julian Date, airmass, filter and exposure time) is directly gathered from the header of the images. At this point, the astrometric calibration is performed: with the task `ECASTRO` the position of the sources in the image is compared to the coordinates of stars in the USNO-A2.0 catalogue[3] or the 2 Micron All Sky Survey (2MASS, Skrutskie et al. 2006). An astrometric solution is found through the `IRAF` task `CCMAP`, therefore converting the coordinates of the pixel into Right Ascension (RA) and Declination (Dec). Oftentimes it is necessary to gather multiple exposures of the same field, in order to increase the signal of the target without saturating the bright stars within the image. In these cases, the task `ECDITHER` is used to combine different frames of the same field, so that a single image is obtained and further processed. The seeing is retrieved with the `ECSEEING` task, which measures the FWHM of selected unsaturated stars: this procedure is repeated for each image since using different filters results in different seeing values, and furthermore the weather can change over the course of the same night.

After the image has been correctly astrometrized and the seeing has been measured, it is possible to proceed with the creation of the PSF model and its subsequent fitting to the target. With the task `ECPSF` it is possible to inspect the PSF profiles of any number of stars in the frame, selecting the most suitable for building a PSF model: ideally, the selected stars should be isolated and bright, but not saturated, like the star on the top right panel of Figure 2.2. The PSF model is then built by averaging the PSF profiles of the selected stars, and the parameters characterizing the model built are stored in a dedicated output file. It is important to notice that a different PSF model must be built for each frame, since the PSF of the sources can change depending on weather conditions, tracking of the telescope or

[3] tdc-www.harvard.edu/catalogs/ua2.html

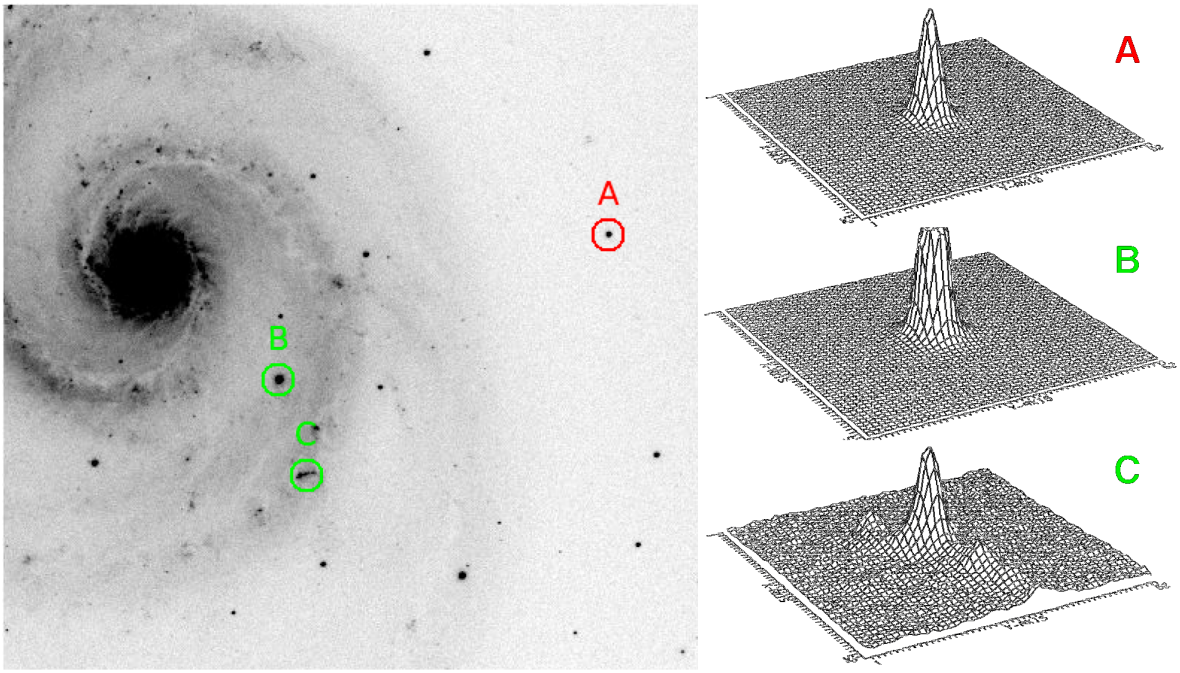

Figure 2.2: On the left, in *i* band image of the face on spiral M51. On the right, PSF profiles of three sources in the frame. In order, from top to bottom: an unsaturated, isolated bright star (A), a saturated star (B), a star in a crowded environment with uneven background (C). Only the first star presents a PSF profile adequate to build a reliable PSF model.

field distortions. To obtain the instrumental magnitude of the transient, the analytical PSF model is fit on the source at the target position through `ECSNFIT`. Within this task, the target position is accurately centered before the fitting procedure, and it is possible to select the background to be subtracted as well as the order of the polynomial fitting. An example of this procedure is shown in Figure 2.3. The error associated with this procedure is estimated thanks to `ECARTERR`, a task where artificial stars identical to the target are placed close to the position of the selected target, and their instrumental magnitude is subsequently measured with `ECSNFIT`. The dispersion in these measures is summed in quadrature with the PSF fitting error provided by `DAOPHOT`, giving as a result the error associated to the instrumental magnitude calculated by `ECSNFIT`.

Transient phenomena are typically quite bright and easily detectable in the early phases of their evolution, but within few months they dim drastically, below the threshold of detectability. The quantity considered to discriminate a detection from the background noise is the *signal to noise ratio* (SNR). SNOoPY adopts a 3-σ criterion, meaning that a source is clearly distinguished from the background if the PSF fitting procedure provides a result with SNR > 3. On the contrary, if the SNR is below 3, only an upper limit can be provided for the brightness of the transient. The SNR clearly depends on the exposure time of the frame and the collecting area of the telescope, but also on the background noise level: a bright night sky illuminated by the full moon will increase the background noise, therefore reducing our capability of detecting faint objects. A crowded environment has a similar effect, increasing the background noise level. For this reason, SNOoPY also contains the task `ECSNDIFF`, which makes use of the `IRAF` package `HOTPANTS` to perform template subtraction on our frames. A

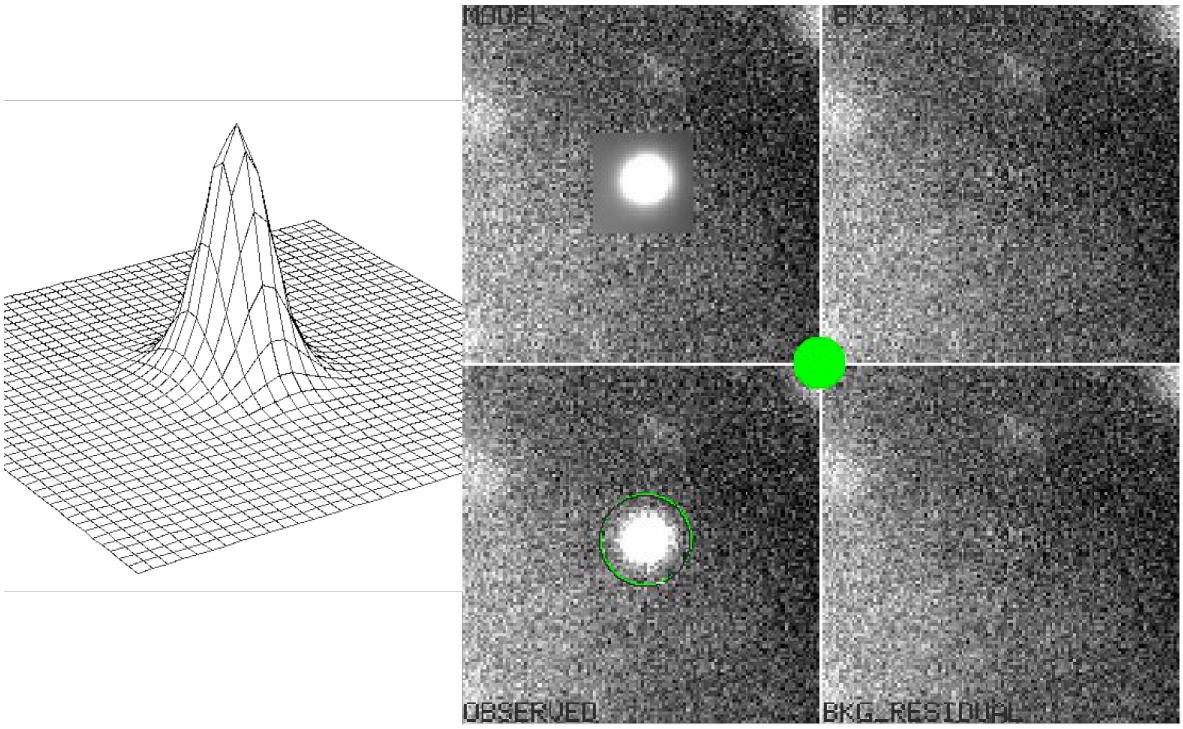

Figure 2.3: On the left, the final PSF model that is fitted to the observed transient. On the right, the results of the fitting and the residual background beneath the source, which confirms the quality of the fit. The green circle in the middle of the right panel indicates a SNR > 10.

high quality template image is fundamental for the template subtraction procedure, which is followed by the PSF fitting procedure described in the previous paragraph.

Once the instrumental magnitude has been calculated, the following step is to perform the calibration to the apparent magnitude, exploiting the standard stars in the frame with a known apparent magnitude. Usually the Landolt catalogue (Landolt 1992), Sloan Digital Sky Survey (SDSS, York et al. 2000), PanSTARRS (Kaiser et al. 2010) or 2MASS contain the apparent magnitude of several stars in the frame, depending on the wavelength domain and the filters considered. The calibration is obtained by solving a system of equation with this form, with one equation for each considered star in each observed band:

$$m_{calib} = m_{instr} + a_\lambda + b_\lambda (colour)_\lambda \tag{2.2}$$

where m_{calib} is the apparent magnitude, m_{instr} is the instrumental magnitude, b_λ is the Colour Term (CT), which varies from instrument to instrument, and a_λ is the Zero Point (ZP), which not only varies from instrument to instrument, but also from night to night. The task `ECPH` is used precisely to infer the values of CT and ZP for different instruments and filters, with the caveat that the image used to estimate CT and ZP should be obtained during a photometric night. However, most observations are obtained during non-photometric nights: the task `ECNIGHTCAL` derives the correct ZP term for the night based on the deviation of the measured apparent magnitudes of standard stars in the field

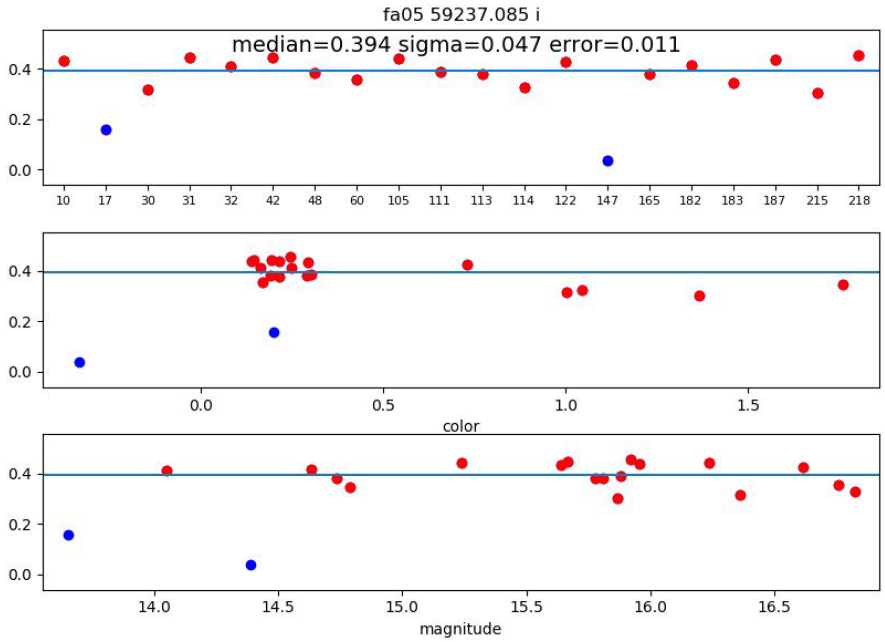

Figure 2.4: Correction of the ZP term based on the comparison between the measured apparent magnitudes of standard stars with the apparent magnitudes, reported in the catalogues. Each dot represents a star, with the blue dots representing outliers that are excluded from the final computation. In this case, on average each star is 0.4 magnitudes fainter than during a photometric night.

compared to the values recorded in the catalogues. In Figure 2.4 is shown the correction of the ZP term through the `ECNIGHTCAL` task. Finally, with the corrected values of CT and ZP, equation 2.2 is systematically applied to derive the apparent magnitudes of the transient from the instrumental ones.

Chapter 3

SN 2020cxd and SN 2021aai, at the edges of the sub–luminous supernovae

During the last two decades, the transient Universe has been inspected in an unprecedented fashion thanks to new instruments and dedicated surveys: therefore, the discovery of new classes of transients did not come as a surprise. In particular, the so called "luminosity gap" (Kasliwal 2012) separating Classical Novae ($M_V \sim -10$ mag) and standard type II Supernovae (SNe; $M_V \sim -15$ mag) has been populated with several peculiar phenomena. Among the "gap transients" (see e.g. Pastorello & Fraser 2019) can be identified stellar mergers (Luminous Red Novae), stellar eruptions (Luminous Blue Variables) and even authentic, though weak, Core–Collapse SNe. In particular, faint SNe explosions are expected to be produced when the sub–energetic explosion of a very massive stars leads the inner stellar mantle to fall back onto the core (Pumo et al. 2017). These SNe are characterized by the ejection of tiny ^{56}Ni amounts (e.g. Moriya et al. 2010). The collapse of an O–Ne–Mg core of a moderate–mass super–AGB star is also expected to produce faint transients known as electron–capture SNe (ECSNe) (e.g. Nomoto 1984; Ritossa et al. 1996; Kitaura et al. 2006; Poelarends et al. 2008), although there is no consensus yet on whether we already witnessed such an explosion. Given their faintness and low synthesised ^{56}Ni mass, the so–called Intermediate–Luminosity Red Transients (ILRTs; Botticella et al. 2009; Stritzinger et al. 2020; Cai et al. 2021) are considered to be among the most promising candidates. The electron–capture SN scenario, however, can potentially produce transients with different observable properties. The peculiar type II SN 2018zd (Hiramatsu et al. 2021) has shown a remarkable compatibility with the ECSN scenario, although no consensus has been reached yet on the nature of this object (Zhang et al. 2020; Callis et al. 2021).

Together with this array of unusual and little studied transients, there is a group of Low Luminosity SNe type IIP (LL SNe IIP) lying towards the upper end of the "luminosity gap". The first identified object of this class was SN 1997D (Turatto et al. 1998; Benetti et al. 2001), which was reported as one of the faintest SN observed to that date, peaking at M_B=–14.65 mag. The late time decline was also unusually faint, compatible with the ejection of just 2×10^{-3} $M_\odot$ of ^{56}Ni, one order of magnitude lower than the typical value for standard SNe IIP (a few 10^{-2} $M_\odot$, Anderson et al. 2014). The first scenario proposed to explain this event envisioned a massive progenitor (25–40 $M_\odot$), and the fallback on the black hole formed during the collapse would account for the low amount of energy emitted (Zampieri et al. 1998b, 2003). Important steps towards understanding the nature of LL SNe IIP progenitors were taken thanks to observational studies on samples of standard type IIP SNe (Smartt et al. 2009; Smartt

2015), which determined that the progenitor stars of SNe IIP were Red Super Giants (RSGs) with low Zero Age Main Sequence (ZAMS) masses between 8 and 18 $M_{\odot}$. These findings disfavoured the scenario of the massive progenitor for LL SNe IIP (Eldridge et al. 2007; Fraser et al. 2011; Crockett et al. 2011). This study was based on the direct detections of the progenitor star in archival images before the SN explosion, and subsequent matching with theoretical evolutionary tracks. A different approach to determine the progenitor mass consists in computing hydrodynamical models to describe observed lights curves and expansion velocities (e.g. Bersten et al. 2011; Utrobin et al. 2007; Utrobin & Chugai 2008; Pumo & Zampieri 2011; Lisakov et al. 2018; Martinez et al. 2021; Kozyreva et al. 2021). The mass estimates obtained with this method are sometimes higher (14–18 $M_{\odot}$) than the ones obtained through direct progenitor detection, possibly due to an overestimate of the ejected mass due to spherical symmetry approximation (Utrobin & Chugai 2009). There has been also a third approach (Fransson & Chevalier 1989; Maguire et al. 2010; Jerkstrand et al. 2012, 2014, 2018; Lisakov et al. 2017, 2018; Dessart et al. 2021): the nebular [OI] doublet $\lambda\lambda$ 6300,6364 observed in the late–time spectra is used as a tracer of the core mass of the progenitor star and hence of its ZAMS mass.

The method described above was developed to study standard SNe IIP, but it was also applied to LL SNe IIP, when possible: spectral modelling results are so far consistent with the lack of massive progenitors ($\sim$ 20 $M_{\odot}$) for LL SNe IIP (Müller-Bravo et al. 2020). Studies on the photometric and spectroscopic evolution of larger samples (up to 15 objects) of LL SNe IIP (Pastorello et al. 2004; Spiro et al. 2014) found that these transients share strikingly similar features. The light curves of LL SNe IIP are characterized by a quick rise to maximum (few days), followed by a plateau lasting $\sim$ 100 days, before finally settling on a late time linear decay compatible with the ejection of a small amount of ^{56}Ni ($<10^{-2}$ $M_{\odot}$). The temperature evolution is quite homogeneous among the various objects observed, with a rapid cooling at early phases leading to a temperature of 10^4 K at 10 days, and a slower subsequent decline (6000–8000 K at 30 days). The expansion velocities inferred from the spectral lines also show a fast decrease from some 10^3 km s^{-1} in the first week after explosion to $\sim$ 2000 km s^{-1} one month after. These findings are consistent with those inferred for standard SNe IIP: transients with dimmer plateaus show lower expansion velocities and eject less ^{56}Ni (Hamuy 2003; Gutiérrez et al. 2017a). Pastorello et al. (2004) and Spiro et al. (2014) proposed that LL SNe IIP are the least energetic end of the continuous distribution of SNe IIP in the parameter space (progenitor mass, plateau luminosity, ^{56}Ni synthesised, expansion velocities). This proposition is corroborated by the presence of "transitional" objects, showing intermediate properties between LL SNe IIP and standard SNe IIP, like SN 2009N (Takáts et al. 2014) and SN 2008in (Roy et al. 2011). Furthermore, Pumo et al. (2017) show that the parameter E / M_{ej} "guide" the distribution of the SNe IIP class in the parameters space, where LL SNe IIP form the underluminous tail.

In the context of LL SNe IIP, we present photometric and spectroscopic data that we collected for two objects belonging to this class: SN 2020cxd[1], one of the faintest LL SNe IIP observed to date, and SN 2021aai, which belongs to the brighter end of the class. In Sect. 3.1 we discuss the methodology used to obtain and reduce the data, while in Sect. 3.2 the photometric data are presented. In Sect. 3.3 we analyse the spectra and in Sect. 3.4 we discuss the physical parameters obtained through blackbody fits. In Sect. 3.5 we estimate the ^{56}Ni ejected mass during the explosion and compare the results with similar objects. In Sect. 3.6 we perform hydrodynamic modeling on our targets in order to infer information on their progenitor stars. Finally, in Sect. 3.8 we summarise the results obtained.

[1]SN 2020cxd has been the studied by Yang et al. (2021). Here we provide additional photometric and spectroscopic coverage of this target. Just before our submission, Kozyreva et al. (2022) presented an additional paper on the modelling of 2020cxd.

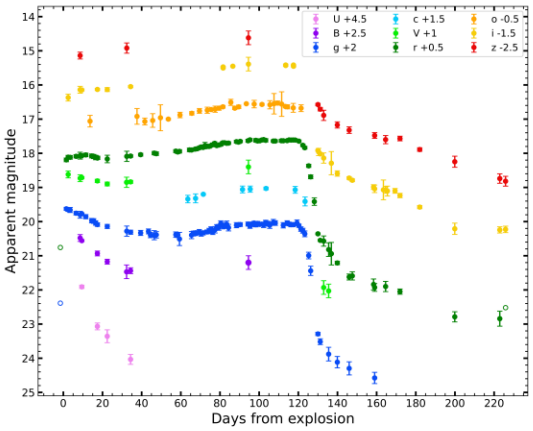

Figure 3.1: Optical light–curves of SN 2020cxd. Empty circles represent upper magnitude limits.

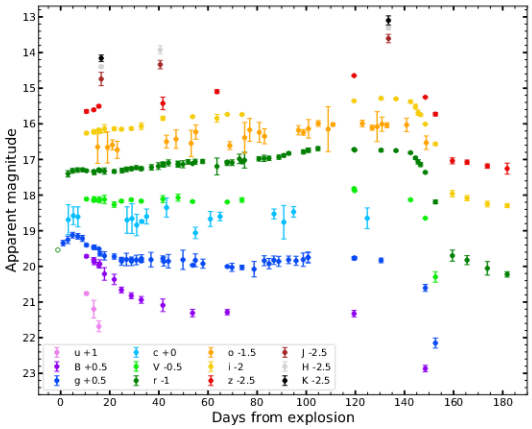

Figure 3.2: Optical and NIR light curves of SN 2021aai. Empty circles represent upper magnitude limits.

3.1 Data reduction

The objects in this paper were followed with several instruments at different facilities, whose details are reported in Table 3.1. In particular, the majority of the private data we present in this work was collected with the Nordic Optical Telescope (NOT) within the NOT Unbiased Transient Survey 2 (NUTS2) collaboration (Holmbo et al. 2019), with the Liverpool telescope and within the Global Supernova Project (Howell 2019). Image reduction was performed through standard `IRAF` tasks (Tody 1986), removing the overscan and then correcting for bias and flat field. When multiple exposures were taken on the same night, we combined them to improve the signal to noise (S/N) ratio. To measure the observed magnitudes of our targets, we used a dedicated, `python` based pipeline called `SNOoPy`[2] (Cappellaro 2014). `SNOoPy` consists in a series of Python scripts calling `IRAF` standard tasks like `DAOPHOT` through `PYRAF`, and it was designed for Point Spread Function (PSF) fitting of multi–wavelength data acquired from different instruments and telescopes. The PSF model was built from the profiles of isolated, unsaturated stars in the field. The instrumental magnitude of the transient was then retrieved by fitting this PSF model and accounting for the background contribution around the target position through a low–order polynomial fit. The error on this procedure was obtained through artificial stars created close to the target, with magnitudes and profiles coincident with those inferred for the object. The dispersion of the artificial stars instrumental magnitudes was combined in quadrature with the PSF fitting error given by `DAOPHOT` to obtain the total error associated with that measure. Zero Point (ZP) and Colour Term (CT) corrections were computed for each instrument by observing standard fields: SDSS (Albareti et al. 2017) was used as reference for Sloan filters, the Landolt (1992) catalogue was used for Johnson filters and the 2MASS (Skrutskie et al. 2006) catalogue was used for Near Infrared (NIR) filters. It is worth noticing that in the NIR we assumed negligible CT, so we only computed the ZP correction. In order to account for non–photometric nights, we selected a series of stars in the field of each transient: measuring the average magnitude variation of the reference stars with respect to the catalogued magnitudes, we computed the ZP correction for each night in each filter. Applying ZP and CT corrections to the instrumental magnitudes of our targets, we

[2] A detailed package description can be found at http://sngroup.oapd.inaf.it/snoopy.html.

Table 3.1: List of instruments and facilities used in our follow–up campaigns, detailing also the filters used to take photometric data. See Table 3.2 for details about the spectra.

Code	Telescope, [m]	Instrument	Filters	Site
EKAR	Schmidt, 0.91	Moravian	V, g, r, i	Osservatorio Astronomico di Asiago, Cima Ekar
fl03–fl15	LCO[†] (LSC site), 1.00	Sinistro	U, B, V, g, r, i, z	Cerro Tololo Inter–American Observatory
fl05–fl07	LCO (ELP site), 1.00	Sinistro	U, B, V, g, r, i, z	McDonald Observatory
fl06–fl14	LCO (CPT site), 1.00	Sinistro	U, B, V, g, r, i, z	South African Astronomical Observatory
fl12	LCO (COJ site), 1.00	Sinistro	U, B, V, g, r, i, z	Siding Spring Observatory
ZTF	Oschin Telescope, 1.22	ZTF	g, r	Palomar Observatory, United States
AFOSC	Copernico Telescope, 1.82	AFOSC	B, V, g, r, i, z	Osservatorio Astronomico di Asiago, Cima Ekar
IO:O	Liverpool Telescope, 2.00	IO:O	B, V, g, r, i, z	Observatorio Roque de Los Muchachos, La Palma
FLOYDS	LCO (FTN/FTS site), 2.00	FLOYDS	–	Haleakala (FTN) and Australia (FTS)
ALFOSC	Nordic Optical Telescope, 2.56	ALFOSC	B, V, g, r, i, z	Observatorio Roque de Los Muchachos, La Palma
NOTCam	Nordic Optical Telescope, 2.56	NOTCam	J, H, K	Observatorio Roque de Los Muchachos, La Palma
LRS	Telescopio Nazionale Galileo, 3.58	DOLORES	B, V, u, g, r, i, z	Observatorio Roque de Los Muchachos, La Palma
OSIRIS	Gran Telescopio CANARIAS, 10.40	OSIRIS	–	Observatorio Roque de Los Muchachos, La Palma

[†] Las Cumbres Observatory

obtained the apparent magnitudes reported in this paper. We adopted the AB magnitudes system for *ugriz* bands and Vega magnitudes for *BVJHK* bands. For the "Asteroid Terrestrial–impact Last Alert System" (ATLAS) data (Tonry et al. 2018), we combined the flux values obtained through forced photometry reported in their archive[3], and converted the result into magnitudes as prescribed in the ATLAS webpage. The photometric measurements we obtained are reported in the appendix.

The original spectra presented in this work (see Table 3.2) were reduced through standard `IRAF` routines contained in the package `CTIOSLIT`. All spectra were corrected for bias and flat-field before extracting the 1-D spectrum. Sky lines and cosmic rays were removed, wavelength and flux calibrations were applied using arc lamps and spectrophotometric standard stars. Finally, spectra were corrected for telluric lines, they were flux calibrated an additional time on the broad–band photometric data obtained at the same phase, and they were corrected for redshift and reddening (discussed in Sect. 3.2). In particular, spectra taken with the NOT were reduced through the `ALFOSCGUI`[4] pipeline (Cappellaro 2014), specifically designed to reduce spectra within the NUTS2 collaboration. The spectra presented in this article will be available on the WISeREP repository (Yaron & Gal-Yam 2012).

3.2 Discovery and photometric evolution

3.2.1 SN 2020cxd photometric properties

SN 2020cxd is a LL SN IIP discovered on 2020 Feb 19 (Nordin et al. 2020) at the coordinates RA = $17^h26^m29^s.26$ Dec = +71°05' 38".58 in the spiral galaxy NGC 6395, classified as Scd (de Vaucouleurs et al. 1991) and with a redshift z = 0.003883 ± 0.000002 (Springob et al. 2005). As noticed by Yang et al. (2021), the distance measurements for the host galaxy vary between 19 and 23 Mpc, depending on the methodology used. In this paper we adopt a distance modulus of μ = 31.60 ± 0.20 mag (or 20.9 ± 1.4 Mpc), obtained by averaging the six different estimates obtained through the Tully–Fisher method and reported on the NED database (Bottinelli et al. 1985; Tully et al. 2013, 2016; Sorce et al. 2014; Willick et al. 1997; Tully & Fisher 1988). We assumed a cosmology where H_0 = 73 km s^{-1} Mpc^{-1}, Ω_Λ = 0.73 and Ω_M = 0.27 (Spergel et al. 2007), which will be used throughout this work. The Galactic absorption in the direction of NGC 6395 is A_V = 0.11 ± 0.03 mag, from Schlafly & Finkbeiner (2011), under the assumption that R_V=3.1 (Cardelli et al. 1989; which will be used throughout this

[3] https://fallingstar–data.com/forcedphot/

[4] More details at https://sngroup.oapd.inaf.it/foscgui.html

work). Early spectra do not show evidence of the interstellar Na I D absorption doublet at the host galaxy redshift, allowing us to estimate as negligible the absorption along the line of sight (see Sect. 3.3).

In Figure 3.1, we report the multi–wavelength photometry of SN 2020cxd collected up to 230 days after explosion. The early rise in luminosity was not observed, since the object was first detected when it was already on the plateau. However, thanks to a deep upper limit ($r > 20.3$ mag) obtained just three days before the discovery by the Zwicky Transient Facility (ZTF; Graham et al. 2019), it is possible to constrain the explosion epoch with small uncertainty to MJD = 58897.0 ± 1.5. Even on the plateau, the brightness was not strictly constant: at first there was a decline, with the transient dimming from M_r = –14.13 mag at 10 days to M_r = –14.00 mag at 22 days (typical photometric error of 0.04 mag). This luminosity decrease was more marked in the blue bands. This behaviour is clear in the g band, where the absolute magnitude declined from M_g = –13.97 mag to M_g = –13.20 mag in the first 60 days. Thereafter, the brightness consistently increased to M_g = –13.58 mag and M_r = –14.48 mag before finally fading from the plateau at ∼120 days. Müller-Bravo et al. (2020) attributed the different behaviour of the g band compared to the r band to the shift of the Spectral Energy Distribution (SED) peak from the ultraviolet (UV) to the optical domain. The drop from the plateau was very sharp, with the object fading by 2.9 mag in the r band and 3.2 mag in the g band in just 10 days. Finally, the luminosity evolution settled on a linear decline powered by the ^{56}Ni synthesised during the explosion. More details in Sect. 3.4.

3.2.2 SN 2021aai photometric properties

SN 2021aai was discovered at the coordinates RA = $07^h14^m26^s.86$ Dec = +84°22' 51".46 on 2021 Jan 12 (Munoz-Arancibia et al. 2021) in NGC2268, an SAB(r)bc (de Vaucouleurs et al. 1991) at a redshift of z = 0.007428 ± 0.000007 (Springob et al. 2005). We adopt a distance modulus of μ = 32.47 ± 0.20 mag (31.2 ± 1.7 Mpc) obtained through one of the most recent Tully–Fisher estimates (Tully et al. 2013). According to Schlafly & Finkbeiner (2011), the reddening internal to the Milky Way along the line of sight towards NGC2268 is A_V = 0.170 ± 0.003 mag. Unlike in SN 2020cxd, the Na I D absorption doublet was detected in the first two spectra obtained (see Sect. 3.3), with an Equivalent Width (EW) of 1.6 Å. Some relationships between reddening and Na I D EW typically saturate with such high values of EW (Poznanski et al. 2012), so we estimate a lower limit to the absorption along the line of sight through the relationship provided in Turatto (2003) for "low reddening", obtaining a total absorption along the line of sight of A_V=0.8 ± 0.1 mag. At the same time, we tried to make use of the homogeneity observed for this class of objects during the plateau (Pastorello et al. 2004; Spiro et al. 2014): we estimated the absorption necessary to bring the colour evolution of SN 2021aai closest to the colour evolution of a sample of LL SNe IIP (taken from Matheson et al. 2003; Pastorello et al. 2004, 2009) between 30 and 100 days. Similar procedures were already performed, for example for SN 2001dc (Pastorello et al. 2004). Through the method of the least squares, we obtained an absorption of A_V=1.92 ± 0.06 mag (A_V=2.09 ± 0.06 mag, accounting for the internal reddening of the Milky Way), which will be referred hereafter as "high reddening scenario". To compare the colour evolution of SN 2021aai with the LL SNe IIP colours available in the chosen sample, we converted the r magnitudes (AB magnitudes system) into Johnson R magnitudes (Vega magnitude system) by applying a constant correction measured through spectrophotometry (we adopt $r - R$ = 0.28 mag, the average value measured during the plateau phase).

The apparent light curves obtained during the six months of follow–up are shown in Figure 3.2. The rise to maximum was not observed, but the explosion epoch was well constrained at MJD = 59223.4

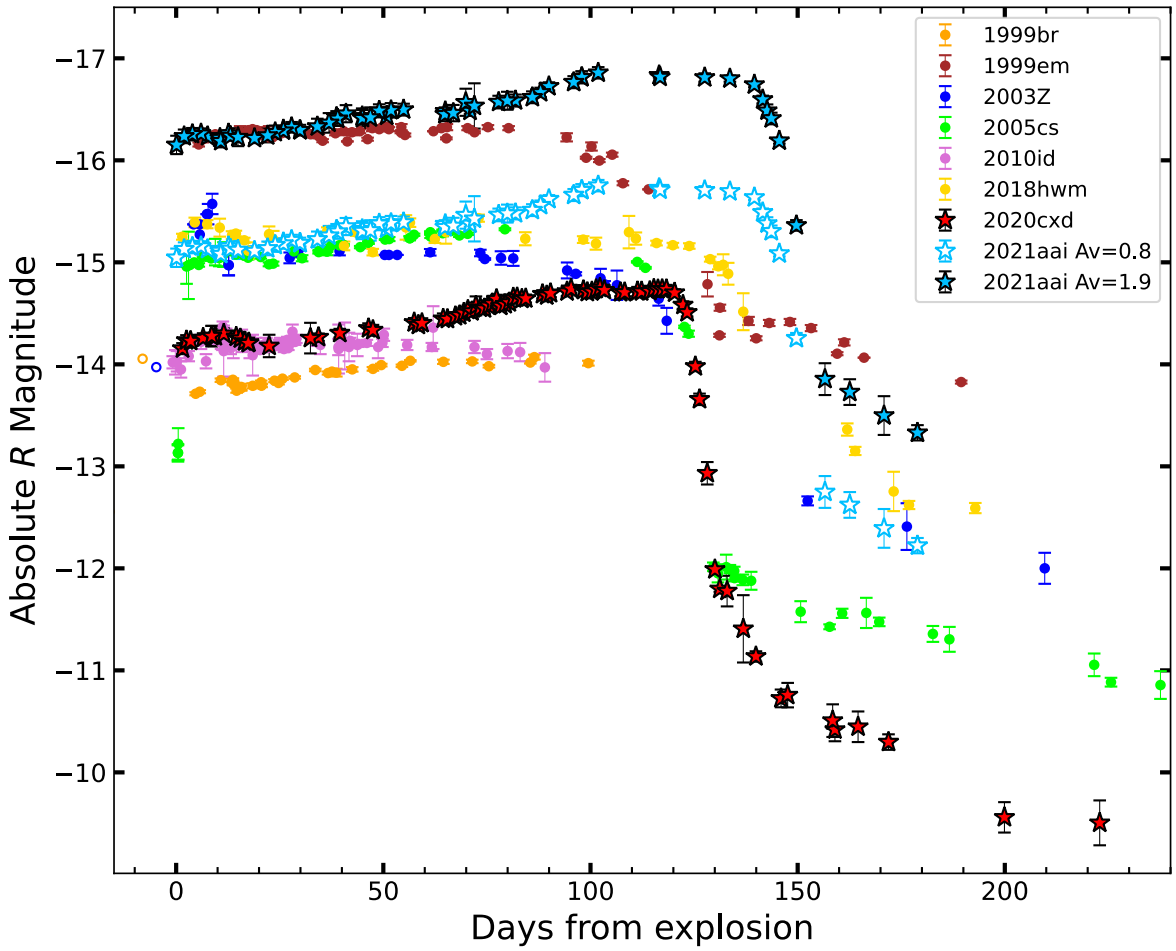

Figure 3.3: Comparison of the *R* band evolution for a sample of SNe IIP, spanning from some of the faintest objects observed, like SN 1999br, up to events like SN 1999em, which are close to the standard SNe IIP.

± 1.0, thanks to an upper limit ($r > 20.5$ mag) obtained by ZTF just two days before the first detection. The plateau phase was unusually long–lasting, with a duration of 140 days: a tentative physical explanation will be discussed in Sect. 3.6. During the plateau, the r band displays a progressive brightening, spanning from −15.87 mag to –16.57 mag (± 0.09 mag) in the high reddening scenario, and from –14.77 mag to –15.47 mag in the low reddening scenario. A similar behaviour is recorded in the NIR, where the transient became one magnitude brighter in the J, H and K bands from 13 d to 130 d. The g band evolution of SN 2021aai was different, with the transient reaching a peak magnitude of –16.41 (–14.84) mag at 5 days after the explosion, and then settling on a constant value of –15.68 (–14.11) mag up until the fall from the plateau in the high (low) reddening scenario. During the fall from the plateau, which was well sampled in the r and i bands, there was a marked drop of 2.88 mag in 16 days.

3.2.3 Comparison with the LL SNe IIP class

We compare SNe 2020cxd and 2021aai with LL SNe II and a borderline standard SN IIP that have good photometric and spectroscopic coverage. For this reason, we choose SN 1999br (Pastorello et al. 2004), SN 1999em (Hamuy et al. 2001), SN 2003Z (Spiro et al. 2014), SN 2005cs (Pastorello et al. 2009), SN 2010id (Gal-Yam et al. 2011), SN 2018hwm (Reguitti et al. 2021). In Figure 4.2, we plot the R band light curves for the chosen sample of faint SNe IIP. We convert the Sloan r magnitudes of SN 2018hwm, SN 2020cxd and SN 2021aai to Johnson R magnitudes by applying the constant correction discussed above for SN 2021aai ($r - R = 0.16$ mag for SN 2020cxd, $r - R = 0.23$ mag for SN 2018hwm). While relatively brighter objects like SN 2005cs or SN 2018hwm display a plateau at $M_r \sim -15$ mag, SN 2020cxd lies towards the low luminosity end of core collapse events, marked by the faint SN 1999br. SN 2021aai is located towards the brighter end of the peak luminosity distribution, especially in the high reddening scenario, when it is comparable to the standard event SN 1999em. The difference in the plateau luminosity can be physically interpreted as a different mass and density profile of the recombining H powering the light curve, a different expansion velocity of the ejected gas, or a different initial radius of the exploding star. During the first 50 days of evolution, the light curve of SN 2020cxd closely resembles that of SN 2010id. However, the two light curves become different after ∼50 days, when SN 2020cxd shows a rebrightening while SN 2010id starts to fade. Indeed, both SNe 2020cxd and 2021aai are characterised by an increase of brightness towards the end of the plateau. This behaviour is not unheard of, as shown by Galbany et al. (2016), and it is more common in the red bands of faint transients with long plateau phases. Indeed, the plateau of SN 2021aai is among the longest observed with its 140 days of duration, outlasting even the peculiar SN 2009ib (Takáts et al. 2015). For context, the average plateau duration for a SN IIP is 83.7 ± 16.7 days (obtained for the V band by Anderson et al. 2014). SN 2021aai shows a late time decline close to that band 2018hwm, while SN 2020cxd displays one of the faintest late time declines observed, even for LL SNe.

In Figure 3.4, we display the $B-V$ and $V-R$ colour evolution of SNe 2020cxd and 2021aai along with the colours observed for LL SNe IIP. Qualitatively, the behaviour of LL SNe IIP is quite homogeneous, as was already shown by Spiro et al. (2014). After a rapid increase in colour during the first 50 days ($\sim$ 1.5 mag increase in $B - V$ and $\sim$ 0.5 mag increase in $V - R$), the colours remain roughly constant up to $\sim$ 120 days, when SNe IIP typically fall from the plateau, leading to a final increase in colour as the transients become redder. The $g - r$ colour curve of SN 2020cxd shows an interesting behaviour after 120 days. We observe a steep increase in colour during the fall from the plateau, and a subsequent inversion in the trend as the colour $g - r$ becomes bluer. Such feature was pointed out for

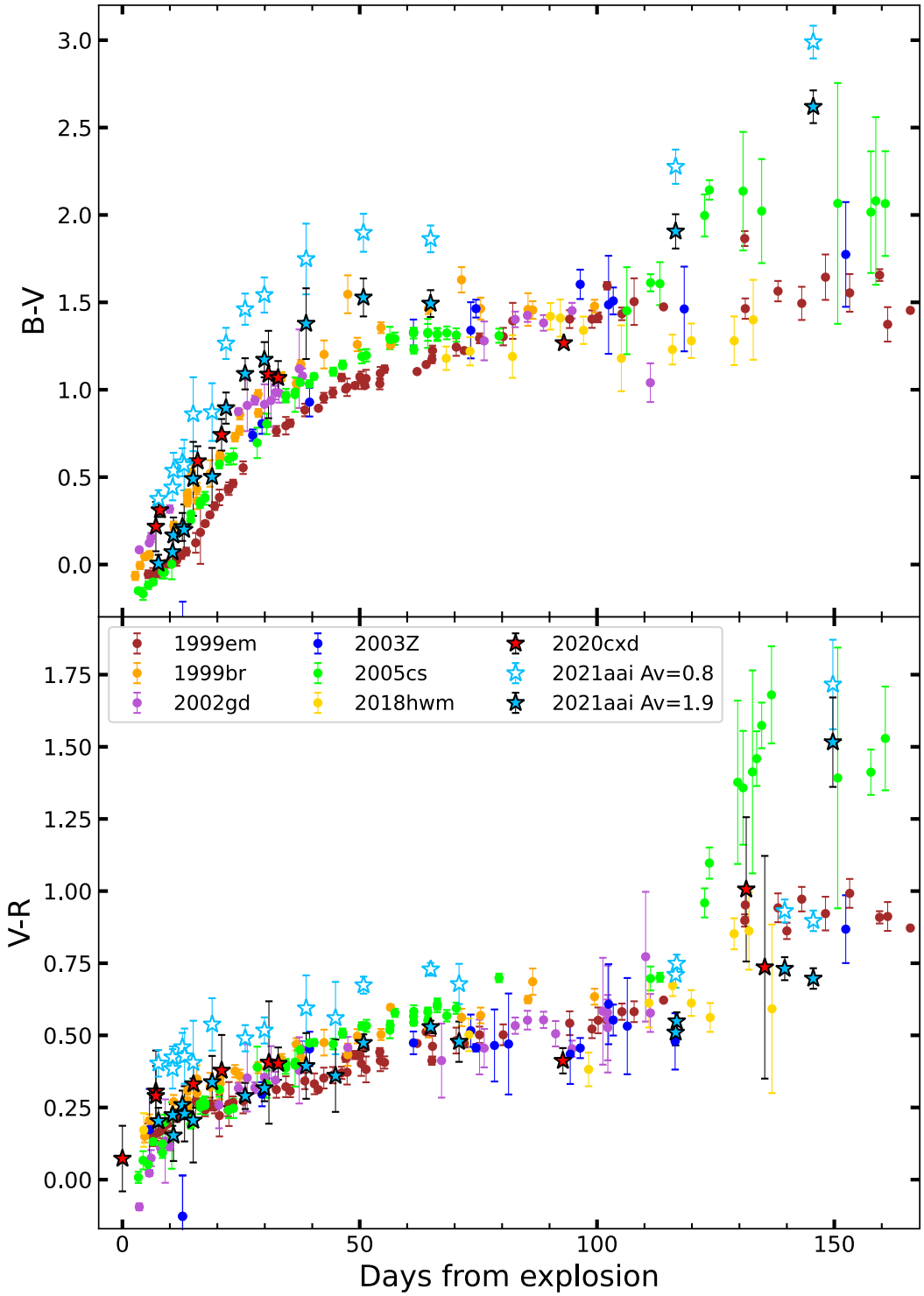

Figure 3.4: $B-V$ and $V-R$ colour evolution for some of the objects presented in Figure 4.2. SN 2021aai is reported twice, both with the low and the high reddening correction discussed in the text.

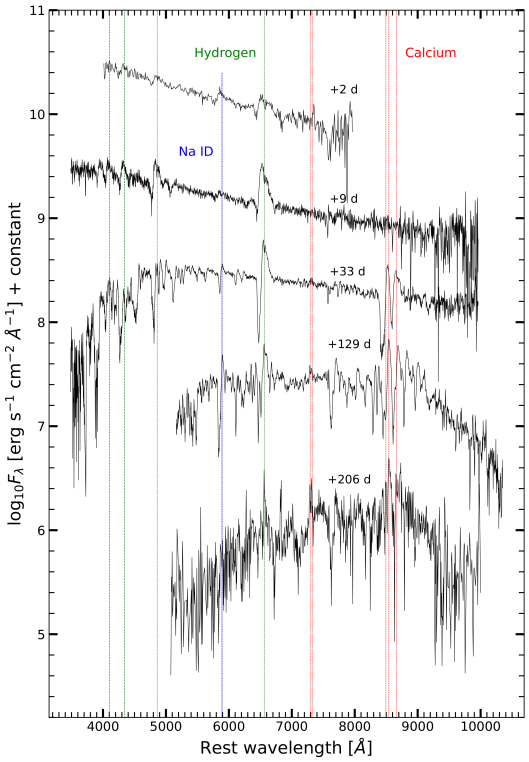

Figure 3.5: Optical spectra of SN 2020cxd. Dashed lines mark the position of the Balmer series lines, Ca and Na I D lines. All spectra were corrected for reddening and redshift. Epochs are reported with respect to the explosion date.

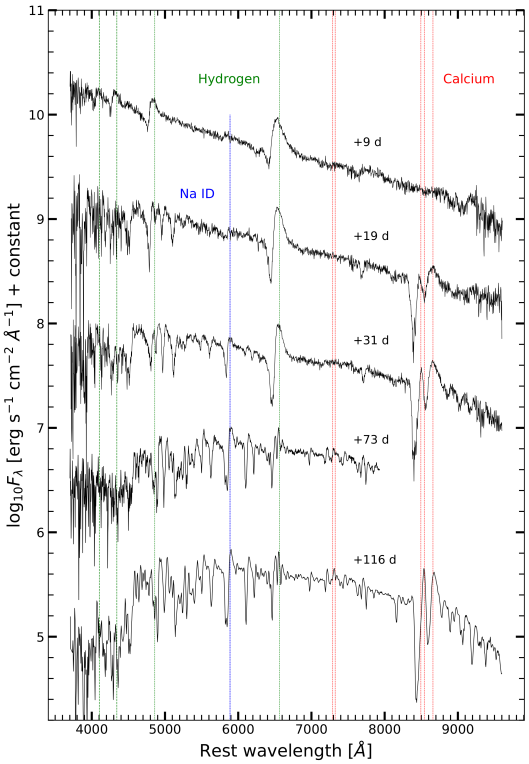

Figure 3.6: Optical spectra of SN 2021aai. Dashed lines mark the position of the Balmer series lines, Ca and Na I D lines. All spectra were corrected for redshift and reddening (in the high reddening scenario). Epochs are reported with respect to the explosion date.

Table 3.2: Log of original spectroscopic observations for SN2020cxd and SN2021aai. Phases are reported with respect to the explosion epoch.

Phase (days)	MJD	Setup	Resolution [Å]
	SN2020cxd		
2.3	58899.3	LT+SPRAT	18.0
8.6	58905.6	LCO+FLOYDS	15.5
32.5	58929.5	LCO+FLOYDS	15.5
128.5	59025.5	GTC+OSIRIS	7.5
205.7	59102.7	GTC+OSIRIS	8.0
	SN2021aai		
8.5	59231.9	NOT+ALFOSC	14.6
10.5	59233.9	TNG+LRS	15.5
18.5	59241.9	NOT+ALFOSC	14.1
30.5	59253.9	NOT+ALFOSC	14.1
35.6	59259.0	TNG+LRS	15.6
61.5	59284.9	NOT+ALFOSC	18.2
72.5	59295.9	TNG+LRS	10.4
115.5	59338.9	NOT+ALFOSC	14.1

the first time for SNe 1997D and 1999eu (Pastorello et al. 2004). As for SN 2021aai, it is possible to appreciate the difference in the colour evolution for the low and high reddening scenario, respectively. By construction, in the high reddening scenario the behaviour of SN 2021aai resembles more closely that of the other LL SNe IIP.

3.3 Spectroscopic evolution

3.3.1 Spectroscopic features

Figures 3.5 and 3.6 show the spectral sequences for SNe 2020cxd and 2021aai. The log of the spectroscopic observations is reported in Table 3.2. In the first two spectra of SN 2020cxd, we notice a blue continuum: a blackbody fit yields a temperature of 10000 K at 2 d, which quickly declined to 8000 K at 9 d. Both spectra display prominent Balmer lines and few weaker lines, such as He I and Na ID displaying a P Cygni profile. The absence of the interstellar sodium absorption doublet leads us to estimate the internal absorption in the host galaxy as negligible. At 30 d, we notice the arising of several new features: Ca II lines start to appear in the red part of the spectrum, in particular the forbidden doublet [CaII] $\lambda\lambda$7291,7323 (with a signal to noise ratio ~3) and Ca II NIR (Figure 3.5). On the blue part of the spectrum, several metal lines are identified, especially those of Fe II triplet 42 ($\lambda\lambda\lambda$4924,5018,5169), Sc II ($\lambda\lambda$5669,6246) and Ba II ($\lambda\lambda$6142,6497). Some of the most prominent metal lines are highlighted in Figure 3.7, where it is also possible to appreciate the similarities between the spectra of SN 2020cxd and SN 2021aai.

The spectral features mentioned so far are extensively observed in LL SNe (Pastorello et al. 2004; Spiro et al. 2014; Müller-Bravo et al. 2020; Reguitti et al. 2021). The presence of a relevant amount of metals gives rise to "line blanketing", where the flux in the bluest part of the spectrum is reduced by the metal absorption lines (see e.g. Moriya et al. 2019). For this reason, when estimating the blackbody temperature from the continuum, it is important to exclude the blanketed region (indicatively, at

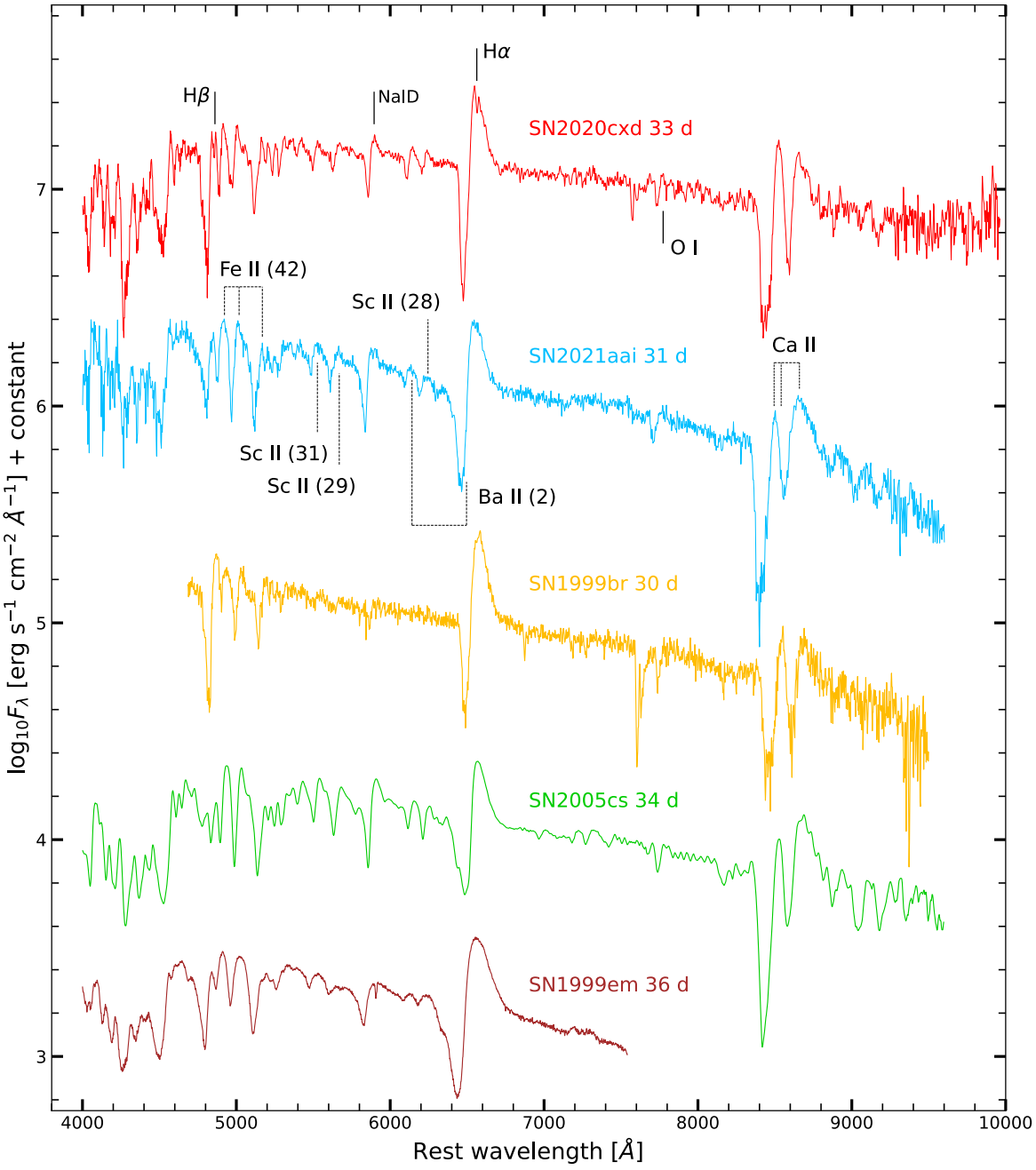

Figure 3.7: Comparison of SN 2020cxd and SN 2021aai together with LL SNe IIP (SN 1999br and SN 2005cs) and a standard event (SN 1999em). All spectra were collected between 30 and 36 days after explosion and corrected for redshift and reddening (in the high reddening scenario for SN 2021aai). On SNe 2020cxd and 2021aai are marked the main spectral features characterising LL SNe IIP (at rest wavelength).

wavelengths shorter than 5000 Å) from the fit. Taking this effect into account, the blackbody fit of the continuum at 31 d yields a temperature of 5460 K, in line with the expectations for H recombination. The last two spectra are taken after the drop from the plateau, during the late tail decline, when the [Ca II] doublet and Ca NIR triplet become prominent.

In Figure 3.6, we present the spectral evolution of SN2021aai. We obtained a high quality sampling of the target during the plateau phase, but unfortunately it was impossible to follow the object after the fall from the plateau due to visibility constraints. The first spectrum, at 8 d, is dominated by H lines. The interstellar Na I D absorption doublet is identified, suggesting a significant line of sight reddening towards SN 2021aai (see Sect. 3.2). At later phases, the broad Na I D feature develops a clear P Cygni profile, at the same phases when the Ca II NIR triplet and the metal lines appear in the spectra. In Figure 3.7, we compare the spectra at $\sim$ 30 d of SN 2020cxd and SN 2021aai with SN 1999br (Pastorello et al. 2004), SN 2005cs (Pastorello et al. 2009) and SN 1999em (Hamuy et al. 2001). The similarity among this sample of objects is striking, considering that they span over two magnitudes in peak luminosity. Beside the obvious P Cygni profile of Hα, all the objects are characterised by evident Ca II NIR triplet lines, Sc II λ6246 and Fe II multiplet 42 ($\lambda\lambda\lambda$4924,5018,5169). The differences lie, of course, in the line velocities: the position of the minimum of the P Cygni profile and the width of the Hα feature in SN 1999em suggests a significantly higher expansion velocity for this object, which separates this standard SN IIP from the other LL SNe shown.

3.3.2 Expansion velocities

We estimate the velocity of the expanding gas by measuring the position of the minimum of the P Cygni absorption profiles. Different species yield a different expansion velocity, reflecting a different position where the line forms through the ejecta (Gutiérrez et al. 2017b). Due to higher optical depth, Hα and Hβ lines form in the outer layers of the expanding materials, therefore yielding higher velocities than other species. Fe II lines, especially those belonging to multiplet 42, have a lower optical depth, and have been widely used to estimate the expansion velocity of the ejecta at the photosphere (Hamuy 2003). The Sc II line λ6246 displays an even lower optical depth, and is sometimes used as a proxy for expansion velocity instead of the Fe II lines (e.g. Maguire et al. 2010). For SN 2020cxd in particular, the velocity measurements performed on the Hα line showed that the line forming region moves in velocity space monotonically from 5900 km s^{-1} at 2 d, to 2560 km s^{-1} immediately after the drop from the plateau (134 d), and finally to 1020 km s^{-1} at 245 d. The Hα expansion velocity after 90 days is measured from the Full Width at Half Maximum (FWHM) of the line, since the rise of the Ba II λ 6497 makes it impossible to identify clearly the position of the minimum of the P Cygni profile. The results are reported in Table 3.3 and plotted in Figure 3.8, along with other values from LL SNe IIP taken from Pastorello et al. (2004, 2009) and Spiro et al. (2014). From the comparison with similar objects, we notice that SN 2020cxd displays low Hα and Sc II expansion velocities in the early phases (before 50 d), compatible with the values obtained for SN 1999br (Pastorello et al. 2004). Later epoch values, however, appear to be more in line with higher velocity objects like SN 2006ov (Spiro et al. 2014). It is important to notice, especially for the Sc II measurements at 95 d, that the resolution of the spectrum was poor, leading to a large error.

For SN 2021aai, the velocities measured from the Hα P Cygni profiles range from 7000 km s^{-1} at 8 d to 4200 km s^{-1} at 35 d. Subsequently, the rise of the Ba II λ 6497 line in the absorption part of the P Cygni profile forces us to estimate the expansion velocities from the FWHM of the emission component of the Hα line, as previously done by Yang et al. (2021) for SN 2020cxd. As already mentioned, metal lines are characterised by a lower optical depth, leading to their formation closer to

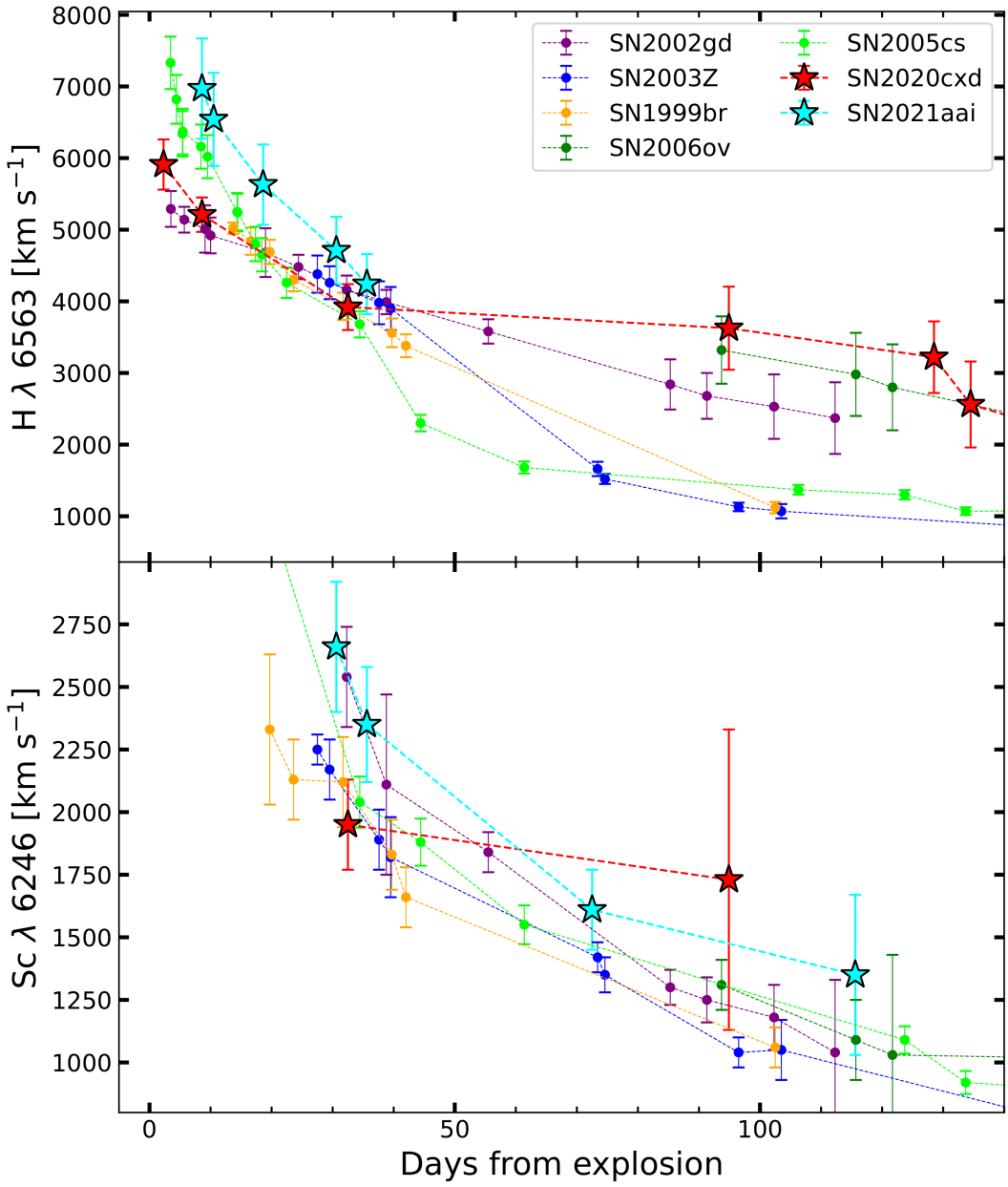

Figure 3.8: Expansion velocities measured on the Hα and Sc II λ 6246 lines. The values obtained for SN 2020cxd and SN 2021aai are compared with those of other LL SNe IIP.

Table 3.3: Expansion velocities measured for relevant lines through the position of the minimum of the P Cygni absorption profile. All velocities are in km s^{-1}. Measurements for SN 2020cxd taken at 94.9 and 134.5 d were performed on spectra presented in Yang et al. (2021).

Phase (days)	Sc II λ 6246	Fe II λ 5169	Hβ	Hα
		SN 2020cxd		
2.3	–	–	5670 (430)	5910 (350)
8.6	–	4800 (600)	5240 (400)	5210 (240)
32.5	1950 (180)	3020 (250)	3520 (300)	3920 (320)
94.9	1730 (600)	–	–	3625 (580)
128.5	–	–	–	3220 (500)
134.5	–	–	–	2560 (600)
		SN 2021aai		
8.5	–	–	6480 (970)	6970 (700)
10.5	–	5180 (620)	6170 (930)	6540 (650)
18.5	–	3850 (480)	4810 (720)	5630 (560)
30.5	2660 (400)	3020 (420)	3580 (540)	4710 (470)
35.6	2350 (350)	2500 (380)	2840 (430)	4240 (420)
72.5	1610 (240)	1970 (340)	–	–
115.5	1350 (320)	–	–	–

the photosphere compared to H lines, which form in the outer layers of the ejecta and therefore yield higher velocity measurements. Both Hα and Sc II expansion velocities for SN 2021aai are shown in Figure 3.8. SN 2021aai shows high velocities both in the H I and Sc II measurements, located consistently at the top end of the velocity distribution for the sample of objects considered. Since it is also among the most luminous LL SNe (adopting the high reddening scenario), this would favour the interpretation in which SNe IIP are characterised by a continuum of properties, spanning from LL SNe IIP to the most luminous ones, with brighter objects showing higher velocities and a larger ejected ^{56}Ni mass, as suggested by Pastorello et al. (2004). Such correlation will be discussed in more detail in Sect. 3.5.

3.4 Blackbody Fitting

In order to estimate physical parameters characterizing SNe 2020cxd and 2021aai, we perform blackbody fits both on our photometric data and on our spectra. For the spectra, we use the `nfit1d` task in the `IRAF` package `stsdas`, fitting the continuum with a blackbody function. For the fit of the photometric points, we perform a Monte Carlo simulation for each epoch, fitting with the `python` tool `curve_fit`[5] 200 sets of fluxes randomly generated with a Gaussian distribution centered on the measured flux value for each band, and σ equal to the measured error. After obtaining a blackbody fit to the SED of the target (which already yields the temperature), we integrate it over wavelength and obtain the total flux emitted. The resulting temperature and total flux for each night are given by the median value of the 200 iterations performed, while the standard deviation of those measures yields the associated errors. Such procedure is described in detail in Pastorello et al. (2021). Both in the spectroscopic and photometric fits, we exclude the regions heavily affected by line blanketing, since

[5]https://docs.scipy.org/doc/scipy/reference/generated/ scipy.optimize.curve_fit.html

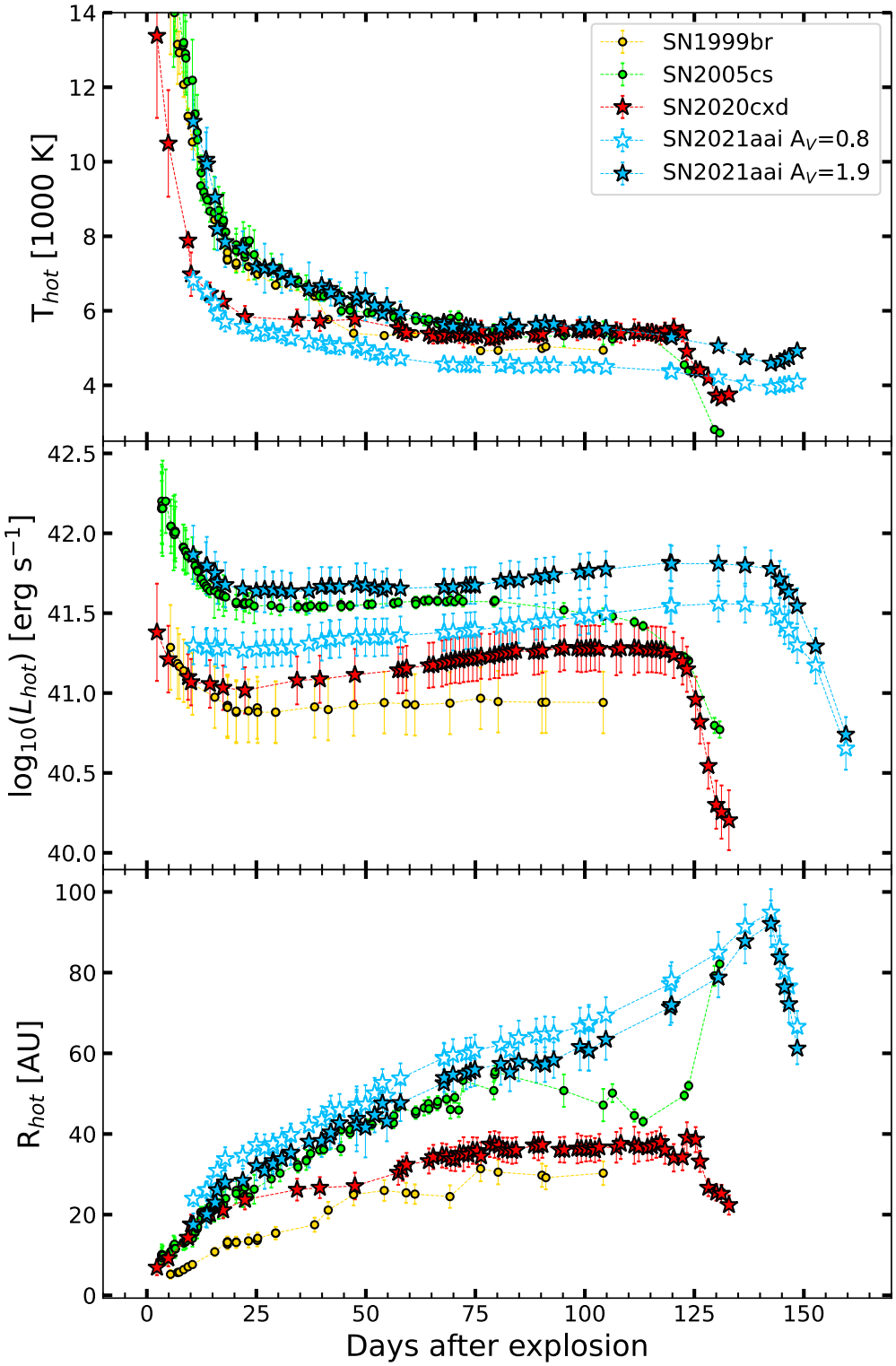

Figure 3.9: Temperature, luminosity and radius evolution of SNe 2020cxd and 2021aai, along with SN 1999br and SN 2005cs for comparison. See text for the details about the blackbody fitting procedure.

they would misleadingly reduce the estimated temperature. In particular, for the epochs after 10 d we excluded the *u* band, and after 20 d we had to further cut *B* and *g* bands.

Adopting the distances given in Sect. 3.2 and assuming spherical symmetry, we calculate the bolometric luminosity of the source. Finally, the radius is estimated through the Stefan–Boltzmann law. The errors on the final luminosity and radius values are obtained through standard error propagation procedures. The temperature, luminosity and radius obtained for SNe 2020cxd and 2021aai are presented in Figure 3.9, together with the same values obtained for SN 1999br (Pastorello et al. 2004) and SN 2005cs (Pastorello et al. 2006). On the top panel we see that SN 2020cxd displayed a very hot continuum (> 13000 K) at 2 d, quickly declining over the following days. At 22 days, the temperature already settles at ∼ 5500 K, corroborating the results obtained in Sect. 3.3. At 121 days, the temperature starts declining, along with the luminosity, as the object fades from the plateau. The bolometric luminosity of SN 2020cxd is presented in the middle panel of Figure 3.9 and shows a clear dip from 2.4×10^{41} erg s^{-1} at 2 d to 1.0×10^{41} erg s^{-1} at 22 d. During the following 90 days the transient steadily rebrightens, reaching 1.9×10^{41} erg s^{-1} at 111 d, before finally falling from the plateau at 120 d. The radius (bottom panel) of the emitting blackbody quickly rises from 7 to 26 AU in the first 30 days, followed by a slower increase. Between 50 and 120 days, the emitting radius remaines roughly constant at ∼35 AU. When SN 2020cxd is fading from the plateau, the radius shows a decrease, which can be interpreted as the photosphere receding before the ejecta finally becomes transparent. We do not fit a blackbody to the epochs in the linear decline, as the transient is transitioning from the photospheric to the nebular phase, where the luminosity is mostly supported by lines rather than continuum opacity.

For SN 2021aai, we discuss both the low reddening case with A_V=0.8 mag, obtained through the Na I D doublet absorption EW, and the high reddening case with A_V=1.9 mag, obtained through the colour comparison with other LL SNe IIP. The low reddening scenario is characterized by lower temperatures at all epochs, with a plateau temperature of only 4300 K. The high reddening scenario is much more promising in this situation, since the plateau temperature of SN 2021aai overlaps with the rest of the sample, at around 5500K. In particular, SN 2021aai in the high reddening case displays the same temperature evolution as SN 2005cs, and it is only marginally brighter when considering the bolometric luminosity. The clearest difference between the two objects is the duration of the plateau: for SN 2005cs the plateau ends ∼120 days after the explosion, but the luminosity starts fading by ∼ 75 days. SN 2021aai, on the other hand, is definitely longer–lasting. In the high reddening scenario, its bolometric luminosity has an early peak (7.2×10^{41} erg s^{-1}), similar to the other LL SNe IIP considered. After few weeks of dimming, SN 2021aai luminosity increases from 4.3×10^{41} erg s^{-1} at 25 d to 6.5×10^{41} erg s^{-1} at 130 d before the fall from its plateau. On the other hand, in the low reddening scenario there is no evidence of the early luminosity peak, and the bolometric luminosity steadily increases from 1.9×10^{41} erg s^{-1} to 3.6×10^{41} erg s^{-1} during the plateau phase. Unfortunately, we do not have enough multi–band observations or spectra during the first 10 days to perform a blackbody fit to confirm if the similarity between SN 2021aai (in the high reddening scenario) and SN 2005cs is present at the earliest phases. The larger luminosity of SN 2021aai compared to SN 2020cxd leads to an estimate of a larger radius, given that their plateau temperature was comparable. While starting off with similar values, the emitting radius of SN 2021aai grows much more than the one of SN 2020cxd, up to 95 AU at 143 days after the explosion. This behaviour appears to be unusual, compared to the other objects, where the radius varies significantly less during the plateau phase.

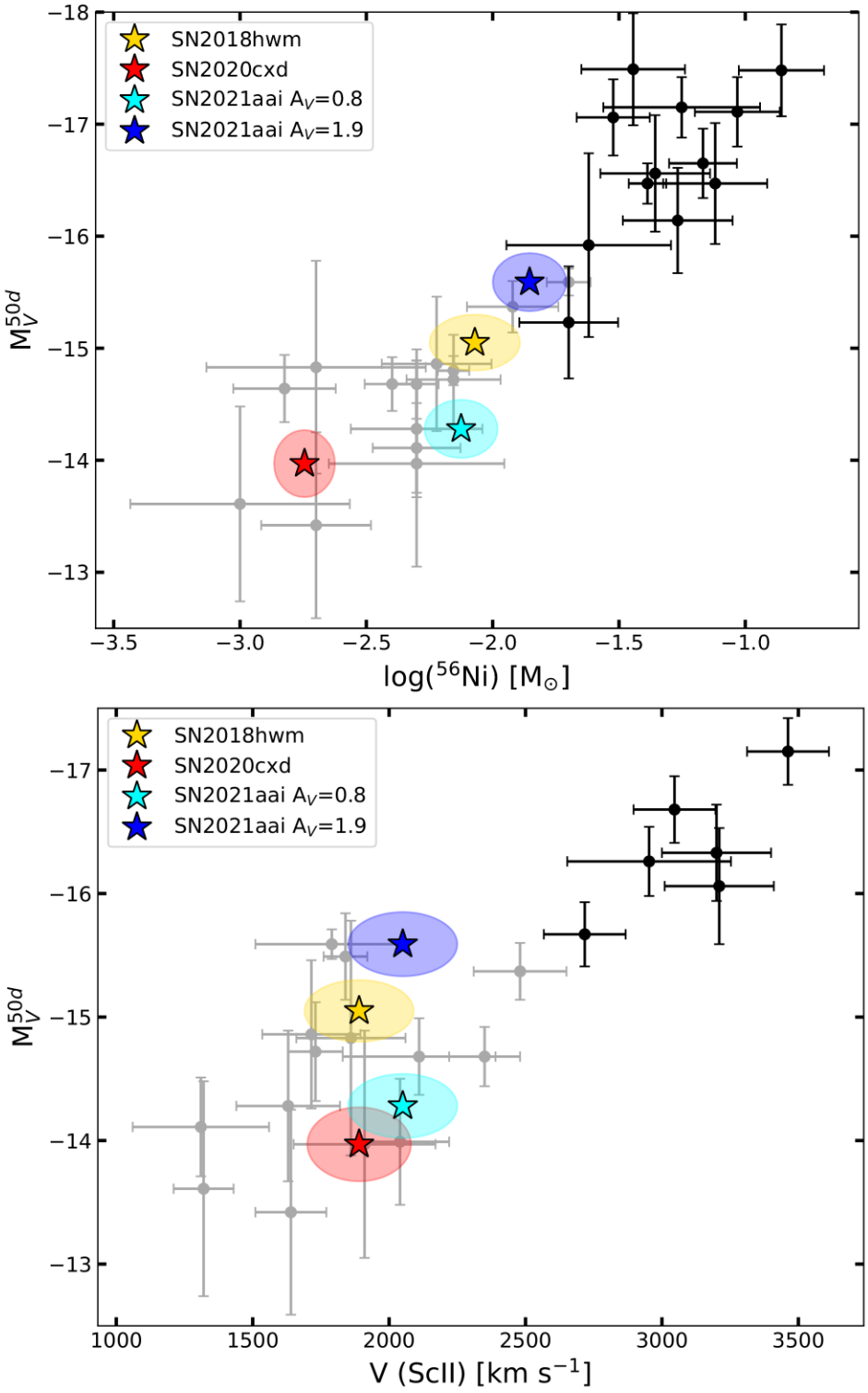

Figure 3.10: Top panel: V band absolute magnitude at 50 days versus ^{56}Ni ejected mass. LL SNe are shown in grey (Pastorello et al. 2004; Spiro et al. 2014; Jäger et al. 2020), while standard SNe IIP are shown in black (Rodríguez et al. 2020). Some relevant objects are reported as coloured stars, with their errors shown as elliptical regions. Lower panel: same as top panel, but with expansion velocity of Sc II λ6246 (Maguire et al. 2010) instead of ^{56}Ni mass.

3.5 ^{56}Ni Estimate

The late tail of the light curve of SNe IIP is powered by the ^{56}Ni → ^{56}Co → ^{56}Fe decay chain, which deposits energy into the expanding gas in the form of photons and positrons (Colgate & McKee 1969). We estimate the ejected mass of ^{56}Ni through a comparison of the late time luminosity with the well studied SN 1987A, as previously done for other LL SNe IIP (e.g. Pastorello et al. 2004; Spiro et al. 2014; Tomasella et al. 2018), through the following equation:

$$M(^{56}Ni)_{SN} = M(^{56}Ni)_{1987A} \times \frac{L_{SN}}{L_{1987A}} \tag{3.1}$$

where we adopt a value for the ^{56}Ni ejected mass by SN 1987A of 0.073 ± 0.012 $M_\odot$, which is the weighted average of the values reported in Arnett & Fu (1989) and Bouchet et al. (1991). Due to a lack of information in the NIR during the late decline, we have to perform some approximations. We compare the integrated luminosity in the observed bands (r, i, z) for our objects with the luminosity integrated through the same wavelength ranges for SN 1987A (since SDSS filters were not available at the time). With this method, we obtain for SN 2020cxd $(1.8 \pm 0.5) \times 10^{-3}$ $M_\odot$ of synthesised ^{56}Ni, quite low compared to the typical value of few 10^{-2} $M_\odot$ for a SN IIP event (see, for example $M(^{56}\mathrm{Ni})_{avg} = 0.033 \pm 0.024$ $M_\odot$ obtained by Anderson et al. 2014). For SN 2021aai, we obtain a value of $(7.5 \pm 2.5) \times 10^{-3}$ $M_\odot$ for the low reddening scenario and $(1.4 \pm 0.5) \times 10^{-2}$ $M_\odot$ for the high reddening scenario, which is still a factor of 2 below the average SN IIP event reported by Anderson et al. (2014).

In Figure 3.10, we display the locations of SN 2020cxd and SN 2021aai in the peak magnitude–^{56}Ni ejected mass plane and the peak magnitude versus expansion velocity plane for SNe IIP, both introduced in Hamuy (2003). As we can see there is no clear separation between standard and LL SNe IIP, but rather a smooth transition between the two classes. According to the classification adopted in the literature, SN 2021aai in the high reddening scenario would be in the transition region between low luminosity and standard objects, when considering the ^{56}Ni ejected mass. Instead, SN 2020cxd is definitely in the lowest end of the parameter spectrum. Considering the expansion velocities measured with Sc II λ6246, instead, both objects display average values for LL SNe IIP.

3.6 Hydrodynamical Modelling

3.6.1 Model details

In order to estimate the physical properties of SNe 2020cxd and 2021aai at the explosion time (progenitor radius R, explosion energy E, total ejected mass M_{ej}), we use the hydrodynamical modelling procedure presented in detail in Pumo et al. (2017), and already well–tested on both faint and standard SNe IIP (e.g. Spiro et al. 2014; Takáts et al. 2014; Tomasella et al. 2018; Reguitti et al. 2021). The procedure consists in a simultaneous χ^2 minimisation aiming at reproducing the observed bolometric luminosity, expansion velocity and photospheric temperature. This operation is performed in two distinct steps. Firstly, a preliminary investigation is carried out through the model presented by Zampieri et al. (2003), solving the energy balance equation under the assumptions of ejecta with constant density in homologous expansion. The parameters obtained during this first fit lay down the framework on which the subsequent detailed calculations are based. The second step makes use of a general–relativistic, radiation–hydrodynamics Lagrangian code (Pumo et al. 2010; Pumo & Zampieri

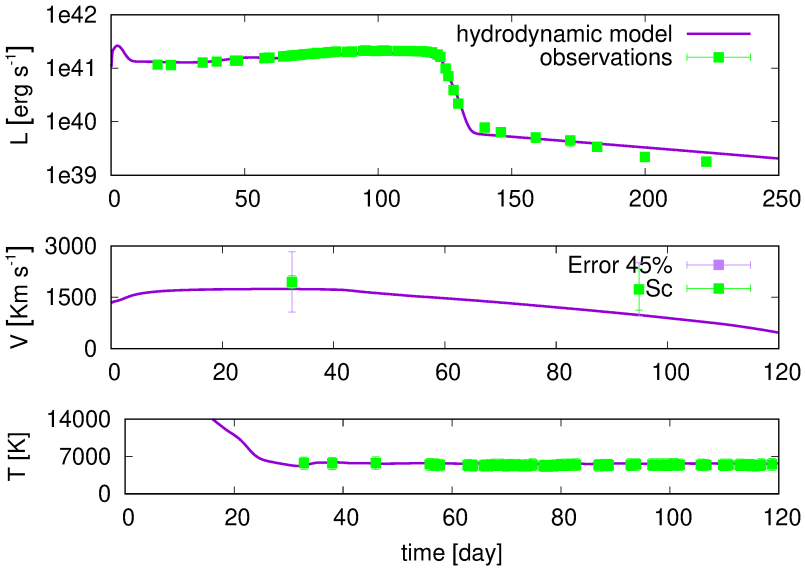

Figure 3.11: Evolution of the main observables of SN 2020cxd compared to the best hydrodynamical model. The parameters characterizing the displayed fit are $R = 4 \times 10^{13}$ cm (~ 575 R$_\odot$), $M_{ej} = 7.5$ M$_\odot$, and $E = 0.097$ foe (see text for details). In the top panel, the bolometric luminosity is displayed. In the middle panel, the photospheric velocity obtained through the ScII lines as described in Sect. 3.3. Notice that the second velocity measurement is affected by a large error due to poor spectral resolution, as displayed in Figure 3.8. Finally, in the bottom panel is shown the temperature evolution.

2011), which reproduces the main observables of the SN, from the onset of the plateau phase up to the nebular phase. The code takes into account the gravitational effects of the compact remnant left by the core collapse and the energy input from the decay of radioactive isotopes synthesised during the explosion. It is important to note that we did not try to reproduce the early phase of the explosions ($\sim$ 15–20 days after explosion), since temperature and luminosity during this phase are significantly affected by emission from the outermost shell of the ejecta, which is not in homologous expansion, rendering the assumptions in our model inaccurate. The best fitting models for SNe 2020cxd and 2021aai are shown in Figures 3.11 and 3.12 respectively.

3.6.2 SN 2020cxd results and progenitor scenarios

Adopting the ^{56}Ni masses inferred in Sect. 3.5 and the well constrained explosion epochs in Sect. 3.2, we find the initial parameters of the progenitor of SN 2020cxd to be: $R = 4 \times 10^{13}$ cm (~ 575 R$_\odot$), M$_{ej}$ = 7.5 M$_\odot$, and E = 0.097 foe (sum of kinetic and thermal energy). The errors on the free model parameters reported due to the χ^2 fitting procedure are about 15% for M$_{ej}$ and R, and 30% for E. To obtain the main sequence (MS) mass of the progenitor star of SN 2020cxd, we need to account for the compact remnant produced by the core collapse (1.3 – 2.0 M$_\odot$) as well as the mass lost during the pre–SN evolutionary phases ($\lesssim$ 0.1 – 0.9 M$_\odot$, as prescribed in Pumo et al. 2017). Considering these corrections, the MS mass of the progenitor of SN 2020cxd is estimated to be 8.9 – 10.4 M$_\odot$. We note that, despite the different methodology applied, our results are consistent with those obtained by Kozyreva et al. (2022): M$_{ej}$ = 7.4 M$_\odot$, E = 0.07 foe and R = 408 R$_\odot$.

The parameters estimated through hydrodynamical modelling are compatible with what is expected

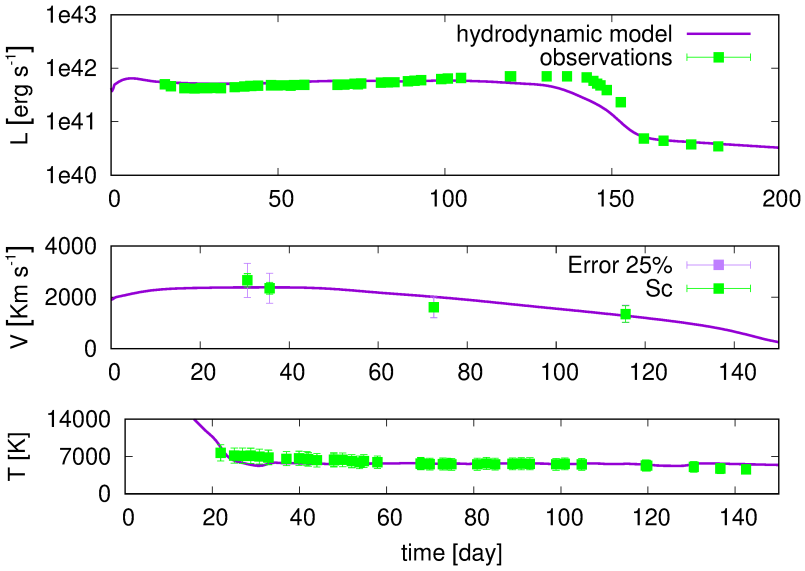

Figure 3.12: Same as Figure3.11, but for SN 2021aai in the high reddening scenario. The parameters characterizing the displayed fit are R = 4×10^{13} cm ($\sim$ 575 $R_\odot$), M_{ej} = 15.5 $M_\odot$, and E = 0.4 foe (see text for details) In this case, the observed ScII lines velocities are more reliable, and better reproduced by the model. At the same time, the bolometric luminosity shows a more extended plateau compared to our fit.

for a red supergiant (RSG) star. The radius is within the 500–1500 $R_\odot$ range associated with RSG, although leaning towards the lower end of the distribution, as reported in the review of Smartt (2009b). Furthermore, the progenitor initial mass is just above the 8 ± 1 $M_\odot$ threshold that defines the minimum progenitor mass needed to produce a SN explosion, based on direct detections of RSG progenitors of SNe IIP (Smartt 2009b). For these reasons, SN 2020cxd could be explained by the explosion of a low mass RSG, resulting in the emission of a limited amount of energy compared to the explosion of more massive RSG. This corroborates the scenario where more massive RSG explode in SNe that are brighter and with faster ejecta compared to the explosion of less massive RSGs, which most likely produce LLSNe IIP (Pastorello et al. 2004; Tomasella et al. 2018). In this context, we display in Figure 3.13 the correlation between the plateau luminosity and ^{56}Ni with the parameter E/M_{ej}, as in Pumo et al. 2017 (see their table 2, figs 5 and 6), including also the two "intermediate-luminosity" objects presented in Tomasella et al. 2018 (i.e. SNe 2013K and 2013am). Like in Pumo et al. 2017 (to which we refers for details), the error bars on the E/M_{ej} ratios are estimated by propagating the uncertainties on E and M_{ej}, adopting a value of 30% for the relative errors of E and 15% for that of M_{ej}. Both in the top and bottom panel of Figure 3.13, SN 2020cxd is at the very end of the distribution of SN IIP, due to the low E/M_{ej} ratio inferred for the explosion and the relatively low amount of ^{56}Ni synthesised.

Considering its faint nature and the inferred best–fitting model parameters, SN 2020cxd also appears to be a fair candidate for being an ECSN from a super-asymptotic giant branch (super–AGB) star. The estimated mass of the progenitor is close to the upper limit of the mass range typical of this class of stars, M_{mas} (see Pumo et al. 2009 and references therein). This seems to corroborate the results of Pumo et al. (2017), showing that some faint SNe IIP may be also explained in terms of ECSNe involving massive super–AGB stars. To investigate this scenario in more detail, we compare the

photometric and spectroscopic properties of SN 2020cxd with other ECSN candidates in Appendix 3.7. We note, however, that we lack conclusive evidence to confidently discriminate between an ECSN scenario and a standard faint SN IIP event with a RSG progenitor.

3.6.3 SN 2021aai results and progenitor scenarios

We also perform hydrodynamic modelling of SN 2021aai in the high reddening scenario, assuming it is the most reliable of the two (Figure 3.12). We obtained R = 4×10^{13} cm ($\sim$ 575 $R_{\odot}$), M_{ej} = 15.5 $M_{\odot}$, and E = 0.4 foe. Given the higher energy and ejected mass compared to SN 2020cxd, we favour the scenario where a RSG explodes through an iron core collapse, excluding the ECSN origin for SN 2021aai. In Figure 3.13 it is possible to appreciate that SN 2021aai belongs to the category labelled as "intermediate-luminosity" SNe (Pumo et al. 2017; Tomasella et al. 2018), which bridge the classes of LL SNe IIP and standard SN IIP events, therefore creating a continuous distribution in the properties of SN IIP. As we remark in Sect. 3.2, this transient is characterized by an extended plateau phase, lasting $\sim$140 days. This feature is not well reproduced by our hydrodynamical model, which predicts a shorter plateau compared to observations (Figure 3.12, top panel). This difference between the model and the observations could be probably explained in terms of a peculiar distribution of the ^{56}Ni within the ejected material. In fact, keeping constant the basic parameters of the models (i.e. M_{ej}, R, E and the total amount of ^{56}Ni initially present in the ejected envelope), different degrees of ^{56}Ni mixing primarily lead to different plateau durations (see e.g. Figure 11 in Pumo & Zampieri 2013). In particular a lower degree of ^{56}Ni mixing (i.e. models where the Ni is more confined to the central region of the ejecta) is linked to a longer plateau, as observed for SN 2020cxd. We also perform some preliminary hydrodynamical modelling of SN 2021aai in the low reddening scenario. Firstly, we notice that the plateau temperature of 4300 K was too low to be fitted by our models, making the high reddening a more reliable scenario. Fitting only the bolometric light curve and the expansion velocities, we obtain values of R and E reduced by a factor of $\sim$1.5–2 and a ratio E/M_{ej} almost unchanged compared to the high reddening scenario.

3.7 Comparison between ECSN candidates

Given the possibility of SN 2020cxd originating from an ECSN scenario, as highlighted in Sect. 3.6.2, in this section we present a comparison between SN 2020cxd and other ECSN candidates. The first object we selected for this purpose is the peculiar type II SN 2018zd (Hiramatsu et al. 2021). Hiramatsu et al. (2021) found several indicators favouring the ECSN event for this transient, in particular the chemical composition of the progenitor and the results of the nucleosynthesis, the light curve morphology and the presence of CSM. We also chose to include in this small sample SN 2008S (Botticella et al. 2009), taken as a prototype of ILRTs. This class was associated to ECSNe due to their faintness (e.g. Humphreys et al. 2011), their progenitors (Prieto 2008; Thompson et al. 2009) and the presence of circumstellar material, clearly evident in all their spectra, which corroborates their origin from a Super-AGB progenitor.

In Figure 3.14, we show the *R* band (correction between *R* and *r* bands were applied as discussed in Sect. 3.2.2) light curves of the three transients mentioned. For SN 2018zd we adopt both distances reported in Hiramatsu et al. (2021) and Callis et al. (2021): the discrepancy between the two lies in the choice of distance indicators. The increase in brightness during the plateau of SN 2020cxd is striking, since it is the only object displaying this behaviour. SN 2018zd shows perhaps a more canonical plateau, slightly declining in brightness over the course of $\sim$ 120 days. The late time decline of SN

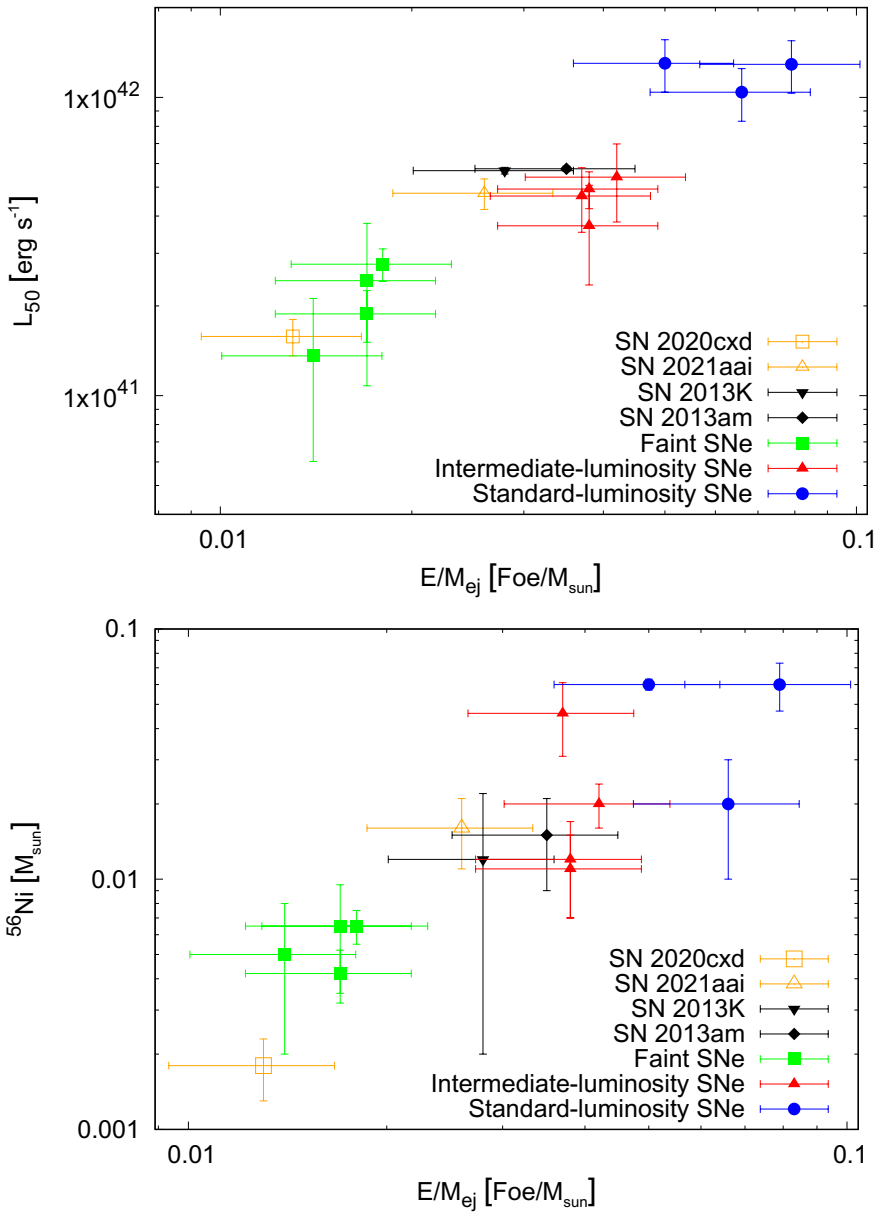

Figure 3.13: Correlations between the plateau luminosity (top panel) and ^{56}Ni mass (bot panel) with the E/M$_{ej}$ ratio. LL SNe are coloured in green, standard SN IIP are shown in blue, while transitional objects are displayed in red and black (Pumo et al. 2017; Tomasella et al. 2018). SNe 2020cxd and 2021aai are marked with orange symbols.

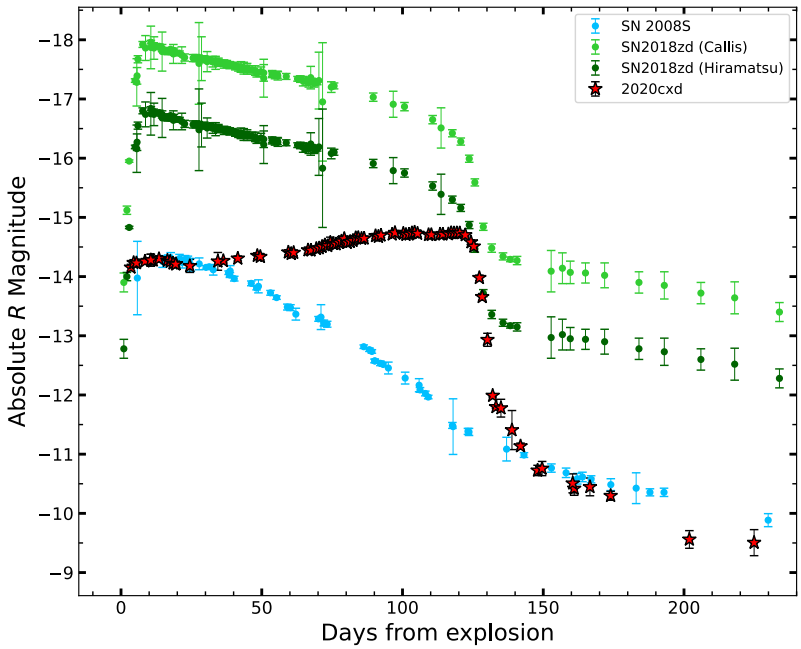

Figure 3.14: Light curve comparison between SN 2020cxd and two other ECSN candidates: the ILRT SN 2008S and the peculiar SN 2018zd. See text for details.

2008S is almost coincident with that of SN 2020cxd.

To better visualize the relationship between these objects and the data shown in Sect. 3.5, in Figure 3.15 we plot SN 2008S and SN 2018zd on the M_V - ^{56}Ni diagram already shown in Figure 3.10. We note that a tight relationship between these two quantities was found for SNe IIP, but SN 2008S fits remarkably well in the lower end of the brightness distribution despite being a member of a different class of transients. SN 2018zd appears to belong to the standard IIP events when correcting for the distance reported by Callis et al. (2021), while it lies towards the region of transitional objects (like SN 2021aai) when adopting the distance prescribed by Hiramatsu et al. (2021).

In Figure 3.16 we present a comparison between the spectra of this small sample of ECSN candidates at early, middle and late phases (top, middle and bottom panel respectively). The earliest phase available for a spectrum of SN 2008S is at 15 days after the explosion, while the spectra of SNe 2018zd and 2020cxd were taken within 4 days from the explosion. However, we note that the spectra of ILRTs evolve very slowly, as they are dominated by CSM emission: for this reason, the main features characterizing the spectra do not change on short time scales. In the early spectrum of SN 2018zd it is possible to notice some narrow H lines without P-Cygni profiles, somehow reminiscent of the ILRT spectrum (although with a much bluer colour), which can be traced back to the presence of CSM, as Hiramatsu et al. (2021) infer from their analysis of the ultraviolet colour evolution. At the same phases, SN 2020cxd already shows P-Cygni profiles and broad H lines, in line with the expectations for a LL SN IIP. At ~ 30-40 days, SN 2008S shows almost no sign of evolution, with the narrow H and Ca lines completely dominating the spectrum. SN 2020cxd, on the other hand, develops an abundance of metal lines (the line-blanketing effect is already evident) and deep P-Cygni profiles. In this phase SN 2018zd transitions towards a more standard SN IIP, although the metal lines are still much weaker compared to SN 2020cxd, the line-blanketing effect is not marked, and some signature

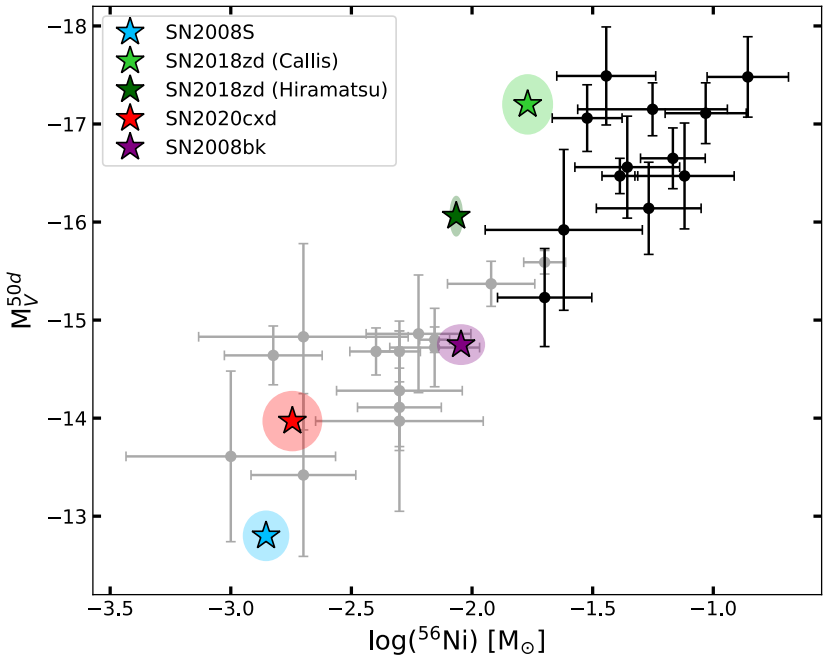

Figure 3.15: *V* band absolute magnitude at 50 days versus ^{56}Ni ejected mass. LL SNe are shown in grey, standard SN IIP are represented in black. SN 2020cxd, SN 2018zd and SN 2008S are highlighted with coloured stars, with their errors reported as elliptical regions. Also SN 2008bk is highlighted, providing an example of an explosion originating from a confirmed low mass RSG (see text).

features such as the Ca II NIR triplet are still missing. Finally, at late times the spectrum of SN 2008S has kept basically the same narrow lines it has shown throughout its evolution, even without a continuum underneath them. SN 2018zd displays an array of prominent emission lines, allowing the detailed analysis performed by Hiramatsu et al. (2021) which stated that this object is compatible with an ECSN event on the basis of the nucleosynthesis and chemical composition expectations[6]. Sadly, it was impossible to perform a similar analysis on SN 2020cxd, due to the very poor signal to noise obtained in our latest spectra.

In conclusion, applying the criteria presented by Hiramatsu et al. (2021) to identify an ECSN event, we notice the following pros and cons:

- The low energy characterizing SN 2020cxd and its light curve shape are consistent with an ECSN origin. As shown in Sect. 3.6.2, hydrodynamical modelling points towards a progenitor between 8.9 and 10.4 M$_\odot$, compatible with the expectations for a super–AGB star.
- We did not have any direct detection of the progenitor, nor we could investigate the nucleosynthesis and chemical composition of the progenitor through nebular spectra.
- The lack of CSM that can be inferred from the spectra seems to point towards a low–mass Red Giant Branch (RGB) progenitor, rather than a super-AGB, therefore favouring the iron core–collapse scenario for SN 2020cxd (although a Super-AGB star could explode without being surrounded by optically thick CSM in some cases, see e.g Pumo et al. 2009).

[6]Despite the presence of prominent emission lines, we note that Hiramatsu et al. (2021) and Callis et al. (2021) disagree on the presence of abundance patterns that support the ECSN hypothesis.

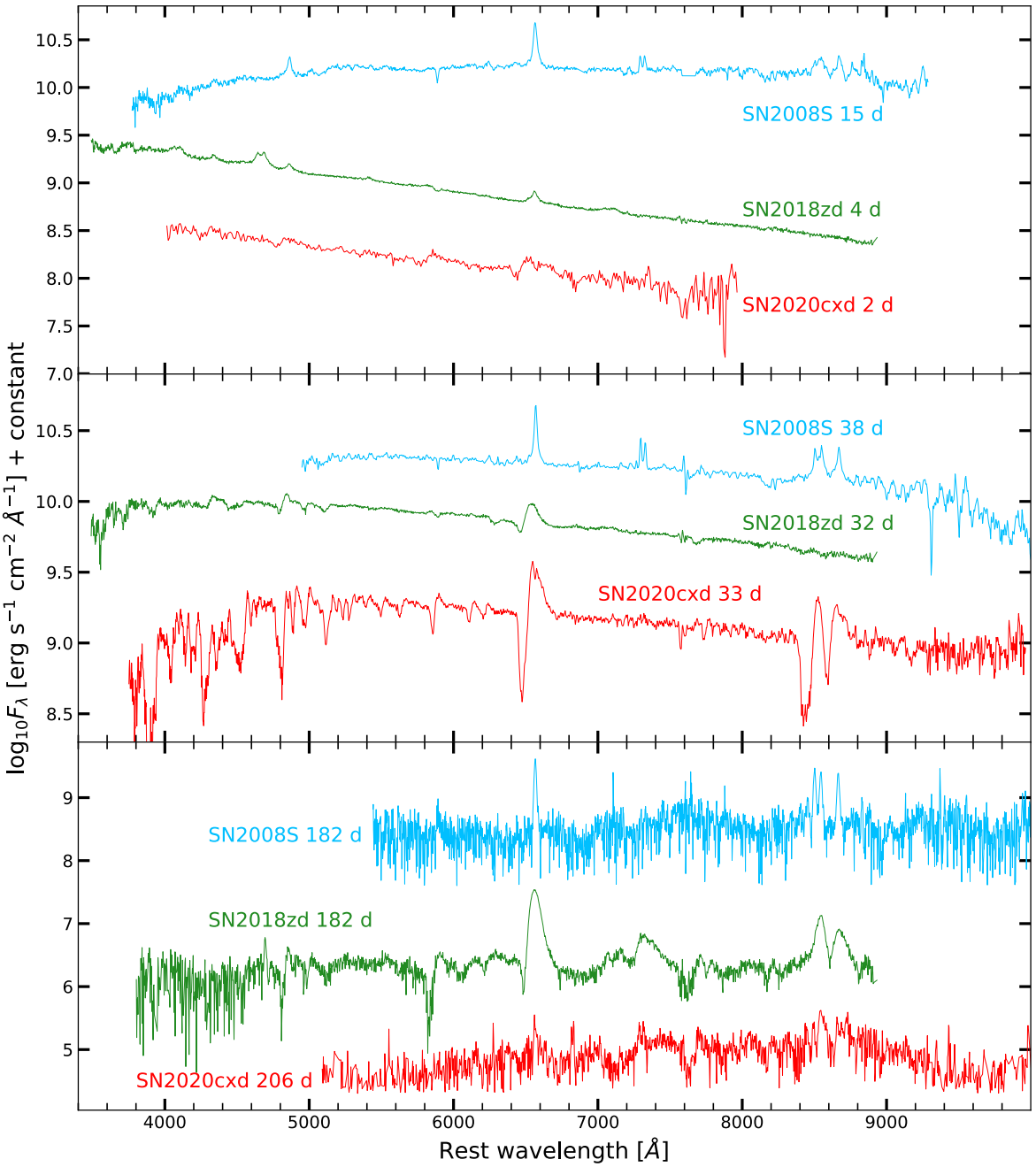

Figure 3.16: Comparison between the spectra of SN 2008S, SN 2018zd and SN 2020cxd. In the top panel are shown the early spectra, in the middle panel are presented the spectra during the plateau phase, and in the bottom panel are shown the late spectra. All spectra were corrected for redshift and reddening.

We know that low–mass RGB progenitors were accurately identified in the past, e.g. for SN 2008bk (Van Dyk et al. 2012; Maund et al. 2014; O'Neill et al. 2021) and SN 2018aoq (O'Neill et al. 2019). A similar scenario could comfortably explain the SN 2020cxd event.

3.8 Summary and conclusions

We present optical photometry and spectroscopy for two LL SNe IIP: 2020cxd and 2021aai. SN 2020cxd appears to be sub–luminous even compared to other transients in its class, with an absolute magnitude of M_r = –14 mag at the start of the plateau, making it one of the faintest LL SNe IIP observed to date. On the other hand, SN 2021aai is a transitional object between LL SNe IIP and more standard SN IIP events, once corrected for the large extinction affecting the target (A_V = 1.9 mag). Both transients display spectra that perfectly match those of other LL SNe IIP (Pastorello et al. 2004; Spiro et al. 2014), characterised by H lines in the early phases and followed by the rise of metal lines (mainly Fe II, Sc II, Ba II, [Ca II] and Ca NIR triplet) during the plateau phase. The expansion velocities obtained by measuring the position of the minimum of the P Cygni line profile, well visible for most lines, yields velocities of few 10^3 km s^{-1}, below those of standard SNe IIP, but in line with what was observed for LL SNe IIP. The temperature trend obtained through spectral energy distribution fitting consists in a very rapid decline during the early phases, reaching a temperature of ∼5500 K at ∼30 days after explosion and throughout all the plateau phase, as expected for H recombination. After fading from the plateau, both objects settle on the linear decline powered by the ^{56}Ni decay chain. By comparing their late time luminosity with that of SN 1987A at the same phase, we estimate the ^{56}Ni synthesised to be $1.8 \pm 0.5 \times 10^{-3}$ $M_\odot$ for SN 2020cxd and $1.4 \pm 0.5 \times 10^{-2}$ $M_\odot$ for SN 2021aai (considering the high reddening scenario).

We also perform hydrodynamical modelling of our targets using the procedure described in Pumo et al. (2017), which uses the general–relativistic, radiation–hydrodynamics, Lagrangian code presented in Pumo & Zampieri (2011). The physical parameters of the progenitor star of SN 2021aai at the moment of explosion are R = 4×10^{13} cm (∼ 575 $R_\odot$), M_{ej} = 15.5 $M_\odot$ and E = 0.4 foe. These values are consistent with the explosion of a RSG star after the collapse of its iron core (Wheeler & Swartz 1993). The transitional properties of SN 2021aai, linking LL SNe IIP and standard SN IIP events, are evident when considering its E/M_{ej} ratio (Figure 3.13). The interpretation of the parameters obtained for SN 2020cxd is more nuanced. The best fit yields R = 4×10^{13} cm (∼ 575 $R_\odot$), M_{ej} = 7.5 $M_\odot$ and E = 0.097 foe, values which can be compatible with the iron core collapse explosion of a low mass (8.9–10.4 $M_\odot$) RSG, but they are also consistent with an explosion triggered by electron captures involving a massive super–AGB (i.e. with an initial mass close to the upper limit of the mass range typical of this class of stars, M_{mas}; see Pumo et al. 2009, and references therein).

In conclusion, we analyse two objects spanning the brightest and faintest edges of the LL SNe IIP class, with SN 2021aai bridging the low luminosity class with more traditional SNe IIP, and SN 2020cxd being so faint that it can be reasonably considered a possible ECSN candidate. The search for ECSNe, however, is not limited to the LL SNe IIP subclass. In the following sections we discuss the properties of another class of appealing ECSN candidates: the Intermediate Luminosity Red Transients.

Chapter 4

Photometric properties of Intermediate Luminosity Red Transients

In the stellar evolution theory, it is well established that stars with initial mass below ~8 $M_\odot$ will end their lives as white dwarfs, cooling down while supported by the electron degeneracy pressure in their cores, while stars with initial masses between ~10 $M_\odot$ and 40 $M_\odot$ will complete all the nuclear burning cycles and will undergo a violent explosion as their core collapses (Woosley et al. 2002). This apparently simple distinction raises a complicated question: which is the exact initial mass limit that separates the two opposite fates?

Stars with a zero-age-main-sequence mass between 8 $M_\odot$ and 10 $M_\odot$ are expected to form a degenerate O-Ne-Mg core during their lifetime (Nomoto 1984). Such stars are labelled Super-AGB stars (SAGB), and the outcome of their evolution is uncertain. In fact, if the O-Ne-Mg core accretes enough material to approach the Chandrasekhar limit, the star will explode as an Electron Capture Supernova (ECSN), but if the core fails to reach this critical mass the star will end its evolution as a O-Ne-Mg white dwarf (e.g. Miyaji et al. 1980; Nomoto 1984; Jones et al. 2013; Moriya et al. 2014; Doherty et al. 2015). Whether such critical mass can be reached depends on the competing effects of mixing, convective overshooting and mass loss rates, which make the modelling of the core and its evolution a challenging endeavor (Poelarends et al. 2008). An additional complication, as pointed out by Kozyreva et al. (2021), is that even small changes in the initial mass and metallicity of the progenitor star may give rise to a Fe core-collapse supernova (SN) instead of an ECSN, overall showing similar observables.

While stellar evolution theory predicts the existence of ECSN, finding their observational counterparts is still an open issue. Proving that a transient originates from the core-collapse of an O-Ne-Mg core, rather than from a classical Fe core collapse, is not trivial. However, there has been no shortage of attempts: Low Luminosity Supernovae Type IIP (LL SNe IIP) (e.g. Spiro et al. 2014; Reguitti et al. 2021; Valerin et al. 2022) and also interacting transients (e.g. Smith 2013; Hiramatsu et al. 2021) have been proposed as ECSN candidates. In order to be a reasonable ECSN candidate, an object should fulfill the key expectations for the explosion following the collapse of an O-Ne-Mg core. First of all, the energy released by an ECSN should be significantly lower ($\sim 10^{50}$ erg) compared to classical supernova explosions, therefore directing the investigation towards faint targets with low velocity ejecta (Janka et al. 2008). Secondly, the nucleosynthesis following the collapse of an O-Ne-Mg core yields limited amounts of ^{56}Ni (few 10^{-3} $M_\odot$), placing constraints on the luminosity of the late time decline of the candidate (Wanajo et al. 2009). Finally, the progenitor star of a candidate should be

Transient	Host Galaxy	Type	Redshift	Distance [Mpc]	μ [mag]	Galactic A_V [mag]	Local A_V [mag]
AT 2019abn	M 51	Sa	0.002 (-)	8.6 (0.1)	29.67 (0.02)	0.096 (0.006)	2.34 (0.06)
AT 2019ahd	NGC 3423	SA(s)cd	0.00335 (0.00001)	11.1 (0.7)	30.22 (0.14)	0.079 (0.003)	0.37 (0.03)
AT 2019udc	NGC 0718	SAB(s)a	0.00578 (0.00003)	19.9 (1.4)	31.49 (0.15)	0.100 (0.001)	0.00 (0.00)
NGC 300 OT	NGC 300	SA(s)d	0.00048 (-)	1.92 (0.14)	26.42 (0.15)	0.034 (0.001)	0.78 (0.06)

Table 4.1: Basic information on the galaxies hosting the transients in the sample. Morphological classifications are from Karachentsev et al. (1985) for M 51 and from de Vaucouleurs et al. (1991) for the other galaxies.

compatible with a luminous ($\sim 10^5$ $L_\odot$) SAGB star, since that is the only kind of star able to produce a degenerate O-Ne-Mg core massive enough to trigger an ECSN explosion (Poelarends et al. 2008).

Intermediate Luminosity Red Transients (ILRTs) are a class of objects, populating the luminosity gap between classical novae and standard SNe (Pastorello & Fraser 2019), which are appealing ECSN candidates. Their physical origin is still debated, with some studies associating ILRTs to non–terminal eruptions of post–main sequence stars (e.g. Humphreys et al. 2011). However, there are several indicators that favour the ECSN interpretation to explain the observed properties of these transients. The low luminosity characterizing ILRTs, evident in their peak magnitudes ranging between $M_r \sim$ –12 mag and –15 mag, is consistent with the expected weak explosion originating from the collapse of an O-Ne-Mg core (Pumo et al. 2009). Likewise, the late time decline in luminosity points towards small ^{56}Ni masses synthesized, fulfilling the condition presented by Wanajo et al. (2009) (see also Cai et al. 2021). Furthermore, all identified the progenitor stars of an ILRT were compatible with a SAGB star, corroborating the ECSN scenario (Thompson et al. 2009; Jencson et al. 2019). Finally, an important step towards the understanding of the nature of ILRTs was performed by Adams et al. (2016), who showed that, few years after their maximum luminosity, the remnants of the two ILRTs SN 2008S (Botticella et al. 2009) and NGC 300 2008OT-1 (Bond et al. 2009; Berger et al. 2009; Humphreys et al. 2011) had become fainter in the mid-infrared (MIR) than their progenitor stars. Extreme dust models are needed to obscure a surviving star in these conditions, therefore favouring a genuine terminal explosion over a non-terminal outburst.

While the considerations presented so far are certainly encouraging, the discussion on ILRTs as ECSN candidates is still ongoing. This is, after all, a relatively young class of transients, which was not clearly identified even two decades ago: seminal works on the already mentioned SN 2008S, NGC 2008OT-1 as well as M85 OT20061 (Pastorello et al. 2007) have been crucial to properly classify these transients. The rates of ILRTs are not low (8% of all the CC SNe, Cai et al. 2021) but their faintness makes their discovery occasional and their follow-up challenging. Since only a handful of ILRTs have been accurately characterized so far, additional data is key to improve our understanding of this poorly studied class of objects. In this context, here we present and analyse original photometric data of 4 ILRTs: NGC 300 2008OT-1, AT 2019abn, AT 2019ahd and AT 2019udc.

4.1 Data reduction

The objects presented in this paper were followed with several instruments at different facilities reported in Table [4.2]. In particular, the majority of the private data was collected with the Nordic Optical Telescope (NOT) within the NOT Unbiased Transient Survey 2 (NUTS2) collaboration (Holmbo et al. 2019), with the Liverpool Telescope (Steele et al. 2004), with the GROND imager (Greiner et al.

Table 4.2: Details about instruments and facilities used in our follow-up campaigns.

Code	Diameter [m]	Telescope	Instrument	Site
PROMPT	0.41	PROMPT Telescope	Apogee Alta	Cerro Tololo Inter-American Observatory, Cerro Tololo, Chile
REM	0.6	REM	ROSS	ESO La Silla Observatory, La Silla, Chile
Swope	1.0	Swope Telescope	SITe # 3	Las Campanas Observatory, Atacama Region, Chile
fl03-fl15	1.00	LCO (LSC site)	Sinistro	LCO node at Cerro Tololo Inter-American Observatory, Cerro Tololo, Chile
fl05-fl07	1.00	LCO (ELP site)	Sinistro	LCO node at McDonald Observatory, Texas, USA
fl06-fl14	1.00	LCO (CPT site)	Sinistro	LCO node at South African Astronomical Observatory, Cape Town, South Africa
fl12	1.00	LCO (COJ site)	Sinistro	LCO node at Siding Spring Observatory, New South Wales, Australia
ZTF	1.22	Oschin Telescope	ZTF	Palomar Observatory, United States
AFOSC	1.82	Copernico Telescope	AFOSC	Osservatorio Astronomico di Asiago, Asiago, Italy
IO:O	2.00	Liverpool Telescope	IO:O	Observatorio Roque de Los Muchachos, La Palma, Spain
IO:I	2.00	Liverpool Telescope	IO:I	Observatorio Roque de Los Muchachos, La Palma, Spain
GROND	2.2	MPG Telescope	GROND	ESO La Silla Observatory, La Silla, Chile
GRONDIR	2.2	MPG Telescope	GRONDIR	ESO La Silla Observatory, La Silla, Chile
ALFOSC	2.56	Nordic Optical Telescope	ALFOSC	Observatorio Roque de Los Muchachos, La Palma, Spain
NOTCam	2.56	Nordic Optical Telescope	NOTCam	Observatorio Roque de Los Muchachos, La Palma, Spain
SOFI	3.58	New Technology Telescope	SOFI	ESO La Silla Observatory, La Silla, Chile
ACAM	4.20	William Hershel Telescope	ACAM	Observatorio Roque de Los Muchachos, La Palma, Spain
LIRIS	4.20	William Hershel Telescope	LIRIS	Observatorio Roque de Los Muchachos, La Palma, Spain

2008), within the ePESSTO+ collaboration (Smartt et al. 2015b) as well as the Global Supernova Project (Brown et al. 2013; Howell 2019). Images obtained were reduced through standard IRAF tasks (Tody 1986), removing the overscan, correcting them for bias and flat field. When multiple exposures were taken the same night, we combined them to improve the signal to noise ratio (S/N). To measure the magnitudes of the transients observed, we used a dedicated, PYTHON-based pipeline called ECSNOOPY (Cappellaro 2014). ECNOOPY is a collection of PYTHON scripts that call IRAF standard tasks like DAOPHOT through PYRAF, and it was designed for Point Spread Function (PSF) fitting of multi-wavelenght data acquired from different instruments and telescopes. The PSF model was built from the profiles of isolated, unsaturated stars in the field. The instrumental magnitude of the transient was then retrieved by fitting this PSF model and accounting for the background contribution around the target position through a low-order polynomial fit. The error on this procedure was obtained through artificially created star close to the target, with magnitudes and profiles coincident with that inferred for the object. The dispersion of the artificial stars instrumental magnitudes was combined in quadrature with the PSF fitting error given by DAOPHOT to obtain the total error associated with that measure. Zero Point (ZP) and Colour Terms (CT) corrections were computed for each instrument by observing standard fields: SDSS (Albareti et al. 2017) was used as reference for Sloan filters, the Landolt (1992) catalogue was used for Johnson filters and the 2MASS (Skrutskie et al. 2006) catalogue was used for Near Infrared (NIR) filters.

For the "Asteroid Terrestrial–impact Last Alert System" (ATLAS) data (Tonry et al. 2018), we combined the flux values obtained through forced photometry released from their archive[1], and converted the result into magnitudes as prescribed in the ATLAS webpage. While reducing WISE[2] (Wright et al. 2010) and SPITZER[3] (Lacy et al. 2005) data we adopted the ZP provided on their respective websites . It is worth noticing that in the NIR and Mid Infrared (MIR) we assumed negligible CT, so we only computed the ZP correction. In order to account for non-photometric nights, we selected a series of stars in the field of each observed transient: measuring the average magnitude variation of the reference stars, we computed the ZP correction for each night in each optical and NIR filter. Applying ZP and CT corrections to the instrumental magnitudes of our targets, we obtained the apparent magnitudes which are reported in this paper. We adopted the AB magnitudes system for u, g, r, i, z, c, o

[1]https://fallingstar–data.com/forcedphot/

[2]https://wise2.ipac.caltech.edu/docs/release/prelim/expsup/sec4_3g.html

[3]https://irsa.ipac.caltech.edu/data/SPITZER/docs/irac/iracinstrumenthand book/14/

bands and Vega magnitudes for $U, B, V, R, I, J, H, K, W1, W2$, [3.6], [4.5] bands. We resorted to template subtraction only at very late epochs, when the transients were too faint to be detected otherwise. The template subtraction procedure was performed on late time observations, again with SNOOPY, with template images taken from SDSS (Albareti et al. 2017), Pan–STARRS1 (Kaiser et al. 2010) as well as archival images from the Liverpool Telescope (Steele et al. 2004). In the NIR bands, no templates were needed as all targets were bright and easily identified. The photometric measurements we obtained are reported in Appendix.

4.2 Photometric follow-up

4.2.1 AT 2019abn

AT 2019abn was discovered on 2019 January 22.6 UT by the Zwicky Transient Facility (ZTF, Graham et al. 2019) on a spiral arm of Messier 51 (M 51) at the coordinates RA= $13^h29^m42^s.41$, Dec = +47°11' 16".6. The discovery and early observations are discussed by Jencson et al. (2019), while the evolution of the transient up until 200 days from the discovery is covered by Williams et al. (2020). In this paper we provide additional optical data, especially at later stages of evolution, while also publishing original NIR and MIR observations obtained with IO:I and NOTCAM, Spitzer and WISE which put constraints on a critical section of the Spectral Energy Distribution (SED). By measuring the magnitude of the standard stars used as reference by Williams et al. (2020) we integrate their dataset with our observations by applying the following magnitude corrections for each band: ΔB = +0.07 mag, ΔV = -0.02 mag, Δr = +0.04 mag, Δi = +0.05 mag and Δz = +0.01 mag. No correction was needed in NIR bands. Similarly, we incorporate the observations performed by Jencson et al. (2019) in our dataset after applying the following corrections: Δg = +0.01 mag, Δr = +0.03 mag, Δi = +0.04 mag, ΔJ = -0.13 mag, ΔH = -0.05 mag and ΔK = -0.06 mag. We adopt a distance modulus of μ = 29.67 ± 0.02 mag to M 51, obtained through the method of the tip of the red giant branch (McQuinn et al. 2016, 2017). The Galactic absorption in the direction of M 51 is A_V = 0.096 ± 0.006 mag, from Schlafly & Finkbeiner (2011), under the assumption that R_V=3.1 (Cardelli et al. 1989). The local absorption is more challenging to estimate and will be discussed in Sect. 4.3.

The light curves of AT 2019abn are shown in the top left panel of Figure 4.1. Thanks to the early discovery, it is possible to follow the evolution of AT 2019abn from very early stages. The rise in luminosity is observed in multiple bands, and lasts roughly 20 days before the transient reaches a peak magnitude of M_r = 16.73 ± 0.01 mag on MJD = 58527.3. Thanks to this unprecedented coverage of the rise, it is possible to estimate the rising rates for the observed bands (γ_1). As pointed out by Williams et al. (2020), AT 2019abn shows a shallow peak, where the luminosity evolution is slow (γ_2) especially in the red bands, while the decline rate becomes more steep after 110 days post maximum (γ_3). Between 180 and 195 days after maximum, there is a sudden decrease in luminosity of $\sim$ 0.9 magnitudes in all observed optical and NIR bands. After this abrupt change, the light curves settle on slow decline rates (γ_4). The MIR sampling of AT 2019abn, obtained through the Spitzer and WISE (survey NEOWISE) space telescopes, is unprecedented for an ILRT. After the first data point, at 50 days after maximum, the MIR light curves show at first a decline faster compared to the optical bands, but after $\sim$100 days the decline becomes more shallow. Interestingly, the luminosity drop at $\sim$180 days is not as evident in the MIR bands. All the measured decline rates are reported in Table 4.3.

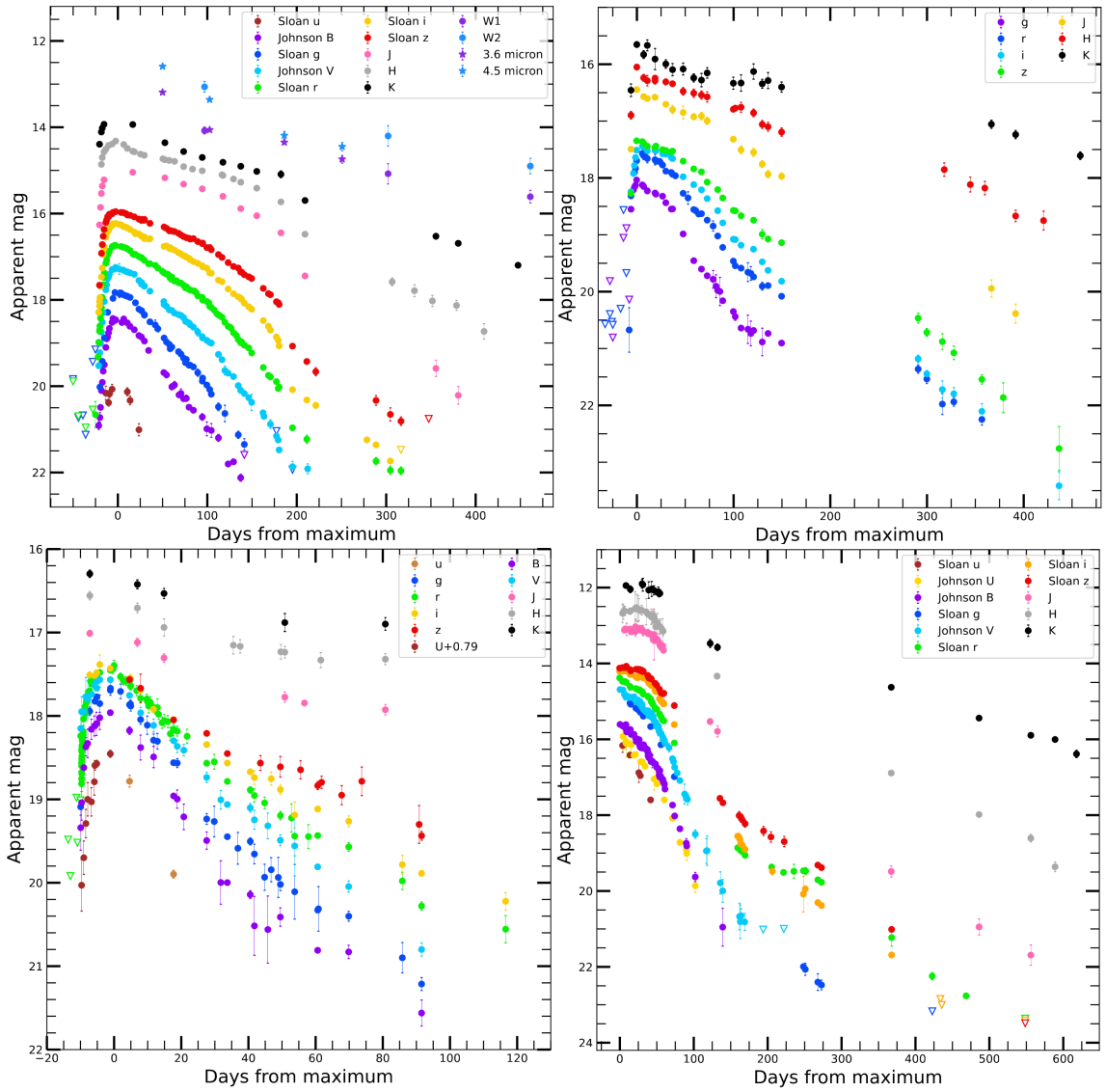

Figure 4.1: Optical and NIR light curves of our sample of ILRTs. Empty symbols represent upper magnitude limits. AT 2019abn is on the top left, AT 2019ahd on the top right, AT 2019udc on the bottom left and NGC 300 OT on the bottom right.

4.2.2 AT 2019ahd

The discovery of AT 2019ahd was reported by the ATLAS survey (Tonry et al. 2018) on 2019 January 29.0 UT. The coordinate of the transient are RA = $10^h51^m11^s.737$ Dec = +05°50' 31".03, 2".6 north and 6".9 south of the centre of its host, the spiral galaxy NGC 3423. As the distance modulus of the host galaxy, we chose to adopt an average of different independent the values reported on the NASA/IPAC Extra-galactic Database (NED) obtaining a distance modulus μ = 30.22 ± 0.14 mag, where the error comes from the standard deviation of the sample (Tully & Fisher 1988; Tully et al. 1992, 2009; Nasonova et al. 2011). We assumed a cosmology where H_0 = 73 km s^{-1} Mpc^{-1}, Ω_Λ = 0.73 and Ω_M = 0.27 (Spergel et al. 2007), which will be used throughout this whole work. The Galactic absorption in the direction of NGC 3423 is A_V = 0.079 ± 0.003 mag (Schlafly & Finkbeiner 2011). The object was initially classified as a Luminous Blue Variable (Jha 2019) due to its narrow Hydrogen features and red spectrum. The following photometric and spectroscopic evolution of the transient proved that it is an ILRT instead. The majority of the follow-up performed for this object is obtained through the GROND telescope, which yielded a remarkably homogeneous data set (top right panel of Figure 4.1). The brightest magnitude is well constrained at m_r = 17.57 ± 0.07 mag, reached on MJD = 58525.0. Similarly to AT 2019abn, AT 2019ahd displays a slow decline just after peak luminosity (γ_1), but this "pseudo-plateau" only lasts for 45 days, followed by a steep decline (γ_2) that ends 105 days after maximum. The subsequent decline rate is again slower, in particular in the NIR bands (Table 4.4).

4.2.3 AT 2019udc

The discovery of AT 2019udc was reported by the survey DLT40 (Tartaglia et al. 2018) on 2019 November 4.1 UT. The transient lies on a spiral arm of the galaxy NGC 0718, at RA = $01^h53^m11^s.190$ Dec = +04°11' 46".96. We adopt a kinematic measure of distance for NGC 0718, that provides μ = 31.49 ± 0.15 mag, obtained through the redshift of the galaxy with respect to 3K CMB (Fixsen et al. 1996). The Galactic absorption towards NGC 0718 is A_V = 0.100 ± 0.001 mag. Similarly to AT 2019ahd, also AT 2019udc was originally classified as an LBV due to its spectral features (Siebert et al. 2019) but its evolution proves that it is actually an ILRT. AT 2019udc is the most distant object studied in this sample. The follow-up campaign was stopped 120 days after maximum, due to solar conjunction. The shape of the light curves (bottom left panel of Figure 4.1) is clearly different compared to the other objects considered so far, displaying a fast linear decline (γ_1) just after peak luminosity (m_r=17.48 ± 0.08, MJD = 58797.0). A change in the decline rate can be noticed in all bands at around 35 days after maximum, when the decline becomes more shallow (γ_2).

4.2.4 NGC 300 2008 OT-1

NGC 300 2008 OT-1 (hereafter NGC 300 OT) was discovered on 2008 May 14 during the SN search program at the Bronberg Observatory (Monard 2008). The event, located in the nearby NGC 300 at RA = $00^h54^m34^s.51$ Dec = -37°38' 31".4, was extensively studied in the subsequent years (Bond et al. 2009; Berger et al. 2009; Humphreys et al. 2011; Adams et al. 2016) and became a prototype for the class of ILRTs together with SN 2008S (Botticella et al. 2009). Here we present additional optical, NIR and MIR data, comparing this object with the remainder of our sample. As done for AT 2019abn, we integrate the dataset provided by Humphreys et al. (2011) with our observations by applying magnitude corrections for each band, calculated by measuring the magnitude of the reference star chosen in their work: ΔB = +0.07 mag, ΔV = +0.01 mag, ΔR = +0.05 mag, ΔI = +0.01 mag. No correction was applied on NIR data. For the distance of NGC 300, we adopt the results published

Filter	γ_1 [-25 to -11]	γ_2 [0 to 110]	γ_3 [110 to 185]	γ_4 [>185]
B	21.8 ± 1.0	2.72 ± 0.05	–	–
V	20.5 ± 0.9	1.70 ± 0.02	2.85 ± 0.10	–
g	19.7 ± 1.3	2.27 ± 0.03	–	–
r	21.0 ± 1.0	1.37 ± 0.01	2.49 ± 0.04	0.80 ± 0.06
i	20.2 ± 1.2	1.04 ± 0.01	2.14 ± 0.07	1.45 ± 0.05
z	16.0 ± 2.3	0.82 ± 0.01	1.67 ± 0.03	1.32 ± 0.09
J	–	0.84 ± 0.08	–	1.56 ± 0.12
H	–	0.65 ± 0.02	–	1.07 ± 0.07
K	–	0.67 ± 0.07	–	0.72 ± 0.04

Table 4.3: Rise and decline rates for the various bands of AT 2019abn. All quantities are reported in [mag/100 days]. For more details about the choice of the time periods used to estimate the decline rates, see the text.

Filter	γ_1 [0 to 45]	γ_2 [45 to 105]	γ_3 [> 105]
g	1.29 ± 0.11	2.51 ± 0.12	–
r	1.12 ± 0.09	2.31 ± 0.10	1.05 ± 0.03
i	0.61 ± 0.06	2.18 ± 0.15	1.21 ± 0.04
z	0.51 ± 0.06	1.70 ± 0.09	1.16 ± 0.04
J	0.71 ± 0.06	–	0.97 ± 0.03
H	0.58 ± 0.03	–	0.57 ± 0.04
K	0.64 ± 0.10	–	0.37 ± 0.03

Table 4.4: Rise and decline rates for the various bands of AT 2019ahd. All quantities are reported in [mag/100 days]. For more details about the choice of the time periods used to estimate the decline rates, see the text.

by Gogarten et al. (2010), where a distance modulus μ = 26.43 ± 0.09 mag is obtained through the Red Clump method. The Galactic absorption towards NGC 300 is A_V = 0.034 ± 0.001 (Schlafly & Finkbeiner 2011). NGC 300 OT is the closest ILRT ever observed, making it a great target. In the bottom right panel of Figure 4.1 we present all the original data we collected for this transient. Sadly, the object was behind the sun during its rise and peak luminosity, so we lack the first part of its evolution. The first 35 days display a slow decline (γ_1), especially in the red bands. From 35 to 75 days, the transient falls from this "pseudo-plateau", and its luminosity starts to fade faster (γ_2). Between 75 and 120 days the decline in luminosity is particularly rapid (γ_3), comparable to the fast declining phase of AT 2019udc. From 120 and 255 days the fast decline stops, and a slow evolution ensues (γ_4) before the final phase (γ_5) that encompasses from 255 days onwards.

4.2.5 Comparison with other transients

In Figure 4.2, we display the absolute *r* band and *H* band evolution of our sample of ILRTs along with that of other transients of comparable luminosity. The first considerations can be made observing the sample of ILRTs, with the addition of the well studied SN 2008S (Botticella et al. 2009) and AT 2017be (Cai et al. 2018). We remark the large spread in the optical peak magnitudes, which span from –12 mag for AT 2017be to –15 mag for AT 2019abn. We note that both AT 2019abn (M_r = –15.00±0.06 at maximum) and AT 2019udc (M_r = –14.50±0.16 at maximum) are brighter at peak

Filter	γ_1 [0 to 35]	γ_2 [> 35]
B	6.46 ± 0.27	2.69 ± 0.24
V	4.37 ± 0.15	3.19 ± 0.09
g	5.6 ± 0.12	2.88 ± 0.16
r	3.93 ± 0.09	2.22 ± 0.12
i	3.41 ± 0.17	2.12 ± 0.14
z	2.95 ± 0.20	1.71 ± 0.22
H	–	0.91 ± 0.15

Table 4.5: Rise and decline rates for the various bands of AT 2019udc. All quantities are reported in [mag/100 days]. For more details about the choice of the time periods used to estimate the decline rates, see the text.

Filter	γ_1 [0 to 35]	γ_2 [35 to 75]	γ_3 [75 to 120]	γ_4 [120 to 255]	γ_5 [¿255]
U	2.57 ± 0.16	4.20 ± 0.12	–	–	–
B	2.16 ± 0.08	4.06 ± 0.08	6.30 ± 0.10	1.50 ± 0.08	–
V	1.38 ± 0.06	3.77 ± 0.07	7.06 ± 0.20	1.49 ± 0.07	–
R	0.81 ± 0.06	3.21 ± 0.05	5.24 ± 0.06	0.95 ± 0.05	–
I	0.49 ± 0.06	2.66 ± 0.06	5.21 ± 0.10	1.35 ± 0.05	–
u	3.38 ± 0.23	–	–	–	–
g	1.73 ± 0.11	4.14 ± 0.34	–	–	–
r	1.11 ± 0.05	3.32 ± 0.08	–	0.69 ± 0.07	1.56 ± 0.05
i	0.64 ± 0.07	3.09 ± 0.09	–	1.54 ± 0.09	1.38 ± 0.10
z	0.33 ± 0.07	2.24 ± 0.07	–	1.29 ± 0.09	1.71 ± 0.10
J	0.03 ± 0.10	1.9 ± 0.09	2.75 ± 0.09	1.94 ± 0.12	1.01 ± 0.23
H	-0.28 ± 0.09	1.46 ± 0.14	2.00 ± 0.13	1.40 ± 0.08	1.21 ± 0.09
K	-0.33 ± 0.30	0.98 ± 0.27	1.50 ± 0.20	0.64 ± 0.10	0.81 ± 0.06

Table 4.6: Rise and decline rates for the various bands of NGC 300 OT. All quantities are reported in [mag/100 days]. For more details about the choice of the time periods used to estimate the decline rates, see the text.

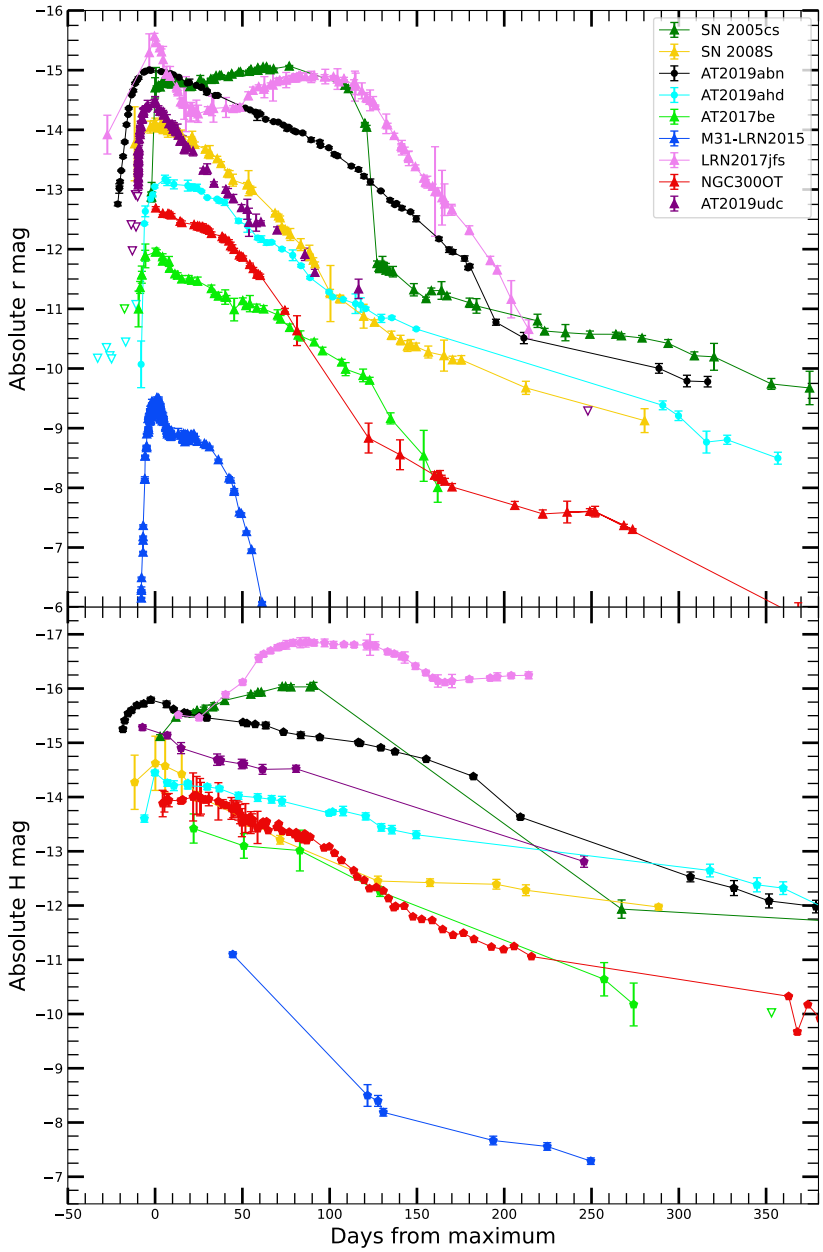

Figure 4.2: Absolute *r* band (upper panel) and *H* band (lower panel) light curve comparison between the ILRTs in our sample and other transients of comparable magnitude. In particular two LRNe, two other ILRTs and one LL SN IIP are considered.

than SN 2008S, which is among the most luminous ILRTs observed so far. AT 2019ahd and NGC 300 OT display more modest peak magnitudes, –13.17±0.16 mag and –12.69±0.11 mag respectively. Another interesting feature is the difference in the light curve shapes within the class. AT 2019abn and AT 2019udc represent the two extreme cases, with the former displaying a long phase of slow decline after peak, almost a pseudo-plateau in the r band (1.37 ± 0.01 mag/100 days), while AT 2019udc is characterized by a decline rate in the same band three times faster (3.93 ± 0.09 mag/100 days) just after peak luminosity. This variability appears to be less evident in the NIR, where both the decline rates and the peak magnitudes span a smaller range of values. To summarize, ILRTs are all characterized by their single peak, monotonically declining light curves.

A clearly different light curve shape is instead associated to Luminous Red Novae (LRNe), another class of transients populating the Gap (Pastorello et al. 2019b). These stellar mergers typically display double peaked light curves, and span an even broader range of luminosity, as shown by M31-LRN-2015 and AT 2017jfs (Williams et al. 2015; Pastorello et al. 2019a). Finally, we also plot absolute r band and H band light curves of SN 2005cs, one of the prototypes of LL SNe IIP (Pastorello et al. 2009). Its luminosity is comparable with that of AT 2019abn both at maximum light and during the late time decline, while during the first 100 days SN 2005cs becomes brighter, rather than fading, leading later to an abrupt drop of more than 3 magnitudes at the end of the plateau. This behaviour can be seen both in the optical and NIR bands, clearly different from the behaviour shown by the ILRT class.

4.3 Reddening Estimate

Estimating the reddening affecting ILRTs is a challenging task, and different approaches are used in previous works, depending on which was the most reliable indicator available. A first method consists in using the empirical relation between the Na ID Equivalent Width (EW) and the absorption along the line of sight (Turatto 2003; Poznanski et al. 2012), as was done by Cai et al. (2018). This method has the advantage of not requiring any assumption on the intrinsic properties of the target, but it needs high S/N spectroscopy in order to be reliable. Furthermore, the EW of Na ID observed may be too large to apply the empirical relation in the first place (Stritzinger et al. 2020), and since the Na ID profile varies with time only early spectra can be used. A second approach consists in assuming that all ILRT reach a temperature of 7500 K at peak luminosity, and applying a reddening correction to the SED in order to obtain a blackbody continuum corresponding to such temperature. This method is based on the observations that the spectral features of ILRTs resemble those of F-type stars, hence the assumption on the temperature at peak (Humphreys et al. 2011; Jencson et al. 2019). Yet another strategy is adopted for SN 2008S by Botticella et al. (2009), who estimate the extinction affecting the target from the MIR excess in the Spectral Energy Distribution (SED) at early stages.

In this work we adopt the same procedure carried out by Stritzinger et al. (2020), who notes that the V-r and r-i colour evolution of several ILRTs is fairly homogeneous. Therefore, we consider the bluest object in our sample, AT 2019udc, together with AT2017be, and we apply a reddening correction to all the other objects in our sample in order to superimpose their $B-V$, $g-r$ and $r-i$ colour curves through a least squares minimization procedure. Only the values measured within 100 days after maximum are considered. The absorption values inferred for each transient are reported in the last column of Table 4.1. AT 2019abn is by far the most reddened object in our sample, with an estimated internal absorption of A_V=2.34 ± 0.06 mag. AT 2019udc, by construction, is assumed to be reddening-free, since it is among the bluest ILRT observed. Following this procedure we assume that ILRTs are

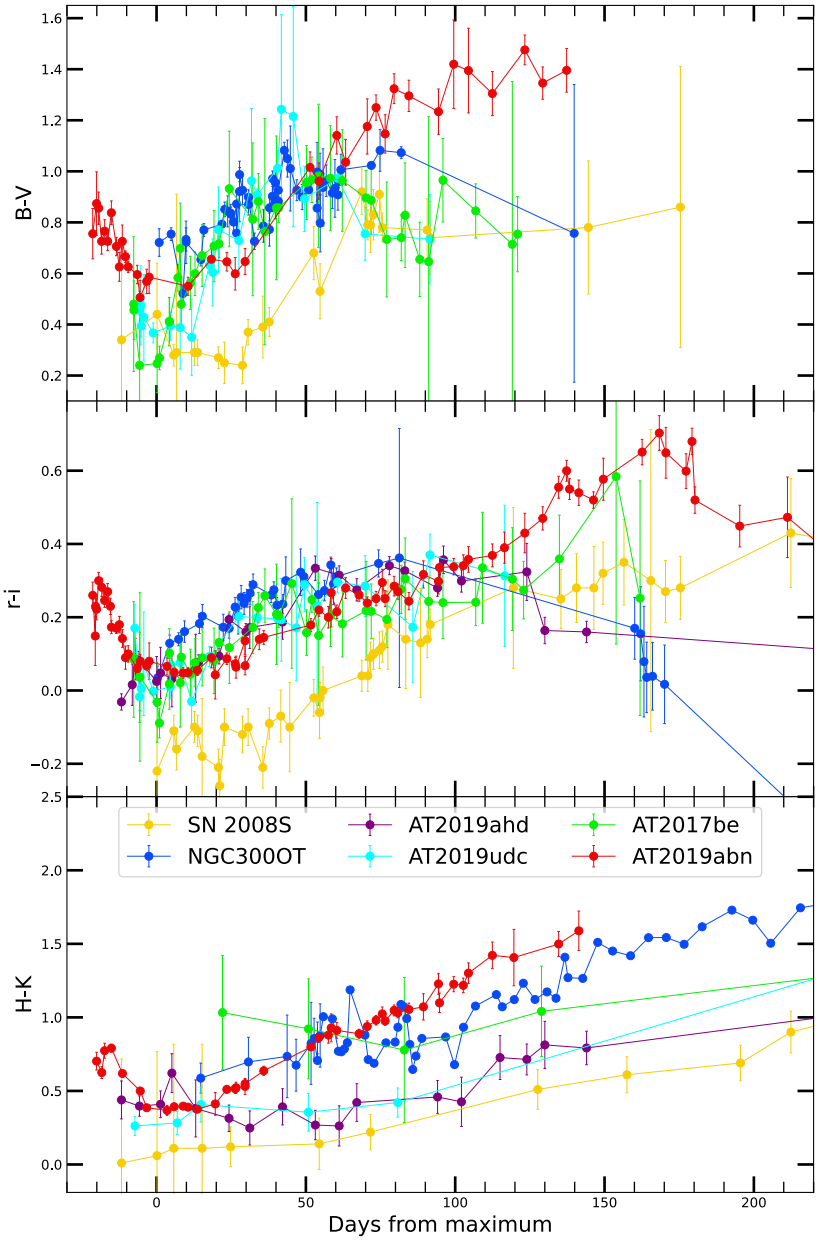

Figure 4.3: Colour curves for the ILRTs belonging to our sample, with the addition of SN 2008S and AT 2017be. In the top two panels the optical colours are shown. In the bottom panel, it is possible to appreciate the NIR colour evolution.

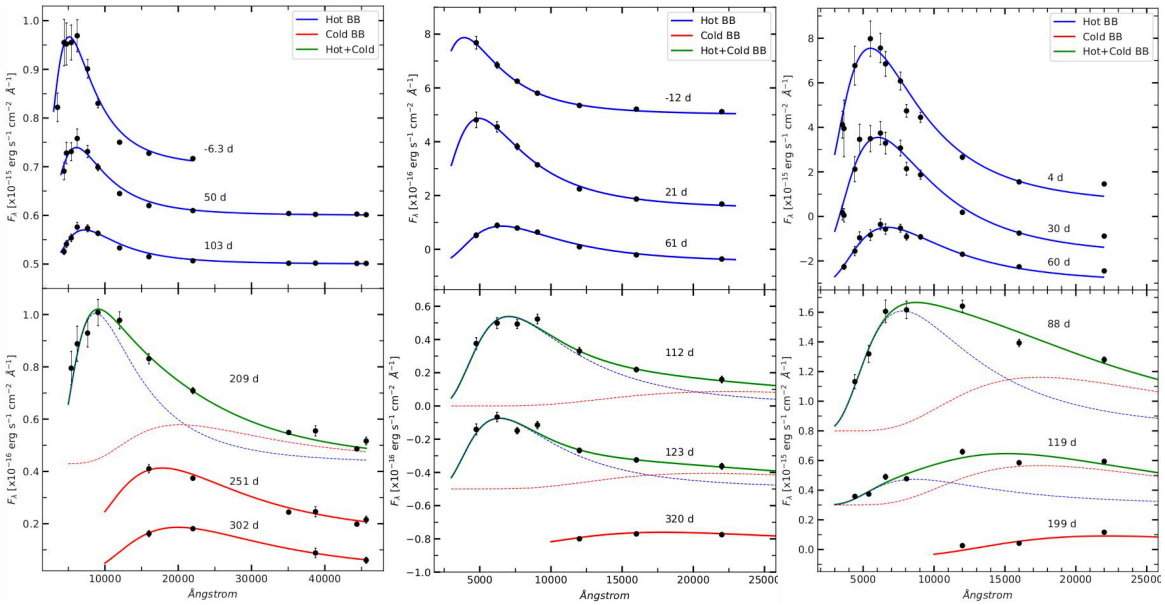

Figure 4.4: SED evolution of AT 2019abn (on the left), AT 2019udc (middle) and NGC 300 OT (on the right). In the upper panel of each figure, a single black body is sufficient to fit the data, represented in blue. At later phases, shown in the lower panels, a second black body is needed to reproduce the NIR flux excess. Epochs are referred to maximum light.

intrinsically homogeneous, which may not be the case: indeed, we are introducing a bias that would prevent the proper characterization of an outlier. In Figure 4.3 we report the colour evolution for our sample of ILRTs after applying the reddening correction. The optical colours, in particular $r-i$, behave in a remarkably homogeneous way during the first 100 days after peak luminosity. The exception is SN 2008S, for which we adopt the absorption values reported by Botticella et al. (2009), which makes it the bluest ILRT to date. On the other hand, the NIR colour evolution (Figure 4.3, bottom panel) is less affected by reddening correction, and the different objects spread on a wider range of colours, with SN 2008S still being the bluest ILRT in the group.

4.4 SED Evolution

In order to retrieve additional information on our targets, we perform blackbody fits on the SED at different epochs. This analysis is carried out through Monte Carlo simulations, using the PYTHON tool CURVE_FIT[4] to perform fits on 200 sets of fluxes randomly generated with a Gaussian distribution centered at the measured flux value, and σ equal to the error associated to the measurement. Such procedure was already adopted and described in Pastorello et al. (2021); Valerin et al. (2022). The blackbody fit to the SED of the target yields the estimated temperature, and by integrating over the wavelength we obtain the total flux emitted. Adopting the distances discussed in Sect. 4.2 and assuming spherical symmetry, we calculate the bolometric luminosity of the source. Finally, the radius is estimated through the Stefan–Boltzmann law. This whole procedure is repeated for each epoch with suitable photometric coverage, in order to study the evolution of the inferred physical parameters with

[4]https://docs.scipy.org/doc/scipy/reference/generated/ scipy.optimize.curve_fit.html

time. During the first phase of evolution all the objects are well fitted by a single black body, associated to the photosphere, throughout the optical and NIR domains. Such phase has a variable duration: up to 180 days for AT 2019abn (Figure 4.4, left), 110 days for AT 2019ahd (Figure 4.4, middle) and only 80 days for NGC 300 OT (Figure 4.4, right). The SED of AT 2019udc is well fit by a single black body at all epochs observed, since due to solar conjunction it was not possible to follow its evolution after ∼100 days after peak luminosity.

The values of temperature, luminosity and radius obtained for this "hot" blackbody are displayed in the left panel of Figure 4.5. The temperature evolution of our sample is especially homogeneous between 25 and 75 days after maximum, due to our reddening estimate through colour curves superposition (Sect. 4.3). However we still find interesting differences between the various targets in the pre–maximum phases. AT 2019abn displays an almost constant temperature at ∼4600 K for several days before slowly reaching the peak temperature of ∼5900K in ∼20 days. AT 2019udc qualitatively follows the same behaviour, but in a shorter timescale (less than 10 days) and reaching 7000 K at peak. AT 2019ahd, on the other hand, starts from a temperature of ∼7500 K, quite hot for an ILRT, before quickly cooling to 6000 K at peak luminosity. From this point onward, AT 2019ahd closely follows the behaviour of AT 2019abn. In this respect, the early temperature evolution of AT 2019ahd is reminiscent of that of SN 2005cs (displayed in Figure 4.5, left panel, for comparison) and LL SN IIP in general, where the temperature quickly declines during the initial phases. NGC 300 OT shows a very simple, monotonic temperature evolution, but in this case we miss the pre–maximum photometric coverage.

In the middle panel of Figure 4.5 (on the left) we present the bolometric luminosity obtained for the "hot" blackbody. The bolometric luminosity behave in a similar way to what is described in Sect 4.2.5, with AT 2019abn being the brightest ILRT, showing a peak luminosity of $1.9\pm\ 0.3 \times 10^{41}$ erg s^{-1}. As previously pointed out, its decline rate is slower compared to other objects of the same class, but it is not flat like the plateau of SNe IIP. AT 2019udc is characterized by a marked peak ($1.4\pm0.5 \times 10^{41}$ erg s^{-1}) followed by a fast decline. AT 2019ahd and NGC 300 OT display more modest peak luminosities, respectively of 4.4 ± 1.1 and $2.7\pm1.0 \times 10^{40}$ erg s^{-1}. As for the evolution of the radius of the emitting source, shown in the bottom panel of Figure 4.5 (on the left left), it appears that all ILRTs in our sample follow a similar behaviour. After maximum, the transients show a roughly constant radius with time, although with different values. AT 2019abn again stands out from the group, showing a blackbody radius that at first quickly increases from 21±2 to 36±3 AU from discovery to peak luminosity, and then remains at 30 to 40 AU in the following 125 days. These values are roughly two to three times those obtained for the other three targets. AT 2019ahd shows qualitatively the same behaviour, with a radius growing from 7±1 to 15±1 AU from discovery to peak magnitude, and a subsequent slow evolution spanning from 14±1 to 18±1 AU within 110 days after maximum. AT 2019udc on the other hand does not show an increase in the radius during the pre–maximum phase, but rather a decrease, from 23±3 to 19±2 AU. The following slow evolution of the blackbody radius between 16±2 and 21±2 AU over the course of 90 days is reminiscent of those of the other two ILRTs already presented. Finally, for NGC 300 OT we do not have pre–maximum data, but the evolution of the blackbody radius after the observed maximum is again slow, spanning from 11±1 to 16±1 in 90 days. Such homogeneous behaviour is in stark contrast with the monotonic and steep increase in radius for SNe IIP and Low Luminosity SNe IIP during the first 80 days, as shown by the radial evolution of SN 2005cs.

So far we described the physical properties of the "hot" blackbody, which is associated to the photosphere of the transient and is usually well visible for ∼100-150 days after maximum. At later phases

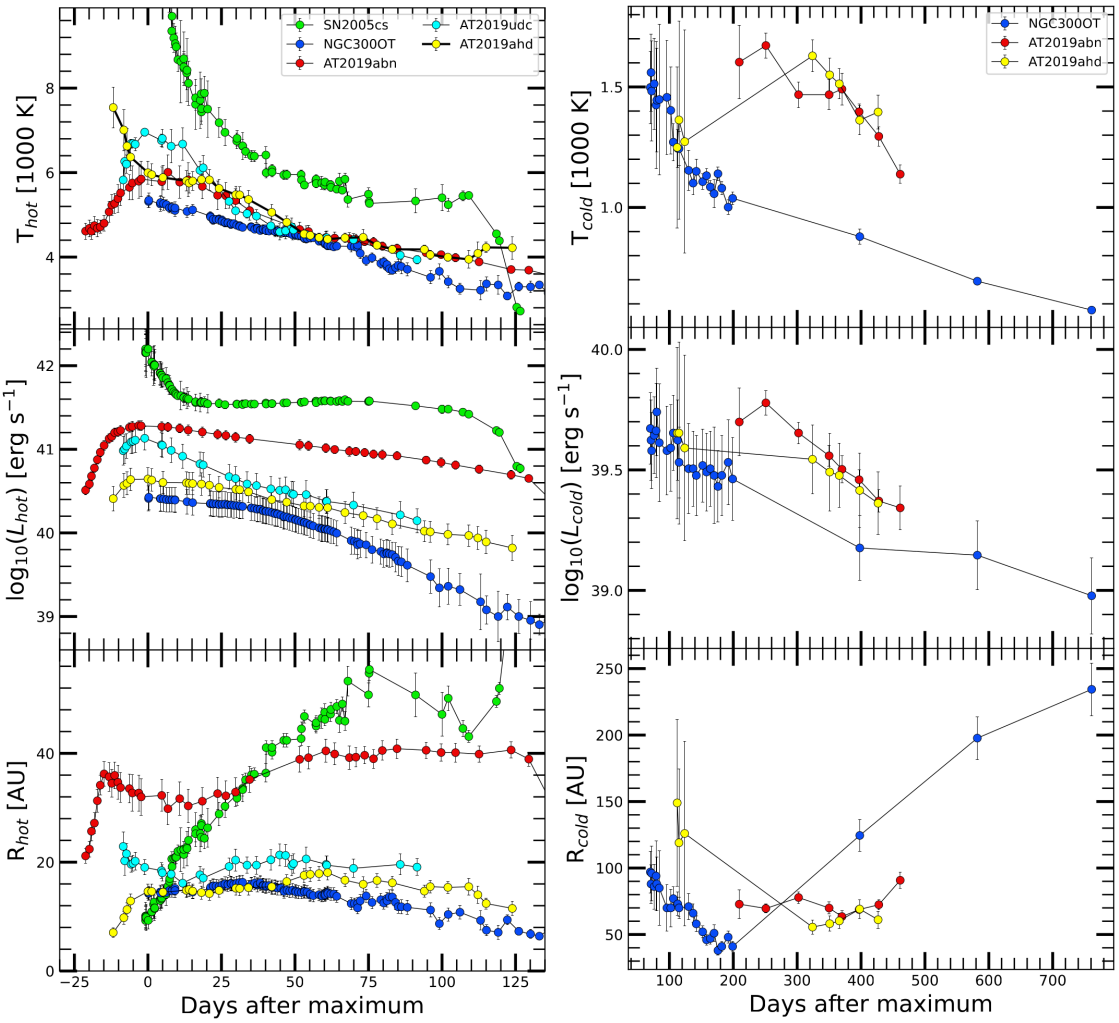

Figure 4.5: Temperature, luminosity and radius evolution of the hot (left panel) and cold (right panel) black body of the three ILRTs in our sample that present a NIR excess in their SED. On the left panel, SN IIP, a low luminosity SN, is shown for comparison.

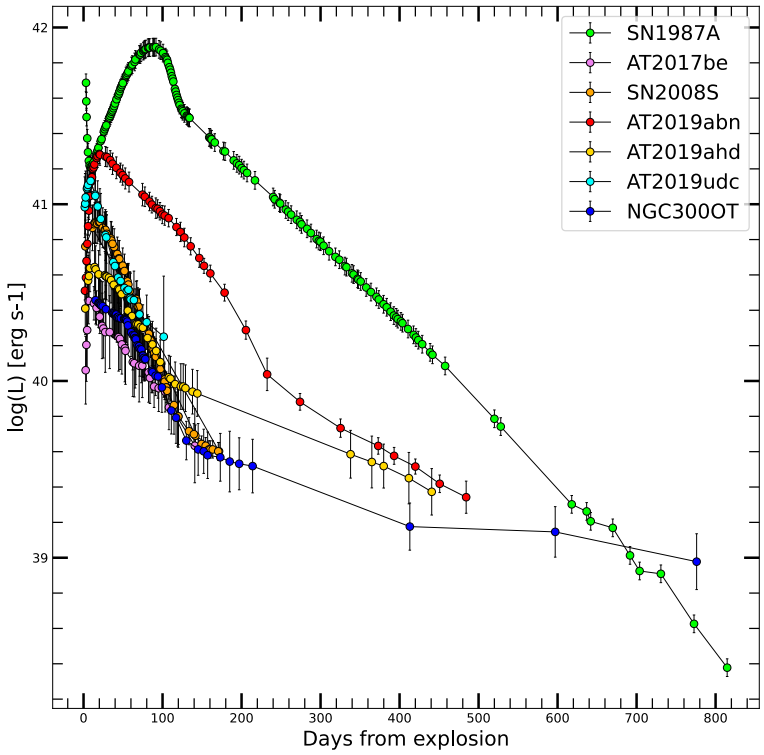

Figure 4.6: Bolometric light curves of several ILRTs compared with SN 1987A.

however, as the gas cools down and expands, an excess in the NIR (and MIR, when available) flux is detected. Such feature has been typically associated with the formation of dust, which contributes to the SED with a second, "cold" ($T \lesssim 1500$ K) black body (Botticella et al. 2009; Cai et al. 2018). In the bottom panels of Figure 4.4 are shown blackbody fits performed to the SED of our targets at epochs when two black bodies coexist. At the latest phases observed, as the objects shift from the photospheric to the nebular phase, the optical flux is entirely supported by emission lines (Hα, Hβ, [CaII], Ca NIR triplet) therefore there is no continuum to fit with a "hot" blackbody. At these epochs we still identify a contribution from the "cold" black body associated with dust emission. This feature is especially clear in AT 2019abn and NGC 300 OT (up to 720 days after maximum) thanks to the MIR measurements. In the right panel of Figure 4.5 we present the physical parameters obtained for the "cold" blackbody component associated with dust emission. AT 2019abn and AT 2019ahd show very similar cold components, with temperatures cooling from ~1600 to ~1200 K over a timescale of hundreds of days. Typical values of luminosity are $3.2 \pm 1.0 \times 10^{39}$ erg s^{-1}. The radius of the emitting source is around 60 AU for AT 2019ahd and 75 AU for AT 2019abn. The most relevant difference between the two is that AT 2019ahd develops the "cold" component sooner, at around 110 days: the blackbody fits at these epochs are affected by large errors, due to the uncertainty in disentangling the "hot" and "cold" components in the SED. A similar issue is found also for NGC 300 OT, but in this case we have a much higher cadence of NIR observations, allowing us to better constrain the evolution of the "cold" component. A first, fast decline in temperature is observed between 71 days and 130 days after maximum, where the dust cools from 1550±170 K to 1150±90 K. The subsequent temperature decline is slower, reaching 570±10 K at 761 days. Such late estimate is possible thanks to original WISE data. The other two late measurements at 398 and 582 days were performed on MIR data taken

by Ohsawa et al. (2010), which we included in our analysis without needing magnitude corrections. The luminosity of this "cold" component fades from $5.5\pm1.9 \times 10^{39}$ erg s^{-1}, just after its emergence, to $9.5\pm0.9 \times 10^{38}$ erg s^{-1} at 761 days. The radius inferred for the dust emission at first shrinks from ∼100 AU to ∼40 AU, but around 180 days the trend inverts and the radius grows to 235±20 AU at 761 days. This late increase in radius appears to be similar to the behaviour of SNe, where the radius of the dust increases as the dust expands together with the ejecta (e.g. Wesson et al. 2015). The previous shrinking of the emitting source is more challenging to explain: one possible explanation is that we are observing dust formation far from the star, with dust condensing at progressively smaller radii as the transient becomes dimmer and the temperature decreases.

In order to obtain the bolometric luminosity of ILRTs, we sum the "hot", photospheric component, and the "cold", dusty component. Furthermore, at late epochs, a blackbody continuum is no longer discernible in the optical domain, with only emission lines dominating the spectra. Therefore, to measure the bolometric luminosity in those cases we integrate the fluxes in the optical domain using the trapezoidal rule, while for the "cold" component at longer wavelengths it is still possible to perform a blackbody fit. The bolometric luminosity obtained for our sample of ILRTs are reported in Figure 4.6, together with the bolometric luminosity of SN 1987A. The late time decline of SN 1987A has often been used as a benchmark for estimating the ^{56}Ni mass synthesized in a stellar explosions in general, and for ILRTs in particular (e.g. Botticella et al. 2009; Cai et al. 2021). We analyse an unprecedented amount of NIR and MIR data for ILRTs, which allow us to better infer the luminosity contribution at longer wavelengths, crucial at late times. In Figure 4.6 it is evident that AT 2019abn, AT 2019ahd and NGC 300 OT are characterized by a late decline shallower compared to SN 1987A, and therefore shallower than what is expected if just ^{56}Ni decay is supporting the late time luminosity of the transients. Of course these more shallow slopes do not exclude the presence of ^{56}Ni, but they rather require additional mechanisms to explain the late time luminosity of ILRTs.

4.5 A toy model for ILRTs light curves

In this subsection we present a simple model that attempts to reproduce the shape of the bolometric light curves of ILRTs in the context of weak SN explosions. The end goal is to obtain a rough estimate of parameters such as the amount of mass ejected and its velocity. The basic concepts are taken from Chatzopoulos et al. (2012), which in turn expand the approach introduced by Arnett (1980, 1982). First of all, ^{56}Ni radioactive decay is expected to be a relevant power source, and its luminosity over time is given by the equation:

$$L_{Ni}(t) = \frac{2M_{Ni}}{t_d} e^{-[\frac{t^2}{t_d^2}+\frac{2R_0 t}{vt_d^2}]} [(\epsilon_{NI} - \epsilon_{Co}) \int_0^t [\frac{R_0}{vt_d} + \frac{t'}{t_d}] e^{[\frac{t'^2}{t_d^2}+\frac{2R_0 t'}{vt_d^2}]} e^{-t'/t_{Ni}} dt' + \epsilon_{Co} \int_0^t [\frac{R_0}{vt_d} + \frac{t'}{t_d}] e^{[\frac{t'^2}{t_d^2}+\frac{2R_0 t'}{vt_d^2}]} e^{-t'/t_{Co}} dt'](1 - e^{-At^{-2}}) \quad (4.1)$$

where M_{Ni} is the mass of synthesised ^{56}Ni, t_{Ni} and t_{Co} are the half lives of ^{56}Ni and ^{56}Co, while ϵ_{Ni} and ϵ_{Co} are the energy generation rates of ^{56}Ni and ^{56}Co released during the radioactive decay. A is a constant that accounts for the opacity of the ejecta to γ-rays, with large values of A corresponding to complete trapping of the photons. For the constant terms we adopt the same values as Chatzopoulos et al. (2012). Equation 4.1 takes into account the diffusion time through an homologously expanding

Transient	^{56}Ni [$M_\odot$]	M_{core} [$M_\odot$]	V_{core} [km s^{-1}]	E_{core} [erg]	R_{core} [cm]	M_{env} [$M_\odot$]	V_{env} [km s^{-1}]	E_{env} [erg]	R_{env} [cm]	t_{CSM} [days]
AT 2019abn	$7.0\text{x}10^{-3}$	7.0	2000	$6.5\text{x}10^{49}$	$2\text{x}10^{13}$	1.0	5500	$2.7\text{x}10^{48}$	$1\text{x}10^{14}$	12
AT 2019ahd	$1.8\text{x}10^{-3}$	3.5	4500	$4.1\text{x}10^{49}$	$5\text{x}10^{12}$	0.5	5000	$7.0\text{x}10^{46}$	$1\text{x}10^{14}$	3
NGC 300 OT	$1.8\text{x}10^{-3}$	4.0	4000	$3.5\text{x}10^{49}$	$4.5\text{x}10^{12}$	-	-	-	-	3
AT 2019udc	$3.5\text{x}10^{-3}$	2.0	22000	$3.7\text{x}10^{49}$	$1.0\text{x}10^{13}$	-	-	-	-	2

Table 4.7: Parameters used in the models displayed in Figure 4.7

gas with mass M, with characteristic expansion velocity v and initial radius R_0. The characteristic timescale t_d of the light curve can be written as a combination of the diffusion timescale t_0 and the hydrodynamical timescale t_h:

$$t_d = \sqrt{t_0 t_h} \qquad t_0 = \frac{kM}{\beta c R_0} \qquad t_h = \frac{R_0}{v}$$

where β is a constant linked to the density profile of the mass, and k is the opacity of the ejecta, for which we adopt a value of 0.33 cm^2 g^{-1}.
As an additional source of luminosity, we consider the radiation emitted by the expanding and cooling gas, originally heated by the blast wave that followed the explosion. This term was already introduced by Arnett (1980) to reproduce the slowly declining light curves of SNe IIP. Using the same formalism as Chatzopoulos et al. (2012), such luminosity term is written as:

$$L_{blast}(t) = \frac{E_{th}}{t_0} e^{-[\frac{t^2}{t_d^2} + \frac{2R_0 t}{v t_d^2}]} \tag{4.2}$$

where E_{th} is the internal energy which was deposited in the ejecta during the explosion. To better reproduce the observed shape of the light curve, we consider two blast terms: one associated with the envelope of the star, less massive and more extended, characterised by a short diffusion time, and another blast term associated with the core, more massive and dense, with a much longer diffusion timescale. Dividing the ejecta in two regions is not a novelty: such approach has been successfully used, for example, by Nagy & Vinkó (2016). The total time dependent luminosity is therefore the sum of these three contributions:

$$L_{tot}(t) = L_{Ni}(t) + L_{core}(t) + L_{envelope}(t). \tag{4.3}$$

The final piece of the model is the thick CSM surrounding the transient. It does not provide additional energy, but it simply reprocesses the total luminosity emitted by the ejecta and ^{56}Ni, delaying its appearance. To reproduce the effect that such dense CSM has on the the observed luminosity of the transient, we adopt the fixed photosphere approximation presented by Chatzopoulos et al. (2012):

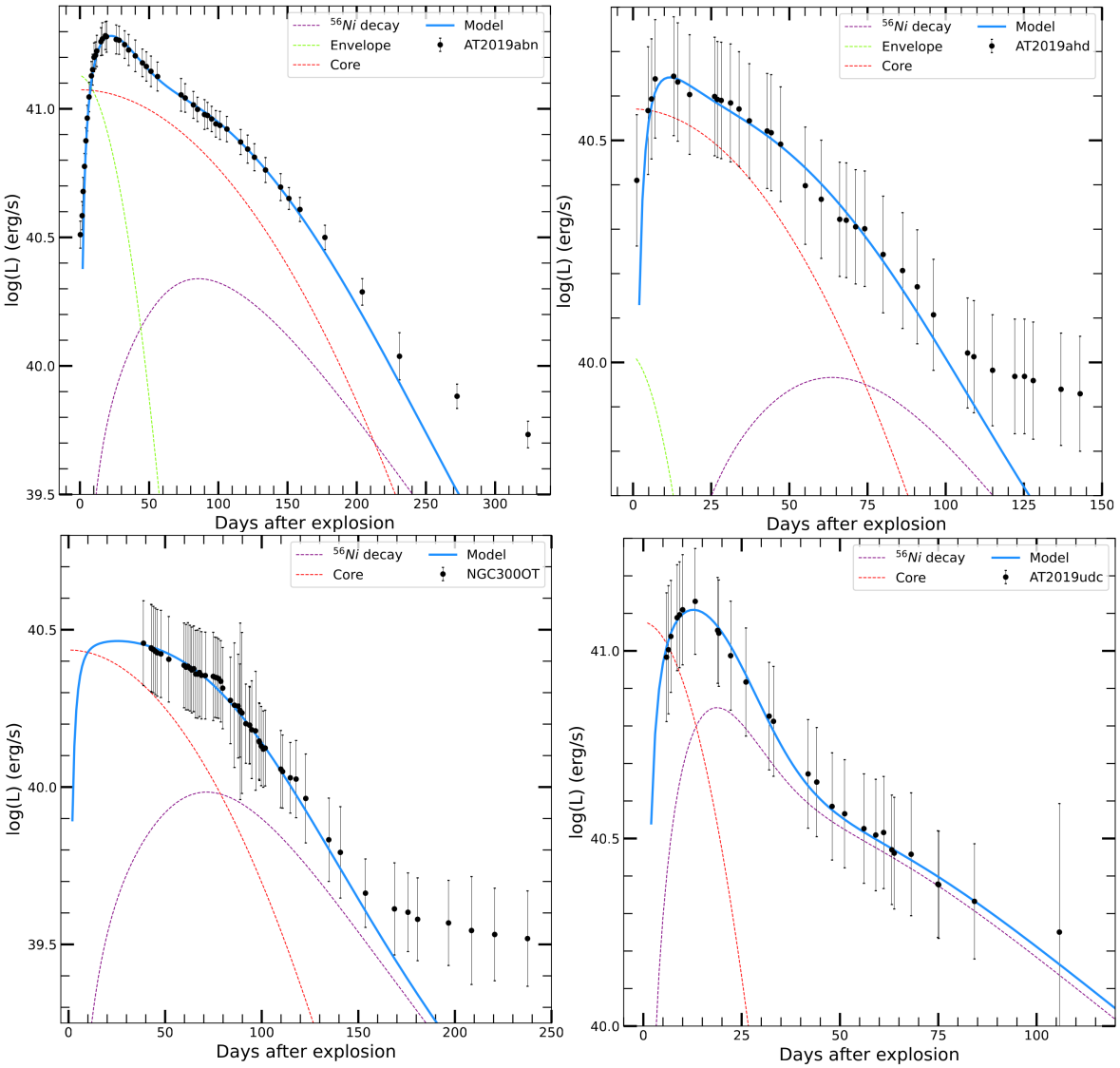

Figure 4.7: Bolometric light curves of our sample of ILRTs with a toy model reproducing their shape.

$$L_{final}(t) = \frac{1}{t_{CSM}} e^{-\frac{t}{t_{CSM}}} \int_0^t e^{\frac{t'}{t_0}} L_{tot}(t') dt' \tag{4.4}$$

where t_{CSM} is the diffusion time through the thick CSM shell surrounding the transient. Equation 4.4 holds true only in the simplified scenario in which the photosphere does not move with time. Although this is an approximation, we do expect the photosphere of ILRTs to be constrained within the dense CSM shell surrounding the star, therefore limiting its movement. The reprocessing effect of the CSM is crucial in the first phases, during which the blast terms L_{core} and $L_{envelope}$ start abruptly from the maximum luminosity, without a rising phase. A CSM shell with a diffusion time of few days allow the models to reproduce the rise observed in ILRTs. In Figure 4.7 are shown the models and the bolometric light curves of our sample of ILRTs. The contribution of each component is shown with different colours: the parameters relative to each of them are reported in Table 4.7.

One weakness of the approach outlined above is the large number of free parameters, as well as the degeneracy between some of them: similar solutions can be obtained while inputting different parameters. Instead of blindly applying a fitting procedure, we tried to input reasonable parameters in the context of SNe, gradually modifying them to improve the agreement with the data.

AT 2019abn is definitely the most successful example within our sample. The emission from a rather massive envelope, combined with a CSM diffusion time of 10 days, seems to properly reproduce the rise and the maximum phases. The subsequent slow decline can be explained by slow ejecta which trap the photons for almost 200 days. The ^{56}Ni is not significant until the late phases, and it is definitely too faint to explain the evolution after 200 days: as mentioned in the previous section, an additional source of energy is likely needed to explain the late time luminosity of ILRTs.
The parameters used to model AT 2019ahd do not differ significantly from the ones used for AT 2019abn: they are mainly scaled down in mass and internal energy of the ejecta. The blast term associated with the envelope is not as crucial, but the overall evolution appears to be reproduced sufficiently well, excluding of course the late shallow decline.

Since we miss the first evolutionary phases of NGC 300 OT, we only use a single blast (associated to the core) term plus ^{56}Ni decay to reproduce the data: the blast term associated with the envelope is relevant during the early phases, so it is difficult to constrain in this case. Apart from this, the parameters used for NGC 300 OT are very similar to the ones used for AT 2019ahd. The same conclusions cannot be reached for AT 2019udc, which is definitely an outlier in this sample. First of all, the fast decline hints at the presence of a single blast term. Most strikingly, the evolution of AT 2019udc is much faster compared to the other transients considered so far. For this reason the diffusion time within the ejecta must be remarkably lower: this leads to a low ejected mass and a high scale velocity, several times larger compared to the other ILRTs mentioned so far. Finally, it is worth noticing that this is the only case where the late time data points are compatible with the ^{56}Ni decay rate. In the scenario in which ILRTs arise from a core collapse event, a compact remnant is expected to be left behind. Since the mass of the remnant can be estimated to be 1.3–2.0 $M_\odot$ (Pumo et al. 2017), the inferred mass of our sample of ILRTs right before the explosion adds up to 5.3–6.0 $M_\odot$ for both AT 2019ahd and NGC 300 OT and 9.3–10 $M_\odot$ for AT 2019abn. Such values are compatible with the expectations for SAGB stars and consequently ECSN events, especially accounting for the fact that some mass was likely lost during the evolution of the star, therefore leading to a slightly higher ZAMS. AT 2019udc, with its estimated progenitor mass of just 3.3–4.0 $M_\odot$ at the time of explosion, sets itself apart from the rest of the sample, although its origin could be tentatively explained as an ECSN arising from a SAGB star that underwent extreme mass loss. We remark that the toy model

presented in this section is an oversimplified approach to the light curve modelling of ILRTs: more detailed models should be used to retrieve more reliable estimates of the explosion parameters of these objects. Furthermore, the puzzling results obtained for AT 2019udc may be significantly revised while using a more refined approach.

Chapter 5

Spectroscopic observations of Intermediate Luminosity Red Transients

In this chapter we present the spectroscopic data gathered for our sample of Intermediate Luminosity Red Transients (ILRTs), reduced following the prescriptions presented in Chapter 2. The logs of spectroscopic observations for each target are reported in Tables 5.1, 5.2, 5.3 and 5.4. ILRTs present homogeneous properties: their spectra consist in an almost featureless black body continuum with superimposed narrow emission lines. Narrow lines, together with the very slow evolution of the spectra, are indicative of the presence of thick Circumstellar Medium (CSM) surrounding the transients. Since the photosphere lies within this dense gas, it is not possible to probe the material underneath the CSM, which would reveal key information on the nature of the transient itself. This configuration is similar to that of SNe IIn, with the key difference that both the temperature ($T_{ILRT} < 8000$ K) and the luminosity ($L_{ILRT} < 10^{42}$ erg s^{-1}) of ILRTs are far lower compared to SNe IIn, which are instead both brighter and bluer than the average SN (Kiewe et al. 2012). The interaction between fast ejecta and slow moving CSM is a key component to explain the high temperature and luminosity shown by SNe IIn (Smith 2017). When the CSM interaction is the dominant source of energy, specific spectral features can be identified, most notably a blue shoulder on the Hα line (Tartaglia et al. 2020). ILRTs, on the other hand, do not show clear signs of interaction in their spectra, and their low temperature and luminosity point towards a rather small contribution of ejecta-CSM interaction throughout their evolution.

In Figures 5.1 and 5.2 are displayed the spectra gathered for NGC 300 OT, while in Figures 5.3 and 5.4 is shown the spectral sequence obtained for AT 2019abn. Figures 5.5 and 5.6 are relative to AT 2019ahd and AT 2019udc, respectively. The Ca H & K absorption lines ($\lambda\lambda$ 3934,3968) are clearly seen in all objects, especially at early phases. Ca NIR triplet ($\lambda\lambda\lambda$ 8498,8542,8662) is detectable at all epochs and becomes dominant during the late phases. The [Ca II] forbidden doublet ($\lambda\lambda$7291,7323) is one of the most interesting features in ILRTs spectra: it originates in a region where the gas density must be low, otherwise collisional de-excitation would prevent the emission of photons through radiative decay and consequently the formation of the lines (Humphreys et al. 2011). While not unique to ILRTs, the presence of the [Ca II] forbidden doublet in all the objects analysed so far has been proposed as a key feature to distinguish ILRTs from other transients that present similar spectra (Pastorello & Fraser 2019). It is also worth noticing that all spectra of ILRTs in our sample become bluer during the rise to maximum. This can be an indicator that the energy released by the transient is

AT 2019abn

Date	Telescope+Instrument	Grism	Range (Å)	Res (Å)	Exp. time (s)
2019-01-27	WHT+LIRIS	zJHK	9000-24000	22	1800
2019-01-29	NOT+ALFOSC	gr4	3200-9600	16	1800
2019-01-29	WHT+LIRIS	zJ	9000-14000	17	2700
2019-02-11	NOT+ALFOSC	gr4	3200-9600	16	2800
2019-02-20	NOT+ALFOSC	gr4	3200-9600	12	3600
2019-02-28	NOT+ALFOSC	gr4	3200-9600	12	2400
2019-03-02	LCO+FLOYDS	red/blu	3500-10000	13	3600
2019-03-15	NOT+ALFOSC	gr4	3200-9600	12	2700
2019-03-18	LCO+FLOYD	red/blu	3500-10000	11	3600
2019-03-23	NOT+ALFOSC	gr4	3200-9600	12	2700
2019-03-29	LCO+FLOYD	red/blu	3500-10000	13	3600
2019-04-09	LCO+FLOYD	red/blu	3500-10000	13	3600
2019-04-23	NOT+ALFOSC	gr4	3200-9600	12	1800
2019-05-09	LCO+FLOYD	red/blu	3500-10000	13	3600
2019-05-15	NOT+ALFOSC	gr4	3200-9600	15	3600
2019-05-20	LCO+FLOYD	red/blu	3500-10000	11	3600
2019-06-04	NOT+ALFOSC	gr4	3200-9600	14	3600
2019-06-22	LCO+FLOYD	red/blu	3500-10000	13	3600
2019-07-20	NOT+ALFOSC	gr4	3200-9600	12	3600
2019-07-26	LCO+FLOYD	red/blu	3500-10000	12	3600
2019-08-20	NOT+ALFOSC	gr4	3200-9600	15	3600
2019-08-30	NOT+ALFOSC	gr4	3200-9600	12	3600

Table 5.1: Log of spectroscopic observations for AT 2019abn.

travelling through the dense CSM with a rather long diffusion time, causing a progressive increase in temperature until maximum luminosity is reached.

AT 2019ahd

Date	Telescope+Instrument	Grism	Range (Å)	Res (Å)	Exp. time (s)
2019-01-30	SALT+RSS	PG0900	3500-9300	5	1890
2019-02-06	NOT+ALFOSC	gr4	3200-9600	12	3600
2019-02-11	NOT+ALFOSC	gr4	3200-9600	16	3600
2019-02-28	NOT+ALFOSC	gr4	3200-9600	12	3600
2019-03-05	SALT+RSS	PG0700	3500-9300	16	1800
2019-03-15	NOT+ALFOSC	gr4	3200-9600	12	2700
2019-04-07	NOT+ALFOSC	gr4	3200-9600	12	3000
2019-04-18	NOT+ALFOSC	gr4	3200-9600	12	3600
2019-05-14	NOT+ALFOSC	gr4	3200-9600	12	3600
2019-05-21	SALT+RSS	PG0700	3500-9300	15	1800
2019-11-23	GTC+OSIRIS	R1000R	5100-10300	6	1350

Table 5.2: Log of spectroscopic observations for AT 2019ahd.

AT 2019udc

Date	Telescope+Instrument	Grism	Range (Å)	Res (Å)	Exp. time (s)
2019-11-04	LCO+FLOYDS	red/blu	3500-10000	18	2700
2019-11-06	LCO+FLOYDS	red/blu	3500-10000	18	2700
2019-11-13	LCO+FLOYDS	red/blu	3500-10000	12	3600
2019-11-14	LCO+FLOYDS	red/blu	3500-10000	12	3600
2019-11-15	LCO+FLOYDS	red/blu	3500-10000	16	3600
2019-11-17	LCO+FLOYDS	red/blu	3500-10000	12	3600
2019-11-18	LCO+FLOYDS	red/blu	3500-10000	15	3600
2019-11-30	LCO+FLOYDS	red/blu	3500-10000	12	3600
2019-12-03	LCO+FLOYDS	red/blu	3500-10000	12	3600
2019-12-07	Baade+FIRE	-	8000-22000	5	1800
2019-12-14	NOT+ALFOSC	gr4	3200-9600	20	2800
2019-12-24	LCO+FLOYDS	red/blu	3500-10000	13	3600
2020-01-19	LCO+FLOYDS	red/blu	3500-10000	12	3600

Table 5.3: Log of spectroscopic observations for AT 2019udc.

NGC 300 OT

Date	Telescope+Instrument	Grism	Range (Å)	Res (Å)	Exp. time (s)
2008-05-16	BMagellan+IMACSshort	g200	4000-10500	6	100x2
2008-05-30	DuPont+B&C	g300	3500-9600	8	300
2008-06-04	DuPont+B&C	g300	3500-9600	8	300
2008-06-06	NTT+EFOSC	gm3-gm5	3300-9200	B11 R15	1460x2
2008-06-11	CMagellan+LDSS3	-	3700-9800	4	300x3
2008-06-13	NTT+EFOSC	gm3-gm5	3300-9200	B11 R15	1460x2
2008-06-15	NTT+EFOSC	gm3-gm5	3300-9200	B11 R15	1460x2
2008-06-16	BMagellan+IMACSlong	g300	3700-7900	4	300x3
2008-07-01	VLT+FORS	300V	3300-9200	11	1800
2008-07-02	VLT+UVES	SHP700+HER_5	3400-8000	B0.12 R0.36	1500x6
2008-07-05	NTT+EFOSC	gm3-gm5	3300-9200	B11 R15	1460x2
2008-07-08	VLT+FORS	300V	3300-9200	11	2160
2008-07-15	NTT+EFOSC	gm3-gm5	3300-9200	B11 R15	1460x2
2008-07-23	CTIO4m+R-CSpec	KPGL3-1	4000-7600	5	720
2008-07-24	CTIO4m+R-CSpec	KPGL3-1	4000-7600	5	1200
2008-07-25	CTIO4m+R-CSpec	KPGL3-1	4000-7600	5	1200
2008-08-05	NTT+EFOSC	gm3-gm5	3300-9200	B11 R15	1460x2
2008-09-17	CMagellan+LDSS3	VPH-All	3700-9400	6	900
2008-10-02	Palomar200i+DBSP	300/3990+158/7500	3300-10300	B11 R16	1800x2
2008-10-08	TNG+NICS	IJHK	8700-24700	IJH16 K30	–
2008-10-14	WHT+ISIS	R158R+R300B	3400-10200	B4 R6	600x3
2009-01-07	CMagellan+LDSS3	VPH-All	4000-8000	6	1580
2009-01-21	CMagellan+LDSS3	VPH-All	4000-8000	6	1800
2009-10-12	VLT+X-Shooter	-	10100-24400	3.6	300

Table 5.4: Log of spectroscopic observations along with main features of the instruments used. FORS spectra were taken from Patat et al. (2010).

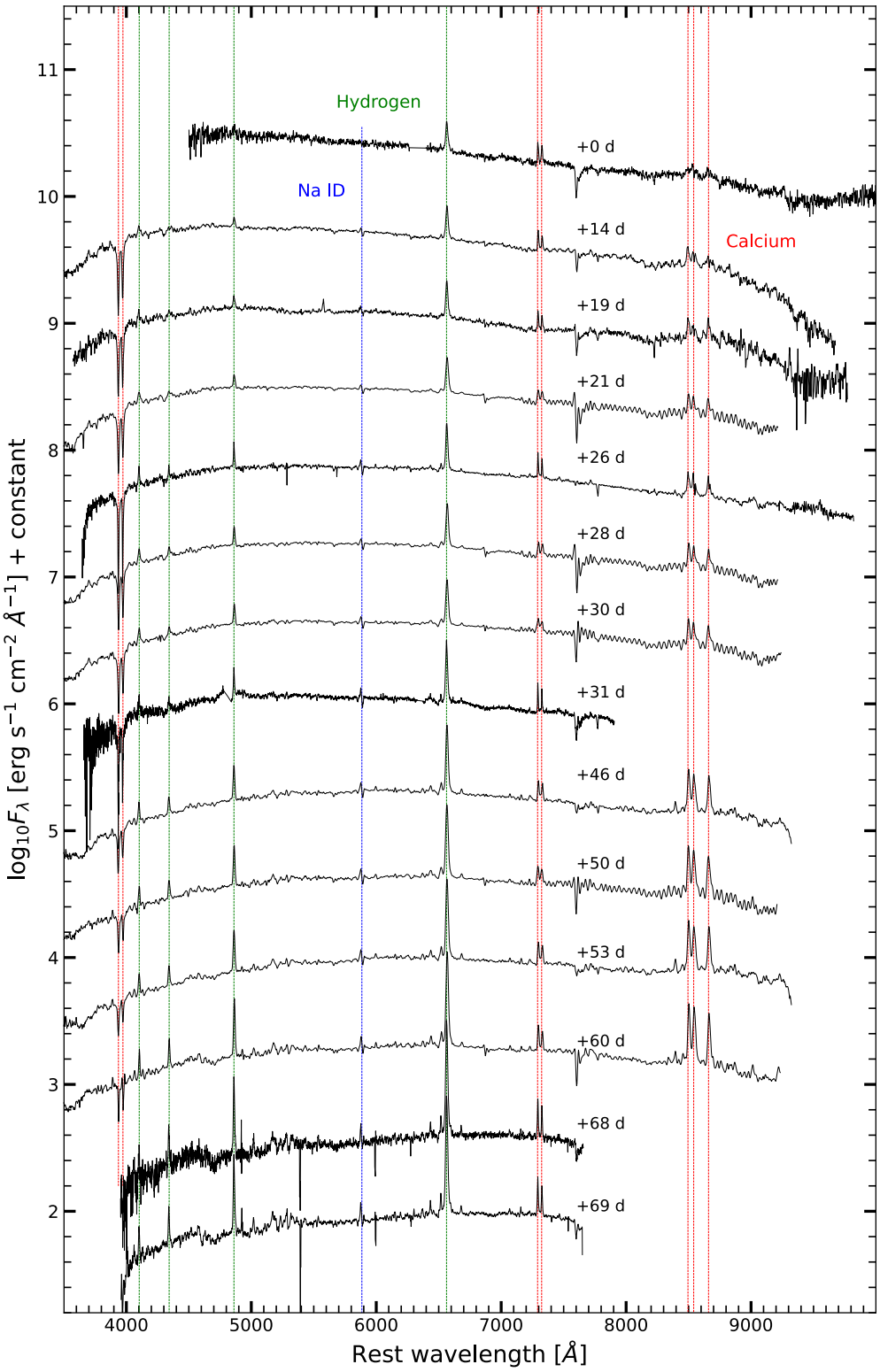

Figure 5.1: NGC 300 OT spectra during the early phases. Ca lines are highlighted in red, H lines in green and the Na ID absorption doublet in blue.

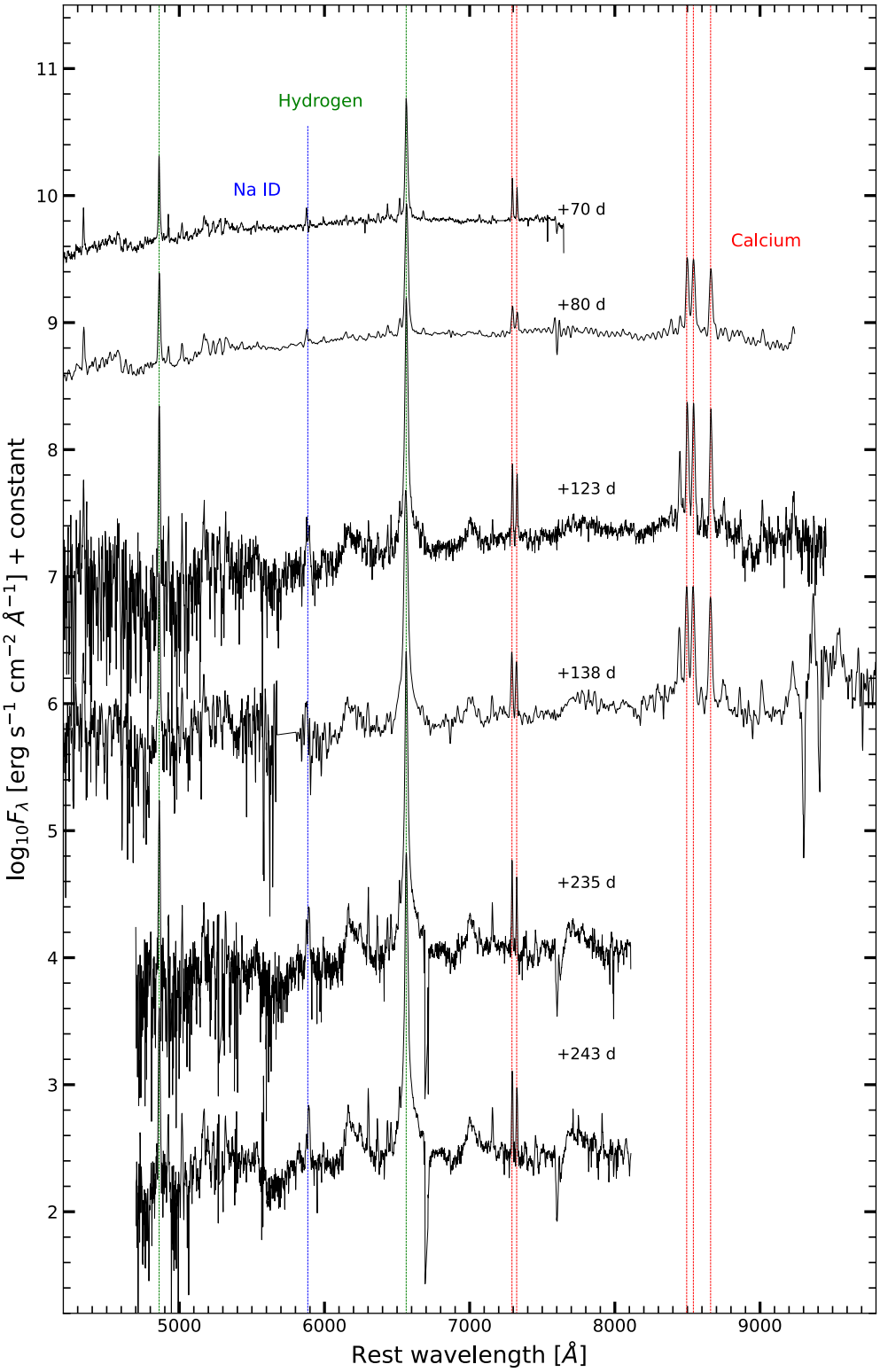

Figure 5.2: NGC 300 OT spectra during the late phases of its evolution. Lines are highlighted with the same colours as in Figure 5.1.

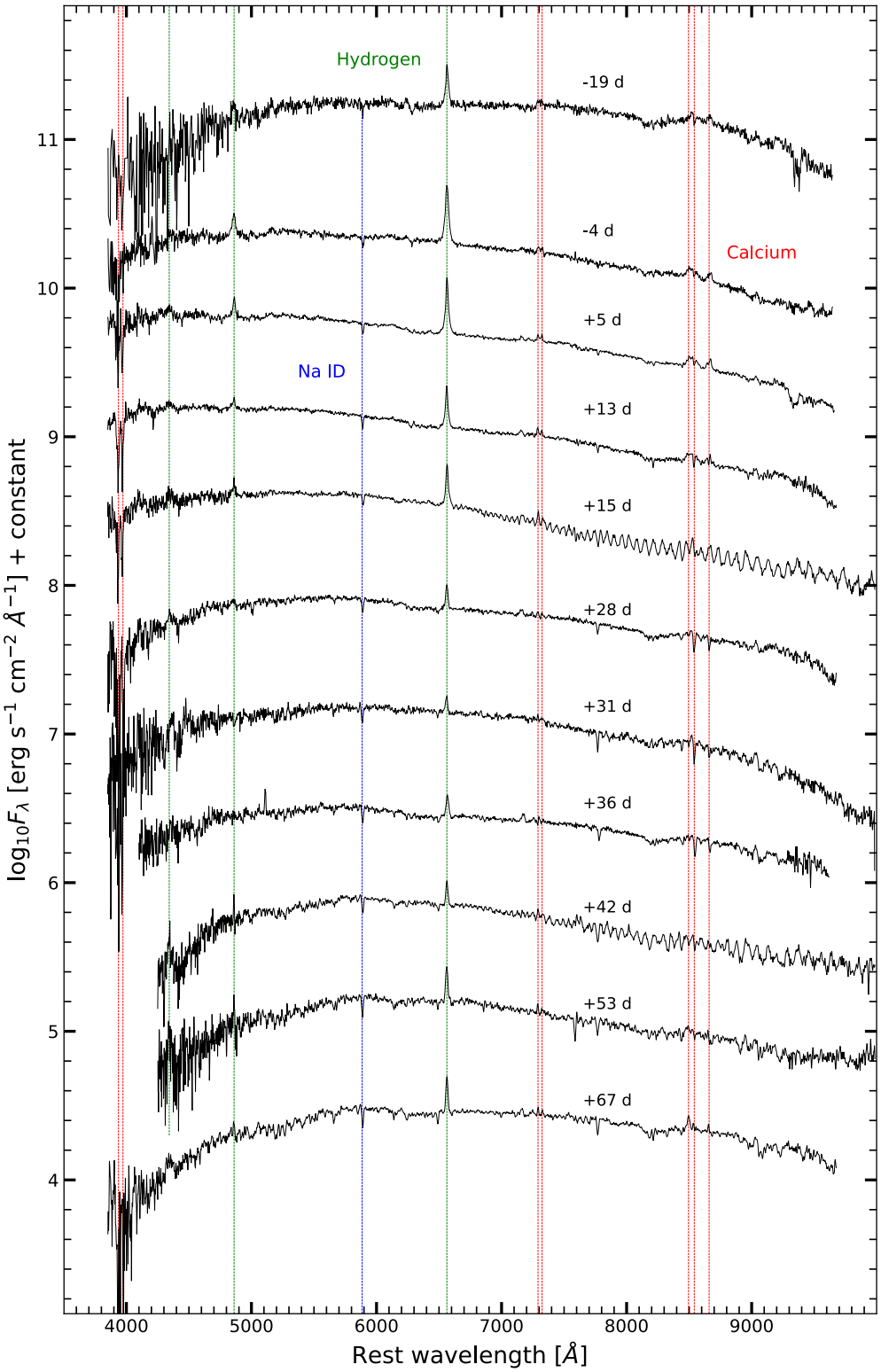

Figure 5.3: AT2019abn spectra collected in the early phases. Lines are highlighted with the same colours as in Figure 5.1.

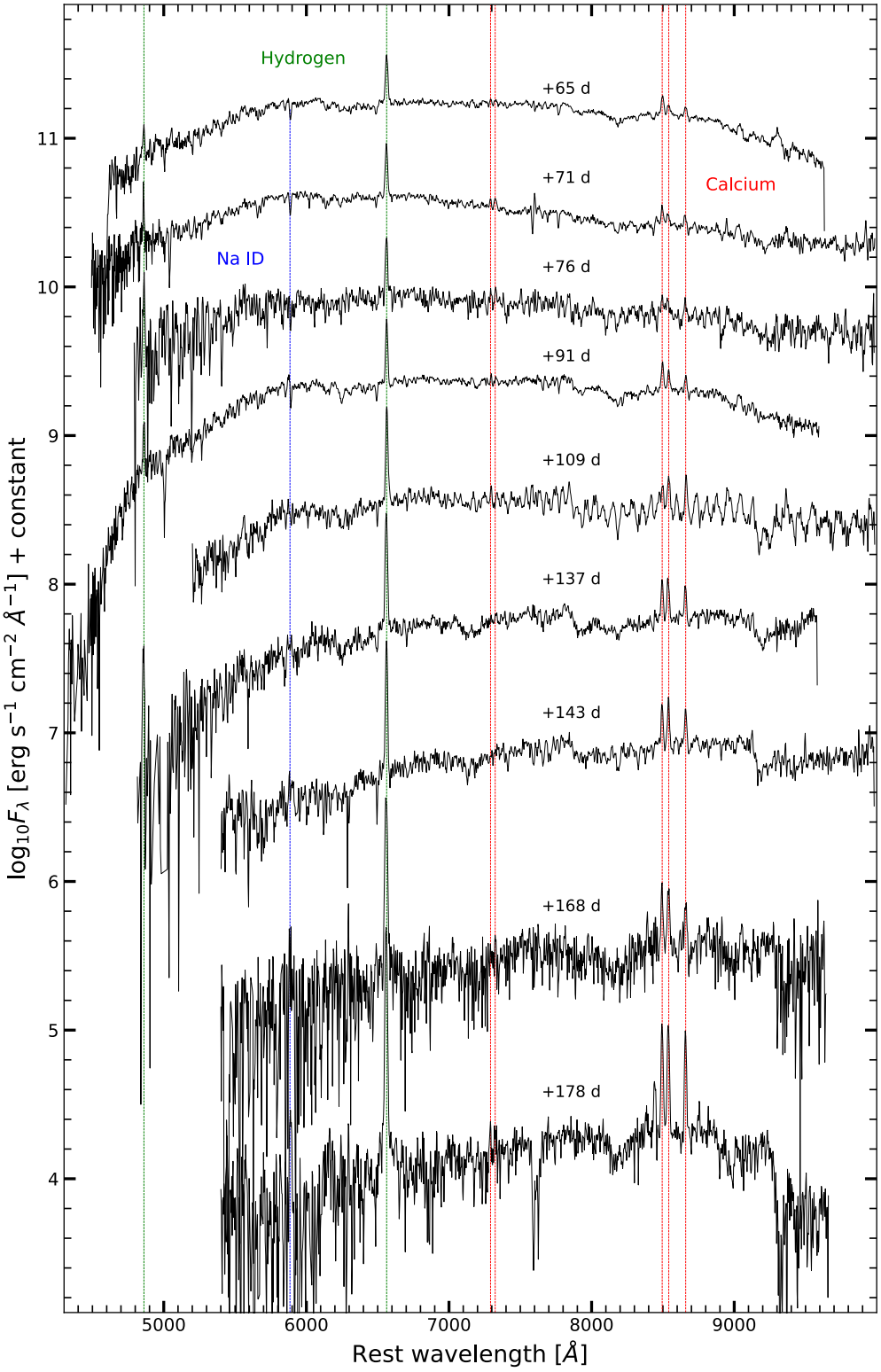

Figure 5.4: AT2019abn late spectra. Lines are highlighted with the same colours as in Figure 5.1.

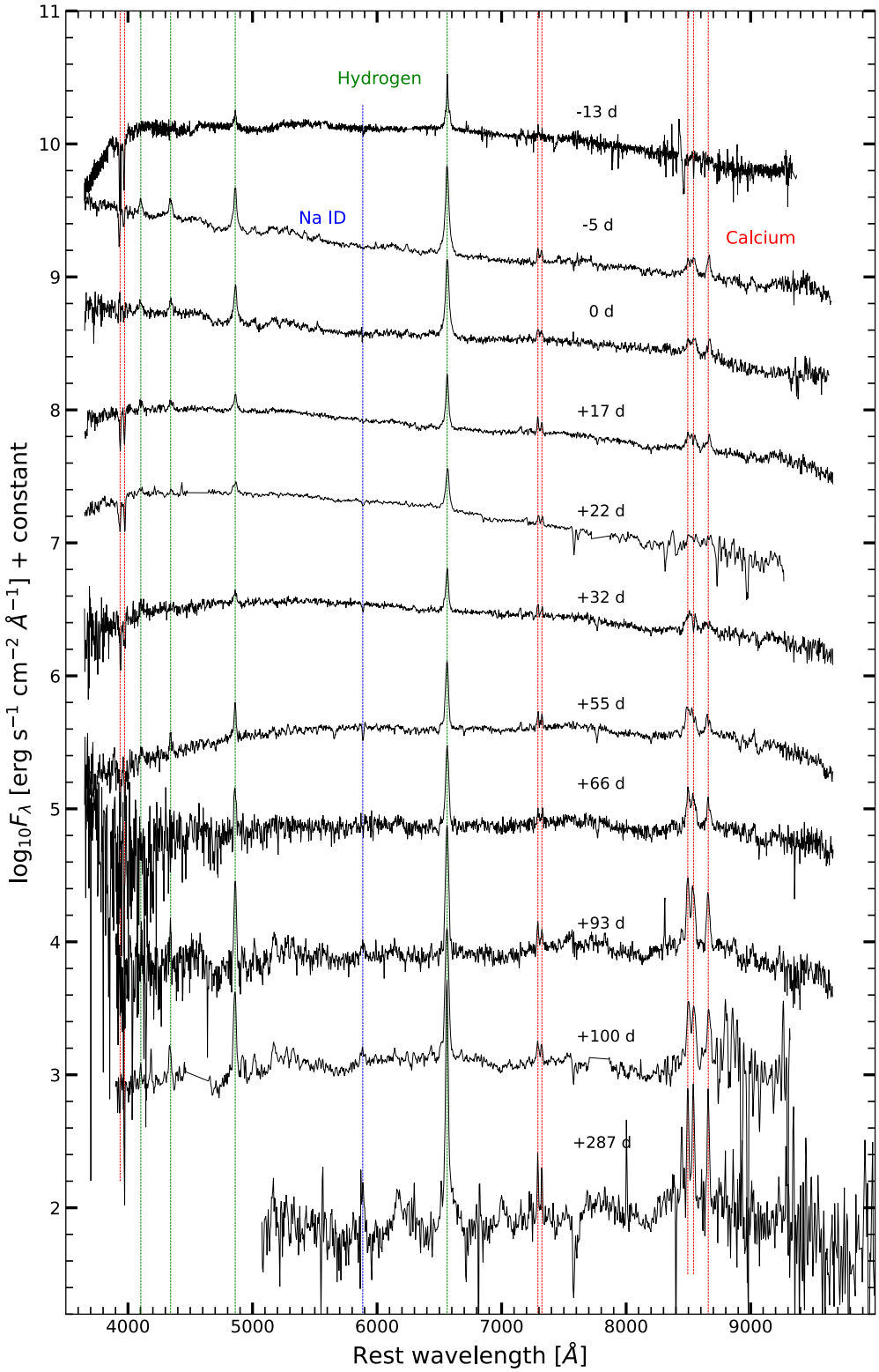

Figure 5.5: Full set of spectra of AT2019ahd. Lines are highlighted with the same colours as in Figure 5.1.

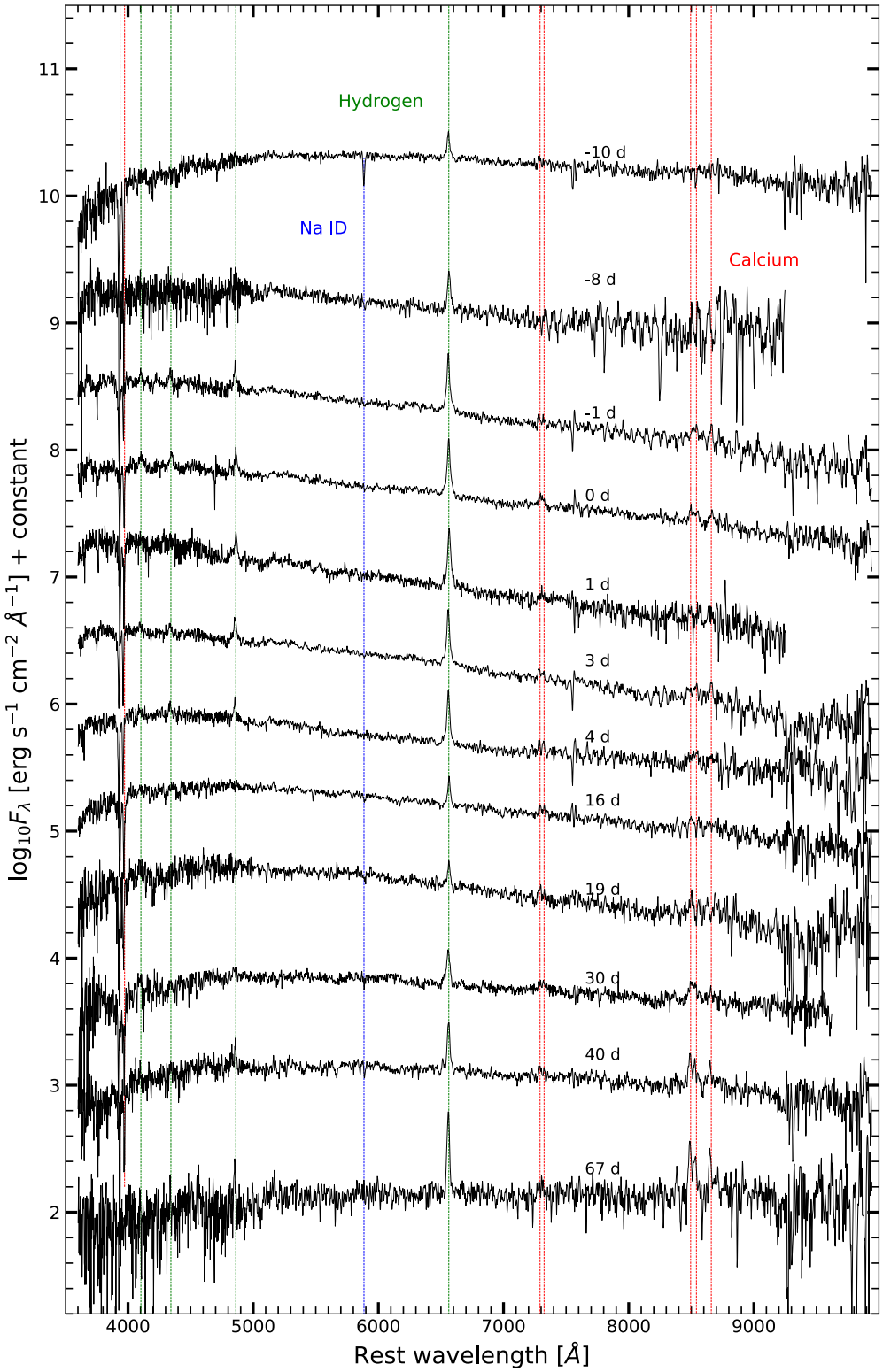

Figure 5.6: Spectra collected for AT2019udc. Lines are highlighted with the same colours as in Figure 5.1.

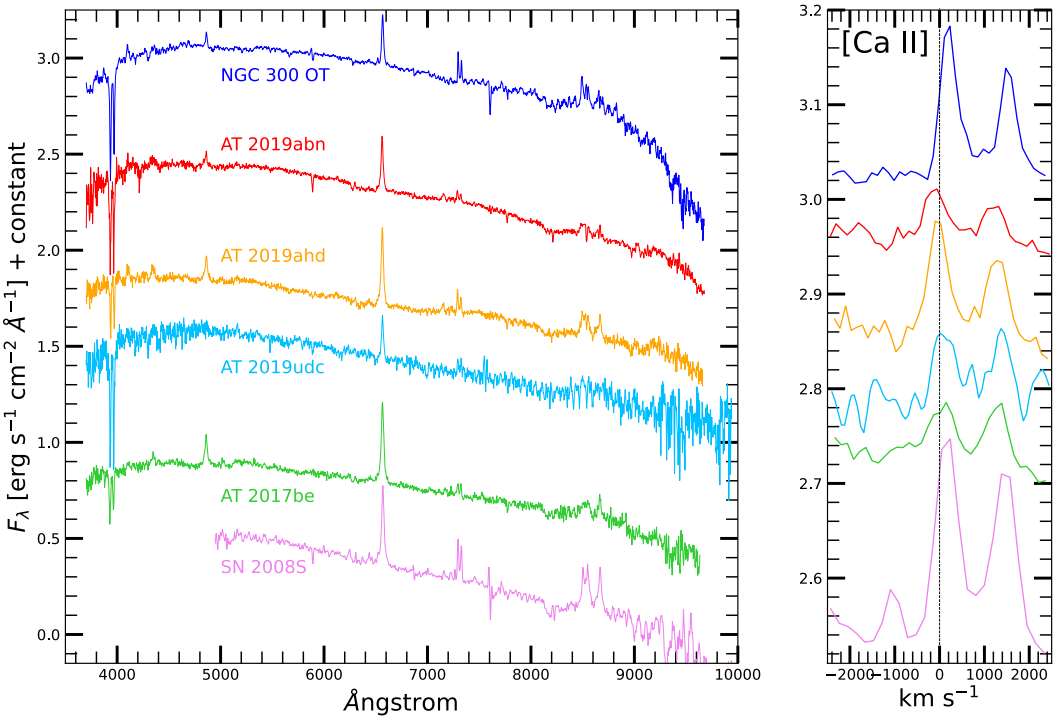

Figure 5.7: Comparison between early spectra of our sample of ILRTs, with the addition of AT 2017be and SN 2008S. On the right panel, a more detailed view of the [Ca II] forbidden doublet feature plotted in the velocity space.

In Figure 5.7 we display spectra of six ILRTs taken between two and three weeks after maximum. Beside the four targets in our sample, SN 2008S (Botticella et al. 2009) and AT 2017be (Cai et al. 2018) are also shown. There is a marked homogeneity in these spectra, which display the same features, and only differ in the strength that such features present: for instance, AT 2019udc is characterised by a strong Ca H& K absorption, but its Balmer lines (except the Hα) and Ca NIR triplet are not detectable at this epoch. The spectral features that define the ILRT class are most prominent in NGC 300 OT and SN 2008S, in particular the [Ca II] forbidden doublet, which is highlighted in the right panel of Figure 5.7. Curiously, not only SN 2008S and NGC 300 OT have the most noticeable [Ca II] lines, but they also appear to be redshifted compared to the rest wavelength position of $\lambda\lambda$7291,7323. A possible explanation for this phenomenon can be found in the shape of the lines, which will be discussed in Sect. 5.3.

5.1 Near Infrared Spectroscopy

Beside the optical spectra, we gathered a total of six NIR spectra of our targets. NIR spectra of AT 2019abn were collected during the early rise, immediately after discovery. The single spectrum available for AT 2019udc was taken in a more advanced phase, three weeks after peak luminosity. Finally, the two spectra of NGC 300 OT monitor the object at late phases, hundreds of days after maximum light. As displayed in Figure 5.8, AT 2019abn and AT 2019udc appear to be quite similar: a nearly featureless continuum, without strong emission or absorption lines superimposed (with the exception of the strong telluric features, which are challenging to completely remove). Conversely, in the spectra collected for NGC 300 OT it is possible to clearly identify several emission features.

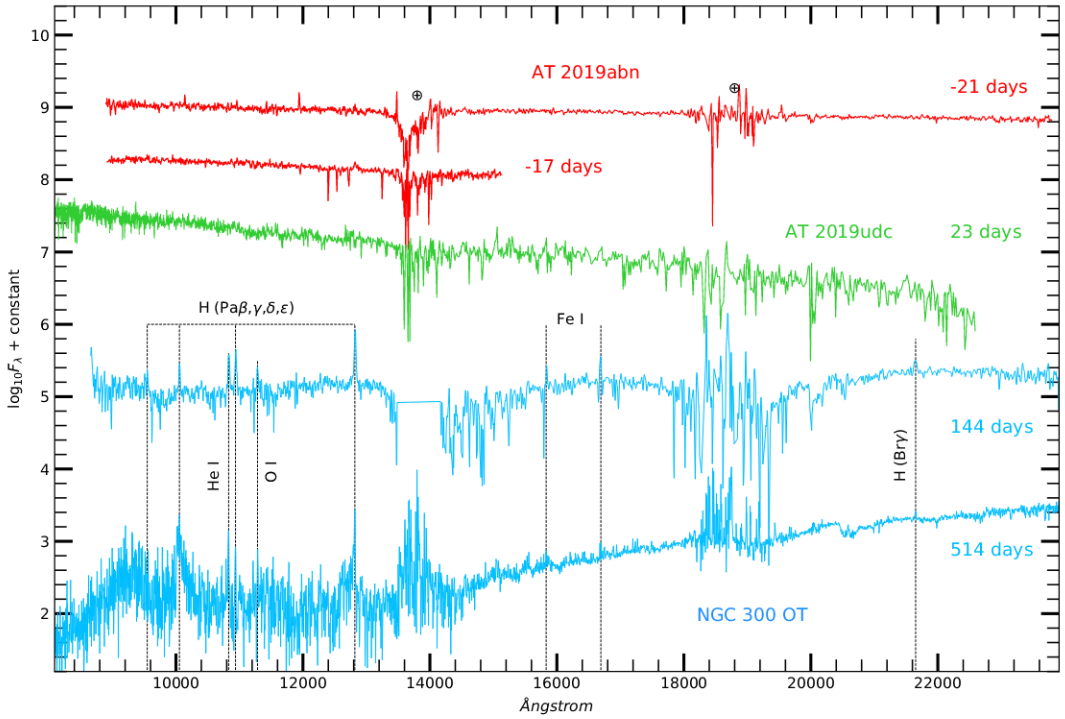

Figure 5.8: Sequence of NIR spectra collected for our sample of ILRTs. In red AT 2019abn, in green AT 2019udc and in blue NGC 300 OT. The most prominent emission lines are identified on the spectra of NGC 300 OT.

Most notably, hydrogen lines of the Paschen (Pa β,γ,δ,ϵ) and Brackett series (Br γ), He I (λ10830), O I (λ11285) and Fe I ($\lambda\lambda\lambda$15831,16679,16693). Indeed, all these atomic species are also detected in the optical spectra. The absence of emission lines in the spectra of AT 2019abn and AT 2019udc may simply be a consequence of the early phase at which they were collected.

5.2 Lines parameters

We estimate the main parameters of the spectral lines through the `SPLOT` task in `IRAF`, in particular by fitting a Lorentzian profile to obtain the FWHM and emitted flux. The percentage error associated to this process can be estimated to be ~20%. The measured FWHM is corrected for the resolution of the instrument (w = $\sqrt{FWHM^2 - resolution^2}$) and then converted into a FWHM velocity in order to recover the speed at which gas is moving at the photosphere. The line flux measured through `SPLOT` is corrected for the distance of the transient (reported in Chapter 4) to obtain the luminosity of the line over time.

The luminosity evolution of Hα, the Ca NIR triplet, the [Ca II] doublet and the Na ID absorption feature is shown in Figure 5.9. Firstly, it is interesting to notice the Hα and Ca NIR triplet luminosity evolution is not monotonic: after an early peak, the luminosity declines sharply over the course of few weeks. A minimum is then reached, and subsequently the lines start to strengthen again forming a sort of broad second peak, this time over a longer period. This peculiar behaviour is clearly observed for AT 2019abn, AT 2019ahd and AT 2019udc, and it was tentatively attributed to CSM interaction by Cai et al. (2018). For NGC 300 OT only the second broad peak is clearly visible, because we could

not sample the first phases of the transient evolution since the object was behind the Sun. This similar behaviour between Hα and the Ca NIR triplet suggests that they originate in the same environment and are produced by material undergoing the same physical processes.

On the other hand, the luminosity of the [Ca II] forbidden doublet does not present a clear second peak, with the flux declining rather steadily after the initial peak for all the objects in the sample (perhaps with the exception of AT 2019abn). Indeed, this observation is in agreement with the formation of the [Ca II] doublet in a low density environment, far from the dense CSM where Hα and Ca NIR triplet lines are formed: if the rebrightening of these lines is indeed caused by CSM interaction, the [Ca II] forbidden doublet would be only marginally affected by this process, since the doublet forms at a large distance from the interaction location. Finally, the Na ID "luminosity" (in absorption) depends on the properties of both the dense CSM and the gas above the photosphere. Possibly for this reason, its behaviour presents a large variance within the sample. AT 2019udc shows a strong Na ID feature in the first days, becoming weaker and weaker during its evolution. On the contrary, AT 2019abn displays a weak Na ID absorption feature at the first phases, significantly increasing in strength in the following months. AT 2019ahd and NGC 300 OT present a similar behaviour, although scaled down by over one order of magnitude compared to AT 2019abn.

AT 2019abn, the brightest and longer lasting ILRT observed to date, also displays the brightest Hα and [Ca II] features among the sample, reaching 1.7×10^{39} erg s^{-1} and 10^{38} erg s^{-1} at peak luminosity, respectively. Conversely, NGC 300 OT is characterised by a weak Hα, over 4 times weaker than the Hα of AT 2019abn at the same phases. The Ca lines, both the NIR triplet and the forbidden doublet, present instead a remarkable homogeneity in luminosity within the sample, especially during the first 100 days. In later phases, NGC 300 OT fades more quickly than AT 2019abn and AT 2019ahd.

Measuring the FWHM velocity of the emission lines of ILRTs can be challenging: very narrow features such as the [Ca II] doublet are often unresolved in our spectra, and even resolved lines like Hβ can be too faint to be accurately fit with a Lorentzian profile. In Figure 5.10 we display the FWHM velocities inferred from the Hα line for our sample of ILRTs. Analysing the Hα line has the significant advantage that the line is bright at all epochs, therefore allowing for an accurate Lorentzian fit. Furthermore, especially at early times, the Hα line is resolved in most spectra, and it is not blended with other features (as happens for the Ca NIR triplet), making it the perfect feature to study for comparing the behaviour of different objects.

During the early phases, when the luminosity is still rising, the FWHM velocity of Hα progressively increases: Interestingly, all the ILRTs in our sample reach a maximum FWHM velocity of ~800 km s^{-1} around the time of their luminosity peak. This behaviour is particularly well monitored for AT 2019udc, which shows an increase in FWHM velocity from 500 to 800 km s^{-1} in just 10 days. Furthermore, AT 2019udc displays the sharpest decline in FWHM velocity after maximum, decreasing by over 200 km s^{-1} in just few days: indeed, AT 2019udc is also characterised by the fastest photometric evolution among ILRTs (see Chapter 4). On the other hand, AT 2019ahd presents the slowest evolution in FWHM velocity within our sample, hovering above 600 km s^{-1} even 100 days after the explosion epoch. AT 2019abn and NGC 300 OT show a surprisingly similar evolution in FWHM velocity, despite being separated by a sizable luminosity gap. It is important to stress that these velocities are not representative of the ejecta speed, but are reflecting the properties of the CSM where the line is produced: as the photosphere moves, gas moving at different speeds will be responsible of the formation of the line, reflecting the evolution in FWHM velocity shown in Figure 5.10.

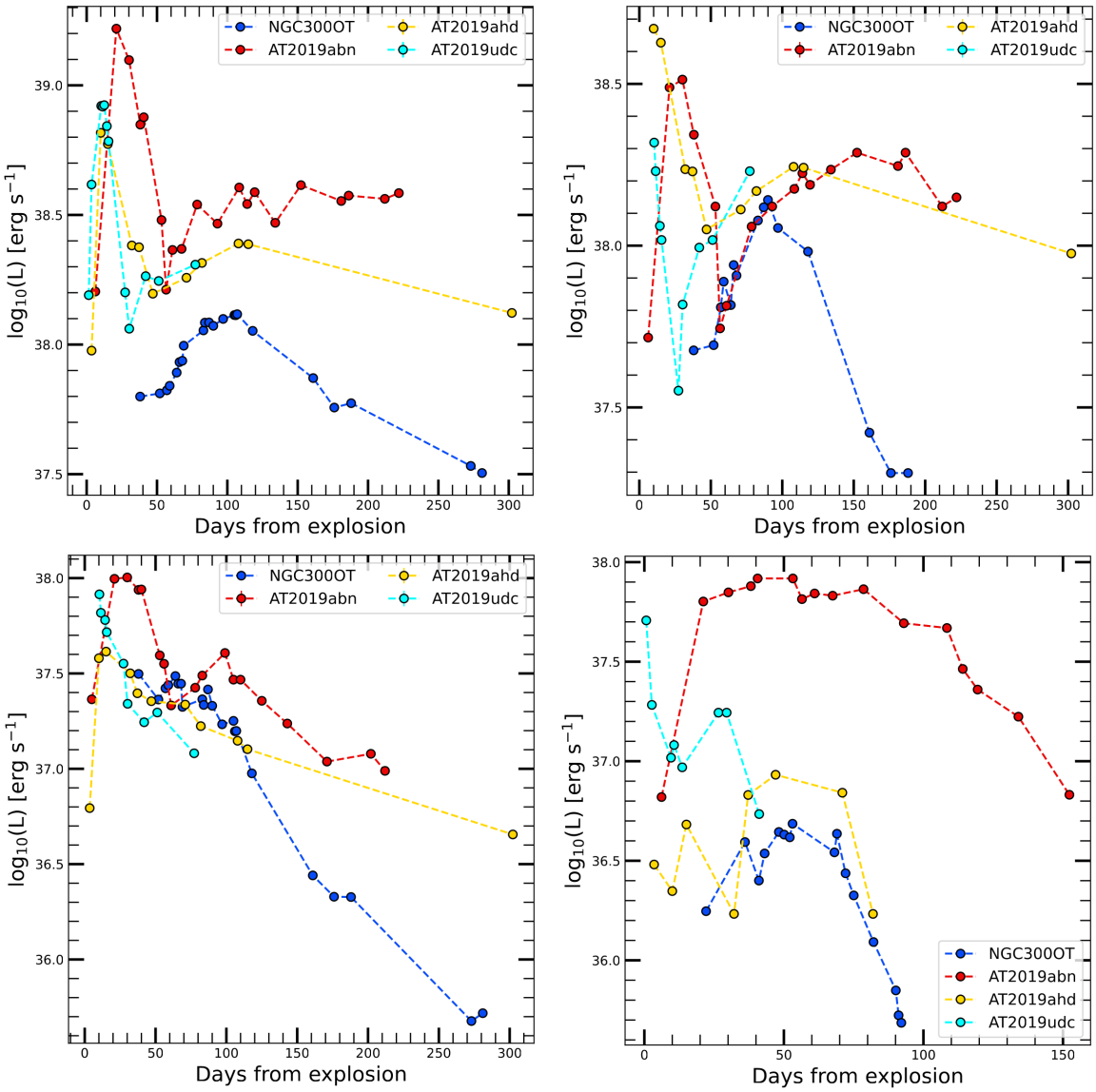

Figure 5.9: Top left panel: evolution Hα luminosity for a sample of ILRTs. Top right: evolution of the Ca NIR triplet luminosity. Bottom left panel: luminosity evolution of the [Ca II] forbidden doublet. Bottom right: evolution of the luminosity absorbed by the Na ID.

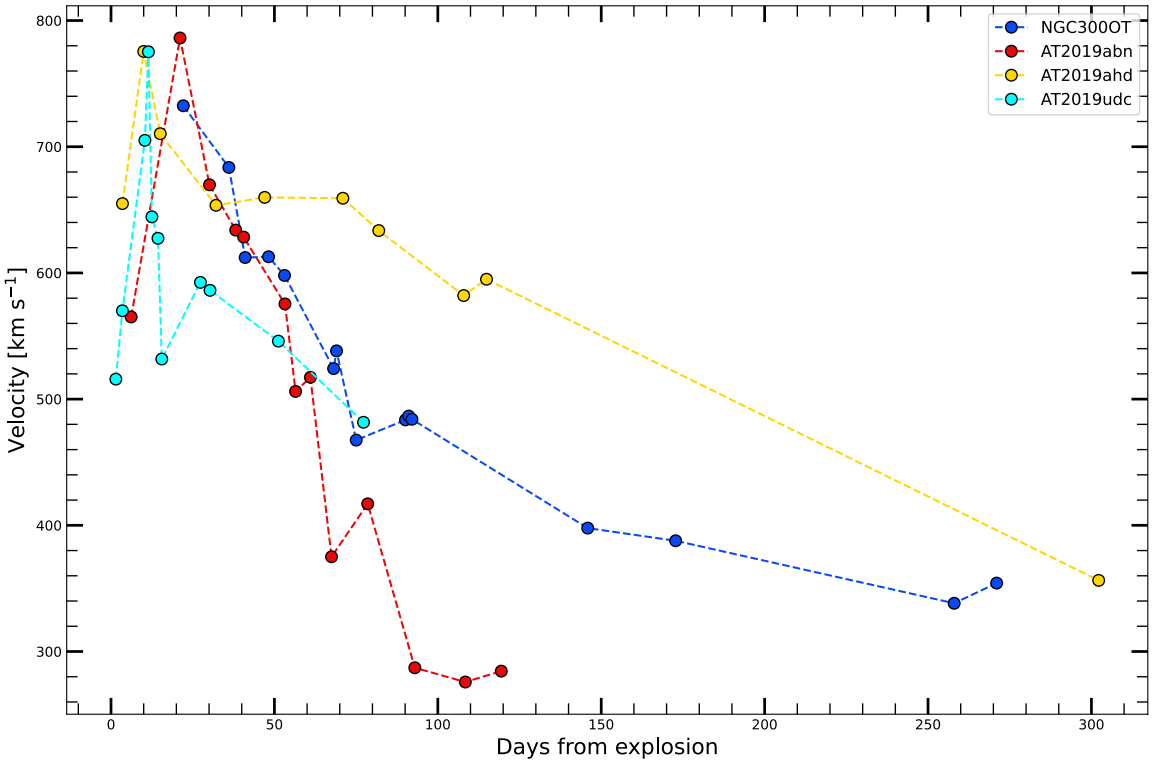

Figure 5.10: Evolution of the Hα FWHM velocity for our sample of ILRTs.

Line	λ_0 (Å)	λ_m (Å)	FWHM (Å)	F (10^{-15} erg s^{-1}cm^{-2})
Hα	6562.8	6562.5	11.4	228
Hβ	4861.3	4860.3	5.7	52.9
Hγ	4340.5	4339.4	5.3	17.0
Hδ	4101.7	4100.7	4.5	13.5
[Ca II]	7291.47	7292.0	2.4	21.7
[Ca II]	7323.89	7323.4	2.5	15.6
Ca II H&K	3933.66	3933.9	4.2	-
Ca II H&K	3968.47	3969.0	3.8	-
Fe II (40)	6516.05	6516.7	5.7	15.2
Fe II (40)	6432.65	6432.8	4.4	7.6
Fe II (40)	6369.45	6368.7	9.1	7.9
Fe II (42)	5169.0	5170.7	8.8	8.2
Fe II (42)	5018.4	5018.6	8.3	10.1
Fe II (42)	4923.9	4925.2	6.4	5.0
Fe II (46)	5991.38	5992.5	6.0	7.5
Fe II (46)	6084.11	6084.4	6.4	3.4
He I	5875.62	5874.9	4.3	10.3
He I	7065.19	7065.7	5.5	5.7
O I	7771.94	7770.5	7.8	-
O I	6363.78	6363.9	1.2	1.6
O I	6300.3	6300.4	1.3	0.8
Na I	5889.9	5889.5	0.25	-
Na I	5895.9	5895.5	0.24	-

Table 5.5: Line identification performed on the UVES spectrum taken on 2008 July 02. The spectrum was redshift corrected for z=0.00048.

5.3 The high resolution spectrum of NGC 300 OT

NGC 300 OT is the closest ILRT ever observed. Thanks to its proximity of the host galaxy, it was possible to obtain a high resolution optical spectrum of the transient on 2008-07-02 with the Very Large Telescope (VLT) equipped with UVES, yielding a resolution of just few tenths of Ångstrom. In Figure 5.11 is shown the identification of the main spectral lines in this high resolution spectrum. The most prominent features are reported in Table 5.5, together with the observed central wavelength, the FWHM and the flux estimated from a Lorentzian fit. Apart from the H, Ca and Na lines, easily recognizable in the low resolution spectra and discussed in the previous section, NGC 300 OT displays a number of metal lines, in particular Fe I and Fe II, although also some Sc lines can be found. Additionally, also O ($\lambda\lambda\lambda$ 6300,6364,7772) and He ($\lambda\lambda$ 5876,7065) are identified. All these features are narrow (FWHM < 10 Å), therefore originating within the dense CSM. We did not find clear evidence of Li lines, in particular at 6708 Å, which have been linked to SAGB stars of masses ~8 $M_\odot$ (e.g. Mucciarelli et al. 2019).

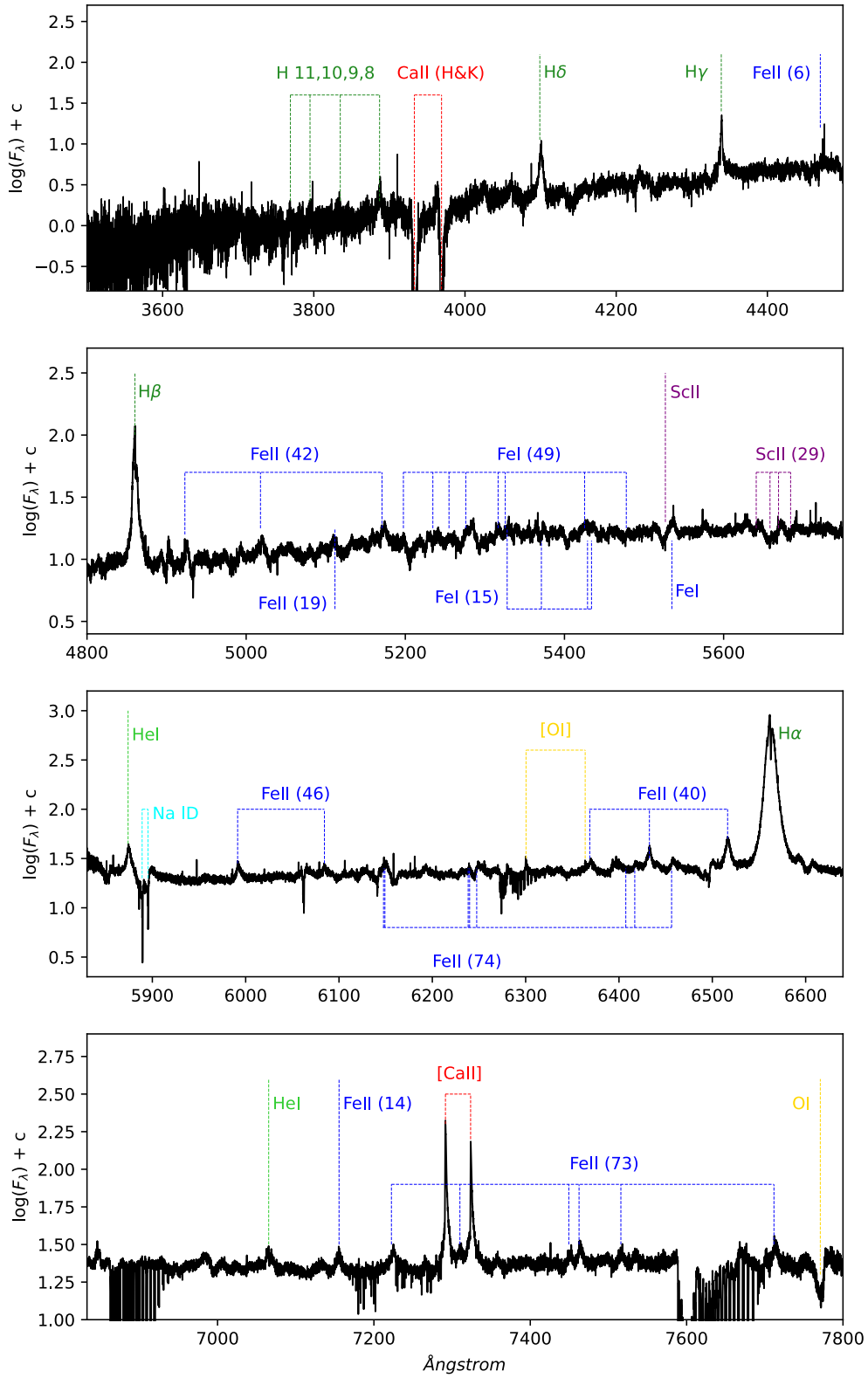

Figure 5.11: Identification of spectral lines for NGC 300 OT, performed on the high resolution UVES spectrum taken on 2008-07-02. Lines originating from different elements are highlighted in different colours.

Thanks to the high resolution, it is possible to accurately compare the expansion velocities associated with different emission features. The broadest feature observed at this epoch is the Hα emission line, with an expansion velocity measured from its FWHM of 520 km s^{-1}. The Ca NIR line λ 8498 is marginally narrower, with a FWHM velocity of 420 km s^{-1}: the fact that Hα and Ca NIR velocities are compatible corroborates the scenario outlined in the previous section, where both these lines are generated in the same environment. The [Ca II] forbidden doublet, instead, is characterised by a FWHM of just 100 km s^{-1}, compatible with an origin in a less dense and slow moving gas.

Finally, the shape of the lines also carries relevant information on the geometry of the emitting region. In Figure 5.12 are shown the profiles of Hα, one Ca NIR line (λ8498), one [Ca II] line (λ 7291) and the Na ID absorption doublet. The Hα line shows a composite profile: superimposed to the emission lines there are two narrow absorption components. The most prominent absorption component has a FWHM of 40 km s^{-1} is close to the Hα rest wavelength position, only 30 km s^{-1} redward of the rest wavelength. The second absorption component is even narrower, with a FWHM close to spectral resolution, and it is situated 130 km s^{-1} blueward of the emission peak. As pointed out by Berger et al. (2009), these absorption components are compatible with the presence of dense CSM shells surrounding the transient and moving at different speeds: in particular, one shell should be slowly expanding, accounting for the redshifted absorption component while the other shell would be infalling, leading to the formation of the blueshifted absorption line.

Once again, the Ca NIR line (λ8498) displays a similar behaviour, showing a prominent absorption component with a FWHM of 40 km s^{-1} situated within 10 km s^{-1} of the rest wavelength position of this line, once again showing that Hα and the Ca NIR lines form in the same region. The slight mismatch between the position of this prominent absorption feature in the Hα and Ca NIR lines can be caused by the wavelength calibration, since the difference is few tenths of Å. The second narrow absorption component is not detected in the Ca II λ8498 line, likely due to a lower signal to noise ratio compared to the Hα. It is worth noticing that an alternative scenario to explain the complex profile of the H and Ca NIR triplet lines is either a bipolar outflow or a rotating disk, as suggested by Humphreys et al. (2011).

On the other hand, the [Ca II] doublet presents a very different line profile: while no absorption feature is superimposed to the emission component, the line is asymmetric, with the blue wing almost completely missing. Berger et al. (2009) tentatively attribute this behaviour to self absorption, in a scenario where the [Ca II] doublet originates in an low density, inflowing gas. However, Humphreys et al. (2011) point out that self absorption is basically impossible for a forbidden transition such as [Ca II]: the peculiar line profile is likely formed through electron scattering in an expanding envelope, which gives rise to the extensive red wing observed. Lastly, in the Na ID absorption profile it is possible to differentiate three components: two narrow, unresolved component associated with the Milky Way and the host galaxy (which are unchanging with time, according to Berger et al. (2009)) and a broader absorption (FWHM $\sim$300 km s^{-1}) originating from the gas expanding around the transient.

5.4 Broad features in the late time spectra

Late time spectra of ILRTs display some particularly intriguing features. Both in the case of NGC 300 OT and AT 2019ahd, along with the narrow lines already described, two broad features start appearing. In Figure 5.13 we show the late time spectra of NGC 300 OT and AT 2019ahd superimposed, in order to highlight the similarities between the two, in particular regarding these broad lines. First of all, the line profile appears to be symmetric, with no clear evidence of extended red wing like

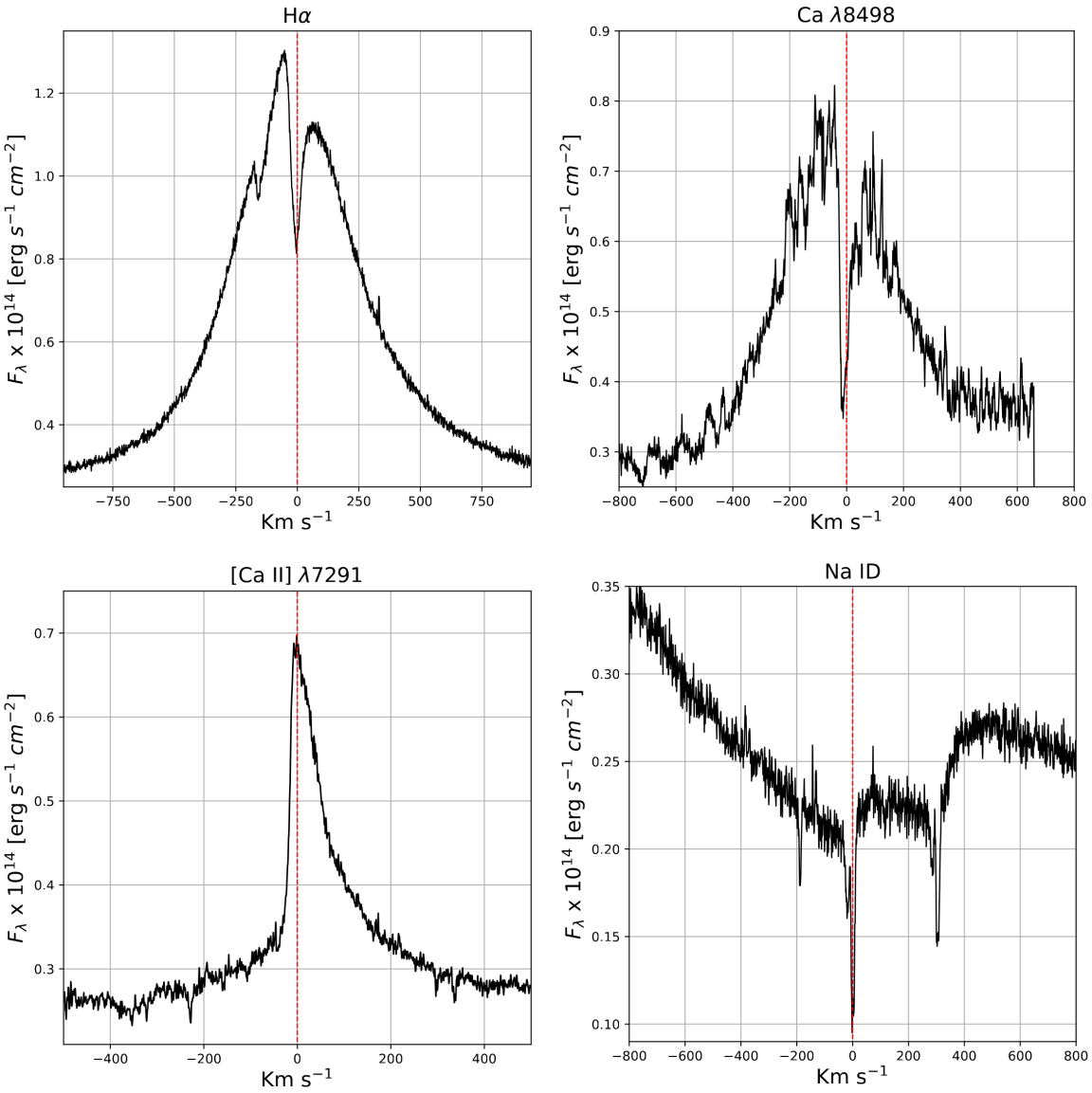

Figure 5.12: Details of the most interesting features in the high resolution spectrum of NGC 300 OT. In particular, Hα, Ca NIR, [Ca II] and Na ID.

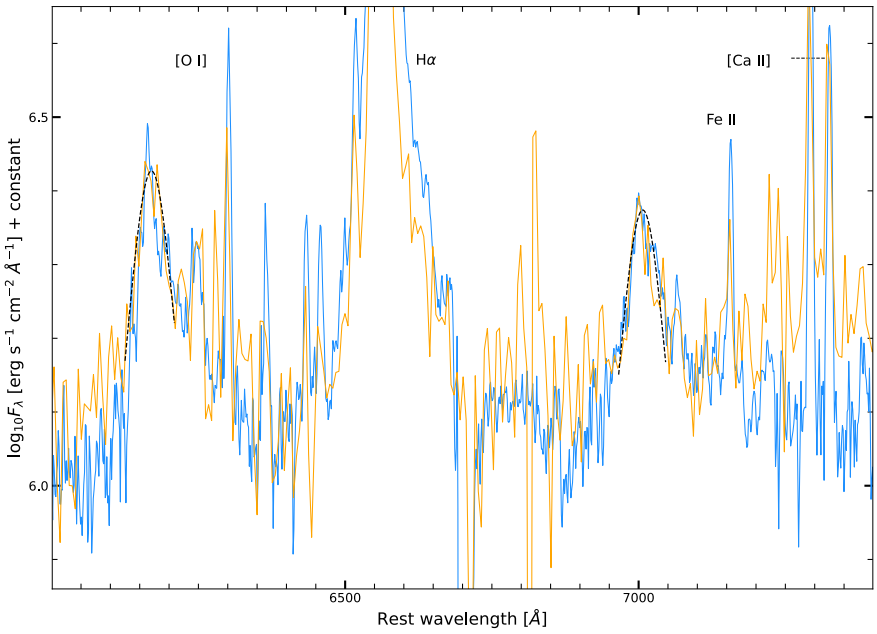

Figure 5.13: Late time spectra of NGC 300 OT (blue) and AT 2019ahd (orange). A shift has been applied to superimpose the two spectra and highlight the similarities between them, in particular the broad features described in the text.

those observed for [Ca II] lines at earlier epochs. It is more challenging to exclude the presence of absorption components, as in the H and Ca NIR lines, given the rather low signal to noise ratio. Performing a Lorentzian fit on these features yield a FWHM of ∼2100 km s^{-1} for the bluer one, situated at λ6168, while the second line is located at λ7002 and is characterised by a FWHM of ∼1900 km s^{-1}. Given the rather symmetric distribution of these broad features around the Hα line, it could be tempting to associate them with Hα emissions within two jets, one strongly redshifted and one strongly blueshifted. However, since the features appear to be almost identical in both AT 2019ahd and NGC 300 OT, it is extremely unlikely to have observed two jets oriented exactly in the same direction relative to the Earth, and therefore we are inclined to exclude this scenario. Most notably, such broad lines were never detected in any spectrum of ILRTs: are we finally seeing the products of the nucleosynthesis emerging from the slow moving CSM that was obscuring our line of sight? If so, this would be a strong evidence supporting the ECSN origin of ILRTs. However, these broad features are challenging to identify, as no other nebular line commonly found in SNe seems to match the observed position of the lines (e.g. Wheeler & Benetti 2000). Few atomic species can account for both the emission lines: according to the tabulated values reported by Moore 1945, a candidate could be Ni I $\lambda\lambda$6177, 7002, which would corroborate the scenario in which explosive nucleosynthesis took place during the ILRT events.

As a simple test, we qualitatively compare the late time spectra of NGC 300 OT and AT 2019abn with the models of nebular spectra presented by Jerkstrand et al. (2017). These models aim to reproduce the late time spectra of core collapse SNe arising from low mass stars (9 M$_\odot$). The first synthetic

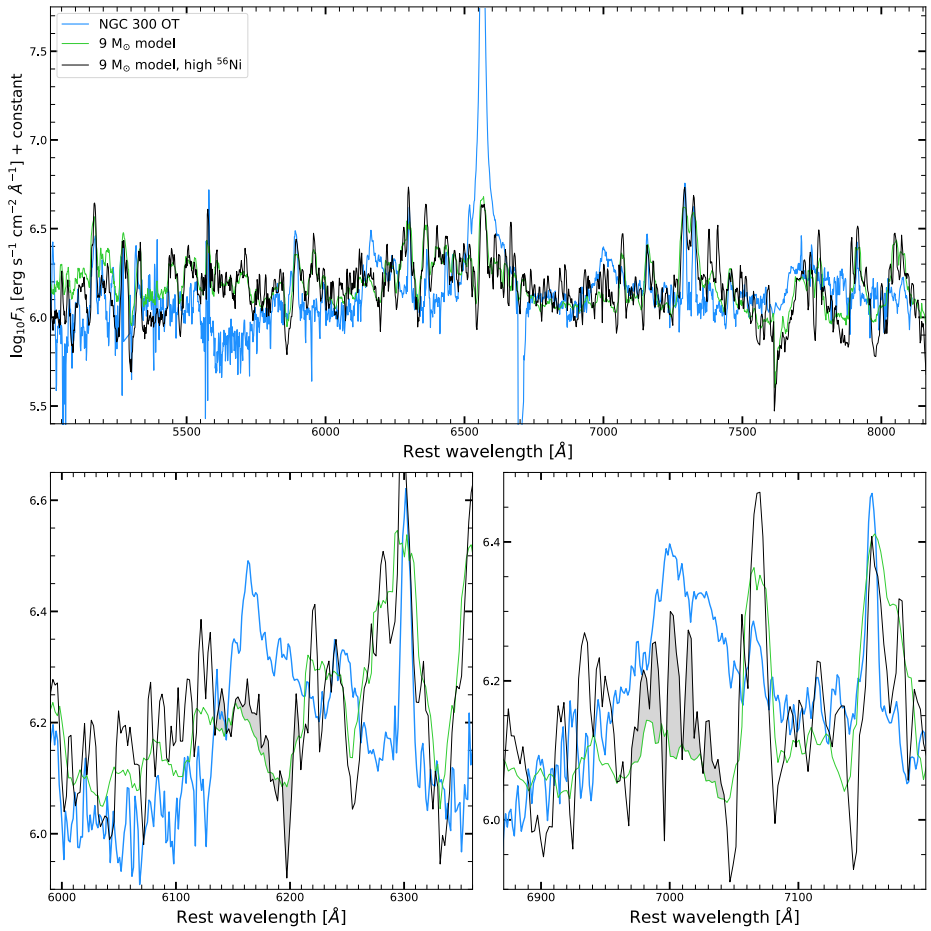

Figure 5.14: Late time spectra of NGC 300 OT compared with models of nebular spectra taken from Jerkstrand et al. (2017). In the bottom panels is shown a zoom on the region where broad lines are observed in ILRTs. The shaded gray area highlights the difference in the two models.

nebular spectrum we consider is relative to a star with solar composition, 300 days after explosion. Interestingly, a high Ni content is expected to be an indicator of an ECSN event (Wanajo et al. 2009): for this reason we consider a second synthetic spectrum, at the same evolutionary stage, in which the ratio Ni/Fe is increased to 30 times the solar value. The comparison between our ILRTs and these two models is presented in Figures 5.14 and 5.15. The synthetic spectra have been scaled down for clarity, so that the emission of the [Ca II] forbidden doublet is matched to the [Ca II] doublet of the ILRTs. A first, straightforward observation is that the Hα line is much more prominent in ILRTs compared to the expectations for a classical core collapse SN. Apart from this glaring difference, several lines are overall well reproduced by the models, most notably Fe ($\lambda\lambda$5169,7155), O (λ6300), He (λ7065) as well as the Ca NIR triplet (visible in AT 2019ahd). Jerkstrand et al. (2017) report that the Ni rich model is characterised by rather strong [Ni II] ($\lambda\lambda\lambda$6667,7378,7412) lines, but we do not find clear evidence of such features in our spectra. However, in the lower panels of Figures 5.14 and 5.15 we display the broad lines found in ILRTs together with the synthetic nebular spectra. In the region of the feature peaking at ~7002 Å, there is a remarkable contribution in flux that is present only in the Ni rich spectrum, supporting the hypothesis that these broad lines are linked with Ni emission. Not only

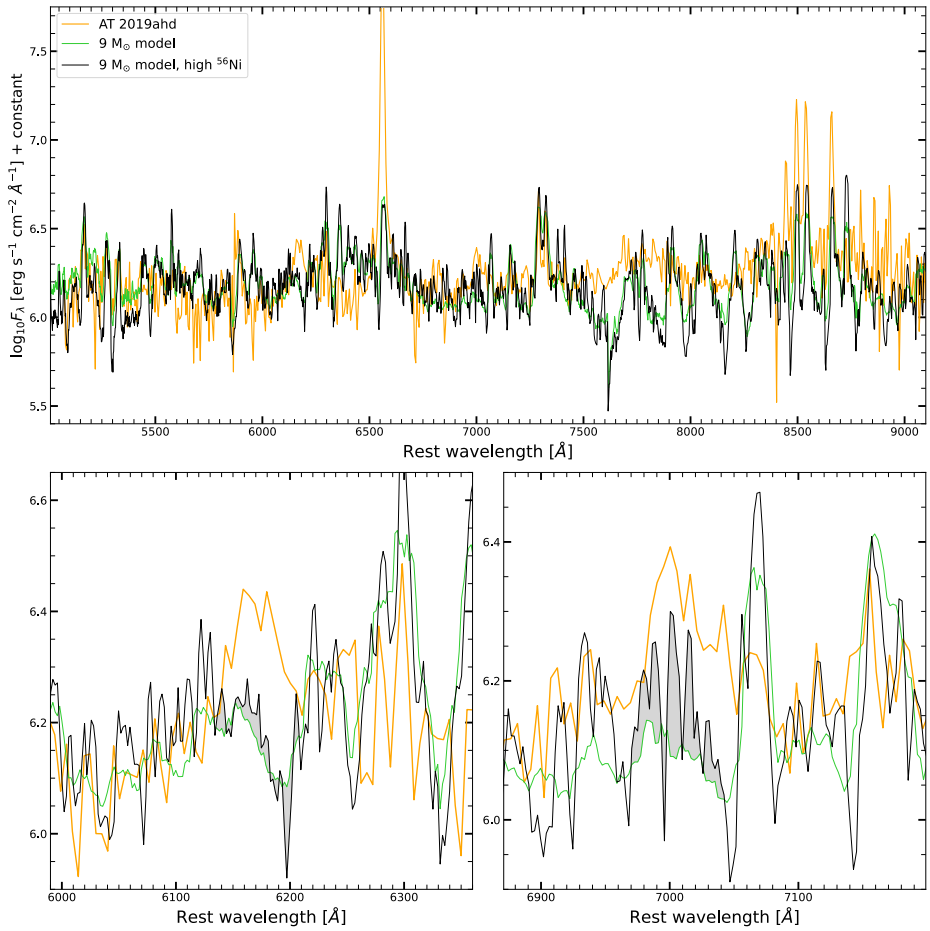

Figure 5.15: Similar to Figure 5.14, here is shown the comparison between the late time spectrum of AT 2019ahd and the nebular models presented by Jerkstrand et al. (2017).

the presence of fast ejecta would strongly supports the terminal explosion scenario, but the unusual Ni lines provide an intriguing argument in favour of an ECSN event, rather than a Fe core collapse. Unluckily, the same evidence is not found for the other broad feature, at 6168 λ: however, more detailed models for ECSN nebular spectra could provide additional insight on these observations.

Chapter 6

Intermediate Luminosity Red Transients: from the progenitor to the late time evolution

As mentioned in the previous chapters, ILRTs are suitable ECSN candidates, both for their photometric and spectroscopic properties (e.g. Botticella et al. 2009; Pastorello & Fraser 2019; Cai et al. 2021). In this context it is particularly interesting to study the progenitor systems that produce ILRTs, since ECSN are expected to arise from the explosion of a Super AGB star (SAGB) (Leung et al. 2019). Unfortunately, only a handful of progenitor systems of ILRTs have been discovered so far.

6.1 Known Progenitors of ILRTs

NGC 300 OT (Bond et al. 2009) and SN 2008S (Botticella et al. 2009) are prototypes of ILRTs, and the discovery of their progenitors has greatly contributed to the identification and characterisation of this class of transients. Thanks to infrared archival images obtained with SPITZER, it is possible to study the SED of their progenitor stars (Figure 6.1, left panel). Black body fits yield similar results: they are cold (340 - 440 K) and extended sources (few 10^2 AU) (Thompson et al. 2009). The luminosity obtained through the SED analysis is only marginally lower than the luminosity predicted for SAGB stars (10^5 $L_\odot$, Poelarends et al. 2008). The masses estimated for the two progenitors are between 5 and 11 $M_\odot$ for NGC 300 OT and ~10 $M_\odot$ (Thompson et al. 2009), which is once again compatible with the expectations for SAGB star. Interestingly, the Hubble Space Telescope archival images can only provide upper limits for the flux of the progenitors in the optical domain. Furthermore, no source is detected even in the deepest pre-outburst NIR observations from ground based telescopes (Botticella et al. 2009). All of this indicates a large extinction along the line of sight. The most reasonable scenario to explain such feature is that these stars are deeply enshrouded in dust, and therefore quite luminous in the mid to far infrared domain, but basically undetectable at optical and NIR wavelengths.

A third ILRT, AT 2019abn, was discovered in M51, close enough to allow for the successful discovery of its progenitor (Jencson et al. 2019). The results are alike the ones presented so far: complete non-detections in the optical domain paired with a luminous infrared source, with magnitude and colour (Spitzer [3.6]-[4.5]) similar to those measured for NGC 300 OT and SN 2008S. The only notable difference is that a long lasting pre-outburst monitoring campaign of AT 2019abn with the Spitzer

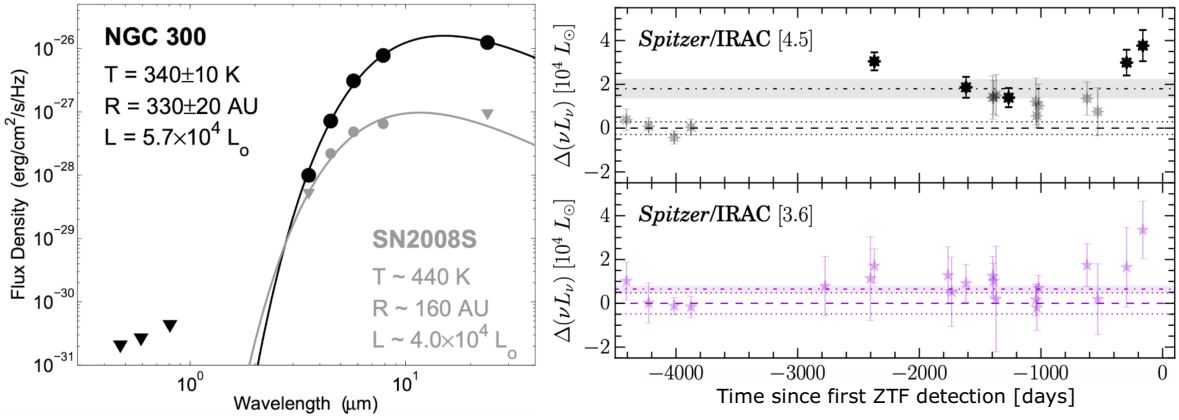

Figure 6.1: Left panel: SED of the progenitors of NGC 300 OT and SN 2008S (Figure from Berger et al. 2009). Right panel: infrared variability of AT 2019abn (Figure from Jencson et al. 2019)

Space telescope found a variability in the [4.5] band with a 3σ significance: a brightening in the source can be seen few hundreds days before the discovery of the optical transient in the right panel of Figure 6.1.

While direct detection of the progenitor in archival images would always be ideal, there are other methods to indirectly constrain the properties of the progenitor of an ILRT. A relevant example is given by Gogarten et al. (2009), who analyses the stars in the region surrounding NGC 300 OT through stellar population modelling, in order to recover the age of the population and therefore a reasonable mass range for the progenitor of the transient. Gogarten et al. (2009) estimate that the progenitor of NGC 300 OT should have a mass between 12 $M_\odot$ (the turnoff mass) and 25 $M_\odot$ (the largest mass found for that population). While there appears to be tension between this result and the measure provided by Thompson et al. (2009) through a direct method, Szczygieł et al. (2012) argue that the mass range provided by Gogarten et al. (2009) is better interpreted as an upper limit, since it would still be possible to have a transient (event a SN) originating from a ~10 $M_\odot$ star even in a region hosting ~20 $M_\odot$ stars. Indeed, Szczygieł et al. (2012) studied the environment of another ILRT, SN 2002bu, for which no direct progenitor detection is available. In this case, the stellar neighbourhood of SN 2002bu did not contain stars more massive than 10 $M_\odot$, suggesting a progenitor mass between 5 and 10 $M_\odot$, in line with the expectations for a SAGB star.

6.2 Dust geometry and composition

Dust plays an important role in ILRTs: first, obscuring the progenitor star in the optical domain, then altering the SED of the transient during the first months of evolution (Cai et al. 2021) and finally providing the bulk of the luminosity at late phases, as discussed in the following section. Botticella et al. (2009) suggest that the dust enshrouding SN 2008S is divided in two dust shells, separated by a cavity (Figure 6.2, left panel). Together, the two dust shells are responsible for the absorption of visible light. However, the explosion of the star sublimates the inner dust shell, causing the transient to become visible even in the optical bands. The outer dust shell, only marginally affected by the explosion, causes the emergence of a NIR excess in the SED of the transient, even at early phases. When analysing the evolution of NGC 300 OT, Prieto et al. (2009) find a similar situation. From the SED of NGC 300 OT at 93 days after discovery, three different black body components can be

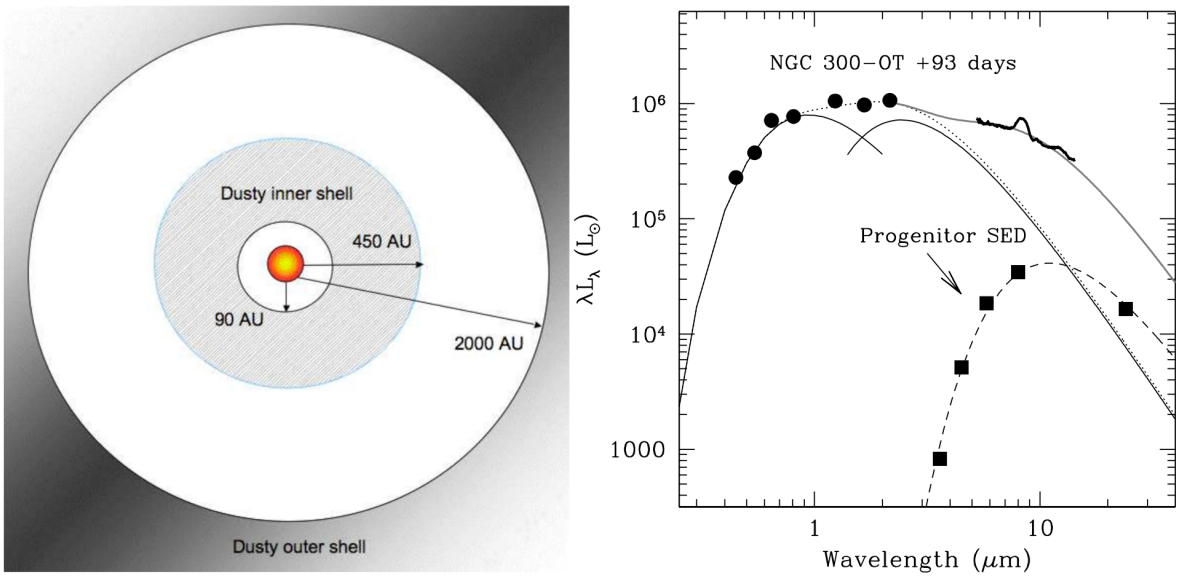

Figure 6.2: Left panel: geometry of the dust surrounding the progenitor star inferred for SN 2008S (Figure from Botticella et al. 2009). Right panel: multiple SED components during the evolution of NGC 300 OT (Figure from Prieto et al. 2009).

identified (Figure 6.2 right panel). The hottest black body, with a temperature T_1 = 3890 K and radius R_1 = 11 AU, is associated to the photosphere within the dense CSM. A second component, traced by the NIR JHK bands, is characterised by a temperature T_2 = 1510 K and radius R_2 = 67 AU, and could be associated with newly formed dust or surviving dust that was shock heated. Finally, the continuum of the Spitzer spectrum obtained by Prieto et al. (2009) traces the existence of a third black body in the MIR, with parameters T_3 = 485 K and radius R_3 = 515 AU. This cool component, far away from the emitting source, could indeed arise from the emission of an outer dust shell which survived the explosion of the star, as suggested by Botticella et al. (2009). Finally, Prieto et al. (2009) point out that in the MIR Spitzer spectrum of NGC 300 OT there are two emission features, at 8 and 12 μm, which are likely linked with carbon. This observation favours a carbon-rich dust composition over an oxygen-rich dust, which would instead be characterised by amorphous silicate emission at 9.7 μm.

6.3 Late time dust evolution in NGC 300 OT

Ohsawa et al. (2010) monitor the evolution of NGC 300 OT in the IR domain (2-5 μm) at 398 and 582 days, finding that the hot dust component progressively cools down to 810 K and ultimately to 680 K. The wavelength range inspected did not provide any information on the cool, pre-existing dust component, which by that time could only contribute to ∼1% of the observed flux in the NIR. Ohsawa et al. (2010) also set lower limits for the optical depth of the dust at 2.4 μm: $\tau_\nu > 12$ at 398 days and $\tau_\nu > 6$ at 582 days, effectively stating that the dust remains optically thick even at very late phases. In this condition, the lower limit to the mass of emitting dust is estimated to be $\sim 10^{-5}$ $M_\odot$.

Thanks to the WISE data collected on 2010-06-17 in the filters W1, W2, W3 and W4, we are able to expand the analysis on the late time evolution of the dust in NGC 300 OT, 761 days after discovery. The late time K band coverage with SOFI, over 853 days after discovery, allowed us to

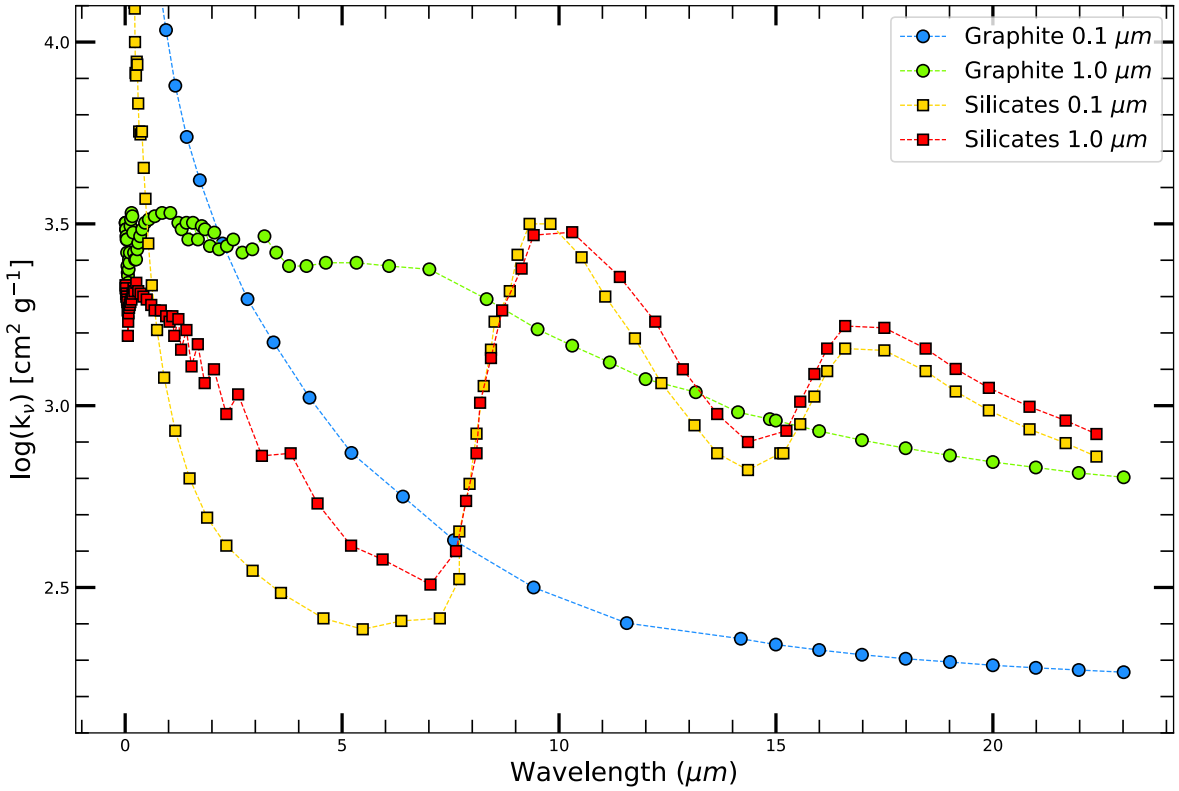

Figure 6.3: Opacity of dust with different composition (graphite and silicates) and different grain size (0.1 and 1 μm)

linearly extrapolate the K-band flux at 761 days in order to have a more detailed SED of the transient. Following in the footsteps of Ohsawa et al. (2010) we fit our flux measures through the same procedure detailed in chapter 4. However, instead of a simple Planck function, the fitting function used is $f(\nu) \propto (1 - e^{-\tau_\nu})B_\nu(T_d)$, where τ_ν is the optical depth, B_ν is the Planck function and T_d is the dust temperature. It is relevant to point out that this model is isothermal, while a cloud of optically thick dust would present a temperature gradient, so this is already an approximation.

To better differentiate the properties of the dust, in particular the size of the dust grains and their chemical composition, we perform the fits using four different sets of opacity k_ν values, tabulated by Fox et al. (2010). Two sets are opacity values for graphite dust, with grain size of 0.1 and 1 μm respectively, while the other two sets of opacity have the same grain size, but present a silicate composition. Since the values presented by Fox et al. (2010) only cover up to 13 μm while our data reach 22 μm (thanks to the W4 channel), we have to extrapolate the behaviour of k_ν in that region. For the graphite dust we follow the prescription from Draine (2016), using a λ^{-2} scaling of the opacity at longer wavelengths. The silicate dust is instead characterised by an additional bump in opacity at around 20 μm: to reproduce it, we mimic the opacity behaviour reported by Voshchinnikov et al. (2017). As displayed in Figure 6.3, graphite dust with grain size of 0.1 μm have a remarkably lower opacity compared to graphite dust with grain size of 1.0 μm. Silicate dust stands out because of the two clear "bumps" in opacity, which contrasts with the smooth behaviour of the graphite opacity.

In Figure 6.4 are reported the results of the fitting procedure for the different dust compositions and

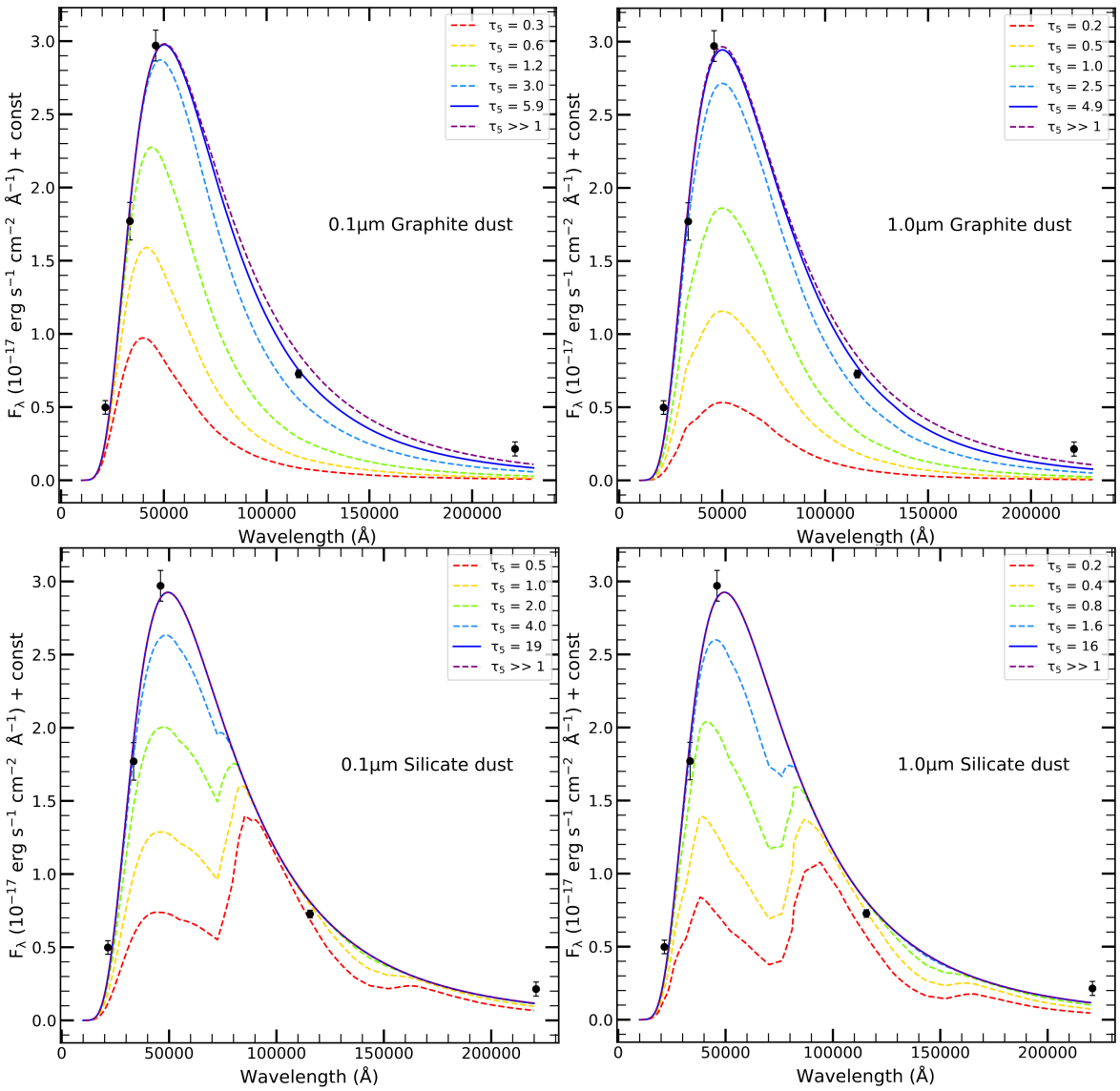

Figure 6.4: Fits to the late time SED of NGC 300 OT. In the different panels are reported the fits for the different dust compositions and grain sizes. The best fit to the data is shown as a solid blue line, while the dashed lines show the effect of changes in the optical depth while keeping temperature and radius of the source fixed.

Model	L [10^{38} erg s^{-1}]	T [K]	R [AU]	τ_5	M_d [10^{-4} $M_\odot$]
Graphite 0.1 μm	9.1 (1.4)	576 (5)	228 (18)	5.9 (0.7)	1.9 (0.5)
Graphite 1.0 μm	9.1 (1.4)	579 (5)	225 (18)	4.9 (0.6)	0.45 (0.11)
Silicate 0.1 μm	9.2 (1.4)	585 (6)	222 (17)	19.4 (2.4)	19 (5)
Silicate 1.0 μm	9.2 (1.4)	586 (6)	222 (18)	16.5 (2.0)	9.5 (2.4)

Table 6.1: Parameters obtained for the different models. Errors are reported in brackets.

grain sizes considered. The parameters obtained are reported in Table 6.1. The parameters of the best fitting black body show little variability, when considering different dust particles sizes. The fit is instead more sensitive to the chemical composition of the dust, i.e. whether we adopt graphite dust or silicate dust. The dust temperature obtained for graphite is slightly lower than the temperature obtained for silicate dust, with a radius that is consequently larger. All things considered, the differences between the black body parameters of silicate dust and graphite dust are negligible: the real difference lies in the optical depth. We consider the optical depth at 5 μm (τ_5), to perform a comparison between the different models. As shown by the dotted lines in Figure 6.4, at low optical depth (τ_5 <1), the models deviate significantly from the Planck function: silicate dust shows a double peaked emission, while the emission of graphite dust with grains of 1.0 μm is characterised by a "shoulder" at around 3.2 μm. Graphite dust with grains of 0.1 μm do not show such clear features, but the shape of the SED is systematically too narrow to properly fit the observed data in the optically thin case. Indeed, all the best fit yield optically thick dust at all wavelengths considered. However, in the case of silicate dust the best fits are obtained with an optical depth of τ_5=19.4 for 0.1 μm grains and τ_5=16.5 for 1.0 μm grains, basically returning to a Planck function. On the other hand, the optical depths inferred for graphite dust are τ_5=5.9 for 0.1 μm grains and τ_5=4.9 for 1.0 μm grains: optically thick, but still distinguishable from a Planck function. Notice that none of the models can accurately fit the point at 22 μm, possibly because an infrared excess due to the cold dust component that drastically cooled down since its detection by Prieto et al. (2009), two years before. Performing a χ^2 test we determine that the best fitting model is the one envisioning graphite dust with 0.1 μm grains, in agreement with the expectations to have carbon-rich dust in NGC 300 OT. Finally, through our measures of optical depth it is possible to obtain an estimate of the dust mass using the equation (as done by Hosseinzadeh et al. 2022):

$$M_{dust} = \frac{4\pi R_{dust}^2 \tau_\nu}{3k_\nu}. \tag{6.1}$$

Here we assume a constant density profile in the dust distribution, which is of course an additional approximation. For the optical depth obtained in our best model, we infer a dust mass of 1.9×10^{-4} $M_\odot$, although this value can grow or shrink by one order of magnitude depending on the composition of the dust and grain size (see Table 6.1). We remark that this fitting procedure was performed on the "warm" dust, which was identified by Prieto et al. (2009) at a temperature of 1510 K, and has cooled down to ∼580 K. Meanwhile, also the dust that survived the explosion has cooled down, and the peak of its emission has shifted outside the MIR domain.

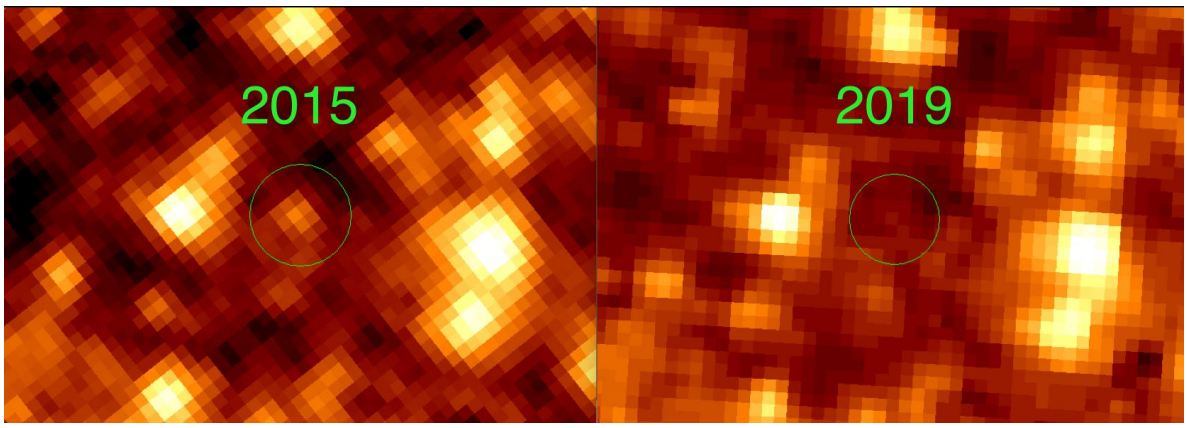

Figure 6.5: Comparison between Spitzer images (channel [4.5]) of NGC 300 OT. While in 2015 the transient was still detected, in 2019 it faded below the detection threshold.

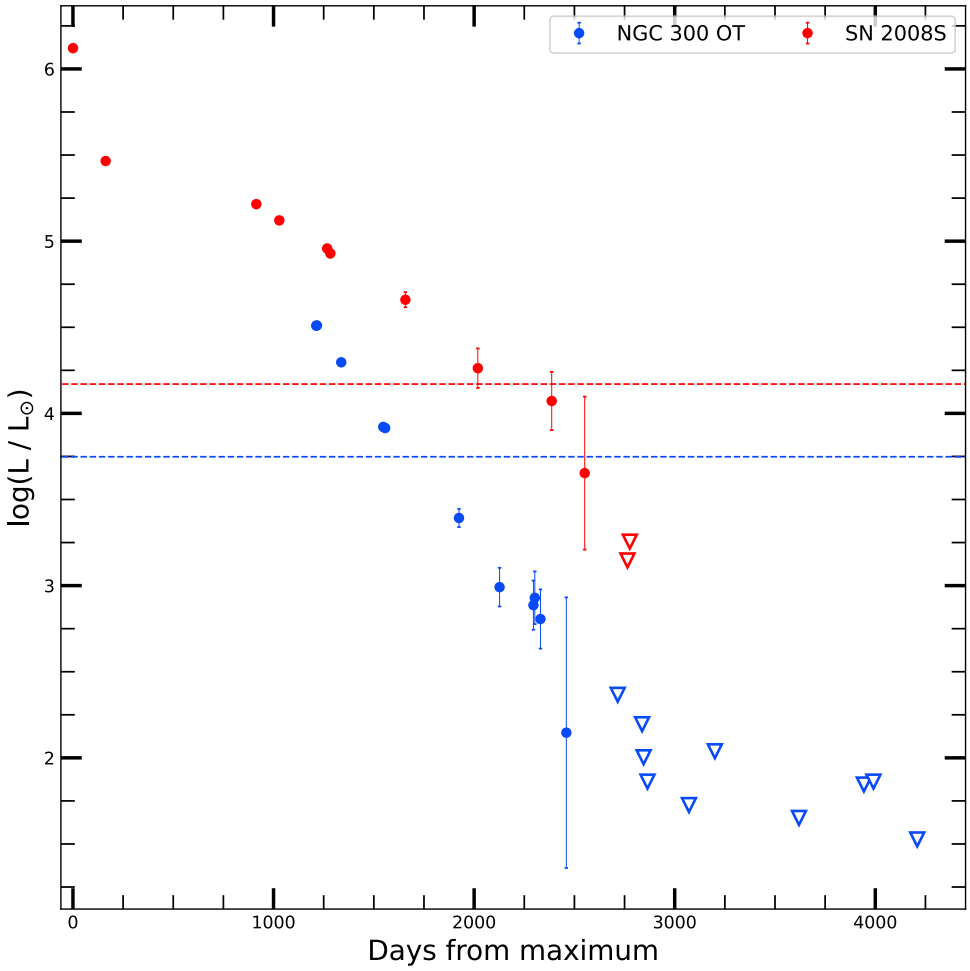

Figure 6.6: Late time decline of NGC 300 OT and SN 2008S monitored with the [4.5] channel of Spitzer. This is an updated version of the figure shown in Adams et al. (2016).

6.4 Photometric decline below the original progenitor luminosity

In Chapter 1 we already mentioned the work of Adams et al. (2016), where NGC 300 OT and SN 2008S are followed with the Spitzer telescope at late phases, until they both fade below their progenitor luminosity. This study is key for understanding ILRTs, since it strongly favours a scenario in which the progenitor star did not survive the event, pointing towards a SN explosion rather than a non-terminal stellar outburst. By inspecting the Spitzer images collected collected between 2015-10-20 and 2019-11-24 with the [4.5] channel, we find that NGC 300 OT has faded even below the detection threshold (Figure 6.5). We perform aperture photometry to provide upper limits to the flux of the transient at these epochs. Adams et al. (2016) point out that when providing upper limits for SN 2008S, to avoid contamination by nearby sources it was necessary to use a rather small aperture of 1.2 arcsec and a 1.2-2.4 arcsec sky annulus to estimate the background. We use exactly the same apertures to measure the upper flux limit for NGC 300 OT, also applying an aperture correction of 1.2322, as prescribed by the Spitzer documentation for a similar configuration. The last data point obtained by Adams et al. (2016) for NGC 300 OT at 4.5 μm is a detection at 5 ± 1 μJy. In Figure 6.6 we report the various upper limits measured from late 2015 to late 2019. In particular, the upper limit measured on 2019-11-24 is 1.2 μJy, definitely proving that the transient has not stopped fading since 2015, pointing towards a SN origin for ILRTs.

Chapter 7

Summary and Conclusions

Throughout this work, I analysed the photometric and spectroscopic data collected for six faint transients potentially linked to the ECSN scenario. In the first part of my thesis, I focused on SNe 2020cxd and 2021aai, two Low Luminosity SNe IIP. In the following chapters, I outlined the characteristics of four Intermediate Luminosity Red Transients, namely AT 2019abn, AT 2019ahd, AT 2019udc and NGC 300 OT.

Regarding SN 2020cxd and 2021aai, they both display an extended period of constant luminosity (in the case of 2021aai the plateau duration is among the longest recorded), hence earning the "IIP" classification. Their rather faint bolometric luminosity paired with the low expansion velocity of their ejecta and small mass of ^{56}Ni synthesised place them among the Low Luminosity subclass for SNe IIP. SN 2020cxd is particularly faint, showing a ^{56}Ni of just 1.8×10^{-3} $M_{\odot}$, while SN 2021aai ejected 1.4×10^{-2} $M_{\odot}$ of ^{56}Ni, almost one order of magnitude more. While they both belong to the LL SNe subclass, SN 2020cxd is exceptionally faint, while SN 2021aai lies on the brighter edge of the subclass, a transitional object that bridges the gap between faint and standard SNe IIP. Hydrodynamical modelling performed on the light curve, temperature and velocity of SN 2021aai yield an ejected mass of 15.5 $M_{\odot}$, well in line with the expectations for SNe IIP to arise from RSG stars. In the case of SN 2020cxd, instead, the hydrodynamical modelling points towards a lower progenitor mass, between 8.9 and 10.4 $M_{\odot}$. This mass range does not exclude a RSG progenitor, but it is also compatible with a SAGB star, making SN 2020cxd a reasonable ECSN candidate.

The data sets presented for the four ILRTs in our sample are remarkably monitored with a high cadence across the electromagnetic spectrum, spanning from the ultraviolet to the MIR domain, especially for AT 2019abn and NGC 300 OT. The NIR excess in the SED typical of ILRTs, tentatively associated with dust formation, is clearly detected in three out of four cases. The only exception is AT 2019udc, characterised by the fastest evolution timescale among the ILRTs observed. At late phases, the contributions in the NIR and MIR domains to the bolometric light curve cause a decline shallower than the luminosity decline supported by the ^{56}Ni decay, hinting at the presence of an additional powering mechanism. A simple model is presented, with the goal to estimate the parameters characterising the transient in the context of a SN explosion. For AT 2019abn, 2019ahd and NGC 300 OT, the low masses ejected and low velocity of the material seems to be compatible with a weak explosion from a low mass star. AT 2019udc appears to be an outlier in this sense, since its very fast decline rate lead to inferring high velocity and remarkably low ejected mass.

Late time spectra of NGC 300 OT and AT 2019ahd display broad features never observed in any ILRT, possibly associated with the emission from fast Ni: this would be another decisive step in the direction of proving the explosive nature of ILRTs, which are often associated with ECSN. The terminal nature of ILRTs transient is further supported by the analysis I performed on Spitzer images taken 11 years after the discovery of NGC 300 OT, which shows that the transient has kept fading without leaving a clear remnant behind. If the association between ILRTs and ECSN is successfully confirmed, it would be an impressive leap forward for our understanding of stellar evolution.

Acknowledgements

I would like to express my most sincere gratitude to Andrea Pastorello for his guidance, and for being an inspiration both as a scientist and as a person.

I am deeply grateful to the whole Padova-Asiago Supernova Group (in particular Enrico Cappellaro, Stefano Benetti, Massimo Turatto, Nancy Elias-Rosa, Lina Tomasella, Leonardo Tartaglia, Achille Fiore, Andrea Reguitti) for their help as well as their precious company.

I wholeheartedly thank my fellow PhD students, in particular Chiara Buttitta, Stefano Torniamenti, Nicolas Estrada, Vito Squicciarini and Irene Salmaso, for making this journey far less burdensome.

I would also like to extend my thanks to all the external collaborators which contributed to this work, in particular Morgan Fraser, Maria Letizia Pumo, Laura Greggio, Maria Teresa Botticella, Maximilian Stritzinger, Erkki Kankare, Michela Mapelli, Raffaele Gratton and Giovanni Carraro.

I could never thank my family enough for all the love and support they provided throughout all these years. Thank you Mom, Dad and Luca.

To my love, Nguyen Thi Ngoc Anh (or, to me, Anna): in the vastness of space and the immensity of time, it is a joy to share a planet and an epoch with you.

Finally, I acknowledge INAF for funding my PhD fellowship within the PhD School in Astronomy at the University of Padova, because also eating is important.

Chapter 8

Appendix: Photometric Data

Table 8.1: Photometric data in the Sloan filters collected for SN 2020cxd (AB mag).

Date	MJD	g	r	i	z	Instrument
2020/02/26	58905.58	17.80 0.10	17.57 0.10	17.64 0.10	–	LCO
2020/02/27	58906.46	17.77 0.02	17.57 0.03	17.65 0.03	–	LCO
2020/03/06	58914.41	18.09 0.05	17.64 0.03	17.63 0.03	–	LCO
2020/03/11	58919.44	18.14 0.06	17.67 0.11	17.64 0.06	–	LCO
2020/03/21	58929.40	18.28 0.15	17.59 0.15	–	17.42 0.15	LCO
2020/03/23	58931.36	18.31 0.06	17.58 0.04	17.55 0.03	–	LCO
2020/05/09	58978.57	–	–	16.98 0.01	–	Pan-STARRS
2020/05/15	58983.56	–	–	16.95 0.01	–	Pan-STARRS
2020/06/10	59010.57	–	–	16.93 0.02	–	Pan-STARRS
2020/06/14	59014.51	–	–	16.92 0.01	–	Pan-STARRS
2020/06/27	59027.03	21.29 0.05	19.86 0.02	19.42 0.02	19.07 0.03	IO:O
2020/06/27	59027.40	–	–	19.46 0.11	–	Pan-STARRS
2020/06/28	59028.22	21.52 0.09	20.05 0.03	19.52 0.04	19.21 0.05	IO:O
2020/06/29	59029.97	–	20.07 0.15	19.64 0.15	19.39 0.15	OSIRIS
2020/07/06	59036.93	22.12 0.17	20.71 0.05	20.09 0.08	19.67 0.09	IO:O
2020/07/12	59042.99	22.30 0.19	21.12 0.09	20.23 0.04	19.82 0.10	IO:O
2020/07/25	59055.99	22.58 0.17	21.43 0.11	20.54 0.11	19.98 0.09	IO:O
2020/07/30	59060.46	–	–	20.57 0.29	–	Pan-STARRS
2020/08/01	59062.50	–	–	20.61 0.14	–	Pan-STARRS
2020/08/07	59068.93	–	21.55 0.08	20.74 0.06	20.07 0.07	IO:O
2020/08/18	59079.01	–	–	21.08 0.05	20.39 0.05	ALFOSC
2020/09/04	59096.91	–	22.29 0.15	21.71 0.17	20.75 0.16	IO:O
2020/09/27	59119.90	–	22.34 0.22	21.74 0.09	21.24 0.14	IO:O
2020/09/30	59122.84	–	>22.02	21.73 0.09	21.32 0.14	IO:O

Table 8.2: Photometric data collected with Johnson filters for SN 2020cxd (Vega mag).

Date	MJD	U	B	V	Instrument
2020/02/26	58905.58	–	17.98 0.10	17.73 0.10	LCO
2020/02/27	58906.44	17.41 0.05	18.06 0.03	17.71 0.03	LCO
2020/03/06	58914.39	18.57 0.10	18.43 0.07	17.81 0.05	LCO
2020/03/11	58919.43	18.86 0.19	18.67 0.07	17.90 0.06	LCO
2020/03/21	58929.30	–	18.97 0.20	17.85 0.15	LCO
2020/03/23	58931.35	19.53 0.15	18.94 0.09	17.84 0.04	LCO
2020/06/28	59029.97	–	–	20.93 0.20	OSIRIS

Table 8.3: Photometric data collected through the ATLAS survey for SN 2020cxd (AB mag).

Date	MJD	*cyan*	*orange*	Instrument
2020/03/02	58910.64	–	17.56 0.17	ATLAS
2020/03/26	58934.63	–	17.42 0.23	ATLAS
2020/03/30	58938.62	–	17.57 0.10	ATLAS
2020/04/03	58942.63	–	17.54 0.20	ATLAS
2020/04/07	58946.61	–	17.46 0.38	ATLAS
2020/04/11	58950.63	–	17.50 0.03	ATLAS
2020/04/17	58956.59	–	17.38 0.08	ATLAS
2020/04/21	58960.58	17.84 0.11	–	ATLAS
2020/04/23	58962.60	–	17.33 0.05	ATLAS
2020/04/25	58964.53	17.82 0.13	–	ATLAS
2020/04/27	58966.52	–	17.26 0.07	ATLAS
2020/04/29	58968.49	17.70 0.02	–	ATLAS
2020/05/01	58970.52	–	17.24 0.09	ATLAS
2020/05/03	58972.52	–	17.22 0.03	ATLAS
2020/05/05	58974.52	–	17.21 0.09	ATLAS
2020/05/07	58976.48	–	17.18 0.06	ATLAS
2020/05/09	58978.50	–	17.14 0.04	ATLAS
2020/05/13	58982.54	–	17.01 0.09	ATLAS
2020/05/15	58984.56	–	17.18 0.04	ATLAS
2020/05/17	58986.55	–	17.14 0.05	ATLAS
2020/05/19	58988.50	17.56 0.10	–	ATLAS
2020/05/21	58990.45	–	17.05 0.01	ATLAS
2020/05/23	58992.44	17.55 0.09	–	ATLAS
2020/05/25	58994.47	–	17.06 0.11	ATLAS
2020/05/29	58998.46	–	17.07 0.03	ATLAS
2020/05/31	59000.52	17.53 0.04	–	ATLAS
2020/06/02	59002.51	–	17.08 0.12	ATLAS
2020/06/04	59004.59	–	17.05 0.30	ATLAS
2020/06/06	59006.41	–	17.03 0.06	ATLAS
2020/06/08	59008.51	–	17.06 0.36	ATLAS
2020/06/10	59010.42	–	17.13 0.04	ATLAS
2020/06/11	59011.47	–	17.14 0.06	ATLAS
2020/06/14	59014.41	–	17.17 0.13	ATLAS
2020/06/15	59015.41	17.57 0.10	–	ATLAS
2020/06/18	59018.43	–	17.18 0.10	ATLAS
2020/06/20	59020.45	17.91 0.13	–	ATLAS
2020/06/28	59028.42	>20.41	>19.93	ATLAS
2020/07/18	59048.41	>20.38	–	ATLAS
2020/07/20	59050.37	–	>20.25	ATLAS

Table 8.4: Photometric data in the Sloan filters collected for SN 2021aai (AB mag).

Date	MJD	u	g	r	i	z	Instrument
2021/01/08	59222.27	–	–	>20.54	–	–	ZTF
2021/01/10	59224.42	–	18.85 0.08	–	–	–	ZTF
2021/01/12	59226.40	–	18.76 0.11	18.40 0.09	–	–	ZTF
2021/01/14	59228.24	–	18.62 0.08	18.32 0.07	–	–	ZTF
2021/01/16	59230.24	–	18.66 0.08	18.30 0.06	–	–	ZTF
2021/01/18	59232.32	–	18.72 0.09	18.29 0.05	–	–	ZTF
2021/01/19	59233.91	19.76 0.04	18.90 0.04	18.32 0.03	18.26 0.03	18.15 0.05	LRS
2021/01/22	59236.90	20.20 0.25	18.97 0.030	18.34 0.02	18.23 0.02	18.11 0.03	ALFOSC
2021/01/23	59237.09	–	18.96 0.07	18.37 0.06	18.22 0.06	–	LCO
2021/01/24	59238.96	20.68 0.15	19.01 0.01	18.29 0.03	18.17 0.03	18.01 0.04	ALFOSC
2021/01/25	59239.41	–	19.14 0.07	18.32 0.04	18.21 0.05	–	LCO
2021/01/27	59241.26	–	19.21 0.12	18.33 0.09	18.14 0.11	–	LCO
2021/01/31	59245.23	–	19.22 0.07	18.34 0.05	18.14 0.05	–	LCO
2021/02/03	59248.17	–	19.31 0.04	–	18.15 0.04	–	LCO
2021/02/03	59248.39	–	19.36 0.11	18.31 0.07	–	–	ZTF
2021/02/05	59250.22	–	19.31 0.18	18.28 0.07	–	–	ZTF
2021/02/07	59252.19	–	19.36 0.12	18.26 0.05	–	–	ZTF
2021/02/07	59252.20	–	19.31 0.04	18.25 0.03	18.13 0.04	–	LCO
2021/02/09	59254.18	–	19.32 0.14	18.23 0.05	–	–	ZTF
2021/02/11	59256.18	–	19.28 0.11	18.26 0.05	–	–	ZTF
2021/02/11	59256.25	–	19.35 0.03	18.26 0.03	18.07 0.09	–	LCO
2021/02/15	59260.39	–	19.31 0.21	18.22 0.08	–	–	ZTF
2021/02/18	59263.21	–	–	18.19 0.10	–	–	ZTF
2021/02/20	59265.04	–	19.28 0.08	18.13 0.06	17.85 0.06	17.93 0.18	ALFOSC
2021/02/20	59265.31	–	19.36 0.13	18.15 0.07	–	–	ZTF
2021/02/22	59267.30	–	19.36 0.19	18.10 0.08	–	–	ZTF
2021/02/26	59271.23	–	–	18.12 0.08	–	–	LCO
2021/02/26	59271.27	–	–	18.14 0.08	–	–	ZTF
2021/02/28	59273.21	–	19.32 0.27	18.13 0.10	–	–	ZTF
2021/03/02	59275.33	–	–	18.07 0.06	–	–	ZTF
2021/03/04	59277.13	–	19.47 0.03	18.12 0.02	17.80 0.02	–	LCO
2021/03/05	59278.18	–	19.33 0.18	18.06 0.07	–	–	ZTF
2021/03/08	59281.21	–	19.42 0.13	18.06 0.06	–	–	ZTF
2021/03/14	59287.06	–	–	18.20 0.24	17.85 0.11	17.60 0.05	AFOSC
2021/03/18	59291.20	–	–	18.10 0.07	–	–	ZTF
2021/03/18	59291.27	–	19.50 0.03	18.07 0.02	17.74 0.01	–	LCO
2021/03/20	59293.21	–	19.53 0.11	18.09 0.08	–	–	ZTF
2021/03/23	59296.22	–	–	17.98 0.13	–	–	ZTF
2021/03/24	59297.25	–	19.53 0.06	18.07 0.03	17.74 0.03	–	LCO
2021/03/25	59298.29	–	–	18.02 0.22	–	–	ZTF
2021/03/29	59302.17	–	19.58 0.22	–	–	–	ZTF
2021/03/31	59304.16	–	–	17.98 0.06	–	–	ZTF

Table B4: **(Continued)** Photometric data in the Sloan filters collected for SN 2021aai (AB mag).

Date	MJD	*u*	*g*	*r*	*i*	*z*	Instrument
2021/04/02	59306.31	–	19.34 0.14	17.97 0.09	–	–	ZTF
2021/04/04	59308.22	–	19.42 0.15	17.97 0.06	–	–	ZTF
2021/04/06	59310.23	–	19.33 0.12	–	–	–	ZTF
2021/04/08	59312.28	–	19.36 0.14	17.94 0.06	–	–	ZTF
2021/04/10	59314.28	–	–	17.89 0.05	–	–	ZTF
2021/04/12	59316.28	–	19.32 0.11	17.83 0.04	–	–	ZTF
2021/04/15	59319.27	–	19.34 0.13	–	–	–	ZTF
2021/04/18	59322.27	–	19.31 0.19	17.79 0.06	–	–	ZTF
2021/04/20	59324.22	–	19.25 0.15	17.74 0.06	–	–	ZTF
2021/04/24	59328.18	–	–	17.70 0.06	–	–	ZTF
2021/05/08	59342.89	–	19.27 0.05	17.72 0.02	17.36 0.01	17.15 0.02	ALFOSC
2021/05/09	59343.12	–	19.26 0.04	17.74 0.02	–	–	LCO
2021/05/19	59353.89	–	19.33 0.07	17.74 0.04	17.28 0.03	–	Moravian
2021/05/25	59359.97	–	–	17.75 0.03	17.30 0.03	–	Moravian
2021/05/31	59365.87	–	–	17.81 0.03	17.38 0.03	–	Moravian
2021/06/02	59367.89	–	–	17.96 0.04	17.52 0.07	–	Moravian
2021/06/03	59368.94	–	–	18.07 0.06	17.69 0.08	–	Moravian
2021/06/04	59369.95	–	–	18.14 0.06	17.74 0.03	–	Moravian
2021/06/06	59371.89	–	20.10 0.10	18.36 0.03	18.01 0.02	17.75 0.02	ALFOSC
2021/06/11	59376.02	–	21.65 0.14	19.19 0.05	18.57 0.03	18.23 0.05	ALFOSC
2021/06/17	59382.91	–	–	20.70 0.16	19.96 0.09	19.54 0.08	ALFOSC
2021/06/23	59388.90	–	–	20.83 0.13	20.09 0.07	19.58 0.06	ALFOSC
2021/07/02	59397.17	–	–	21.06 0.19	20.25 0.08	19.69 0.06	ALFOSC
2021/07/10	59405.23	–	–	21.22 0.08	20.30 0.05	19.76 0.16	ALFOSC

Table B5: Photometric data in the Johnson filters collected for SN 2021aai (Vega mag).

Date	MJD	*B*	*V*	Instrument
2021/01/19	59233.91	19.22 0.04	18.61 0.03	LRS
2021/01/22	59236.89	19.32 0.07	18.65 0.03	ALFOSC
2021/01/23	59237.08	19.38 0.08	18.61 0.07	LCO
2021/01/24	59238.95	19.46 0.07	18.64 0.04	ALFOSC
2021/01/25	59239.32	19.43 0.12	18.63 0.09	LCO
2021/01/27	59241.24	19.71 0.18	18.62 0.12	LCO
2021/01/31	59245.22	19.87 0.15	18.76 0.08	LCO
2021/02/03	59248.15	20.16 0.08	18.67 0.04	LCO
2021/02/07	59252.18	20.32 0.08	18.63 0.04	LCO
2021/02/11	59256.23	20.44 0.10	18.67 0.03	LCO
2021/02/20	59265.03	20.59 0.18	18.61 0.10	ALFOSC
2021/02/26	59271.22	–	18.57 0.10	LCO
2021/03/04	59277.11	20.81 0.11	18.68 0.02	LCO
2021/03/18	59291.26	20.79 0.08	18.69 0.02	LCO
2021/03/24	59297.23	–	18.64 0.06	LCO
2021/05/08	59342.89	20.83 0.09	18.32 0.04	ALFOSC
2021/05/09	59343.12	–	18.38 0.03	LCO
2021/05/31	59365.88	–	18.63 0.03	Moravian
2021/06/06	59371.89	22.37 0.09	19.15 0.02	ALFOSC
2021/06/11	59376.01	–	20.80 0.15	ALFOSC

Table B6: Photometric data collected through the ATLAS survey for SN 2021aai (AB mag).

Date	MJD	*cyan*	*orange*	Instrument
2021/01/24	59238.48	–	18.15 0.46	ATLAS
2021/01/28	59242.48	–	18.16 0.44	ATLAS
2021/01/30	59244.47	–	18.09 0.14	ATLAS
2021/02/01	59246.45	–	18.23 0.24	ATLAS
2021/02/05	59250.43	18.70 0.37	–	ATLAS
2021/02/07	59252.45	18.66 0.42	–	ATLAS
2021/02/09	59254.38	18.84 0.30	–	ATLAS
2021/02/11	59256.41	18.74 0.04	–	ATLAS
2021/02/13	59258.40	18.60 0.21	–	ATLAS
2021/02/21	59266.49	18.35 0.27	18.00 0.18	ATLAS
2021/02/25	59270.39	–	17.93 0.26	ATLAS
2021/03/03	59276.55	–	18.05 0.37	ATLAS
2021/03/05	59278.43	19.06 0.16	17.73 0.20	ATLAS
2021/03/11	59284.36	18.67 0.21	–	ATLAS
2021/03/15	59288.32	18.60 0.12	–	ATLAS
2021/03/19	59292.27	–	18.11 0.11	ATLAS
2021/03/25	59298.34	–	17.89 0.43	ATLAS
2021/03/27	59300.38	–	17.67 0.32	ATLAS
2021/03/31	59304.29	–	17.74 0.28	ATLAS
2021/04/02	59306.42	–	17.85 0.21	ATLAS
2021/04/06	59310.28	18.53 0.14	–	ATLAS
2021/04/10	59314.26	18.76 0.47	–	ATLAS
2021/04/14	59318.26	18.47 0.15	–	ATLAS
2021/04/16	59320.25	–	17.68 0.13	ATLAS
2021/04/18	59322.26	–	17.74 0.08	ATLAS
2021/04/20	59324.31	–	17.64 0.26	ATLAS
2021/04/24	59328.31	–	17.49 0.08	ATLAS
2021/04/28	59332.32	–	17.65 0.63	ATLAS
2021/04/30	59334.29	–	17.52 0.04	ATLAS
2021/05/12	59346.26	–	17.49 0.09	ATLAS
2021/05/14	59348.26	18.65 0.29	–	ATLAS
2021/05/16	59350.25	–	17.61 0.07	ATLAS
2021/05/18	59352.26	–	17.58 0.42	ATLAS
2021/05/20	59354.25	–	17.51 0.20	ATLAS
2021/05/22	59356.26	–	17.54 0.07	ATLAS
2021/05/30	59364.26	–	17.53 0.19	ATLAS
2021/06/07	59372.26	–	18.03 0.19	ATLAS
2020/12/17	59200.47	>20.11	–	ATLAS
2020/12/19	59202.62	>20.08	–	ATLAS
2020/12/25	59208.44	–	>19.48	ATLAS
2020/12/29	59212.58	–	>18.86	ATLAS
2020/12/31	59214.53	–	>19.13	ATLAS
2021/01/06	59220.49	–	>19.76	ATLAS
2021/08/14	59440.56	–	>19.59	ATLAS

Table B7: Photometric data collected in the NIR for SN 2021aai (Vega mag).

Date	MJD	*J*	*H*	*K*	Instrument
2021/01/25	59239.93	17.24 0.19	16.90 0.04	16.66 0.09	NOTCAM
2021/02/18	59263.96	16.84 0.12	16.42 0.12	–	NOTCAM
2021/05/22	59356.88	16.11 0.12	15.81 0.05	15.60 0.13	NOTCAM

Table B8: Photometric data collected in Johnson bands for NGC 300 OT (Vega mag).

Date	MJD	U (err)	B (err)	V (err)	R (err)	I (err)	Source
20080516	54602.89	...	15.609(0.049)	14.688(0.023)	14.275(.016)	13.833(.025)	PROMPT3+5
20080520	54606.88	15.920(0.361)	15.654(0.016)	14.700(0.019)	14.240(.012)	13.853(.025)	PROMPT2+5
20080521	54607.84	...	...	...	14.291(060)	13.834(.038)	REM
20080522	54608.83	...	...	14.819(.072)	14.338(084)	...	REM
20080523	54609.55	...	...	14.819(0.021)	14.320(.015)	13.837(0.016)	PROMPT5
20080524	54610.87	16.088(0.123)	15.719(0.018)	...	...	...	PROMPT3
20080524	54610.87	16.065(0.191)	15.613(0.018)	14.892(0.023)	14.360(.011)	13.851(.016)	PROMPT2+5
20080525	54611.87	...	15.802(0.038)	14.869(0.025)	...	...	PROMPT2
20080525	54611.87	16.089(0.383)	15.788(0.079)	14.866(0.025)	14.337(.031)	13.827(0.028)	PROMPT3+5
20080529	54615.82	...	...	...	...	13.851(.028)	REM
20080529	54615.66	...	...	14.9 (.2)	14.3 (.2)	13.8(.200)	Monard AAVSO
20080530	54616.85	16.128(0.360)	15.742(0.020)	14.888(0.014)	14.407(.014)	13.897(0.02)	PROMPT2+5
20080531	54617.85	16.147(0.288)	15.870(0.020)	14.900(0.015)	14.444(.013)	13.904(0.02)	PROMPT2+5
20080602	54619.67	...	...	...	14.4 (.2)	...	Monard AAVSO
20080603	54620.63	...	...	...	14.4 (.2)	...	Monard AAVSO
20080606	54623.80	...	...	...	...	13.908(.082)	REM
20080606	54623.90	16.400(.018)	15.969(.008)	14.976(.009)	14.432(.011)	...	EFOSC
20080607	54624.84	...	16.056(0.023)	15.005(0.017)	14.475(0.012)	13.907(0.011)	PROMPT2+5
20080608	54625.82	...	16.023(0.037)	14.980(0.048)	14.450(0.035)	13.883(0.026)	PROMPT3+5
20080609	54626.81	...	15.998(0.030)	14.962(0.018)	14.401(0.010)	13.882(0.011)	PROMPT4
20080609	54626.82	...	16.022(0.021)	14.989(0.017)	14.508(0.015)	13.902(0.027)	PROMPT2+5
20080610	54627.82	...	16.030(0.030)	15.029(0.016)	14.422(0.012)	13.937(0.014)	PROMPT3+5
20080611	54628.81	...	16.112(0.049)	15.040(0.017)	14.408(0.017)	13.972(0.019)	PROMPT4
20080611	54628.81	...	16.012(0.025)	15.054(0.018)	14.453(0.015)	13.914(0.011)	PROMPT3+5
20080612	54629.80	...	16.130(0.117)	15.009(0.020)	14.431(0.015)	13.966(0.015)	PROMPT4
20080612	54629.81	...	16.185(0.024)	14.998(0.014)	14.480(0.012)	13.941(0.014)	PROMPT2+5
20080613	54630.80	...	16.220(0.054)	15.094(0.018)	14.492(0.010)	13.931(0.024)	PROMPT4+5
20080613	54630.93	16.591(.013)	...	...	...	...	EFOSC
20080614	54631.81	...	...	15.116(0.018)	14.52(0.011)	13.921(0.017)	PROMPT4
20080614	54631.81	...	...	15.099(0.016)	14.47(0.014)	13.966(0.017)	PROMPT5
20080615	54632.80	...	16.23(0.032)	15.161(0.026)	14.50(0.011)	13.950(0.011)	PROMPT4
20080615	54632.80	...	16.18(0.023)	15.083(0.019)	14.52(0.014)	13.940(0.014)	PROMPT2+5

Table B9: Photometric data collected in Johnson bands for NGC 300 OT (Vega mag).

Date	MJD	U (err)	B (err)	V (err)	R (err)	I (err)	Source
20080615	54632.92	16.597(.011)	...	...	...	...	EFOSC
20080616	54633.80	...	16.20(0.022)	...	14.520(0.020)	13.95(0.011)	PROMPT2+5
20080617	54634.80	...	16.14(0.027)	15.218(0.017)	14.587 (0.014)	13.98(0.013)	PROMPT2+5
20080620	54637.79	...	16.259(0.058)	15.273(0.026)	14.532 (0.013)	13.97(0.014)	PROMPT4
20080622	54639.79	...	16.267(0.054)	15.295(0.036)	14.614 (0.021)	14.02(0.042)	PROMPT4
20080622	54639.85	...	16.307(0.044)	15.250(0.026)	14.601 (0.021)	13.99(0.023)	PROMPT2+5
20080623	54640.78	...	16.348(0.055)	15.246(0.024)	14.564 (0.012)	13.99(0.016)	PROMPT4
20080623	54640.86	...	16.428(0.025)	15.257(0.017)	14.601 (0.011)	14.00(0.013)	PROMPT2+5
20080624	54641.78	...	16.458(0.055)	15.381(0.031)	14.639 (0.015)	14.08(0.013)	PROMPT4
20080624	54641.78	...	16.483(0.057)	15.327(0.020)	14.573 (0.013)	14.06(0.011)	PROMPT2+5
20080625	54642.78	...	16.417(0.043)	15.334(0.022)	14.628 (0.020)	14.10(0.017)	PROMPT4
20080625	54642.78	...	16.425(0.022)	15.299(0.016)	14.600 (0.033)	14.07(0.014)	PROMPT2+5
20080626	54643.78	...	...	15.350(0.048)	14.65(0.021)	14.10(0.030)	PROMPT4
20080626	54643.78	...	...	15.349(0.046)	14.68(0.016)	14.13(0.017)	PROMPT5
20080627	54644.78	...	16.588(0.023)	15.306 (0.022)	14.703(0.019)	14.146(0.019)	PROMPT2+5
20080628	54645.81	...	16.568(0.065)	15.318 (0.032)	14.717(0.018)	14.126(0.014)	PROMPT4
20080628	54645.77	...	...	15.419(0.024)	14.690(0.015)	14.109(0.014)	PROMPT5
20080629	54646.79	...	16.584(0.164)	15.373 (0.029)	14.784(0.015)	14.104(0.016)	PROMPT4
20080629	54646.76	...	...	15.416(0.043)	14.737(0.020)	...	PROMPT5
20080630	54647.76	...	...	15.407(0.019)	14.822(0.024)	...	PROMPT5
20080701	54648.97	17.04(0.29)	16.634(0.033)	15.508 (0.024)	14.851(0.019)	14.185(0.015)	PROMPT5
20080703	54650.77	...	16.650(0.045)	15.551 (0.020)	14.924(0.013)	14.247(0.010)	PROMPT3+5
20080704	54651.83	...	...	15.660(0.035)	14.915(0.013)	14.257(0.010)	PROMPT3+5
20080705	54652.94	17.17(.014)	16.746(.006)	15.619(.006)	14.949(.005)	...	EFOSC
20080707	54654.75	...	...	15.652(.253)	15.023(.173)	14.328(.096)	REM
20080708	54655.75	...	16.947(0.111)	15.750 (0.035)	15.038(0.015)	14.336(0.015)	PROMPT4
20080708	54655.75	...	16.850(0.048)	15.794 (0.025)	15.040(0.022)	14.346(0.013)	PROMPT3+5
20080709	54656.81	...	16.825(0.102)	15.828 (0.048)	15.109(0.028)	14.357(0.024)	PROMPT4
20080709	54656.74	...	16.997(0.076)	15.808 (0.031)	15.071(0.020)	14.331(0.024)	PROMPT3+5
20080710	54657.74	...	16.970(0.144)	15.833 (0.046)	15.148(0.032)	14.406(0.018)	PROMPT4
20080710	54657.73	...	17.000(0.122)	...	15.160(0.016)	14.381(0.021)	PROMPT3+5
20080710	54657.70	...	...	15.840(.182)	...	...	REM
20080711	54658.82	...	17.024(0.057)	15.861 (0.024)	15.220(0.018)	14.424(0.02)	PROMPT3+5
20080713	54660.86	...	17.060(0.056)	15.945 (0.024)	15.217(0.017)	14.519(0.01)	PROMPT3+5
20080714	54661.73	...	17.140(0.109)	16.007 (0.030)	15.324(0.021)	14.486(0.01)	PROMPT3+5
20080715	54662.93	17.597(.021)	17.189(.018)	16.028(.019)	15.317(.010)	...	EFOSC
20080715	54662.72	...	17.166(0.054)	16.058 (0.026)	15.329(0.018)	14.595(0.01)	PROMPT3+5
20080716	54663.73	...	17.312(0.043)	16.106 (0.043)	15.315(0.023)	14.632(0.01)	PROMPT3+5
20080721	54669.37	...	...	16.222(.107)	...	...	Mendicini
20080726	54673.91	18.083(.026)	17.735(.008)	16.512(.004)	15.(.005)	...	EFOSC
20080727	54675.25	...	...	16.59 (.05)	...	...	GCO AAVSO
20080729	54676.84	...	18.022(0.068)	16.74(0.046)	15.(0.02)	14.980(0.018)	PROMPT3+5
20080801	54680.30	...	...	16.89(.07)	...	...	GCO AAVSO
20080805	54683.92	18.721(.081)	18.360(.021)	17.08(.010)	16.11(.004)	...	EFOSC
20080811	54690.26	...	...	17.44(.262)	...	...	Mendicini
20080813	54692.21	...	...	17.50(.051)	...	...	Mendicini
20080815	54694.25	...	...	17.58(.142)	...	...	Mendicini
20080910	54719.70	...	...	18.94(.328)	...	...	REM
20080911	54720.71	...	...	18.93(.388)	17.808(.105)	...	REM
20080915	54724.86	...	...	...	...	17.23(.341)	REM

Table B10: Photometric data collected in sloan bands for NGC 300 OT (AB mag).

Date yyyymmdd	JD -2400000	u (err)	g (err)	r (err)	i (err)	z (err)	source
20080516	54602.380	...	...	14.383(0.021)	14.210(0.024)	14.124(0.022)	PROMPT
20080520	54606.400	...	...	14.474(0.018)	14.207(0.014)	14.108(0.025)	PROMPT
20080520	54606.400	16.653(0.040)	15.129(0.011)	...	...	...	Swope
20080523	54609.390	...	...	14.477(0.013)	14.199(0.012)	14.109(0.031)	PROMPT
20080524	54610.380	...	...	14.487(0.034)	...	...	PROMPT
20080525	54611.367	...	...	14.501(0.023)	14.202(0.018)	14.074(0.014)	PROMPT
20080530	54616.350	...	15.246(0.014)	14.607(0.024)	14.286(0.013)	14.160(0.013)	PROMPT
20080530	54616.325	17.065(0.065)	15.286(0.006)	...	...	...	Swope
20080531	54617.345	...	15.29 (0.04)	14.628(0.027)	14.287(0.017)	14.196(0.021)	PROMPT
20080607	54624.335	...	15.368(0.01)	14.663(0.032)	14.352(0.015)	14.155(0.021)	PROMPT
20080608	54625.320	...	15.409(0.020)	...	...	...	PROMPT
20080609	54626.315	...	15.439(0.027)	14.684(0.021)	14.376(0.017)	14.152(0.036)	PROMPT
20080610	54627.315	...	15.489(0.018)	14.688(0.013)	...	14.167(0.014)	PROMPT
20080611	54628.310	...	15.464(0.014)	14.701(0.024)	14.335(0.011)	14.162(0.017)	PROMPT
20080611	54628.325	17.226(0.035)	15.483(0.007)	...	...	...	Swope
20080612	54629.315	...	15.511(0.009)	14.696(0.048)	14.355(0.008)	14.157(0.014)	PROMPT
20080613	54630.335	...	...	14.721(0.030)	14.328(0.011)	14.179(0.013)	PROMPT
20080613	54630.360	17.290(0.032)	15.537(0.009)	...	...	...	Swope
20080614	54631.317	...	...	14.732(0.020)	14.356(0.022)	14.197(0.018)	PROMPT
20080615	54632.315	...	...	14.740(0.022)	14.350(0.010)	14.177(0.029)	PROMPT
20080616	54633.325	...	...	14.758(0.022)	14.354(0.023)	14.212(0.017)	PROMPT
20080617	54634.317	...	15.590(0.015)	14.810(0.025)	14.383(0.015)	14.206(0.013)	PROMPT
20080623	54640.385	...	...	14.862(0.016)	14.463(0.013)	14.315(0.016)	PROMPT
20080624	54641.300	...	...	14.888(0.018)	14.475(0.012)	14.354(0.053)	PROMPT
20080625	54642.295	...	...	14.899(0.019)	14.528(0.009)	14.388(0.013)	PROMPT
20080627	54644.255	17.691(0.093)	15.838(0.008)	...	...	...	Swope
20080627	54644.273	...	...	14.937(0.022)	14.563(0.014)	14.390(0.039)	PROMPT
20080628	54645.273	...	...	15.016(0.059)	14.578(0.027)	14.411(0.029)	PROMPT
20080629	54646.280	...	...	15.033(0.032)	...	...	PROMPT
20080630	54647.260	...	...	15.077(0.017)	...	...	PROMPT
20080703	54650.250	...	...	15.171(0.030)	14.710(0.056)	14.523(0.010)	PROMPT
20080704	54651.330	...	...	15.193(0.015)	14.744(0.012)	...	PROMPT
20080705	54652.425	...	...	15.208(0.020)	...	14.571(0.019)	PROMPT
20080709	54656.245	...	...	15.330(0.023)	14.930(0.022)	14.681(0.021)	PROMPT
20080711	54658.230	...	16.399(0.029)	15.398(0.017)	14.987(0.022)	14.776(0.050)	PROMPT
20080713	54660.365	...	...	15.491(0.016)	15.010(0.014)	14.787(0.026)	PROMPT
20080714	54661.230	...	...	15.494(0.022)	15.065(0.052)	14.800(0.024)	PROMPT
20080715	54662.220	...	...	15.514(0.021)	15.065(0.011)	14.787(0.016)	PROMPT
20080729	54676.345	...	17.112 (0.032)	16.097(0.029)	15.612(0.023)	15.111(0.039)	PROMPT
20080805	54683.300	...	17.88(0.25)	16.44 (0.25)	15.94(0.25)	15.65 (0.25)	Spectrophot
20080917	54724.300	...	20.46(0.25)	18.24 (0.25)	...	...	Spectrophot
20080929	54738.100	...	...	...	...	17.557(0.070)	PROMPT
20081002	54742.300	...	...	18.52 (0.25)	...	...	Spectrophot

Table B11: Photometric data collected in sloan bands for NGC 300 OT (AB mag).

Date yyyymmdd	JD -2400000	u (err)	g (err)	r (err)	i (err)	z (err)	source
20081003	54742.090	...	...	...	...	17.674(0.052)	PROMPT
20081023	54762.097	...	...	18.862(0.056)	18.554(0.063)	...	PROMPT
20081025	54764.085	...	...	18.881(0.074)	18.588(0.105)	18.012(0.105)	PROMPT
20081026	54765.197	...	...	18.859(0.075)	18.642(0.131)	...	PROMPT
20081027	54766.120	...	...	18.932(0.069)	18.758(0.067)	18.044(0.086)	PROMPT
20081029	54768.060	...	...	18.962(0.046)	18.785(0.080)	18.118(0.081)	PROMPT
20081102	54772.100	...	...	19.058(0.055)	18.903(0.092)	18.225(0.090)	PROMPT
20081127	54797.080	...	...	...	...	18.417(0.117)	PROMPT
20081207	54807.060	...	...	...	...	18.576(0.135)	PROMPT
20081208	54808.060	...	...	19.368(0.066)	...	...	PROMPT
20081209	54809.080	...	...	...	19.478(0.096)	...	PROMPT
20081224	54824.090	...	...	19.511(0.067)	...	...	PROMPT
20081225	54825.070	...	...	...	...	18.698(0.134)	PROMPT
20090120	54851.040	...	21.99(0.043)	19.467(0.044)	...	...	GMOS-S
20090107	54838.050	...	...	19.480(0.182)	...	...	GMOS-S
20090122	54853.555	...	22.064(0.160)	19.475(0.014)	19.943(0.012)	...	Magellan Clay
20090208	54870.539	...	22.403(0.218)	19.705(0.020)	20.305(0.038)	19.317(0.024)	Magellan Clay
20090213	54875.544	...	22.606(0.193)	19.770(0.012)	20.382(0.014)	19.384(0.011)	Magellan Clay
20090123	54854.050	...	...	19.473(0.089)	...	...	GMOS-S
20090519	54970.403	...	...	21.228(0.228)	21.686(0.039)	21.013(0.056)	GMOS-S
20090713	55025.360	...	...	22.244(0.094)	...	...	GMOS-S
20090713	55025.380	...	23.173	...	...	...	*GMOS-S
20090724	55036.420	...	...	...	22.848(0.500)	...	*GMOS-S
20090726	55038.280	...	...	...	23.004(12.00)	...	*GMOS-S
20090828	55071.150	...	...	22.764(0.069)	...	...	GMOS-S
20091116	55151.133	...	...	23.364	23.415	23.487	*GMOS-S

Table B12: Photometric data collected in NIR bands for NGC 300 OT (Vega mag).

Date	MJD	J (err)	H (err)	K (err)	source
20/5/08	54606.35109	...	12.67(0.24)	...	REM
21/5/08	54607.33718	...	12.64(0.18)	...	REM
22/5/08	54608.82834	13.12(0.033)	12.608(0.10)	...	REM
23/5/08	54609.82545	13.09(0.056)	12.617(0.12)	...	REM
24/05/0	54610.908	...	...	11.94(0.067)	REM
25/5/08	54611.82019	13.10(0.161)	...	...	REM
30/5/08	54616.80650	13.09(0.054)	12.631(0.050)	12.044(0.089)	REM
31/5/08	54617.80371	13.16(0.069)	12.609(0.038)	...	REM
06/6/08	54623.78490	13.03(0.195)	12.558(0.443)	...	REM
07/6/08	54624.79958	13.10(0.046)	12.533(0.042)	...	REM
08/6/08	54625.79018	13.11(0.052)	12.531(0.351)	...	REM
09/6/08	54626.77918	13.12(0.073)	...	...	REM
10/6/08	54627.77623	13.11(0.067)	12.562(0.344)	...	REM

Table B13: Photometric data collected in NIR bands for NGC 300 OT (Vega mag).

Date	MJD	J (err)	H (err)	K (err)	source
11/6/08	54628.27788	...	12.58 (0.29)	...	REM
12/6/08	54629.77144	13.07(0.057)	...	...	REM
13/6/08	54630.76827	13.11(0.088)	12.608(0.063)	...	REM
14/6/08	54631.83902	13.09(0.039)	12.592(0.051)	...	REM
15/6/08	54632.76271	13.10(0.093)	12.597(0.124)	11.900(0.113)	REM
16/6/08	54633.76298	13.13(0.137)	...	11.924(0.168)	REM
17/6/08	54634.85931	13.16(0.070)	...	...	REM
21/6/08	54638.25460	...	12.6(0.344)	...	REM
22/6/08	54639.74469	13.19(0.078)	...	...	REM
23/6/08	54640.74067	13.19(0.096)	12.689(0.082)	...	REM
24/6/08	54641.76544	...	...	12.066 (.216)	REM
25/6/08	54642.74297	13.21(0.066)	12.713(0.051)	...	REM
28/6/08	54645.72723	13.23(0.036)	12.770(0.201)	12.035 (0.196)	REM
29/6/08	54646.72454	13.28(0.045)	12.784(0.157)	...	REM
30/6/08	54647.72185	13.37(0.089)	12.789(0.122)	...	REM
01/7/08	54648.71903	13.23(0.669)	12.748(0.130)	12.073(0.119)	REM
02/7/08	54649.71640	13.40(0.042)	12.817(0.168)	...	REM
03/7/08	54650.71790	13.33(0.038)	12.874(0.177)	...	REM
04/7/08	54651.71084	13.35(0.064)	13.032(0.259)	...	REM
06/7/08	54653.73209	13.37(0.095)	12.947(0.266)	12.124(0.083)	REM
07/7/08	54654.74791	13.42(0.090)	12.964(0.066)	12.108(0.121)	REM
08/7/08	54655.89660	13.46(0.057)	13.010(0.054)	12.150(0.094)	REM
09/7/08	54656.77837	13.52(0.046)	13.031(0.202)	12.154(0.074)	REM
10/7/08	54657.69441	13.54(0.059)	13.035(0.166)	...	REM
11/7/08	54658.69177	13.57(0.059)	...	...	REM
13/7/08	54660.68630	13.53(0.042)	13.120(0.297)	...	REM
14/7/08	54661.68248	13.65(0.047)	13.148(0.119)	...	REM
15/9/08	54724.75556	15.53(0.074)	...	13.47(0.104)	REM
25/9/08	54734.73999	15.79(0.144)	14.335(0.075)	13.57(0.087)	REM
12/11/09	54782.55899	17.18(0.540)	...	...	REM
13/11/0	54783.55234	17.15(0.161)	16.309(0.157)	...	REM
14/11/09	54784.290	17.42(0.522)	16.236(0.254)	15.257(0.099)	REM
18/05/09	54969.905	19.48(0.144)	16.890(0.042)	14.628(0.019)	SOFI
14/09/09	55088.695	20.94(0.214)	17.984(0.045)	15.441(0.011)	SOFI
23/11/09	55158.731	21.69(0.268)	18.607(0.098)	15.895(0.021)	SOFI
26/12/09	55191.534	...	19.361(0.127)	16.005(0.031)	SOFI
24/01/10	55220.529	...	...	16.387(0.096)	SOFI

Table B14: Photometric data collected in sloan bands for AT 2019abn (AB mag).

Date	MJD	g (err)	r (err)	i (err)	z (err)	Instrument
20190127	58510.520	20.019 0.056	18.607 0.022	17.950 0.019	9999 –	fa05
20190127	58510.070	9999 –	18.723 0.079	18.139 0.016	17.660 0.013	ACAM
20190129	58512.255	19.520 0.034	18.186 0.021	17.469 0.013	16.920 0.020	ACAM
20190130	58513.200	19.425 0.048	17.942 0.017	17.261 0.008	16.718 0.012	ACAM
20190201	58515.475	18.879 0.023	17.379 0.013	16.771 0.012	9999 –	fa05
20190205	58519.170	18.289 0.014	16.961 0.018	16.384 0.016	16.071 0.007	ALFOSC
20190211	58525.140	17.965 0.011	16.756 0.015	16.241 0.012	15.973 0.009	ALFOSC
20190213	58527.295	17.828 0.014	16.733 0.007	16.231 0.007	9999 –	fa05
20190218	58532.280	17.859 0.085	9999 –	16.252 0.020	9999 –	fa05
20190220	58534.105	17.840 0.030	16.763 0.016	16.262 0.017	15.974 0.011	ALFOSC
20190222	58536.500	17.881 0.013	16.779 0.011	16.294 0.006	15.977 0.012	fa05
20190225	58539.500	17.903 0.014	16.797 0.012	16.314 0.010	16.000 0.019	fa05
20190227	58541.155	17.916 0.012	16.817 0.010	16.333 0.009	16.031 –	IO:O
20190302	58544.265	17.944 0.012	16.859 0.012	16.369 0.007	16.040 0.026	fa05
20190308	58550.250	18.067 0.052	16.946 0.057	16.468 0.033	9999 –	fa05
20190312	58554.130	18.214 0.020	16.994 0.012	16.472 0.010	16.128 0.008	IO:O
20190314	58556.930	18.252 0.027	17.028 0.013	16.520 0.012	16.159 0.013	IO:O
20190315	58557.205	18.252 0.029	17.021 0.024	16.522 0.018	16.135 0.024	fa05
20190318	58560.225	18.355 0.044	17.115 0.032	16.544 0.021	16.154 0.034	fa05
20190318	58560.240	18.342 0.023	17.084 0.015	16.581 0.020	16.134 0.019	IO:O
20190324	58566.480	18.509 0.027	17.163 0.015	16.583 0.011	16.227 0.031	fa05
20190409	58582.260	18.883 0.019	17.375 0.014	16.761 0.010	16.311 0.019	fa05
20190411	58584.980	18.977 0.030	17.405 0.013	16.750 0.011	16.341 0.013	IO:O
20190415	58588.125	19.032 0.049	17.443 0.025	16.808 0.015	16.400 0.054	fa05
20190416	58589.070	19.133 0.039	17.495 0.087	16.793 0.034	16.393 0.023	ALFOSC
20190417	58590.945	19.093 0.052	17.472 0.014	16.822 0.012	16.404 0.015	IO:O
20190425	58598.405	19.200 0.027	17.602 0.014	16.906 0.010	16.457 0.025	fa05
20190428	58601.145	19.257 0.036	17.610 0.014	16.936 0.009	16.495 0.015	IO:O
20190501	58604.095	19.350 0.028	17.660 0.017	16.974 0.010	16.532 0.016	IO:O
20190503	58606.175	19.455 0.032	17.722 0.034	16.992 0.012	9999 –	fa05
20190504	58607.130	19.381 0.025	17.696 0.015	17.010 0.016	16.559 0.017	IO:O
20190507	58610.140	19.514 0.031	17.757 0.020	17.037 0.018	16.573 0.015	IO:O
20190508	58611.390	19.514 0.031	17.773 0.016	17.068 0.013	16.591 0.036	fa05
20190512	58615.090	19.554 0.040	17.791 0.016	17.112 0.017	16.582 0.012	IO:O
20190516	58619.940	19.687 0.082	17.906 0.035	17.154 0.012	16.650 0.014	IO:O
20190521	58624.990	19.881 0.064	17.944 0.028	17.211 0.020	16.697 0.014	IO:O
20190522	58625.340	19.811 0.061	18.003 0.025	17.232 0.013	16.683 0.038	fa05
20190527	58630.100	19.974 0.048	18.039 0.018	17.266 0.013	16.789 0.017	IO:O
20190530	58633.300	20.077 0.042	18.150 0.026	17.374 0.014	16.787 0.034	fa05
20190601	58635.020	20.185 0.064	18.175 0.028	17.382 0.021	16.837 0.018	IO:O
20190609	58643.030	20.478 0.087	18.347 0.024	17.543 0.020	16.950 0.023	IO:O
20190616	58650.235	20.633 0.189	18.517 0.030	– –	– –	fa05
20190701	58665.220	21.127 0.081	18.919 0.026	17.929 0.015	17.262 0.025	fa05
20190707	58671.980	21.349 0.131	19.051 0.029	18.076 0.019	17.415 0.022	IO:O
20190716	58680.185	– –	19.230 0.050	18.218 0.028	17.504 0.030	fa07
20190729	58693.175	– –	19.567 0.029	18.481 0.019	17.734 0.034	fa07

Table B15: Photometric data collected in sloan bands for AT 2019abn (AB mag).

Date	MJD	g (err)	r (err)	i (err)	z (err)	Instrument
20190803	58698.930	– –	19.749 0.045	18.611 0.015	17.855 0.036	ALFOSC
20190806	58701.135	– –	19.785 0.038	18.701 0.058	17.880 0.023	fa07
20190812	58707.885	– –	19.895 0.044	18.861 0.018	18.044 0.024	ALFOSC
20190812	58707.885	>21.040 –	– –	– –	– –	ALFOSC
20190830	58725.860	– –	20.964 0.050	20.080 0.027	19.072 0.052	ALFOSC
20190830	58725.860	>21.936 –	– –	– –	– –	ALFOSC
20190915	58741.840	– –	21.229 0.094	20.321 0.057	19.428 0.059	ALFOSC
20190925	58751.850	– –	– –	20.444 0.067	19.664 0.091	ALFOSC
20191123	58809.000	– –	– –	21.243 0.037	– –	ALFOSC
20191202	58819.220	– –	21.737 0.081	21.359 0.043	20.330 0.112	ALFOSC
20191218	58835.260	– –	21.949 0.097	21.734 0.052	20.654 0.151	ALFOSC
20191230	58847.125	– –	21.960 0.088	– –	20.811 0.097	ALFOSC
20191230	58847.125	– –	– –	>21.475 –	– –	ALFOSC
20200130	58878.140	– –	– –	– –	>20.757 –	ALFOSC

Table B16: Photometric data collected in Johnson bands for AT 2019abn (Vega mag).

Date	MJD	B (err)	V (err)	Instrument
20190127	58510.515	20.726 0.115	19.223 0.047	fa05
20190201	58515.465	19.503 0.037	18.036 0.028	fa05
20190213	58527.285	18.479 0.045	17.281 0.016	fa05
20190218	58532.270	– –	17.286 0.121	fa05
20190222	58536.500	– –	17.310 0.017	fa05
20190225	58539.500	– –	17.342 0.016	fa05
20190227	58541.150	18.532 0.031	17.353 0.017	IO:O
20190302	58544.260	– –	17.374 0.015	fa05
20190312	58554.130	18.826 0.032	17.551 0.017	IO:O
20190314	58556.930	18.861 0.058	17.633 0.026	IO:O
20190315	58557.190	– –	17.597 0.027	fa05
20190318	58560.220	– –	17.684 0.045	fa05
20190318	58560.235	18.954 0.047	17.678 0.019	IO:O
20190324	58566.480	– –	17.798 0.020	fa05

Table B17: Photometric data collected in Johnson bands for AT 2019abn (Vega mag).

Date	MJD	B (err)	V (err)	Instrument
20190408	58581.980	19.685 0.058	18.040 0.017	ALFOSC
20190409	58582.250	– –	18.107 0.017	fa05
20190411	58584.980	19.739 0.067	18.148 0.023	IO:O
20190415	58588.110	– –	18.232 0.052	fa05
20190417	58590.940	20.014 0.071	18.244 0.016	IO:O
20190425	58598.400	– –	18.340 0.023	fa05
20190428	58601.140	20.167 0.103	18.362 0.033	IO:O
20190501	58604.090	20.291 0.035	18.412 0.035	IO:O
20190503	58606.160	– –	18.495 0.040	fa05
20190504	58607.130	20.281 0.073	18.505 0.018	IO:O
20190507	58610.130	20.487 0.046	18.534 0.036	IO:O
20190508	58611.380	– –	18.575 0.046	fa05
20190512	58615.085	20.558 0.051	18.633 0.034	IO:O
20190516	58619.935	– –	18.745 0.089	IO:O
20190521	58624.990	20.714 0.076	18.851 0.046	IO:O
20190522	58625.330	– –	18.882 0.053	fa05
20190527	58630.100	20.989 0.161	18.940 0.064	IO:O
20190530	58633.270	– –	18.986 0.025	fa05
20190601	58635.020	21.025 0.158	19.001 0.050	IO:O
20190609	58643.030	21.198 0.080	19.264 0.032	IO:O
20190616	58650.220	– –	19.637 0.100	fa05
20190701	58665.210	– –	19.987 0.052	fa05
20190707	58671.980	– –	20.169 0.054	IO:O
20190707	58671.980	>21.594 –	– –	IO:O
20190716	58680.180	– –	20.375 0.184	fa07
20190729	58693.890	– –	20.700 0.048	ALFOSC
20190806	58701.120	– –	20.879 0.098	fa07
20190812	58707.890	– –	21.155 0.106	ALFOSC
20190830	58725.860	– –	21.866 0.121	ALFOSC
20190916	58742.840	– –	21.915 0.114	ALFOSC

Table B18: Photometric data collected in NIR bands for AT 2019abn (Vega mag).

Date	MJD	J (err)	H (err)	K (err)	Instrument
20190127	58510.110	16.263 0.061	– –	14.393 0.034	LIRIS
20190128	58511.210	15.856 0.024	– –	– –	LIRIS
20190129	58512.160	15.534 0.026	14.860 0.039	14.110 0.030	LIRIS
20190130	58513.177	15.361 0.025	14.701 0.034	14.019 0.041	LIRIS
20190201	58515.120	15.219 0.020	14.571 0.027	13.932 0.056	LIRIS
20190227	58541.160	– –	14.490 0.012	– –	IO:I
20190305	58547.240	15.043 0.014	14.556 0.021	13.937 0.012	NOTCAM
20190307	58549.030	– –	14.569 0.016	– –	IO:I
20190313	58555.930	– –	14.623 0.027	– –	IO:I
20190407	58580.930	– –	14.732 0.018	– –	IO:I
20190410	58583.180	15.173 0.018	14.752 0.019	14.358 0.017	NOTCAM
20190414	58587.920	– –	14.768 0.011	– –	IO:I
20190501	58604.130	15.318 0.010	14.912 0.016	14.563 0.016	NOTCAM
20190521	58624.940	15.427 0.018	15.009 0.033	14.700 0.017	NOTCAM
20190613	58647.020	– –	15.101 0.025	– –	IO:I
20190614	58648.040	15.601 0.026	15.117 0.030	14.812 0.026	NOTCAM
20190703	58668.000	15.885 0.016	15.274 0.026	14.904 0.020	NOTCAM
20190721	58685.890	16.050 0.018	15.411 0.017	15.023 0.024	NOTCAM
20190817	58712.890	16.447 0.022	15.730 0.031	15.090 0.078	NOTCAM
20190913	58739.850	17.445 0.047	16.479 0.043	15.697 0.041	NOTCAM
20191219	58837.250	– 0	17.582 0.091	– –	IO:I
20200113	58862.180	– 0	17.788 0.138	– –	IO:I
20200202	58882.260	– 0	18.025 0.129	– –	IO:I
20200207	58886.170	19.589 0.186	– –	16.526 0.064	NOTCAM
20200301	58909.180	– –	18.129 0.116	– –	IO:I
20200303	58911.125	20.212 0.204	– –	16.690 0.036	NOTCAM
20200331	58940.000	– –	18.731 0.178	– –	IO:I
20200508	58977.980	– –	– –	17.198 0.049	NOTCAM

Table B19: Photometric data collected in MIR bands for AT 2019abn (Vega mag).

Date	MJD	W1 (err)	W2 (err)	Instrument
20190524	58627.520	14.078 0.079	13.063 0.122	WISE
20191215	58832.730	15.077 0.238	14.202 0.232	WISE
20200522	58991.710	15.61 0.15	14.90 0.18	WISE

Table B20: Photometric data collected in MIR bands for AT 2019abn (Vega mag).

Date	MJD	[3.6] (err)	[4.5] (err)	Instrument
20190407	58580.58	13.19 0.02	12.59 0.02	Spitzer
20190530	58633.22	14.06 0.04	13.36 0.03	Spitzer
20190821	58716.66	14.35 0.02	14.19 0.09	Spitzer
20191025	58781.37	14.74 0.09	14.45 0.1	Spitzer

Table B21: Photometric data collected in Sloan bands for AT 2019ahd (AB mag).

Date	MJD	g (err)	r (err)	i (err)	z (err)	Instrument
20190130	58513.250	18.549 0.016	18.315 0.018	18.242 0.013	18.274 0.021	GROND
20190205	58519.110	18.036 0.012	17.697 0.020	17.511 0.015	17.347 0.019	ALFOSC
20190211	58525.040	18.122 0.030	17.571 0.067	17.442 0.012	17.361 0.015	ALFOSC
20190212	58526.350	18.150 0.011	17.609 0.069	17.457 0.012	17.389 0.034	GROND
20190216	58530.130	18.227 0.051	17.658 0.075	17.522 0.015	17.442 0.026	GROND
20190224	58538.120	18.265 0.035	17.679 0.091	17.514 0.018	17.461 0.035	GROND
20190225	58539.045	18.284 0.015	17.702 0.015	17.521 0.014	17.439 0.031	IO:O
20190303	58545.935	18.321 0.018	17.773 0.016	17.575 0.014	17.502 0.023	IO:O
20190307	58549.280	18.436 0.018	17.880 0.010	17.582 0.011	17.516 0.031	GROND
20190312	58554.920	18.547 0.026	17.904 0.014	17.640 0.018	17.541 0.024	IO:O
20190314	58556.230	18.545 0.026	17.935 0.036	17.659 0.044	17.528 0.020	GROND
20190325	58567.180	18.985 0.041	18.270 0.036	17.979 0.030	17.705 0.029	GROND
20190405	58578.160	19.455 0.027	18.556 0.029	18.118 0.016	17.840 0.022	GROND
20190413	58586.150	19.603 0.022	18.628 0.018	18.209 0.018	17.893 0.028	GROND
20190419	58592.050	19.720 0.043	18.742 0.022	18.363 0.021	18.073 0.029	GROND
20190429	58602.960	19.978 0.025	19.021 0.021	18.576 0.013	18.205 0.027	ALFOSC
20190505	58608.130	20.159 0.026	19.221 0.020	18.790 0.013	18.352 0.021	GROND
20190516	58619.090	20.350 0.043	19.462 0.016	19.078 0.016	18.571 0.023	GROND
20190518	58621.080	20.439 0.065	19.545 0.025	19.084 0.028	18.578 0.023	GROND
20190524	58627.090	20.640 0.032	19.586 0.017	19.183 0.025	18.665 0.024	GROND
20190605	58639.890	– –	– –	19.253 0.026	– –	ALFOSC
20190606	58640.010	20.683 0.042	19.740 0.023	– –	18.743 0.046	GROND
20190614	58648.980	20.885 0.242	19.904 0.068	19.476 0.038	18.990 0.081	GROND
20190621	58655.010	20.735 0.034	19.893 0.025	19.625 0.026	19.074 0.049	GROND
20190704	58668.980	20.904 0.027	20.081 0.019	19.817 0.022	19.139 0.021	GROND
20191123	58810.200	– –	21.361 0.074	21.181 0.064	20.465 0.088	ALFOSC
20191202	58819.190	– –	21.536 0.080	21.446 0.059	20.716 0.069	ALFOSC
20191218	58835.235	– –	21.977 0.183	21.721 0.150	20.879 0.140	ALFOSC
20191230	58847.100	– –	21.938 0.076	21.796 0.107	21.076 0.119	ALFOSC
20200128	58876.120	– –	22.247 0.100	22.105 0.133	21.543 0.082	ALFOSC
20200219	58898.210	– –	– –	– –	21.863 0.260	ALFOSC
20200416	58955.950	– –	– –	23.414 0.244	22.760 0.385	ALFOSC

Table B22: Photometric data collected in NIR bands for AT 2019ahd (Vega mag).

Date	MJD	J (err)	H (err)	K (err)	Instrument
20190130	58513.250	17.494 0.044	16.896 0.067	16.457 0.110	GRONDIR
20190205	58519.270	16.446 0.042	16.050 0.048	15.653 0.050	GRONDIR
20190212	58526.350	16.569 0.029	16.239 0.060	15.830 0.068	GRONDIR
20190216	58530.135	16.603 0.038	16.289 0.091	15.668 0.096	GRONDIR
20190224	58538.150	– –	16.244 0.039	– –	IO:I
20190224	58538.120	16.580 0.034	16.290 0.058	15.909 0.185	GRONDIR
20190307	58549.270	16.704 0.045	16.310 0.051	15.996 0.074	GRONDIR
20190314	58556.230	16.799 0.069	16.343 0.045	16.095 0.107	GRONDIR
20190325	58567.180	16.849 0.110	16.476 0.066	16.084 0.104	GRONDIR
20190405	58578.160	16.923 0.053	16.508 0.071	16.240 0.070	GRONDIR
20190413	58586.150	16.912 0.067	16.541 0.070	16.279 0.117	GRONDIR
20190419	58592.050	16.995 0.062	16.574 0.089	16.153 0.092	GRONDIR
20190516	58619.095	17.318 0.043	16.792 0.037	16.333 0.105	GRONDIR
20190518	58621.080	– 0.000	16.772 0.041	– 0.000	GRONDIR
20190524	58627.090	17.506 0.069	16.756 0.087	16.330 0.143	GRONDIR
20190606	58640.010	17.550 0.070	16.855 0.066	16.128 0.134	GRONDIR
20190614	58648.980	17.757 0.061	17.058 0.070	16.344 0.078	GRONDIR
20190621	58655.010	17.934 0.064	17.100 0.078	16.287 0.140	GRONDIR
20190704	58668.980	17.969 0.055	17.193 0.072	16.401 0.088	GRONDIR
20191220	58837.240	– –	17.853 0.117	– –	IO:I
20200116	58864.130	– –	18.116 0.130	– –	IO:I
20200131	58879.170	– –	18.178 0.117	– –	IO:I
20200206	58885.980	19.943 0.150	– –	17.055 0.072	NOTCAM
20200303	58911.030	20.386 0.165	18.668 0.100	17.237 0.072	NOTCAM
20200331	58939.910	– –	18.750 0.166	– –	IO:I
20200508	58977.880	– –	– –	17.608 0.066	NOTCAM

Table B23: Photometric data collected in Sloan bands for AT 2019udc (AB mag).

Date	MJD	u (err)	g (err)	r (err)	i (err)	z (err)	Instrument
20191107	58794.025	– –	17.944 0.050	17.702 0.054	17.510 0.037	– –	Prompt5
20191108	58795.605	– –	17.825 0.020	17.526 0.029	17.521 0.024	– –	fa12
20191109	58796.135	– –	17.771 0.018	17.510 0.023	17.482 0.025	– –	fa15
20191110	58797.025	– –	17.852 0.104	17.479 0.082	17.384 0.115	– –	Prompt5
20191113	58800.175	– –	17.692 0.018	17.451 0.018	17.431 0.024	– –	fa15
20191118	58805.890	18.783 0.072	17.866 0.039	17.587 0.021	17.555 0.023	17.564 0.045	ALFOSC
20191119	58806.165	– –	17.857 0.047	17.642 0.043	17.551 0.048	– –	Prompt5
20191122	58809.180	– –	18.044 0.055	17.788 0.057	17.690 0.040	17.668 0.169	Prompt5
20191126	58813.035	– –	18.291 0.075	17.911 0.049	17.919 0.042	– –	Prompt5
20191201	58819.000	19.898 0.047	18.561 0.013	18.159 0.018	18.044 0.021	18.048 0.032	ALFOSC
20191203	58820.090	– –	18.565 0.053	18.182 0.059	– –	– –	Prompt5
20191211	58828.855	– –	19.235 0.064	18.567 0.034	18.343 0.027	18.209 0.026	IO:O
20191217	58835.005	– –	19.448 0.014	18.785 0.022	18.564 0.020	18.451 0.026	ALFOSC
20191224	58841.830	– –	19.504 0.043	18.888 0.039	18.670 0.033	– –	fa14
20191226	58843.060	– –	19.656 0.117	18.954 0.079	18.739 0.081	– –	Prompt5
20191227	58844.850	– –	– –	– –	– –	18.565 0.089	fa06
20191231	58848.063	– –	19.844 0.144	– –	18.753 0.078	– –	Prompt5
20200102	58850.800	– –	– –	– –	– –	18.610 0.123	fa14
20200102	58850.805	– –	20.020 0.074	19.194 0.049	18.883 0.055	– 0.000	AFOSC
20200107	58855.055	– –	20.108 0.327	19.441 0.236	19.189 0.156	– –	fa03
20200108	58856.800	– –	– –	– –	– –	18.646 0.108	fa06
20200113	58861.905	– –	20.328 0.019	19.434 0.018	19.116 0.024	18.835 0.048	ALFOSC
20200115	58863.060	– –	– –	– –	– –	18.796 0.073	fa03
20200121	58869.040	– –	– –	– –	– –	18.950 0.114	fa03
20200123	58871.145	– –	20.401 0.059	19.570 0.052	19.263 0.065	– –	fa07
20200127	58875.030	– –	– –	– –	– –	18.784 0.171	fa15
20200208	58887.100	– –	20.899 0.182	19.978 0.103	19.783 0.112	– –	fa07
20200213	58892.830	– –	21.214 0.077	20.279 0.050	19.887 0.027	19.437 0.053	ALFOSC
20200213	58892.100	– –	– –	– –	– –	19.301 0.226	fa07
20200309	58917.850	– –	– –	20.557 0.163	20.222 0.103	– –	ALFOSC
20200719	59049.180	– –	– –	>22.604 –	– –	– –	ALFOSC
20200720	59050.150	– –	– –	– –	– –	>22.046 –	ALFOSC

Table B24: Photometric data collected in Johnson bands for AT 2019udc (Vega mag).

Date	MJD	U (err)	B (err)	V (err)	Instrument
20191104	58791.35	– –	19.34 0.27	18.15 0.23	SWIFT
20191104	58791.62	19.24 0.31	19.04 0.21	17.95 0.18	SWIFT
20191105	58792.28	18.91 0.2	18.62 0.14	17.95 0.20	SWIFT
20191105	58792.89	18.50 0.17	18.37 0.11	17.77 0.2	SWIFT
20191106	58793.41	18.21 0.2	18.33 0.17	17.80 0.22	SWIFT
20191107	58794.55	18.24 0.17	18.16 0.12	17.74 0.21	SWIFT
20191108	58795.42	18.00 0.16	18.12 0.12	– –	SWIFT
20191108	58795.590	17.803 0.057	18.119 0.028	17.636 0.031	fa12
20191109	58796.125	17.782 0.040	18.091 0.031	17.669 0.030	fa15
20191109	58796.020	– –	18.095 0.139	17.592 0.068	Prompt5
20191110	58797.035	– –	18.022 0.141	17.566 0.091	Prompt5
20191113	58800.160	17.664 0.042	17.961 0.030	17.566 0.025	fa15
20191118	58805.890	– –	18.176 0.045	17.754 0.033	ALFOSC
20191122	58809.195	– –	18.379 0.149	17.963 0.065	Prompt5
20191126	58813.050	– –	18.492 0.128	18.114 0.076	Prompt5
20191201	58819.000	– –	18.959 0.021	18.298 0.019	ALFOSC
20191203	58820.095	– –	18.997 0.109	18.365 0.073	Prompt5
20191205	58822.045	– –	19.210 0.153	18.411 0.069	Prompt8
20191211	58828.850	– –	19.494 0.103	18.737 0.060	IO:O
20191216	58833.065	– –	19.997 0.260	19.006 0.111	Prompt8
20191217	58835.000	– –	19.998 0.018	19.062 0.015	ALFOSC
20191224	58841.815	– –	20.142 0.047	19.102 0.051	fa14
20191226	58843.070	– –	20.517 0.353	19.246 0.114	Prompt8
20191230	58847.065	– –	20.561 0.402	19.318 0.154	Prompt8
20200102	58850.785	– –	20.411 0.110	19.491 0.065	AFOSC
20200107	58855.045	– –	– 0.000	19.559 0.358	fa03
20200113	58861.895	– –	20.810 0.026	19.809 0.022	ALFOSC
20200123	58871.130	– –	20.829 0.079	20.046 0.067	fa07
20200213	58892.830	– –	21.562 0.156	20.800 0.079	ALFOSC

Table B25: Photometric data collected in NIR bands for AT 2019udc (Vega mag).

Date	MJD	J (err)	H (err)	K (err)	Instrument
20191107	58794.055	17.010 0.037	16.558 0.050	16.296 0.042	SOFI
20191121	58808.225	17.118 0.049	16.706 0.058	16.423 0.053	SOFI
20191129	58816.155	17.305 0.051	16.939 0.102	16.532 0.061	SOFI
20191219	58836.810	– –	17.152 0.105	– –	IO:I
20191221	58838.830	– –	17.166 0.079	– –	IO:I
20200102	58850.920	– –	17.232 0.088	– –	IO:I
20200104	58852.117	17.775 0.061	17.236 0.069	16.881 0.108	SOFI
20200109	58857.960	17.845 0.030	– –	– –	NOTCAM
20200114	58862.830	– –	17.331 0.091	– –	IO:I
20200203	58882.040	17.926 0.063	17.320 0.065	16.899 0.075	SOFI
20200717	59047.000	– –	19.031 0.105	– –	NOTCAM

Table B26: Photometric data collected for AT 2019udc by the DLT40 survey (AB mag).

MJD	mag (err)	MJD	mag (err)
58791.614	18.813 0.0931	58792.197	18.0373 0.077
58787.624	19.4826 0.1	58792.572	17.9317 0.0814
58790.096	18.9805 0.1	58792.649	17.8879 0.0729
58791.261	19.0114 0.1	58792.673	17.8858 0.0529
58791.622	18.5988 0.0876	58792.713	17.9704 0.0521
58791.632	18.6765 0.0912	58793.006	17.8366 0.0831
58791.645	18.755 0.0751	58793.09	17.8071 0.0648
58791.646	18.5542 0.0862	58793.228	17.8323 0.0678
58791.646	18.5652 0.0762	58793.608	17.714 0.0427
58791.647	18.7568 0.0894	58793.657	17.7136 0.0423
58791.651	18.5639 0.0888	58794.605	17.6134 0.0644
58791.66	18.4281 0.0801	58794.703	17.5726 0.0546
58791.662	18.3993 0.0769	58800.994	17.436 0.0539
58791.665	18.4102 0.0763	58804.056	17.579 0.0458
58791.678	18.5166 0.0809	58804.803	17.5826 0.0502
58791.687	18.5128 0.0728	58808.013	17.6971 0.0608
58791.694	18.4858 0.085	58811.014	17.7981 0.0583
58791.7	18.6956 0.0831	58811.559	17.8801 0.082
58791.707	18.4038 0.079	58812.014	17.8329 0.0626
58791.717	18.5729 0.0817	58813.565	17.9227 0.0527
58791.73	18.3541 0.0671	58814.542	17.9798 0.0597
58791.741	18.3938 0.0808	58815.559	18.0809 0.0674
58791.747	18.4071 0.072	58816.257	18.0555 0.0729
58791.772	18.3719 0.0715	58817.27	18.0685 0.0731
58791.787	18.2971 0.0757	58818.027	18.2143 0.0791
58791.803	18.2481 0.0688	58819.017	18.1709 0.0688
58792.088	18.2304 0.0801	58823.022	18.2443 0.0838
58792.099	18.1909 0.0698		

Bibliography

Adams, S. M., Kochanek, C. S., Prieto, J. L., et al. 2016, Monthly Notices of the Royal Astronomical Society, 460, 1645

Albareti, F. D., Allende Prieto, C., Almeida, A., et al. 2017, ApJS, 233, 25

Anderson, J. P., González-Gaitán, S., Hamuy, M., et al. 2014, ApJ, 786, 67

Arcavi, I. 2017, Hydrogen-Rich Core-Collapse Supernovae, ed. A. W. Alsabti & P. Murdin (Cham: Springer International Publishing), 239–276

Arnett, W. D. 1980, APJ, 237, 541

Arnett, W. D. 1982, APJ, 253, 785

Arnett, W. D. & Fu, A. 1989, ApJ, 340, 396

Ashall, C., Mazzali, P., Sasdelli, M., & Prentice, S. J. 2016, MNRAS, 460, 3529

Barbon, R., Ciatti, F., & Rosino, L. 1979, AAP, 72, 287

Benetti, S., Turatto, M., Balberg, S., et al. 2001, MNRAS, 322, 361

Berger, E., Soderberg, A. M., Chevalier, R. A., et al. 2009, The Astrophysical Journal, 699, 1850

Bersten, M. C., Benvenuto, O., & Hamuy, M. 2011, ApJ, 729, 61

Bethe, H. A. 1990, Reviews of Modern Physics, 62, 801

Bond, H. E., Bedin, L. R., Bonanos, A. Z., et al. 2009, The Astrophysical Journal, 695, L154

Botticella, M. T., Pastorello, A., Smartt, S. J., et al. 2009, MNRAS, 398, 1041

Bottinelli, L., Gouguenheim, L., Paturel, G., & de Vaucouleurs, G. 1985, A&AS, 59, 43

Bouchet, P., Danziger, I. J., & Lucy, L. B. 1991, AJ, 102, 1135

Branch, D., Falk, S. W., McCall, M. L., et al. 1981, APJ, 244, 780

Branch, D. & Wheeler, J. C. 2017a, Supernova Explosions, 1st edn. (Springer), 441–477

Branch, D. & Wheeler, J. C. 2017b, Supernova Explosions, 1st edn. (Springer), 80–85

Branch, D. & Wheeler, J. C. 2017c, Supernova Explosions, 1st edn. (Springer), 267–280

Branch, D. & Wheeler, J. C. 2017d, Supernova Explosions, 1st edn. (Springer), 185–190

Brown, T. M., Baliber, N., Bianco, F. B., et al. 2013, PASP, 125, 1031

Cai, Y. Z., Pastorello, A., Fraser, M., et al. 2021, A&A, 654, A157

Cai, Y. Z., Pastorello, A., Fraser, M., et al. 2018, Monthly Notices of the Royal Astronomical Society, 480, 3424

Callis, E., Fraser, M., Pastorello, A., et al. 2021, arXiv e-prints, arXiv:2109.12943

Cappellaro, E. 2014, http://sngroup.oapd.inaf.it/snoopy.html

Cardelli, J. A., Clayton, G. C., & Mathis, J. S. 1989, ApJ, 345, 245

Chatzopoulos, E., Wheeler, J. C., & Vinko, J. 2012, APJ, 746, 121

Chevalier, R. A. & Fransson, C. 2017, in Handbook of Supernovae, ed. A. W. Alsabti & P. Murdin, 875

Colgate, S. A. & McKee, C. 1969, ApJ, 157, 623

Crockett, R. M., Smartt, S. J., Pastorello, A., et al. 2011, MNRAS, 410, 2767

Davidson, K. & Fesen, R. A. 1985, ARAA, 23, 119

de Vaucouleurs, G., de Vaucouleurs, A., Corwin, Herold G., J., et al. 1991, Third Reference Catalogue of Bright Galaxies

Dessart, L., Hillier, D. J., Sukhbold, T., Woosley, S. E., & Janka, H. T. 2021, A&A, 652, A64

Dexter, J. & Kasen, D. 2013, APJ, 772, 30

Doherty, C. L., Gil-Pons, P., Siess, L., & Lattanzio, J. C. 2017, Publications of the Astronomical Society of Australia, 34, e056

Doherty, C. L., Gil-Pons, P., Siess, L., Lattanzio, J. C., & Lau, H. H. B. 2015, MNRAS, 446, 2599

Draine, B. T. 2016, APJ, 831, 109

Eldridge, J. J., Mattila, S., & Smartt, S. J. 2007, MNRAS, 376, L52

Elmhamdi, A., Danziger, I. J., Chugai, N., et al. 2003, MNRAS, 338, 939

Falk, S. W. & Arnett, W. D. 1977, APJ, 33, 515

Fixsen, D. J., Cheng, E. S., Gales, J. M., et al. 1996, ApJ, 473, 576

Foley, R. J., Challis, P. J., Chornock, R., et al. 2013, APJ, 767, 57

Foley, R. J., Chornock, R., Filippenko, A. V., et al. 2009, The Astronomical Journal, 138, 376

Fox, O. D., Chevalier, R. A., Dwek, E., et al. 2010, APJ, 725, 1768

Fransson, C. & Chevalier, R. A. 1989, ApJ, 343, 323

Fransson, C., Chevalier, R. A., Filippenko, A. V., et al. 2002, APJ, 572, 350

Fraser, M., Ergon, M., Eldridge, J. J., et al. 2011, MNRAS, 417, 1417

Fraser, M., Magee, M., Kotak, R., et al. 2013, APJL, 779, L8

Gal-Yam, A., Arcavi, I., Ofek, E. O., et al. 2014, NAT, 509, 471

Gal-Yam, A., Kasliwal, M. M., Arcavi, I., et al. 2011, ApJ, 736, 159

Galbany, L., Hamuy, M., Phillips, M. M., et al. 2016, AJ, 151, 33

Gessner, A. & Janka, H.-T. 2018, APJ, 865, 61

Gogarten, S. M., Dalcanton, J. J., Murphy, J. W., et al. 2009, The Astrophysical Journal, 703, 300

Gogarten, S. M., Dalcanton, J. J., Williams, B. F., et al. 2010, ApJ, 712, 858

Graham, M. J., Kulkarni, S. R., Bellm, E. C., et al. 2019, Publications of the Astronomical Society of the Pacific, 131, 078001

Greiner, J., Bornemann, W., Clemens, C., et al. 2008, PASP, 120, 405

Gutiérrez, C. P., Anderson, J. P., Hamuy, M., et al. 2017a, ApJ, 850, 90

Gutiérrez, C. P., Anderson, J. P., Hamuy, M., et al. 2017b, ApJ, 850, 89

Hamuy, M. 2003, The Astrophysical Journal, 582, 905

Hamuy, M., Phillips, M. M., Suntzeff, N. B., et al. 1996, AJ, 112, 2391

Hamuy, M., Pinto, P. A., Maza, J., et al. 2001, ApJ, 558, 615

Heger, A. & Woosley, S. E. 2002, APJ, 567, 532

Hiramatsu, D., Howell, D. A., Van Dyk, S. D., et al. 2021, Nature Astronomy, 5, 903

Holmbo, S., Stritzinger, M., Nowack, G., et al. 2019, The Astronomer's Telegram, 12661, 1

Hosseinzadeh, G., Sand, D. J., Jencson, J. E., et al. 2022, arXiv e-prints, arXiv:2210.06499

Howell, D. 2019, in American Astronomical Society Meeting Abstracts, Vol. 233, American Astronomical Society Meeting Abstracts #233, 258.16

Humphreys, R. M., Bond, H. E., Bedin, L. R., et al. 2011, The Astrophysical Journal, 743, 118

Jäger, Zoltán, J., Vinkó, J., Bíró, B. I., et al. 2020, MNRAS, 496, 3725

Janka, H. T., Langanke, K., Marek, A., Martínez-Pinedo, G., & Müller, B. 2007, Physics Reports, 442, 38

Janka, H. T., Müller, B., Kitaura, F. S., & Buras, R. 2008, A&A, 485, 199

Jencson, J. E., Adams, S. M., Bond, H. E., et al. 2019, ApJ, 880, L20

Jerkstrand, A., Ertl, T., Janka, H. T., & Müller, E. 2017, MEMSAI, 88, 278

Jerkstrand, A., Ertl, T., Janka, H. T., et al. 2018, MNRAS, 475, 277

Jerkstrand, A., Fransson, C., Maguire, K., et al. 2012, A&A, 546, A28

Jerkstrand, A., Smartt, S. J., Fraser, M., et al. 2014, MNRAS, 439, 3694

Jha, S. 2019, Transient Name Server Classification Report, 2019-1237, 1

Jha, S. W. 2017, in Handbook of Supernovae, ed. A. W. Alsabti & P. Murdin, 375

Jones, S., Hirschi, R., Nomoto, K., et al. 2013, ApJ, 772, 150

Kaiser, N., Burgett, W., Chambers, K., et al. 2010, in Ground-based and Airborne Telescopes III, Vol. 7733, 77330E

Karachentsev, I., Lebedev, V., & Shcherbanovski, A. 1985, Bulletin d'Information du Centre de Donnees Stellaires, 29, 87

Kasen, D. & Bildsten, L. 2010, APJ, 717, 245

Kashi, A., Frankowski, A., & Soker, N. 2010, APJL, 709, L11

Kasliwal, M. M. 2012, Publications of the Astronomical Society of Australia, 29, 482

Keller, S. C., Schmidt, B. P., Bessell, M. S., et al. 2007, Publications of the Astronomical Society of Australia, 24, 1

Khokhlov, A. M. 1991, AAP, 245, 114

Kiewe, M., Gal-Yam, A., Arcavi, I., et al. 2012, APJ, 744, 10

Kitaura, F. S., Janka, H. T., & Hillebrandt, W. 2006, AAP, 450, 345

Kozyreva, A., Baklanov, P., Jones, S., Stockinger, G., & Janka, H.-T. 2021, MNRAS, 503, 797

Kozyreva, A., Janka, H.-T., Kresse, D., & Taubenberger, S. 2022, arXiv e-prints, arXiv:2203.00473

Lacy, M., Wilson, G., Masci, F., et al. 2005, ApJS, 161, 41

Landolt, A. U. 1992, AJ, 104, 340

Law, N. M., Kulkarni, S., Ofek, E., et al. 2009, in Bulletin of the American Astronomical Society, Vol. 41, American Astronomical Society Meeting Abstracts #213, 418

Leung, S.-C., Nomoto, K., & Suzuki, T. 2019, arXiv e-prints, arXiv:1901.11438

Li, W., Leaman, J., Chornock, R., et al. 2011, Monthly Notices of the Royal Astronomical Society, 412, 1441

Lisakov, S. M., Dessart, L., Hillier, D. J., Waldman, R., & Livne, E. 2017, MNRAS, 466, 34

Lisakov, S. M., Dessart, L., Hillier, D. J., Waldman, R., & Livne, E. 2018, MNRAS, 473, 3863

MacAlpine, G. M. & Satterfield, T. J. 2008, AJ, 136, 2152

Maeda & Terada. 2016, International Journal of Modern Physics D, 25, 1630024

Maguire, K. 2017, in Handbook of Supernovae, ed. A. W. Alsabti & P. Murdin, 293

Maguire, K., Di Carlo, E., Smartt, S. J., et al. 2010, MNRAS, 404, 981

Martinez, L., Bersten, M. C., Anderson, J. P., et al. 2021, arXiv e-prints, arXiv:2111.06529

Matheson, T., Challis, P., Kirshner, R., & Calkins, M. 2003, IAU Circ., 8063, 2

Mauerhan, J. C., Smith, N., Silverman, J. M., et al. 2013, MNRAS, 431, 2599

Maund, J. R., Mattila, S., Ramirez-Ruiz, E., & Eldridge, J. J. 2014, MNRAS, 438, 1577

Maund, J. R., Smartt, S. J., & Danziger, I. J. 2005, MNRAS, 364, L33

McCully, C., Jha, S. W., Foley, R. J., et al. 2014, NAT, 512, 54

McCully, C., Jha, S. W., Scalzo, R. A., et al. 2022, APJ, 925, 138

McQuinn, K. B. W., Skillman, E. D., Dolphin, A. E., Berg, D., & Kennicutt, R. 2016, ApJ, 826, 21

McQuinn, K. B. W., Skillman, E. D., Dolphin, A. E., Berg, D., & Kennicutt, R. 2017, AJ, 154, 51

Mezzacappa, A. 2005, Annual Review of Nuclear and Particle Science, 55, 467

Minkowski, R. 1941, Publications of the Astronomical Society of the Pacific, 53, 224

Miyaji, S., Nomoto, K., Yokoi, K., & Sugimoto, D. 1980, PASJ, 32, 303

Monard, L. A. G. 2008, International Astronomical Union Circular, 8946, 1

Moore, C. E. 1945, Contributions from the Princeton University Observatory, 20, 1

Moriya, T., Tominaga, N., Tanaka, M., et al. 2010, ApJ, 719, 1445

Moriya, T. J. & Eldridge, J. J. 2016, MNRAS, 461, 2155

Moriya, T. J., Mazzali, P. A., & Tanaka, M. 2019, MNRAS, 484, 3443

Moriya, T. J., Tominaga, N., Langer, N., et al. 2014, A&A, 569, A57

Mucciarelli, A., Monaco, L., Bonifacio, P., et al. 2019, AAP, 623, A55

Müller-Bravo, T. E., Gutiérrez, C. P., Sullivan, M., et al. 2020, MNRAS, 497, 361

Munoz-Arancibia, A., Mourao, A., Forster, F., et al. 2021, Transient Name Server Discovery Report, 2021-112, 1

Nagy, A. P. & Vinkó, J. 2016, AAP, 589, A53

Nasonova, O. G., de Freitas Pacheco, J. A., & Karachentsev, I. D. 2011, A&A, 532, A104

Nomoto, K. 1984, ApJ, 277, 791

Nomoto, K. & Leung, S.-C. 2017, in Handbook of Supernovae, ed. A. W. Alsabti & P. Murdin, 483

Nordin, J., Brinnel, V., Giomi, M., et al. 2020, Transient Name Server Discovery Report, 2020-555, 1

Ohsawa, R., Sakon, I., Onaka, T., et al. 2010, APJ, 718, 1456

O'Neill, D., Kotak, R., Fraser, M., et al. 2021, A&A, 645, L7

O'Neill, D., Kotak, R., Fraser, M., et al. 2019, A&A, 622, L1

Pastorello, A., Chen, T. W., Cai, Y. Z., et al. 2019a, A&A, 625, L8

Pastorello, A., Della Valle, M., Smartt, S. J., et al. 2007, NAT, 449, 1

Pastorello, A. & Fraser, M. 2019, Nature Astronomy, 3, 676

Pastorello, A., Fraser, M., Valerin, G., et al. 2021, A&A, 646, A119

Pastorello, A., Mason, E., Taubenberger, S., et al. 2019b, A&A, 630, A75

Pastorello, A., Sauer, D., Taubenberger, S., et al. 2006, MNRAS, 370, 1752

Pastorello, A., Valenti, S., Zampieri, L., et al. 2009, Monthly Notices of the Royal Astronomical Society, 394, 2266

Pastorello, A., Zampieri, L., Turatto, M., et al. 2004, MNRAS, 347, 74

Pastorello & Fraser. 2019, Nature Astronomy, 3

Patat, F., Cappellaro, E., Danziger, J., et al. 2001, APJ, 555, 900

Patat, F., Maund, J. R., Benetti, S., et al. 2010, Astronomy and Astrophysics, 510, A108

Pian, E. & Mazzali, P. A. 2017, in Handbook of Supernovae, ed. A. W. Alsabti & P. Murdin, 277

Podsiadlowski, P., Langer, N., Poelarends, A. J. T., et al. 2004, APJ, 612, 1044

Poelarends, A. J. T., Herwig, F., Langer, N., & Heger, A. 2008, ApJ, 675, 614

Poelarends, A. J. T., Wurtz, S., Tarka, J., Cole Adams, L., & Hills, S. T. 2017, APJ, 850, 197

Poznanski, D., Prochaska, J. X., & Bloom, J. S. 2012, MNRAS, 426, 1465

Prieto, J. L. 2008, The Astronomer's Telegram, 1550

Prieto, J. L., Sellgren, K., Thompson, T. A., & Kochanek, C. S. 2009, The Astrophysical Journal, 705, 1425

Pumo, M. L., Turatto, M., Botticella, M. T., et al. 2009, ApJ, 705, L138

Pumo, M. L. & Zampieri, L. 2011, ApJ, 741, 41

Pumo, M. L. & Zampieri, L. 2013, MNRAS, 434, 3445

Pumo, M. L., Zampieri, L., Spiro, S., et al. 2017, MNRAS, 464, 3013

Pumo, M. L., Zampieri, L., & Turatto, M. 2010, Memorie della Societa Astronomica Italiana Supplementi, 14, 123

Rakavy, G. & Shaviv, G. 1967, APJ, 148, 803

Reguitti, A., Pumo, M. L., Mazzali, P. A., et al. 2021, MNRAS, 501, 1059

Riess, A. G., Filippenko, A. V., Challis, P., et al. 1998, AJ, 116, 1009

Ritossa, C., Garcia-Berro, E., & Iben, Icko, J. 1996, ApJ, 460, 489

Rodríguez, Ó., Pignata, G., Anderson, J. P., et al. 2020, MNRAS, 494, 5882

Roy, R., Kumar, B., Benetti, S., et al. 2011, ApJ, 736, 76

Schlafly & Finkbeiner, D. P. 2011, The Astrophysical Journal, 737, 103

Shappee, B., Prieto, J., Stanek, K. Z., et al. 2014, in American Astronomical Society Meeting Abstracts, Vol. 223, American Astronomical Society Meeting Abstracts 223, 236.03

Siebert, M. R., Dimitriadis, G., Kilpatrick, C. D., et al. 2019, Transient Name Server Classification Report, 2019-2287, 1

Siess, L. 2007, Astronomy and Astrophysics, 476, 893

Skrutskie, M. F., Cutri, R. M., Stiening, R., et al. 2006, AJ, 131, 1163

Smartt, S. J. 2009a, Annual Review of Astronomy and Astrophysics, 47, 63

Smartt, S. J. 2009b, ARA&A, 47, 63

Smartt, S. J. 2015, Publ. Astron. Soc. Australia, 32, e016

Smartt, S. J., Eldridge, J. J., Crockett, R. M., & Maund, J. R. 2009, MNRAS, 395, 1409

Smartt, S. J., Valenti, S., Fraser, M., et al. 2015a, Astronomy and Astrophysics, 579, A40

Smartt, S. J., Valenti, S., Fraser, M., et al. 2015b, A&A, 579, A40

Smith, N. 2013, MNRAS, 434, 102

Smith, N. 2014, ARAA, 52, 487

Smith, N. 2017, in Handbook of Supernovae, ed. A. W. Alsabti & P. Murdin, 403

Smith, N. & McCray, R. 2007, APJL, 671, L17

Sorce, J. G., Tully, R. B., Courtois, H. M., et al. 2014, MNRAS, 444, 527

Spergel, D. N., Bean, R., Doré, O., et al. 2007, ApJS, 170, 377

Spiro, S., Pastorello, A., Pumo, M. L., et al. 2014, MNRAS, 439, 2873

Springob, C. M., Haynes, M. P., Giovanelli, R., & Kent, B. R. 2005, ApJS, 160, 149

Steele, I. A., Smith, R. J., Rees, P. C., et al. 2004, in Society of Photo-Optical Instrumentation Engineers (SPIE) Conference Series, Vol. 5489, Ground-based Telescopes, ed. J. Oschmann, Jacobus M., 679–692

Stritzinger, M. D., Taddia, F., Fraser, M., et al. 2020, A&A, 639, A103

Szczygieł, D. M., Kochanek, C. S., & Dai, X. 2012, APJ, 760, 20

Taddia, F., Sollerman, J., Fremling, C., et al. 2015, AAP, 580, A131

Taddia, F., Stritzinger, M. D., Bersten, M., et al. 2018, AAP, 609, A136

Takáts, K., Pignata, G., Pumo, M. L., et al. 2015, MNRAS, 450, 3137

Takáts, K., Pumo, M. L., Elias-Rosa, N., et al. 2014, MNRAS, 438, 368

Tartaglia, L. 2015, PhD thesis, Università degli studi di Padova

Tartaglia, L., Pastorello, A., Sollerman, J., et al. 2020, AAP, 635, A39

Tartaglia, L., Sand, D. J., Valenti, S., et al. 2018, ApJ, 853, 62

Tauris, T. M., Langer, N., Moriya, T. J., et al. 2013, APJL, 778, L23

Thompson, T. A., Prieto, J. L., Stanek, K. Z., et al. 2009, The Astrophysical Journal, 705, 1364

Tody, D. 1986, in Society of Photo-Optical Instrumentation Engineers (SPIE) Conference Series, Vol. 627, Instrumentation in astronomy VI, ed. D. L. Crawford, 733

Tody, D. 1993, in Astronomical Society of the Pacific Conference Series, Vol. 52, Astronomical Data Analysis Software and Systems II, ed. R. J. Hanisch, R. J. V. Brissenden, & J. Barnes, 173

Tomasella, L., Cappellaro, E., Pumo, M. L., et al. 2018, MNRAS, 475, 1937

Tominaga, N., Blinnikov, S. I., & Nomoto, K. 2013, APJL, 771, L12

Tonry, J. L., Denneau, L., Heinze, A. N., et al. 2018, PASP, 130, 064505

Tully, R. B., Courtois, H. M., Dolphin, A. E., et al. 2013, AJ, 146, 86

Tully, R. B., Courtois, H. M., & Sorce, J. G. 2016, AJ, 152, 50

Tully, R. B. & Fisher, J. R. 1988, Catalog of Nearby Galaxies

Tully, R. B., Rizzi, L., Shaya, E. J., et al. 2009, AJ, 138, 323

Tully, R. B., Shaya, E. J., & Pierce, M. J. 1992, ApJS, 80, 479

Turatto, M. 2003, in Supernovae and Gamma-Ray Bursters, ed. K. Weiler, Vol. 598, 21–36

Turatto, M., Mazzali, P. A., Young, T. R., et al. 1998, ApJ, 498, L129

Utrobin, V. P. & Chugai, N. N. 2008, A&A, 491, 507

Utrobin, V. P. & Chugai, N. N. 2009, A&A, 506, 829

Utrobin, V. P., Chugai, N. N., & Pastorello, A. 2007, A&A, 475, 973

Valenti, S., Sand, D., Stritzinger, M., et al. 2015, MNRAS, 448, 2608

Valerin, G., Pumo, M. L., Pastorello, A., et al. 2022, arXiv e-prints, arXiv:2203.03988

Van Dyk, S. D., Davidge, T. J., Elias-Rosa, N., et al. 2012, AJ, 143, 19

Voshchinnikov, N. V., Henning, T., & Il'in, V. B. 2017, APJ, 837, 25

Wanajo, S., Nomoto, K., Janka, H. T., Kitaura, F. S., & Müller, B. 2009, The Astrophysical Journal, 695, 208

Wesson, R., Barlow, M. J., Matsuura, M., & Ercolano, B. 2015, MNRAS, 446, 2089

Wheeler, J. C. & Benetti, S. 2000, in Allen's Astrophysical Quantities, ed. A. N. Cox, 451

Wheeler, J. C. & Swartz, D. A. 1993, Space Sci. Rev., 66, 425

Williams, S. C., Darnley, M. J., Bode, M. F., & Steele, I. A. 2015, ApJ, 805, L18

Williams, S. C., Jones, D., Pessev, P., et al. 2020, A&A, 637, A20

Willick, J. A., Courteau, S., Faber, S. M., et al. 1997, ApJS, 109, 333

Woosley, S. E., Heger, A., & Weaver, T. A. 2002, Reviews of Modern Physics, 74, 1015

Wright, E. L., Eisenhardt, P. R. M., Mainzer, A. K., et al. 2010, AJ, 140, 1868

Yang, S., Sollerman, J., Strotjohann, N. L., et al. 2021, arXiv e-prints, arXiv:2107.13439

Yaron, O. & Gal-Yam, A. 2012, PASP, 124, 668

York, D. G., Adelman, J., Anderson, John E., J., et al. 2000, AJ, 120, 1579

Zampieri, L., Pastorello, A., Turatto, M., et al. 2003, MNRAS, 338, 711

Zampieri, L., Shapiro, S. L., & Colpi, M. 1998a, ApJ, 502, L149

Zampieri, L., Shapiro, S. L., & Colpi, M. 1998b, ApJ, 502, L149

Zhang, J., Wang, X., József, V., et al. 2020, MNRAS, 498, 84

Zhang, W., Woosley, S. E., & Heger, A. 2008, APJ, 679, 639

Zwicky, F. 1968, Publications of the Astronomical Society of the Pacific, 80, 462